

Challenging the Standard Model with the Compact Muon Solenoid in W/Z + jets studies and SUSY searches with b -jets

Lukas Vaneldereren
2011-2012



Challenging the Standard Model with the Compact Muon Solenoid in W/Z + jets studies and SUSY searches with b -jets

Lukas Vaneldereren

PhD thesis, 2011-2012
Universiteit Gent, Faculty of Sciences

Challenging the Standard Model with the Compact Muon Solenoid in $W/Z + \text{jets}$ studies and SUSY searches with b -jets

Lukas Vanelderren

Promotoren: Prof. Dr. Dirk Ryckbosch
Dr. Michael Tytgat

Proefschrift ingediend tot het verkrijgen van de graad van
Doctor in de Wetenschappen: Fysica

Vakgroep Fysica en Sterrenkunde, academiejaar 2011–2012

Thanks!

The last months, while writing this thesis, I surprised myself. Usually I'm not easily impressed by what I do, but this time I am: How much I learned and how much I changed over the past four years! Now, I do not know how to thank all the people that made this happen. The least I can do is to tell in a few words how great you are.

Dirk, I am very fortunate you suspected a good PhD candidate in me about 4 years ago. The door of your office has always been open, where you had some wise words ready for most of my questions and problems. Thank you for your thrust and all your efforts to make my PhD practically possible. Michael, thank you for introducing me to CERN and CMS, and for bringing me in contact with the right people: Maria, Maurizio and the entire VecBos group.

Dear Maria and Maurizio, your support has been tremendous. You have encouraged me with so much enthusiasm and sincere concern and taught me so many things until I finally got on track and did my thing in the $W/Z + \text{jets}$ measurement. Those (in)famous VecBos meetings, they were long, chaotic and temperamentful. Still, I look back to them with much nostalgia. Many thanks to you, the other VecBos people and the entire $V + \text{jets}$ group.

Sezen, you are simply fantastic! Since Maria brought us together to do the sPlot thing you took me under your wing and I cannot count all the things I caught up from you (your obsession for clarity is contagious, let's hope it takes epidemic forms). Working with you is a pleasure and great fun, and I hope we can take up many more interesting challenges in the future. I'm honored to have you as a friend and I hope to cook or have many more dinners at Hotel Sekmen.

Harrison, together with Sezen you reshaped my way of thinking about experimental physics and science in general. I consider this a very precious gift. I've never met anyone else spreading wisdom in such a clear, simple, generous and kind way.

Dear Nadja, I guess we walked our first Bayesian steps together. Advising someone who is smart and eager as you and has such genuine interest for physics, is a pleasure, especially with the expert help from Sezen and Harrison. Your master thesis was a great starting point to the SUSY part of my thesis. Many thanks!

Special thanks to all the previously mentioned people for reading (parts of) this thesis so carefully and their many helpful comments.

To all inhabitants of the INW. Although our institute is housed in a typical cold-war building (strangely without nuclear shelter), it has a special, warm atmosphere. People are nice. They say hi, keep their doors open, are always happy to help, and there are always a few nutcases hanging around when you need them. Special credits go to my office mates, Filip and Piet. Dear friends, you were the perfect guys to share the joy and frustration that come with a PhD. Let's keep in touch!

To all my friends in and outside physics and my two adorable sisters. You made sure that I did not forget about what happens when it's all work and no play. Without the marvelous dinners, the crazy parties, the beautiful bicycle rides, and the many times we simply spent together (met beertjesthee), I would never have had the energy and courage to finish my PhD. Special thanks to all who helped us creating our home and to the many homeless friends we've sheltered in it.

Mama en papa. Ik ben er geraakt! Ik ben nu iets meer dan vier jaar het huis uit, maar jullie liefdevolle steun is niet afgenomen. Enkele memorabele momenten zijn jullie bezoek aan Genève tijdens mijn eerste verblijf daar in 2007, het aanleggen van de waterleiding in ons huis in de Brugse Poort in 2008, mijn veredeld kluizenaarsschap in Merendree tijdens het schrijven van deze thesis in September 2011, jullie vreugde tijdens het feest na mijn doctoraatsverdediging. Aan mijn ganse familie en schoonfamilie en in het bijzonder aan mijn grootouders, bedankt voor de steeds oprechte interesse en de morele steun!

Bovenste beste beesje. Eh, waar moet ik beginnen? Wij hebben samen een warm thuis gemaakt, waarin ik mij supergoed voel. Wij zien elkaar zo graag, we hebben zoveel respect voor elkaar en we steunen elkaar altijd door en door. Jouw bijdrage aan dit werk kan niet overschat worden. Waar we terechtkomen de volgende jaren, dat weten we nog niet, maar als we verhuizen dan nemen we die goeie dingen gewoon mee. Ik kijk uit naar al wat komen mag samen met jou.

Gent, January 2012

Contents

I	Challenging the Standard Model with proton collisions	1
1	Introduction	3
2	The Standard Model of particle physics	7
2.1	Challenges	8
2.2	Supersymmetric alternatives	9
3	A proton collision walkthrough	11
3.1	Minimum bias interactions	11
3.2	Hard interaction	13
3.3	Showering	13
3.4	Hadronization	14
3.5	Proton structure	15
3.6	Underlying event	15
3.7	Monte Carlo event generators	16
4	The Large Hadron Collider	19
5	The Compact Muon Solenoid	23
5.1	Coordinate system	23
5.2	Magnet system	24
5.3	Silicon tracker	24
5.4	Electromagnetic calorimeter	26
5.5	Hadronic calorimeter	26
5.6	Muon system	27
5.7	Trigger	28
6	Collision reconstruction with CMS	31

CONTENTS

6.1	Reconstruction of Particle Flow elements	32
6.2	Particle reconstruction and identification	33
6.3	Physics objects for analyses	37
II	Early measurements of W/Z + jets production	45
7	Introduction	47
8	Analysis strategy	51
8.1	Introduction	51
8.2	Measurements	52
8.3	Analysis path for $W(\rightarrow \mu\nu)$	54
9	Data and simulation for $W(\rightarrow \mu\nu)$ measurements	57
9.1	Data	57
9.2	MC simulation	57
9.3	Selection	59
9.4	Selection efficiency for $W(\rightarrow \mu\nu)$	61
10	Measurements of $W(\rightarrow \mu\nu)$ + jets production	69
10.1	Discriminating variables	69
10.2	Maximum Likelihood fits	70
10.3	Fit performance	82
10.4	Estimates for shape parameters	86
10.5	Measured signal on reconstruction level	94
10.6	Systematic uncertainties	96
10.7	Unfolding	101
10.8	Measurement of Berends-Giele scaling	103
10.9	Measurement of charge asymmetry	105
10.10	Summary	106
11	Results	111
12	Discussion	125
III	Search for SUSY in all-hadronic events with b-jets	131
13	Introduction	133
14	A Bayesian statistical framework	137

CONTENTS

14.1	Bayes' Theorem	137
14.2	Bayesian hypothesis testing	138
14.3	Bayesian optimization	146
14.4	Combination of count experiments	148
14.5	Integration over the parameter space	149
14.6	Summarizing example	150
15	The phenomenological MSSM	151
15.1	Impact from existing measurements	152
16	Search with jets, b-jets and E_T^{miss}	157
16.1	Data samples	158
16.2	Standard Model predictions	159
16.3	Predictions for the pMSSM	160
16.4	Definition of physics objects	161
16.5	Event selection	164
16.6	Results	169
17	Bayesian tools for the design of searches for new physics	179
17.1	Optimization of single count experiments	180
17.2	Refinements and generalization	182
	Appendices	189
	A Calculations for the Bayesian statistical framework	189
	B Notes on the interpretation	195
	Samenvatting	199
	Summary	205
	List of acronyms	211
	Bibliography	213

Part I

Challenging the Standard Model with proton collisions

1

Introduction

Our current understanding of nature's small scales is synthesized in *The Standard Model of Particle Physics* [1]. According to this model, nature provides us with a variety of elementary particles: quarks, leptons, the photon, W and Z bosons, gluons and the Higgs boson. However, most of these particles do not reveal themselves easily. Therefore, to study these particles, physicists often turn to the spectacular environment of highly energetic collisions between particles.

It was mainly through the study of particle collisions that the Standard Model was established. Indeed, positrons were first observed in 1932 [2] and muons in 1936 [3] in the remnants of collisions between highly energetic cosmic particles and nuclei in the earth's atmosphere; first experimental evidence for the compositeness of protons and thus the existence of quarks was found in electron-proton collisions at the Stanford Linear Collider in 1968 [4][5]; weak neutral currents were discovered in collisions between muon neutrinos and nuclei in freon molecules by the Gargamelle experiment in 1973 [6]. These and many more such experimental findings enabled theorists to construct the Standard Model during the 1970s. Since then, further studies of particle collisions have proved the Standard Model to be spectacularly predictive: e.g. the W and Z bosons were first observed in proton-proton collisions at the Super Proton-antiproton Synchrotron in 1983 [7][8][9][10]; proof for three generations of low-mass neutrinos was found in electron-positron collisions at the Stanford Linear Collider in 1989 [11]; the predicted top quark was first observed in 1995 at the Tevatron [12][13].

Yet, the Standard Model is not the final theory of particle physics. First of all, the theory is not complete. E.g., it incorporates neither general relativity nor neutrino oscillations and does not provide a dark matter candidate. Furthermore, the Standard Model suffers from at least two fine tuning problems: the hierarchy problem [14] and the strong CP problem [15]. Although these problems are not actual inconsistencies, many physicists argue that they hint to physics beyond the Standard Model. Last but not least, an experimental corner stone is missing: up till now, no evidence was found for the existence of the Higgs particle.

These defects and tensions motivate both theoretical and experimental physicists to continue challenging the predictive power of the Standard Model. They confront predictions with measurements, both of ever greater precision. Theorists improve their computational techniques, while experimentalists build more powerful particle colliders with higher energies and luminosities, and improve their detector apparatus. At the same time, they turn to ever more powerful data analysis techniques. Theorists also invent extensions and alternatives to the Standard Model, which serve as guidelines to the many searches for new phenomena that are not included in the Standard Model.

The driving force in this challenge for the coming years and maybe decades, is the latest and greatest particle collider, the Large Hadron Collider. This proton-proton collider with its center of mass energy, eventually near 14 TeV, and expected integrated luminosity of several 1000s of fb^{-1} , spectacularly overpowers any previous collider. Therefore, hopes are high that it will provide answers to many of the pending questions in physics and confirm the Standard Model or pave the path towards a new Standard Model of particle physics, maybe even a theory of everything.

The last four years I took part in this challenge, contributing to the Compact Muon Solenoid experiment at the Large Hadron Collider. There, I conducted research on two quite distinct subjects. The first one is the Standard Model production process of W and Z bosons in association with jets. This production process is studied because it is an important background to several searches for new phenomena and studies of other Standard Model processes. Moreover, these processes provide relatively clean probes for perturbative QCD, and therefore, are very important for the validation and tuning of the predictions for many Standard Model production processes. In Part II of this thesis, I will describe the first detailed study of jet multiplicity in W and $Z + \text{jet}$ production in proton-proton collisions at $\sqrt{s} = 7$ TeV [16]. Most emphasis will lay on the study of $W(\rightarrow \mu\nu) + \text{jets}$ to which I am one of the main

INTRODUCTION

contributors.

The second subject is the search for Supersymmetry in proton-proton collision at $\sqrt{s} = 7$ TeV. Together with colleagues I performed a search in pp events with jets, b -jets and missing transverse energy in the final state, focusing on scenarios leading to and enhanced production of bottom and top quarks. This search is described in Part III of thesis, with special emphasis on a Bayesian method for the interpretation of search results, which is quite unusual for our field.

Before moving to these topics of research, I will elaborate on their theoretical and experimental context in Part I.

2

The Standard Model of particle physics

The Standard Model of particle physics (SM) summarizes our current knowledge about the fundamental building blocks of nature. This model was developed during the sixties and seventies, driven by a number of spectacular experimental findings and revolutionary theoretical ideas. The following decades, the SM became one of the greatest successes in physics ever, as it was able to describe almost all subsequent experimental findings in particle physics. A comprehensive description of the Standard Model, its problems, extensions and alternatives, falls outside the scope of this thesis. However, the short summary in this chapter will introduce some of its main properties and terminology and point to relevant documentation.

According to the SM, nature is built from 6 flavors of particles called quarks (u, d, c, s, t, b) and another 6 flavors called leptons ($e, \nu_e, \mu, \nu_\mu, \tau, \nu_\tau$). Both leptons and quarks are fermions, having spin $1/2$. Particles are subject to three types of interactions: the electromagnetic and the weak interaction, which affect all matter particles, and the strong interaction which only affects the quarks. Interactions take place between particles that carry a certain charge, through the exchange of particles called gauge bosons. The charges associated to the electromagnetic, weak and strong interactions are respectively the electric charge, the weak isospin charge and the color charge. The gauge bosons that are exchanged between the charged particles

and mediate the interactions are the photon (γ) for the electromagnetic charge, the W^+ , W^- and Z^0 bosons for the weak charge and the 8 kinds of gluons (g) for the strong charge. Particles acquire mass through interaction with yet another particle the Higgs boson.

The SM describes these particles and their interactions with a relativistic quantum field theory, a quantum mechanical formulation of nature in which particles are treated as fields in space and time and to which the symmetries of the theory of special relativity apply. In this formulation, the electromagnetic and weak interaction and the strong interaction are described by respectively the Electroweak Theory (EWK) and Quantum Chromodynamics (QCD). The property of mass is incorporated in the SM by applying the Brout-Englert-Higgs mechanism to the electroweak symmetry breaking and by introducing Yukawa couplings between the associated Higgs boson and the quarks and leptons.

All of this is explained very well and in much detail in several text books. An excellent extensive theoretical introduction to quantum field theory and the Standard Model is for instance Reference [17]. References [1] [18] [19] treat the SM in a more phenomenological way, paying much attention to the present experimental status and interests for future experimental measurements. The present experimental evidence for the SM is quite overwhelming. In fact, at present, the last missing experimental corner stone is the long anticipated discovery of the Higgs boson. The experimental status of the SM, its evidence and the measurements of its properties, are summarized in the publications of the Particle Data Group (PDG) [20].

2.1 Challenges

The SM is most probably not the final theory of particle physics. Various arguments motivate this statement. Some are of rather philosophical or aesthetic origin, other arguments are almost indisputable.

The most important argument is probably that the SM is not consistent with general relativity and is not able to incorporate the gravitational interaction [21]. Along the same lines, but on more aesthetic grounds, many physicists believe that all of nature's interactions can be unified in a single type of interaction, which, through the mechanism of spontaneous symmetry breaking, gives rise to the different types of interaction that we have observed today. At present, in the SM, this unification has only been established for the electromagnetic and weak interactions.

Furthermore, the SM suffers from fine tuning problems, of which the most famous is the so called Hierarchy problem [14]. Quantum corrections to the Higgs mass are of the same order of magnitude as the scale at which the SM description of nature breaks down. These quantum corrections are orders of magnitude higher than the expected physical Higgs mass of about 100 GeV, unless unknown phenomena take place at scales around 1 TeV.

Another important and often used argument against the SM rises from the concepts of dark matter and dark energy. Observations of galactic rotation curves and the fluctuation of the cosmic microwave background strongly suggest the existence of dark matter [22]. The observed acceleration of the expansion of the Universe is often explained by the concept of dark energy which would provide a repulsive gravitational force. None of the SM particles possess the right properties to constitute such matter or energy.

The relatively large number of free parameters of the SM is also a source of doubt for many particle physicists. Some argue that a fundamental theory can only have a few parameters and should explain why e.g. quarks and leptons possess the masses we have observed.

2.2 Supersymmetric alternatives

The arguments mentioned above, and several others, have served as inspiration for the development of extensions and alternatives to the SM. The most popular such models are the many models with broken Supersymmetry (SUSY), a symmetry between fermions and bosons [14]. The most important motivation for SUSY is its elegant solution to the Hierarchy problem. Furthermore, SUSY provides means to unify the electroweak and strong interactions and can provide a dark matter candidate. Finally, SUSY may pave the way to the unification of the SM interactions with the gravitational interaction through for example string theory [21].

According to SUSY models, there exists a superpartner for each of the SM particles. The superpartner of a certain SM particle has the same quantum numbers except for the spin. The superpartners of SM fermions are bosons and the superpartners of SM bosons are fermions. In addition, SUSY predicts besides the SM Higgs boson plus several additional Higgs bosons, each with superpartner. None of the superpartners has ever been observed, consequently, Supersymmetry must be broken and the mass eigenstates of the superpartners must be heavier than the masses of the SM particles.

CHAPTER 2

The mass eigenstates of the SUSY particles are the *squarks* and *sleptons*, which are superpartners of the SM quarks and leptons, the *neutralinos*, mixtures of the superpartners of the neutral SM bosons, and *charginos*, mixtures of the superpartners of the charged SM bosons.

SUSY is in fact not a model. Rather it is a theoretical framework in which extensions of the SM can be developed. A well known example is the Minimal Supersymmetric extension of the Standard Model (MSSM). In this thesis we will interpret searches for SUSY particles at the Large Hadron Collider within a submodel of the MSSM, the phenomenological MSSM (pMSSM) [23]. The pMSSM makes use of well-motivated constraints to the MSSM to reduce the high dimensionality of the MSSM parameter space.

3

A proton collision walkthrough

Proton-proton collisions at high energies are extremely complex. The protons themselves are highly composite and the interactions between the constituents of colliding protons may result in hundreds or even thousands of outgoing particles. The high number of actors and the strong interaction's properties of confinement make a complete detailed understanding of the evolution from incoming protons to collision products impossible. However, it appears that these processes can be factorized to a good approximation in the way described in this section and summarized in Figure 3.1. In this approximation, collisions are factorized into subprocesses of different energy scales or, equivalent, time scales [18] [24] [25].

3.1 Minimum bias interactions

Minimum bias interactions are the collection of all proton-proton interactions with a “detectable” final state, a final state in which the transverse momenta of the outgoing particles, relative to the direction of the incoming protons, is sufficient to allow detection.

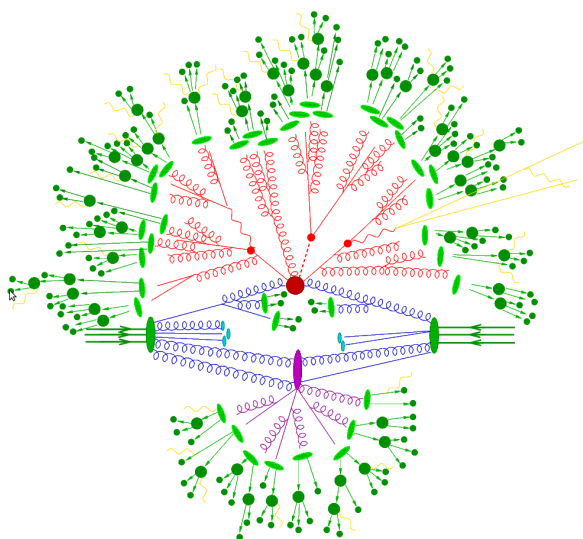


Figure 3.1 – Graphical summary of a proton-proton collision. The constituents of two protons interact (blue) After undergoing initial state radiation, one constituent per proton takes part in the hard interaction (dark red) and the other constituents take part in the underlying event (purple). Outgoing particles undergo showering (red) and hadronization (green). Brehmsstrahlung is also shown (yellow). This figure was adopted from [26].

3.2 Hard interaction

In a very small subset of the minimum bias interactions, the final states possess particles of high transverse momentum relative to the incoming protons. It appears that such a proton-proton collision can be described to a good approximation as if it were the interaction between two partons, one from each proton, that gives rise to a limited number of outgoing elementary particles with high momentum relative to the direction of the incoming protons. This parton-parton interaction is referred to as *the hard interaction*. It can be imagined as a skeleton that is dressed up by other interactions in the collision without significantly changing the principal properties of the interaction.

By definition, the hard interaction takes place at a high energy scale Q , where the running coupling constant of the strong interaction, $\alpha_s(Q^2)$, is much smaller than 1. Therefore, it can be described by perturbative Quantum Chromo Dynamics (QCD). The definition of the hard interaction is slightly arbitrary. In fact, this definition depends on the way collisions are observed and described. If the hard interaction is described at Leading Order in the strong coupling constant, then the hard interaction is, most commonly, the tree-level interaction between two incoming and two outgoing particles. If higher order calculations are used in the description, the hard interaction involves more incoming and outgoing particles and/or loops.

Describing the hard interaction with higher order calculations yields a more precise description of the collisions, and thus better predictions. However, even Next to Leading Order (NLO) calculations are extremely complicated and have, for many important processes, become available only recently. A practical alternative are the partial higher order calculations that only take into account tree-level diagrams. These calculations take into account parton emission for which the the transverse momentum of the emitted parton, relative to the original parton, is above a certain threshold. This threshold is required because diagrams for collinear parton-emission are divergent, and compensated by divergent loop-diagrams.

3.3 Showering

Proton-proton interactions can be calculated exactly to only a few orders of perturbation, as just explained. Still, the partons in proton-proton interactions give rise to abundant emission of multiple soft gluons and quasi-collimated partons (parton-splitting), both higher-order effects. These emissions are most often referred to as

showering. Fortunately for our understanding, the showering processes are practically independent from the hard interaction and do not change the main properties of the collision as defined by the hard interaction. Indeed, the emission of soft gluons has for most purposes no observable effect, and the main effect of parton splitting is that the outgoing partons of the hard interaction are replaced by showers or jets of multiple quasi-collimated partons. Still, a good description of these higher order effects is important since they determine to a great extent the experimental signatures of collisions.

The multiple parton emissions can approximately be included to all orders of perturbation into the proton-proton description as for example explained in Reference [18]. This description treats the showering independent from the hard interaction and provides a probability density function for a parton of given properties to emit another parton of other given properties. This allows a simplified description of showering; the partons that take part in the hard interaction emit partons which on their turn undergo parton emission and so forth. Emission from partons entering the hard interaction is referred to as *initial state radiation*, and emissions from partons leaving the hard interaction is referred to as *final state radiation*.

This shower description can not deal correctly with the most collinear parton splittings nor can it describe gluon emission in the non-perturbative regime below about 1 GeV. Therefore, when comparing measurements to predictions, it is often required to use observables that are insensitive to such emissions. Such observables are called *infrared safe* [27], and many observables that are not infrared safe themselves have very similar infrared safe variants.

This approximative shower description includes also hard parton emissions. This causes a double counting of hard parton emission if exact higher order corrections are incorporated in the hard interaction, for example when using full NLO calculations or when higher order tree-level diagrams are included. Several procedures are available to remove such double counting (e.g. [28] [29] [30]).

3.4 Hadronization

The strong interaction's property of confinement causes the colored partons, originating from the hard interaction and subsequent showering, to interact and form hadrons. The initial hadrons are usually unstable and start a decay chain to other, stable hadrons, leptons and photons. This stage of the collision is referred to as

hadronization.

At present these interactions are not understood from first principle. They take place at low energy scales where the strong coupling constant is of the order of 1 and thus cannot be described with perturbation theory. However, several phenomenological models attempt to describe these interactions. The best known, and a widely used model for hadron formation, is the Lund string model [24]. In this model, flux tubes span between color-connected partons. The energy inside the flux tube rises linearly with the distance between partons and when it becomes energetically more favorable, a quark-anti-quark pair is formed, breaking the tube. Hadronization models possess a high level of arbitrariness but most of them can be tuned to reproduce the observations at particle colliders reasonably well.

3.5 Proton structure

Protons, and hadrons in general, are composed of gluons and quarks, collectively referred to as partons. The so called Parton Density Functions (PDFs) summarize our knowledge about the hadronic structure. A PDF $f_i^a(x, Q^2)$ provides the probability to find inside a hadron a a parton of flavor i carrying a fraction x of the hadron's momentum when probing the hadron with a probe of virtuality Q^2 . Within the perturbative regions of QCD, the GLAP evolution equations, completely define the dependence of the PDFs on Q^2 . The dependence on x , on the other hand, is sensitive to the non perturbative regions of QCD and cannot be derived from first principle.

Therefore, PDFs are measured with fits in the combined data of many experiments, covering a large region of x and Q^2 . With help of the GLAP functions, the measurements in different regions of Q^2 are combined and extrapolated to to e.g. the high Q^2 LHC-conditions. Reference [31] documents a recent such fit and gives a nice overview of which data is used to constrain the PDFs. A preliminary update including LHC data is found in [32].

3.6 Underlying event

When two protons collide, several, mostly soft, parton-parton interactions take place. This implies that simultaneously to any hard interaction, several soft interactions between the proton constituents take place. Theses soft interactions are collectively referred to as the *underlying event*. The additional interactions are in general much softer than the primary interaction, but still give rise to additional observ-

able hadronic activity and thus must be included in the description of proton-proton collisions. Because the underlying event involves soft interactions, its description has phenomenological ingredients and also involves scale parameters, both of which require tuning to measurements in collisions.

3.7 Monte Carlo event generators

The best of our knowledge about the hard interaction, showering, hadronization, underlying event and other collision subprocesses is brought together in *Monte Carlo (MC) event generators*, algorithms for the simulation of particle collisions at high energies. In these algorithms collisions are factorized into a long series of subprocesses, each described in a probabilistic language.

First, the MC event generator samples hard interactions where the kinematics, flavors and charges of the final and initial states are distributed according to a given set of matrix elements. If in the hard interaction short living particles are produced their decay may be included in the matrix elements. The generated events are then weighted according to the PDFs of the proton, evaluated for the flavors and kinematics of the generated initial states. Thereafter, both incoming and outgoing partons of the hard interaction are subject to showering. Effects of underlying event are superimposed and also the evolution of the proton remnants after is included in the simulation. After these steps, the outgoing partons are subject to hadronization.

At the LHC, one bunch crossing gives rise to multiple proton-proton interactions. The proton-proton interactions additional to the processes under study are referred to as *pile up events*. They are included in the simulation by superimposing the final state of the main collision with the final states of minimum bias interactions.

As explained, MC event generators factorize collisions into several subprocesses. The boundaries between the subprocesses are rather arbitrary and are defined with a number of relatively free parameters. Also the approximate descriptions and the phenomenological modeling for the subprocesses relies on a number of relatively free parameters. As such a typical MC event generator has between 10 and 30 free parameters. Before a MC event generator can provide an accurate description of collisions these parameters must be tuned such that the simulation reproduces some of the main observed properties of collisions [33]. Parameters related to showering and hadronization do not depend on the nature of the incoming particles of the collisions and are usually tuned to precision measurements at e^+e^- colliders. Other

A PROTON COLLISION WALKTHROUGH

parameters related to e.g. the underlying event are tuned to measurements at hadron colliders.

4

The Large Hadron Collider

The Large Hadron Collider (LHC) [34] is the latest and greatest particle collider built. This superconducting particle accelerator is located near Geneva and constructed in the tunnel of the former Large Electron Positron collider (LEP), 26.7 km in circumference and 45 to 170 m below the surface. Two beams of proton bunches are accelerated in two adjacent parallel rings and in opposite directions. At four interaction points, the beams cross and the bunches collide

LHC is a discovery machine. Indeed, the relatively heavy protons can be accelerated and stored at relatively high energies since the energy loss through synchrotron radiation is rather limited compared to e.g. electrons. With these higher energies, the production cross sections for heavy resonances are higher, increasing the discovery potential. The higher production cross sections come with a price though. The composite nature of protons lead to complex final states and the center of mass frame of the parton-parton interactions does not coincide with the lab frame, leading to great challenges in the interpretation of the observations.

The LHC signifies important progress with respect to the previous most powerful discovery machine the Tevatron. This is because the LHC collides protons to protons while the Tevatron collided protons to antiprotons. Protons are stable, unlike antiprotons, leading to a much greater lifetime of the beams and thus enabling a higher integrated luminosity.

At design conditions, the LHC could provide up to about 600 million proton-proton collisions per second and per interaction point, with a center of mass energy of 14 TeV. Each of the two beams consist of 2808 bunches separated by at least 25 ns. The bunches contain each about 1.15×10^{11} protons spread over a few centimeters in length and about a millimeter in width. However, at the interaction points, bunches are squeezed to a width of about $16 \mu\text{m}$, such that on average more than 20 proton-proton collisions are expected per bunch crossing. The design luminosity of the LHC is $10^{34} \text{ cm}^{-2}\text{s}^{-1}$.

Producing, accelerating and maintaining the proton bunches involves a complex set of systems. An overview of the LHC injection system is given in Figure 4.1. Prior to injection in the LHC, protons are collected in bunches and accelerated to 450 GeV making use of the LINAC2, PS and SPS accelerators, which are part of the CERN accelerator facility. In the LHC, eight radio-frequency cavities are responsible for the acceleration and maintenance of the proton bunches and 392 quadrupole magnets keep the beams focused. Bending power is provided by the 1232 dipole magnets, made of copper-clad niobium-titanium, operating at 1.9 K and providing a magnetic field up to 8.3 T. It is the twin-bore magnet technology that enables the two proton beams to be stored in the same magnet system, which was an absolute requirement in order to install a proton-proton collider in the narrow former LEP tunnels. These and other magnets, numbering about 9600 in total, are involved in manipulating the beams in the LHC.

At the four interaction points, detectors record the collision products. The two main detectors, CMS and ATLAS, are large general purpose detectors, designed to cover a wide spectrum of physics studies in data mainly from proton-proton collisions. ALICE and LHCb are smaller and specialized detectors. The first is dedicated to the study of heavy ion collisions, the latter to b -physics. The position of the 4 detectors with respect to LHC is indicated in Figure 4.1.

The LHC became operational in November 2009. Since then, protons were collided at several energies, mainly 3.5 TeV per beam. In 2010, the joined proton-proton collision data recorded by ATLAS and CMS reached an integrated luminosity of about 80 pb^{-1} [35] [36]. This has led to a rich array of studies and over a hundred publications. Now, with the 2011 proton-proton runs ended, ATLAS and CMS have recorded an additional amount of proton-proton collisions, each about 5 fb^{-1} . For 2012, the plans are still highly uncertain, but an integrated luminosity between 10 and 20 fb^{-1} per experiment is probably realistic. Furthermore, the proton energy

THE LARGE HADRON COLLIDER

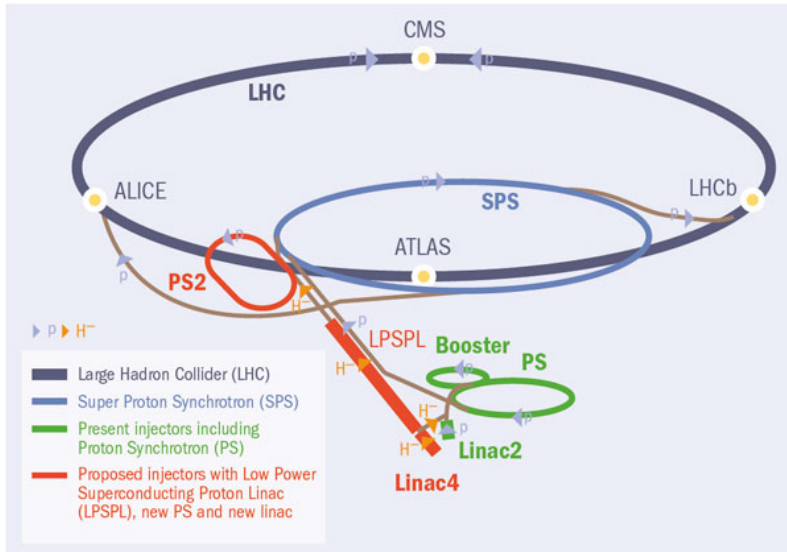


Figure 4.1 – Sketch of the LHC, the location of its detectors and its injector system. Figure taken from [37].

might be increased to 4 TeV per beam.

While 2010 was mainly a year of commissioning for both detectors and analyses, the data of the 2011-2012 period certainly enable precision measurements of SM processes and the exploration of vast untrodden regions in the parameter spaces of the many new physics models! Most spectacularly, it is expected that the 2011-2012 combined ATLAS and CMS measurements will yield the final answer on whether or not a SM Higgs Boson exists. At the end of 2012, the LHC will shut down for two years and upgrade the injection and acceleration apparatus to produce proton-proton collisions at, or almost at, the design center of mass energy of 14 TeV.

5

The Compact Muon Solenoid

The Compact Muon Solenoid (CMS) [38] is one of the two multi-purpose detectors at the LHC, built around the LHC interaction point at Cessy, France. An overview of the CMS detector is given in Figure 5.1. The detector consists of several layers of subdetectors and is organized in a *barrel region*, which is cylindrically shaped around the beam axis, and two *endcap regions*, disks closing the barrel region at both sides. The different subdetector systems are briefly explained in the next paragraphs. The role of each system in the reconstruction and identification of muons, electrons, charged and neutral hadrons and photons emerging from the interaction point, is illustrated in Figure 5.2.

5.1 Coordinate system

The origin of the CMS space coordinates is the beam interaction point. The x -axis points towards the center of the LHC ring, the y -axis points up and the z -axis lies parallel to the LHC beam, completing the right handed coordinate system. Particle momenta are measured in the lab-frame. The *transverse momentum*, p_T , is the projection of the momentum on the x - y plane. The azimuthal angle ϕ is measured in the x - y plane and defined such that the x -axis points to $\phi = 0$ and the y -axis to $\phi = \pi/2$. The polar angle θ is the angle measured from the z -axis. Most often the *pseudorapidity* $\eta = -\ln(\tan(\theta/2))$ is used rather than θ , because the difference in pseudorapidity between 2 particles is approximately invariant under longitudinal

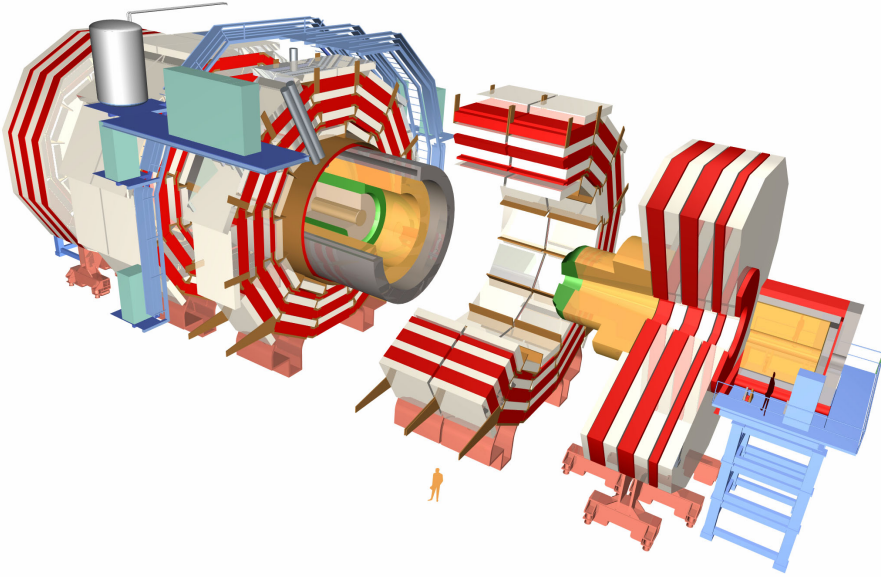


Figure 5.1 – Schematic overview of the CMS detector.

boosts, an important advantage when measuring hadron collisions. The angular distance between particles is usually expressed as $\Delta R = \sqrt{\eta^2 + \phi^2}$.

5.2 Magnet system

To enable the measurement of the momenta of charged particles traversing CMS, their trajectories are bent by the magnetic field produced by the CMS solenoid. This superconducting solenoid encompasses a cylindrical volume, 12.5 m in length and 6 m in diameter centered around the interaction point. Inside this volume, the magnet produces a uniform 3.8 T magnetic field. Outside the solenoid, most of the magnetic flux is returned by the three layers of a 10000 ton iron yoke. The yoke causes the magnetic field outside the CMS solenoid to stay within a compact volume. This leads to significant bending power within the first few meters around the solenoid, beneficial for the momentum measurement of muons by the muon spectrometer located in between the yoke layers.

5.3 Silicon tracker

The trajectories of charged particles in collision products are measured with a silicon tracker, the innermost of the CMS subdetectors. This detector occupies a cylindrical

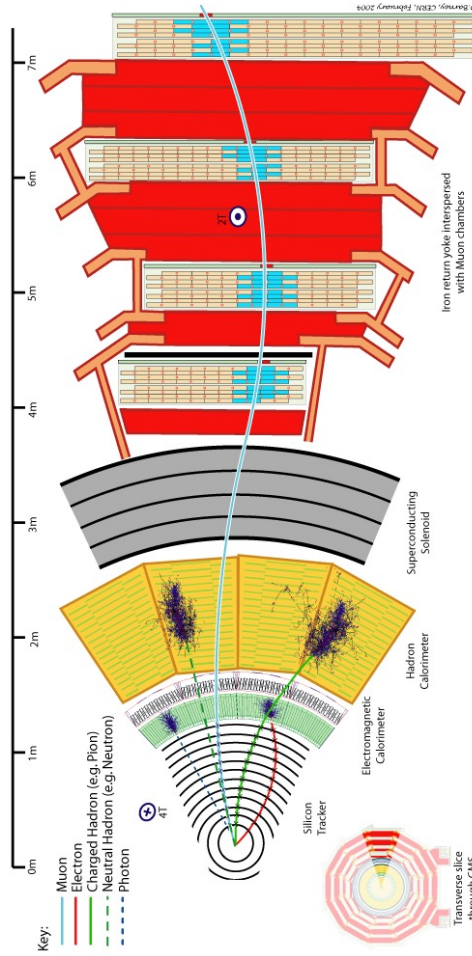


Figure 5.2 – A slice of the barrel region of the CMS detector, illustrating the detection and identification principle for muons, electrons, charged and neutral hadrons and photons emerging from the interaction point.

volume inside the solenoid, 5.8 m in length and 2.5 m in diameter, and consists of multiple layers of silicon detectors. The innermost layers are highly granular, made of silicon pixel detectors with typical sizes of $100 \times 150 \mu\text{m}^2$. The other layers are made of silicon strip detectors, configured parallel to the beam axis in the barrel region and radial in the endcap region. The typical strip size is about $10 \text{ cm} \times 150 \mu\text{m}$. In several of the tracker's layers, silicon strip modules are mounted back to back with a stereo angle of 100 mrad, enabling measurements in three dimensions. The silicon tracker enables efficient reconstruction of charged particle trajectories with pseudorapidity $|\eta|$ up to 2.5 and transverse momentum down to about 500 GeV.

5.4 Electromagnetic calorimeter

The energy of electrons and photons is measured with the ECAL, a hermetic and homogeneous electromagnetic calorimeter surrounding the silicon tracker. This calorimeter is built of lead tungstate (PbWO_4) crystals of elongated and truncated pyramidal shape. The crystals are configured side by side such that their axes point slightly away from the interaction point, thereby avoiding cracks. The length of the crystals corresponds to 25.8 radiation lengths (X_0), in the barrel and 24.7 X_0 in the endcaps, and thus most electrons and photons deposit all their energy while traversing the crystals. In the barrel, the front faces of the crystals measure 0.0174×0.0174 in $\eta - \phi$ or $22 \times 22 \text{ mm}$ and are at a distance of 1.29 m from the beam axis. In the endcaps, the front faces measure $28.62 \times 28.62 \text{ mm}^2$ and are at distance 315.4 cm from the interaction. Scintillation light is measured for each crystal separately. The molière radius of the crystals is 22 mm and thus an electron or photon traversing the calorimeter deposits most of its energy within one crystal.

In the ECAL endcap, granularity is typically insufficient to resolve the two photons from a π^0 decay. Therefore, a sampling calorimeter, the preshower (PS), is installed just in front of the ECAL endcaps. This calorimeter has two layers. The first is a lead layer of thickness 2-3 X_0 that initiates showering of traversing electrons and photons. Behind the lead radiator, two layers of silicon strip sensors configured orthogonally measure the showers. The strips have a width of 1.9 mm.

5.5 Hadronic calorimeter

The energies of the hadrons in collision products are measured with the hadronic calorimeter (HCAL). The HCAL in fact consists of four significantly different calorime-

ter systems.

In the barrel region, located in between the ECAL barrel and the solenoid, HB measures hadronic energies in the region $|\eta| < 1.3$. It is a sampling calorimeter constructed from flat brass absorber plates interleaved with layers of plastic scintillator plates. The absorber thickness ranges from 5.82 interaction lengths (λ_I) at $\eta = 0$ to 10.6 λ_I at $|\eta| = 1.3$ and the ECAL adds about another 1.1 λ_I . The plastic scintillator plates are segmented in sections of 0.087×0.087 in $\eta \times \phi$. For each such section, the light originating from the different scintillator layers is brought together and measured as one signal with a single sensor.

The radiation thickness of HB is relatively limited and therefore an additional outer calorimeter (HO) is installed just outside the solenoid. It consists of additional layers of scintillator plates covering the region $|\eta| < 1.3$. As such, it makes use of the additional $1.4/\sin(\theta)\lambda_I$ provided by the solenoid's material.

The region $1.3 < |\eta| < 3$ is covered by HE, located just behind the ECAL endcaps, still within the volume of the solenoid. Just like HB, it is constructed from brass absorber plates interleaved with scintillator plates. The total thickness of the calorimeter, including the ECAL endcaps, corresponds to about 10 λ_I . The granularity of the calorimeters is 0.087×0.087 in η - ϕ for $|\eta| < 1.6$ and about 0.17×0.17 for $|\eta| \geq 1.6$. The different scintillator layers in each of those segments are organized in 2 or 3 regions of depth, which are each read out separately.

Located just outside the endcaps of the iron yoke, the forward calorimeter HF measures hadronic energy in the region $3 < |\eta| < 5.2$. This calorimeter consists of about 10 λ_I of steel interwoven with quartz fibers running parallel to the beam pipe. Charged shower particles with energy above the Čerenkov threshold generate Čerenkov light while traversing the quartz fibers. The fibers are bundled and read out in segments of 0.175×0.175 in η - ϕ .

5.6 Muon system

Three systems are set up to measure the trajectories of muons. For precise measurements, Drift Tubes (DTs) are used in the barrel and Cathode Strip Chambers (CSC) in the endcaps. For triggering and timing purposes, Resistive Plate Chambers (RPCs) are used in both the barrel and the endcap regions.

DTs cover the region $|\eta| < 1.2$ and are located in between and just outside the barrel

layers of the iron yoke. They are organized in 4 stations, detector modules installed in concentric cylinders around the beam pipe. Each station consists of several layers of drift tubes configured both parallel and orthogonal to the beam line. A single DT station not only enables the reconstruction of the position of a traversing muon, it also enables a coarse reconstruction of the muon's direction.

CSCs cover the region $0.9 < |\eta| < 2.4$, and are located in between and just outside the endcap disks of the iron yoke. They are organized in 4 stations, planes of detector modules orthogonal to the beam pipe. Each station has several layers of cathode strips with radial orientation interleaved with layers of anode wires with azimuthal orientation. Both cathode strips and anode wires are read out, enabling measurement in both η , ϕ and r . Just like DTs, CSCs enable a coarse reconstruction of a traversing muon's direction.

RPCs cover the region $|\eta| < 1.6$. The RPC modules are located in between both the barrel and the endcap layers of the iron yoke. The barrel region has 6 layers of RPC modules and the endcap layer has 3 layers. Each module consists of double gaps operated in avalanche mode with common pick-up read-out strips in between. These detectors possess a very rough spatial resolution but have excellent timing resolution and are therefore very well suited for triggering purposes.

5.7 Trigger

At LHC design conditions, proton beams will cross every 25 ns. and at each crossing several hard or semi-hard proton interactions will take place. Storing and processing all these events is impossible and thus a well motivated data reduction is necessary.

In CMS, this data reduction is organized in two steps. The Level 1 (L1) trigger system must reduce the event rate to about 30 kHz. To this purpose it uses coarsely segmented data from the muon systems and calorimeters and provides a first rough filtering of events. In the meanwhile the high resolution data are stored in pipelined memories. These can store the data for no more than $3.2 \mu\text{s}$ and thus within this time span, the L1 trigger must decide whether or not to accept the event.

If an event is accepted by the L1 trigger, the high resolution data are read out and is made available for the next step in the data reduction, the High Level Trigger (HLT). The HLT is fully based on software and runs on a processor farm. Its purpose is to further reduce the event rate to about 100 Hz. To keep the CPU usage manageable,

THE COMPACT MUON SOLENOID

the HLT bases its decision on an *online reconstruction*, a simplified version of the full event reconstruction. Events accepted by the HLT are stored for further analysis.

6

Collision reconstruction with CMS

The raw data collected for each bunch crossing that fires the HLT, serves as input to a detailed *offline reconstruction* of the collision final states. CMS has developed an algorithm, the Particle Flow (PF) [39] [40], that attempts to identify and to reconstruct the kinematic properties of each individual particle in the final states. For that purpose, information from all subdetectors in CMS is combined in a quasi-optimal way, relying heavily on the precise measurement of the momenta of charged particles with the silicon tracker, and the precise measurement of photon and electron energies with the highly granular and hermetic ECAL, to overcome the coarser granularity of the HCAL.

The last few years, this algorithm has gradually taken over from the classic “calorimetric” approach, where jets are reconstructed directly from calorimeter information without attempting to reconstruct the individual jet constituents. The new PF approach has led to important improvements in the jet energy and direction resolution, electron and τ -lepton reconstruction and the isolation of leptons and photons.

6.1 Reconstruction of Particle Flow elements

A particle traversing CMS leaves traces in several of the CMS subdetectors. The first step in the PF algorithm reconstructs these traces in each of the subdetectors separately. The reconstructed traces are called *particle flow elements* and come in three types: *charged-particle tracks* are reconstructed from hits in the silicon tracker; *calorimeter clusters* combine hits in the calorimeters; *muon tracks* are muon trajectories reconstructed from hits in the muon detectors.

Charged-particle tracks

Charged particles traversing the tracker produce hits, i.e. clusters of signals in the tracker's silicon pixels and strips. Making use of a Kalman Filter (KF) technique [41], these hits are combined to reconstruct the trajectories charged-particle tracks.

CMS has developed an iterative tracking procedure that is able to achieve high efficiency while maintaining a modest fake rate [42][43]. During the first iterations, tracks are seeded and reconstructed, imposing stringent quality criteria such that the fake rate is negligible. The hits associated to the reconstructed tracks are removed from the hit list after each iteration. Then, at further iterations, quality criteria are gradually relaxed resulting in a higher track reconstruction efficiency. However, due to the reduced amount of available hits, the combinatorial background and thus the fake rate remains low.

Calorimeter clusters

The PF algorithm attempts to cluster in each separate calorimeter the energy deposits of each individual particle. Considered as separate calorimeters are the ECAL barrel, the ECAL endcap, the first layer of the PS, the second layer of the PS, the HCAL barrel, the HCAL endcap and the HF.

A simple clustering procedure is adopted. First, cluster seeds are selected. Each calorimeter cell with signal above a certain *cluster seed threshold* and above the signal of each neighboring cell serves as cluster seed. Then, clusters are grown from each seeds by including the adjacent cells with signal above a certain *cluster cell threshold*. If cells are shared between clusters, each cluster is assigned a fraction of the shared cell's signal, where the fraction depends on the relative distance between the cluster position and the cell.

This procedure is performed iteratively. At each iteration, neighboring cells are included and the cluster position is recalculated as the weighted average of the position of the clusters' cells. Clustering has ended when, during an iteration, the position of the cluster moves less than a certain fraction of the cluster position resolution.

The parameters involved in this procedure, such as the cluster seed threshold and the cluster cell threshold, are optimized for each specific calorimeter type. The cluster energies are calibrated based on studies in MC simulation, depending on the calorimeter system and on the type of particle to which the cluster is assigned in the next step of the PF algorithm, the particle reconstruction.

Muon tracks

Muon tracks are reconstructed from the information from the muon system [44][45]. They combine track segments in CSCs and DTs and hits in RPCs using a KF technique similar to the one used for the reconstruction of charged-particle tracks. The reconstruction of the muons is performed under the hypothesis that the muon originates from a point close to the interaction point.

6.2 Particle reconstruction and identification

The second step in the PF algorithm is the particle reconstruction. The PF algorithm reconstructs and identifies particles by matching PF elements from the different sub-detectors to each other. An iterative procedure is adopted; each time a matching set of PF elements is found and a particle is reconstructed, the corresponding PF elements are removed from the list of PF elements that is considered for further reconstructions of particles.

Muons

In general, a muon causes the reconstruction of a charged-particle track and a muon track. To reconstruct and identify muons, the PF algorithm attempts to combine the hits of a charged-particle track with the track segments and hits associated to a muon track with a global fit [44]. Whether the charged-particle track and the standalone muon are compatible with a muon is decided based on the χ^2 of the fit. On successful reconstruction, the corresponding charged-particle track and stand-alone muon are removed from the list of PF elements and not used in the subsequent reconstruction of particles. The as such reconstructed muons are also referred to as *global muons*.

Electrons

Electrons emerging from the interaction point leave hits in the tracker and deposit their energy in one or few adjacent ECAL cells. Between the interaction point and the ECAL, electrons undergo Brehmsstrahlung and may emit several photons. These photons may on their turn converge to electron-positron pairs before reaching the ECAL. Thus, these effects lead to additional hits in the tracker and in the ECAL.

To reconstruct electrons, the PF algorithm attempts to combine all these elements [46][47]. First, hits in the tracker are combined to reconstruct tracks, making use of a dedicated tracking algorithm, the Gaussian Sum Filter (GSF) [48]. Unlike the default track reconstruction with the Kalman Filter, the GSF can cope with the sudden changes in the electron direction related to Brehmsstrahlung.

The GSF is CPU intensive. Therefore, it is seeded with a limited number of seed tracks that must pass loose electron identification criteria. Two seed strategies are being used simultaneously [49]. A first strategy, an *ECAL-driven* approach is particularly effective for the reconstruction of isolated electrons with high transverse momenta. It starts off with the reconstruction of an *ECAL supercluster*. This is a cluster of hits in the ECAL with an elongated shape of about 0.3×0.09 in η - ϕ to incorporate Brehmsstrahlung. Then, an electron candidate is backpropagated from the barycenter of the supercluster to the pixel layers of the tracker. The matching pixel hits serve to reconstruct a seed track for the GSF.

The second, *tracker-driven* approach, is intended for soft, non-isolated electrons for which often no ECAL supercluster can be reconstructed. A first set of such seeds are charged-particle tracks with hits in the outer tracker layer that are compatible, both in direction and momentum, with an ECAL cluster. A second set of such seeds is obtained from charged-particle tracks with a low number of hits or a low fit quality, which is an indication for Brehmsstrahlung. Such tracks first seed a lightweight version of the GSF. If the lightweight GSF track can be propagated to an ECAL cluster, it is decided whether or not the track and matched calorimeter cluster are compatible with the electron hypothesis, based on a boosted decision tree [50]. If compatible, the lightweight GSF track is added to the set of seeds.

For each of the seeds, a full GSF track reconstruction is attempted. Only the GSF tracks that can be extrapolated to ECAL clusters are retained. The set is furthermore cleaned from duplicates and from tracks that are compatible with electrons originating from converted Brehmsstrahlung photons. Finally, Brehmsstrahlung photons are

recovered. To do so, each GSF track is extrapolated linearly to the ECAL at each traversing of a tracker layer, where Brehmsstrahlung is most likely to occur due to interaction with the material of the tracker. ECAL clusters that match these extrapolated tracks are assigned to the electron. The momentum of the thus reconstructed electrons is determined combining the momentum measurement from the GSF track with the energy measurement from the ECAL clusters. All tracks and calorimeter clusters associated to the reconstructed electrons are discarded for the further reconstruction of particles.

Charged and neutral hadrons, photons

The reconstruction of muons and electrons is followed by the reconstruction of photons and charged and neutral hadrons. Photons deposit their energy in the ECAL, leading to ECAL clusters. Hadrons deposit most of their energy in the HCAL and some energy in the ECAL, leading to ECAL and HCAL clusters. If charged, hadrons also leave traces in the silicon tracker, leading to the reconstruction of charged-particle tracks.

Reconstructing the individual photons and charged and neutral hadrons in collision final states is challenged by the coarse granularity of the HCAL. A first important consequence of this coarseness is that the deposits of several hadrons may end up in a single HCAL cluster. In such case it is impossible to separate the different hadrons based on HCAL information only. A second important consequence is the difficulty to identify a photon that is produced nearby a hadron. Indeed, the large HCAL cluster from the hadron may overlap with the ECAL cluster of the photon, making it difficult to determine whether the ECAL cluster is indeed due to the photon or due to the traversing hadron.

To overcome these difficulties, the PF algorithm carefully compares the information from the tracker with the information from the ECAL, the HCAL and the muon system. First, the bulk of fake tracks is removed by imposing loose quality criteria. Then, the contributions from muons to calorimeter clusters are removed. If a muon passes through a cluster, its expected energy deposit is subtracted from the cluster energy. Finally, for each HCAL cluster the disambiguities are resolved as follows:

1. All charged-particle tracks passing through the HCAL cluster are considered as charged hadron candidates that contribute to the energy of the HCAL cluster. If a charged-particle track passes through more than one HCAL cluster, it is

only considered to contribute to the closest cluster.

2. If a charged hadron candidate passes through one or more ECAL clusters, the closest ECAL cluster is associated to the candidate.
3. If charged hadron candidates pass through more than one ECAL cluster, the additional ECAL clusters are ranked according to increasing distance to the closest charged hadron candidate. The ECAL clusters are associated to the hadron candidates, one after another, as long as the total calibrated energy of the associated clusters remains lower than the total associated track momentum.
4. If all associated charged-particle tracks indeed originate from charged hadrons, the total momentum of the tracks cannot be above the total calibrated energy of the associated calorimeter clusters. The PF algorithm verifies whether this is indeed the case. If not, the number of hadron candidates is reduced by considering the charged-particle tracks for a relaxed muon reconstruction and by removing tracks that fail more stringent track quality criteria.
5. The remaining charged hadron candidates are considered as reconstructed charged hadrons. Their momentum and energy is taken from the track momentum measurement, adopting the pion hypothesis.
6. If the total calibrated energy of the associated clusters shows a significant excess with respect to the total reconstructed energy of the charged hadrons, photons and neutral hadrons are reconstructed. First photons are reconstructed from the ECAL clusters that were earlier associated to the charged hadrons. If the excess remains a neutral hadron is reconstructed from the remaining excess.
7. In contrast, if the total calibrated energy of the associated clusters is compatible with the total reconstructed energy of the charged hadrons, the energies and momenta of the hadrons are recomputed with a fit on the track momenta and the cluster energies. This combination of measurements is especially relevant for charged hadrons with high momenta, for which the energy measurement from the calorimeters is of a higher precision than the momentum measurement of the tracker.
8. Remaining ECAL clusters are reconstructed as photons and the remaining HCAL clusters as neutral hadrons.

Figure 6.1 shows the energy resolution for the reconstructed hadrons as function of the true hadron energy. Between 0 and 200 GeV, the resolution steeply falls from 25% to 10% and then gradually decrease to 7% at 1000 GeV.

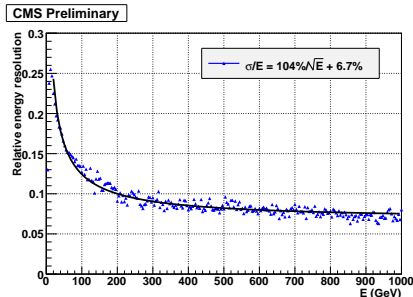


Figure 6.1 – Hadron energy resolution σ/E in simulation as function of the true hadron energy (left). The smooth curve is obtained from a fit of the data points with an *ad-hoc* function. A simulated sample of single hadrons was used for this figure [39].

6.3 Physics objects for analyses

Most of the particles reconstructed by the PF algorithm are not used directly in analyses. Instead, analyses are usually based on a limited set of physics objects and variables computed from the PF particles. This section describes the most important properties of the objects and variables that are used in the analyses described in the further sections.

Primary Vertices

Determining the positions, or Primary Vertices (PV), of the collisions in a single bunch crossing is crucial when dealing with pile up effects and to detect long lived particles such as the many mesons that contain valence c and b -quarks. In CMS, the PVs are reconstructed from the vertices of all good-quality charged-particle tracks in the event [42]. First, the tracks are clustered according to the z -coordinate of their closest approach to the beam line [51]. Then, a PV is reconstructed from each cluster with two or more constituents using a dedicated fit procedure. Which PV corresponds to the hardest interaction in the event is determined based on the tracks associated to the PV. The transverse momenta of all tracks associated to the PV are summed and the vertex with the highest sum is chosen.

Isolated Leptons

Leptons originating from the decay of heavy resonances such as W and Z bosons are usually isolated from all other particles in the event. In contrast, leptons originating from hadron decays in jets are usually surrounded by numerous other particles. To separate these two kinds of leptons from each other a variable, the relative isolation I_{rel}^R , is defined as the scalar sum of the transverse momenta of all PF particles in a cone of certain radius R around the lepton, divided by the momentum of the lepton. If I_{rel}^R is below a given threshold value, the lepton is considered isolated.

This elegant definition could not be adopted at the time of the W/Z +jets study presented in Part II. For the isolation, this measurement makes use of the somewhat less rigorous calorimetric approach. In this case I_{rel}^R is defined as

$$I_{rel}^R = (I_{ECAL}^R + I_{HCAL}^R + I_{TRACK}^R)/p_T^l \quad (6.1)$$

with I_{ECAL}^R , I_{HCAL}^R and I_{TRACK}^R isolation variables based on respectively the ECAL, the HCAL and tracker information, and p_T^l the transverse momentum of the lepton. I_{ECAL}^R is the energy measured in the ECAL in a cone of radius R around the lepton, I_{HCAL}^R is the energy measured in the HCAL in a cone of radius R around the lepton, and I_{TRACK}^R is the scalar sum of the p_T of all tracks in a cone of radius R around the lepton. The track and the calorimeter deposits associated to the lepton itself are not included.

What makes I_{rel}^R less elegant than I_{PF}^R is the fact that the energies of charged hadrons and electrons inside the isolation cone are counted twice, once for the tracker and once for the calorimeters. Furthermore, in calorimetric approach, the method to determine which calorimeter deposits originate from the lepton itself is rather crude, while the PF algorithm by definition has a very advanced way of assigning energy deposits in the calorimeters to particles. Finally, I_{HCAL}^R suffers from the coarse granularity of the HCAL and does not take into account the low- p_T charged hadrons that are bent outside the isolation cone. Also these problems are dealt with by the PF algorithm, that reconstructs hadrons with excellent angular resolution making optimal use of tracker information.

Jets

As mentioned earlier, quarks and gluons produced in hard interactions do not reveal themselves as such. Instead, they give rise to bunches of quasi-collimated hadrons, leptons and photons, called jets. Jets are ambiguous objects [27]. It is tempting

to assign the properties of a jet to the properties of some parton from which the jet's constituents originate. However, partons are ill-defined objects because of their divergent branching probabilities (See section 3).

Because a jet does not directly represent a common origin of its constituents, there is no definition for jets from first principle and several definitions to cluster the particles of an event into jets are in use. Jet definitions should be infrared safe (see Section 3.3). Indeed the measured properties of jets cannot be compared directly to the properties of partons. Rather they must be compared to the properties of jets in simulated events that include the higher order effects of parton showers, which requires the jet definition to be infrared safe.

The default jet definition used by CMS is the anti- k_t algorithm with radius parameter $R=0.5$ [52]. It is a fast, infrared and collinear safe algorithm. Non-overlapping anti- k_t jets have the shape of disks with radius R^{jet} in η - ϕ space. In case of overlap, one jet has the usual shape and the other has the usual shape minus the overlap. This simple shape behavior is beneficial from the experimental point of view as it simplifies calibration and subtraction of pile-up and underlying event contributions. The momentum of a jet is the sum of the momenta of all its constituents. All the reconstructed PF particles, except for isolated leptons, are included in the clustering.

Figure 6.2 shows the energy and direction resolution for reconstructed jets as a function of the jet p_T . The resolution for jets clustered from PF particles is shown in blue and the resolution for jets as clustered in the calorimetric approach is shown in red. Clearly, below a p_T of 100 GeV, the PF jets perform much better and have an excellent resolution. At higher p_T , the performance of the two approaches becomes very similar.

Transverse hadronic energy, H_T

An often used jet-related variable is H_T , the total jet energy in the event, defined as follows:

$$H_T = \sum_i p_T^{jet_i}, \quad (6.2)$$

where the sum runs over all jets passing certain selection criteria. This variable proves very useful in searches for new physics, because many new physics scenarios give rise to final states with multiple and highly energetic jets.

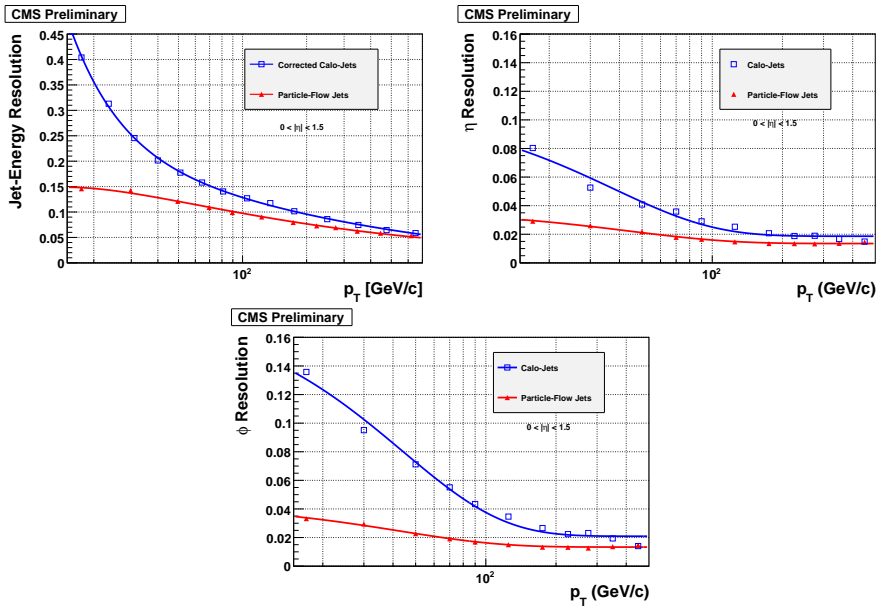


Figure 6.2 – Resolution of the reconstructed jet energy (top-left), η (top-right) and ϕ (bottom) in simulated QCD multi-jet events as a function of the jet p_T in the barrel region of CMS. Red triangles show the resolution for jets clustered from PF particles. Blue squares show the resolution for jets as clustered in the calorimetric approach. The full lines show the results of fits of the data points [39].

Missing transverse energy

Detection of weakly interacting particles is crucial both for SM measurements and searches for new physics. Although such particles leave no trace in any of CMS's subdetectors, their transverse momenta can be estimated as the missing transverse energy in the event, making use of momentum conservation:

$$\vec{E}_T^{miss} = - \sum_j \vec{p}_T^j, \quad (6.3)$$

where the sum runs over all reconstructed PF particles in the event and \vec{p}_T^j is the transverse momentum of PF particle j .

Figure 6.3 shows the energy and ϕ resolution of the reconstructed E_T^{miss} in simulation versus the true E_T^{miss} . Again, the PF approach is compared to the calorimetric-based approach and performs substantially better.

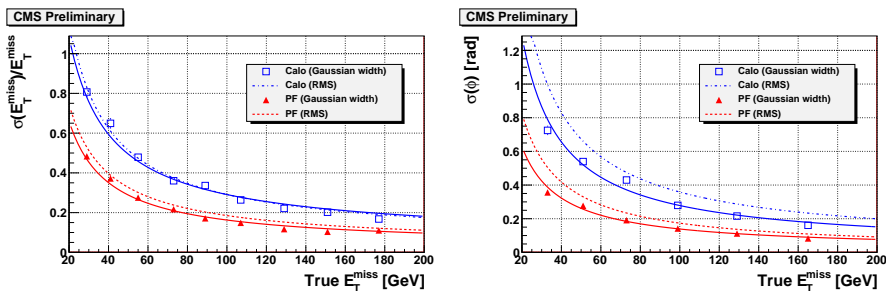


Figure 6.3 – The energy and ϕ resolution of the E_T^{miss} in simulation. Red triangles show the resolution for the PF approach. Blue squares show the resolution for the calorimetric approach. The full lines show the results of fits of the data points and the dashed lines show the results of fits of an alternative resolution measure [39].

Transverse mass

Many interesting processes involve real W bosons decaying leptonically. An important variable to identify the presence of such a boson is the transverse mass m_T of the decay products of the W , the charged lepton and the neutrino.

$$m_T = \sqrt{2p_T^l p_T^\nu (1 - \cos \Delta\Phi)} \quad (6.4)$$

with p_T^l and p_T^ν the transverse momentum of the charged lepton and the neutrino respectively, and $\Delta\Phi$ the azimuthal angle between the charged lepton and the neutrino.

This transverse mass is equal to the mass of a system with two massless particles with momenta p_T^l and p_T^{ν} .

***b*-tagging**

b-quarks are produced in many interesting SM and new physics processes: e.g. top quarks almost exclusively decay to W bosons and *b*-quarks; many new physics scenarios involve decay chains with abundant production of *b*-quarks. Therefore, determining whether or not, and how many *b*-quarks are produced in collisions is an important prerequisite for many analyses performed at the LHC. Just like other partons, *b*-quarks take part in the showering and give rise to jets, called *b*-jets. The methods to identify such jets are referred to as *b*-tagging algorithms or *b*-taggers. These algorithms usually define a certain *b*-tag discriminator, a summarizing variable that quantifies the “*b*-ness” of a jet.

b-taggers exploit the particular properties of *b*-quarks, or rather the properties of the hadrons in which valence *b*-quarks are bound after showering and hadronization. In pp collisions, these hadrons give rise to secondary vertices that are typically hundreds of micrometers away from the primary vertex with multiple outgoing charged particles with relatively large angles in between. These properties are related to the long lifetime of the hadrons, between 1.4 and 1.7×10^{-12} s, their short decay chain and their high mass between 5.2 and 5.7 GeV.

CMS has developed several *b*-tagging algorithms based on the presence and properties of these secondary vertices. A first such algorithm used in this thesis is the Track-Counting-High-Efficiency (TCHE) tagger [53]. First, reconstructed tracks of charged particles are associated to a jet if they are within a radius of $\Delta R = 0.5$ around the jet axis. For each track the impact parameter significance $S_{\text{IP}} = \text{IP}/\sigma_{\text{IP}}$ is determined, where the Impact Parameter (IP) is the distance in the x - y plane between the PV and the track and where σ_{IP} is the uncertainty on the IP. Because of the secondary vertex associated to the *b*-quark, *b*-jets have several tracks with a large impact parameter significance. The TCHE tagger uses the second largest impact parameter significance within the jet as *b*-tag discriminator.

A second algorithm that is used in this thesis is the Combined-Secondary-Vertex (CSV) tagger [54]. Again, reconstructed tracks are associated to the jets, but then an attempt is made to reconstruct a secondary vertex from these tracks, making use of a Kalman Filter technique. A multivariate discriminator is defined based on the

properties of the reconstructed secondary vertices: the invariant mass of the system of associated tracks, the number of associated tracks, the distance to the PV, the energies of the associated tracks relative to the jet energy, the impact parameter significance of the associated tracks. This CSV tagger is more powerful than the TCHE tagger. However, because it combines so many properties of b -jets, it is harder to calibrate.

Part II

Early measurements of W/Z + jets production

7

Introduction

The production of W and Z bosons accompanied by jets ($W/Z + \text{jets}$) is one of the most important and interesting Standard Model (SM) processes to be studied at hadron colliders. On the one hand, these processes provide excellent probes to test perturbative QCD. On the other hand, they constitute an often dominating background to searches for new physics. Thus, an excellent understanding of the $W/Z + \text{jets}$ physics is crucial for the sensitivity of these searches.

Many of the new physics scenarios do not possess “candles”, i.e. easy-to-detect signatures showing up as clear narrow resonances. Rather, these scenarios cause, with respect to SM expectations, an excess of events with high jet multiplicity, spread over a broad range of values of some jet related variable. For many of the searches for such scenarios, the production of $W/Z + \text{jets}$ is an abundant and notoriously difficult background. For instance, searches in channels with E_T^{miss} and multiple jets suffer from background from $Z(\rightarrow \nu\nu) + \text{jets}$ production and $W(\rightarrow l\nu) + \text{jets}$ production if the lepton remains undetected [55] [56]. Searches in channels with leptons or E_T^{miss} with leptons are obviously also faced with important $W/Z + \text{jets}$ backgrounds [57] [58]. Clearly, the sensitivity of these searches to any new physics depends dramatically on the understanding of the $W/Z + \text{jets}$ physics.

Fortunately, driven by the Tevatron experiments, the expectations of LHC, extensive efforts by theorists and the steep increase in available computing power, the understanding of $W/Z + \text{jets}$ production has shown exceptional progress during the

last decade. In the early 2000s, the development of automated tree-level matrix-element generators has known a remarkable boost, resulting in the birth of e.g. ALPGEN [59], MADGRAPH [60] and AMEGIC [61]. These tools enable full Leading Order (LO) calculations of diagrams with W or Z boson production plus multiple hard outgoing additional partons. They are interfaced with parton shower and hadronization codes using the MLM [28], CKKW [29] or Lönnblad's [30] jet matching algorithms and found to agree remarkably well with $W/Z + \text{jets}$ measurements performed at the Tevatron experiments [62] [63] [64]. Recently, important progress was accomplished in Next to Leading Order (NLO) matrix-element calculations for $W + \text{jets}$ production. NLO calculations including diagrams with up to 3 outgoing partonic legs became available in 2009 [65] [66]. A recent detailed study of $W + \text{jets}$ by the D0 collaboration has compared observed $W + \text{jets}$ differential cross sections to these predictions and found again excellent agreement [67]. The latest NLO predictions even include diagrams with up to 4 outgoing partonic legs [68]. These NLO calculations dramatically decrease the theoretical uncertainties on predictions for vector boson plus jet production but are difficult to interface with parton shower and hadronization codes [69]. As long as this obstacle is not overcome, tree-level matrix-element generators remain invaluable for the modeling of $W/Z + \text{jets}$ as background to searches and to measurements of other SM processes.

The main focus of $W/Z + \text{jets}$ studies has been the measurement of differential cross sections of these processes versus the number of jets, the transverse momenta of the jets and the transverse momentum of the vector bosons. These were the main $W/Z + \text{jets}$ measurements used for testing the predictions described above. However, several dedicated analyses have studied $W/Z + \text{jets}$ production in more detail. The study of $W + b\text{-jets}$ production is here of special interest because it is an important background to searches for b -rich new phenomena and studies of the top quark [70]. At the same time, the high mass of the b -quark forms an additional challenge for predictions. The measurement of $W + c\text{-jets}$ production rates and the measurement of the vector boson rapidity distribution provide us with valuable information as well. These observables are sensitive to the proton structure and help us constraining hadron Parton Density Functions (PDFs) [71] [72].

So, obviously, searches profit from all these studies through a better understanding of backgrounds related to $W/Z + \text{jets}$ production. However, there are also less direct benefits. Indeed, these studies lead to better predictions for SM backgrounds in general and for the new phenomena themselves. There is the just mentioned improved understanding of PDFs, but probably more important is the following:

INTRODUCTION

the techniques that enabled the breakthroughs for the predictions for $W/Z + \text{jets}$ production were also applied in predictions for other SM production processes and in the predictions for new phenomena. Because $W/Z + \text{jets}$ production is relatively abundant and is relatively easy to reconstruct in data, the study of these processes has served and still serves as a validation of these techniques in a more general context.

LHC has brought new challenges and new opportunities for $W/Z + \text{jets}$ physics. On the one hand, the searches for new physics at LHC explore extremely remote corners of phase space, with multiple highly energetic jets and/or high missing transverse momentum, driving the modeling of $W/Z + \text{jets}$ and SM physics in general to its limits. On the other hand, LHC produces $W/Z + \text{jets}$ at rates never seen before. This may enable a $W/Z + \text{jets}$ physics program of unprecedented precision and detail. The first steps have already been taken; the ATLAS experiment has measured differential cross sections for $W/Z + \text{jets}$ as a function of the jet multiplicity and the transverse momenta of jets [73] [74] [75], and cross sections for the production of $W/Z + b\text{-jet}$ [76] [77]; CMS has measured the polarization of W bosons in $W + \text{jets}$ [78], the cross sections for $W + c\text{-jets}$ [79], and observed of $Z + b\text{-jet}$ production [80].

This part of the thesis describes the most extensive study of $W/Z + \text{jets}$ production performed at CMS up till now [16]. We analyzed the proton-proton data collected by CMS in 2010 at a centre of mass energy of $\sqrt{s} = 7 \text{ TeV}$, and corresponding to 36 pb^{-1} . The $W/Z + \text{jets}$ production cross section and the asymmetry between W^+ and W^- production, are measured, both as a function of the number of produced jets. We also perform the first direct measurement of what is often called the Berends-Giele scaling [81] [82] [83].

8

Analysis strategy

8.1 Introduction

The following chapters describe a measurement of various properties of jet production in association with W and Z bosons in the first $35.9 \pm 1.4 \text{ pb}^{-1}$ of proton-proton collision data collected by CMS in 2010 at a center of mass energy of $\sqrt{s} = 7 \text{ TeV}$ [16]. The development of this analysis was initiated almost half a decade ago and was gradually refined over the years, witnessed by the long list of references directly related to this analysis ([84] to [99] and several more).

The analysis is designed for early measurements, anticipating an inaccurate understanding of the detector performance. Therefore, wherever possible, we avoid the use of MC simulated data. Still, some aspects of the measurements do rely on MC simulation. For those particular cases, we validate the MC simulation, comparing the measured data to the simulated data in control samples. Furthermore we choose to measure observables that show only little dependence on the detector performance.

For these early measurements, we consider the W and Z decay channels that are easiest to recognize:

- $W(\rightarrow \mu\nu)$, W bosons decaying to a muon and a muon antineutrino or an antimuon and a muon neutrino,

- $W(\rightarrow e\nu)$, W bosons decaying to an electron and a electron antineutrino, or an anti-electron and a neutrino,
- $Z(\rightarrow \mu\mu)$, Z bosons decaying to a muon and an anti-muon,
- $Z(\rightarrow ee)$, Z bosons decaying to an electron and an anti-electron

The presence of isolated muons or electrons in the final states of these decays provides the crucial and robust handle to filter out most of the overwhelming background from QCD multi-jet production. In the following, we will use the symbol V to denote any of these 4 vector boson production channels.

8.2 Measurements

We measure the following quantities:

- The cross section for V production in association with n or more jets, normalized to the inclusive V production cross section,

$$\frac{\sigma(V + \geq n \text{ jets})}{\sigma(V)}, \quad (8.1)$$

with $n = 1, 2, 3, 4$ and $V = W(\rightarrow \mu\nu)$, $W(\rightarrow e\nu)$, $Z(\rightarrow \mu\mu)$ and $Z(\rightarrow ee)$. We quote this ratio rather than the absolute $V + \text{jets}$ cross sections, because in the ratio, systematic uncertainties in the cross sections that do not depend on the jet multiplicity, such as the luminosity uncertainty and to some extent the lepton efficiency, cancel out.

- The ratio of the cross section for V production in association with n or more jets to the cross section of V production in association with $(n - 1)$ or more jets,

$$\frac{\sigma(V + \geq n \text{ jets})}{\sigma(V + \geq (n - 1) \text{ jets})}, \quad (8.2)$$

with $n = 1, 2, 3, 4$ and $V = W(\rightarrow \mu\nu)$, $W(\rightarrow e\nu)$, $Z(\rightarrow \mu\mu)$ and $Z(\rightarrow ee)$. Also here, systematic uncertainties that do not depend on the jet multiplicity cancel out. This ratio quantifies how the $V + \text{jets}$ cross section scales with the number of jets and how this scaling evolves with the number of jets.

- Alternatively we quantify the scaling of the $V + \text{jets}$ cross section with the number of jets, using the parameters α and β ,

$$\alpha + \beta n = \frac{\sigma(V + \geq n \text{ jets})}{\sigma(V + \geq (n + 1) \text{ jets})}, \quad (8.3)$$

ANALYSIS STRATEGY

with $n = 1, 2, 3$ and $V = W(\rightarrow \mu\nu)$, $W(\rightarrow e\nu)$, $Z(\rightarrow \mu\mu)$ and $Z(\rightarrow ee)$. With this relation we describe the scaling of the $V + \text{jets}$ cross sections with the number of jets. The parameter α describes the Berends-Giele (BG) scaling [82]. If β differs from zero, this scaling is broken. The case $n = 0$ is not included in the measurement of α and β because the production process of vector bosons without jets differs significantly from $V + \text{jets}$ production and is not expected to follow the scaling. Again, systematic uncertainties cancel out to the extent that they do not depend on the jet multiplicity.

- The ratio of the normalized cross section for $W(\rightarrow \ell\nu)$ to the normalized cross section for $Z(\rightarrow \ell\ell)$ both in association with n or more jets,

$$\left[\frac{\sigma(W(\rightarrow \ell\nu) + \geq n \text{ jets})}{\sigma(W(\rightarrow \ell\nu))} \right] / \left[\frac{\sigma(Z(\rightarrow \ell\ell) + \geq n \text{ jets})}{\sigma(Z(\rightarrow \ell\ell))} \right], \quad (8.4)$$

with $n = 1, 2, 3, 4$ and $\ell = \mu, e$. This observable allows a detailed comparison of the $W + \text{jets}$ and the $Z + \text{jets}$ cross sections. Many systematic uncertainties have very little impact on this observable. Most important, the systematic uncertainty related to the jet energy scale cancels almost entirely. Because the analyses in the W and the Z channels adopted very similar strategies for the boson selection, also systematic uncertainties related to the lepton efficiency cancel out.

- The charge asymmetry A_W^n for W boson production in association with n or more jets,

$$A_W^n = \frac{\sigma(W^+ + \geq n \text{ jets}) - \sigma(W^- + \geq n \text{ jets})}{\sigma(W^+ + \geq n \text{ jets}) + \sigma(W^- + \geq n \text{ jets})}, \quad (8.5)$$

with $n = 0, 1, 2, 3$ and $W = W(\rightarrow \mu\nu)$, $W(\rightarrow e\nu)$. The charge asymmetry quantifies the difference in production rate between W^+ and W^- . The charge asymmetry is an interesting observable because it is very sensitive to the structure of the proton. Also here, many systematic uncertainties cancel out almost entirely.

We quote our results within the part of phase space that we probe with our analysis, i.e. the part of phase space within the kinematic acceptance of the detector and the trigger. Thus, the results are not extrapolated to cover the whole phase space. We define the part of phase space within acceptance on the particle level [100]:

- The visible lepton from the W decay or the lepton from the Z decay with the highest p_T must have $p_T > 20$ GeV. In the muon channels, this lepton must have $|\eta| < 2.1$ while in the electron channels we require $|\eta| < 2.5$ and

neglect the transition region between the barrel and the endcap of ECAL, $1.4442 < |\eta| < 1.566$.

- In the Z channels, the second lepton must have $p_T > 10$ GeV and $|\eta| < 2.5$. In the $Z(\rightarrow ee)$ channel, the region $1.4442 < |\eta| < 1.566$ is neglected.
- The invariant mass of the Z , m_Z , is required to be within the region $60 < m_Z < 120$ GeV.
- Jets are clustered with the anti- k_T algorithm and a cone radius $R = 0.5$ from all visible particles. In the muon channels, the muons from the vector boson decays are not included in the clustering.
- Jets are counted if they have $p_T > 30$ GeV and $|\eta| < 2.4$. In the electron channels jets are not counted if they are within a cone $\Delta R < 0.3$ from any of the electrons from the vector boson decay.

We correct our measurements for detector effects and quote results on the particle level. This implies that any of the predictions can be compared to our measurements by incorporating these predictions into a MC event generator that includes showering and hadronization and by applying the phase space requirements listed above to the simulated events. Our measurements can then be compared directly to the corresponding quantities observed in the simulation.

The Chapters 9 and 10 will detail the V+jets measurements in the $W(\rightarrow \mu\nu)$ channel to which I have made important contributions. Before that, an overview of the analysis is given in the next Section 8.3. Chapter 11 will discuss the results of the complete V+jets analysis as published in [16].

8.3 Analysis path for $W(\rightarrow \mu\nu)$

We perform our measurements in a sample of proton-proton events at $\sqrt{s} = 7$ TeV, corresponding to 36 pb^{-1} , collected with muon triggers during the 2010 data taking and reconstructed with the PF algorithm (**Sections 9.1 and 9.3**). The analysis starts by selecting events containing at least one reconstructed isolated muon of high quality, originating from the primary vertex. The leading muon acts as the $W(\rightarrow \mu\nu)$ candidate and must be within the acceptance of the measurement as defined earlier. We reconstruct the transverse mass m_T of the $W(\rightarrow \mu\nu)$ candidate, defined in Equation 6.4, from the leading muon and the E_T^{miss} , and reduce background contributions requiring $m_T > 20$ GeV. Jets are clustered from all PF particles except the leading muon and must have $p_T > 30$ GeV, $|\eta| < 2.4$.

ANALYSIS STRATEGY

The efficiency of the reconstruction of the leading muon and the isolation, vertex and quality criteria is measured as a function of the muon kinematics and the jet multiplicity, using the Tag and Probe (TnP) technique in $Z(\rightarrow \mu\mu)$ events (**Section 9.4**). The efficiency of the m_T requirement is measured in MC as a function of the jet multiplicity. To correct our measurement for the loss of signal ($W(\rightarrow \mu\nu)$) events associated to these selection criteria, we weight the selected sample event-by-event with the inverse of the efficiency.

The thus selected sample of events mainly originates from $W(\rightarrow \mu\nu)$ production, the signal for this measurement. Important background contributions stem from QCD multi-jet production and, in events with 3 or more jets, top quark production. In events with 4 or more jets, top quark production even dominates over the $W(\rightarrow \mu\nu)$ signal.

We proceed by measuring the $W(\rightarrow \mu\nu)$ signal contribution in the selected sample as a function of the jet multiplicity. The selected data are binned according to the jet multiplicity (0 jets, 1 jet, 2jets, 3 jets and ≥ 4 jets). Jet bins containing events with exactly n jets are referred to as *exclusive jet bins*, while jet bins holding events with n or more jets are referred to as *inclusive jet bins*. Then, we make use of the m_T distribution to discriminate between $W(\rightarrow \mu\nu)$ and QCD production. The distribution of the number of b -tagged jets is used to discriminate between $W(\rightarrow \mu\nu)$ and top quark production (**Section 10.1**). The discriminating power of these variables allows to measure in each jet bin the $W(\rightarrow \mu\nu)$ signal contribution by performing a Maximum Likelihood (ML) fit of m_T and $n^{b \text{ tag}}$ (**Section 10.2**). The robustness of the ML fit was tested extensively, both with toy MC experiments and with full MC simulation (**Section 10.3**). The modeling of signal and background in the fit relies as little as possible on MC simulation. However the few assumptions that are based on MC simulation are validated in control samples in data (**Section 10.4**).

The ML fits provide us with estimates for the $W(\rightarrow \mu\nu)$ signal contribution within the acceptance as a function of reconstructed jet multiplicity (**Section 10.5**). We determine the uncertainties on these estimates related to our limited knowledge of the detector response and the finite jet reconstruction and selection efficiency (**Section 10.6**). Then, we correct the measured jet spectrum for resolution effects (**Section 10.7**). The resulting signal yields as function of the jet multiplicity are used to compute, the observables in Equations 8.1 and 8.2 and, in combination with the $Z(\rightarrow \mu\mu) + \text{jets}$ measurements, to compute the observable in Equation 8.4.

Then, we measure the $W^-(\rightarrow \mu\nu)$ and $W^+(\rightarrow \mu\nu)$ contributions separately in the

exclusive 0, 1 and 2 jet bins and the inclusive 3 jet bin (**Chapter 10.9**). For that purpose the data are binned according to the jet multiplicity and according to the charge of the $W(\rightarrow \mu\nu)$ candidate, the leading muon. In each bin, the signal contribution is extracted with the ML fit mentioned earlier, which allows the computation of the charge asymmetry defined in Equation 8.5.

Finally, the BG parameters are derived from ML fits on m_T and $n^{b \text{ tag}}$, simultaneously performed on the exclusive jet bins 0, 1, 2 and 3 and the inclusive 4th jet bin. To obtain estimates of α and β , the signal yields in the separate bins are related using the BG relation in Equation 8.3 (**Chapter 10.8**). Corrections for jet resolution effects are incorporated in the likelihood function itself. This requires that, although the BG scaling is only measured for jet multiplicities from 1 to 4, the exclusive 0 jet bin is included in the measurement because it affects higher jet multiplicity bins through jet resolution effects.

9

Data and simulation for $W(\rightarrow \mu\nu)$ measurements

9.1 Data

This analysis makes use of data from proton-proton collisions at a center of mass energy of $\sqrt{s} = 7$ TeV, collected by CMS in 2010 with muon triggers and corresponding to an integrated luminosity of 35.9 ± 1.4 pb⁻¹. The considered muon triggers are HLT_Mu9, HLT_Mu11, HLT_Mu13_v1 or HLT_Mu15_v1, which fire on the presence of a muon with transverse momentum above respectively 9, 11, 13 or 15 GeV muon reconstructed at HLT-level. These data are reprocessed with CMSSW_3_8_7 and events were reconstructed with the PF algorithm.

9.2 MC simulation

Several aspects of the analysis rely on MC simulated events. We make use of simulated proton-proton collisions centrally produced by the CMS collaboration during the Fall10 simulation campaign [101]. The processes included in the analysis are listed in Table 9.1 together with the covered phase space. Numbers of simulated events are scaled to the integrated luminosity of the analyzed data making use of cross sections calculated at Leading Order (LO), Next-to-Leading Order (NLO) or

Next-to-Next-to-Leading Order (NNLO), as indicated in the table.

We consider as QCD production, the strong production of gluons and u, d, c, s and b -quarks. The production of top quarks is considered as a separate process. For QCD, the hard interaction is generated with PYTHIA 6.422 [24] while for all other processes MADGRAPH 4.4.13 [60] is used. The advantage of using MADGRAPH for the hard interaction with respect to PYTHIA is that in MADGRAPH the hardest parton emissions are modeled with matrix elements, leading to a more accurate description of the associated jet production. The PDFs, parton showering, hadronization and underlying event are described by PYTHIA 6.422. MADGRAPH is interfaced with PYTHIA using the MLM jet matching prescription [28], which avoids double counting of hard parton emission. The CTEQ6L1 PDFs [102] are used and TuneZ2 [103] is used for the underlying event.

Generated events are processed through a full simulation of the CMS detector based on GEANT4 [104] as implemented in CMSSW_3_8_4. with the detector calibration and alignment conditions set to a realistic start-up scenario (global tag: START38_V12). As for the actual data, simulated events are reconstructed with the PF algorithm. Minimum-bias events are superimposed on the generated events to mimic the effect of pile-up under the 2010 luminosity conditions.

Table 9.1 – Processes included in the MC simulated proton-proton collisions used in the $W(\rightarrow \mu\nu)$ analysis together with the covered phase space and the cross sections σ_{eff} within this phase space, used to scale numbers of events observed in MC to expected numbers of events in data. Also indicated is the origin of the cross sections: LO, NLO and NNLO for respectively Leading Order, Next to Leading Order and Next to Next to Leading Order calculations.

process	phase space	σ_{eff} (pb)
W + jets	$W \rightarrow l\nu$ only	3.1×10^4 (NNLO)
QCD	$p_T^\mu > 15$ GeV, $\eta^\mu < 2.5$ GeV, g, u, d, c, s, b	8.5×10^4 (LO)
$t\bar{t}$	inclusive	1.6×10^2 (NLO)
t (s-channel)	$W \rightarrow l\nu$ only	1.4×10^0 (NLO)
t (t-channel)	$W \rightarrow l\nu$ only	2.1×10^0 (NLO)
t (tW -channel)	inclusive	1.1×10^1 (LO)
Z + jets	$Z \rightarrow ll$ only decays	3.0×10^3 (NNLO)

9.3 Selection

Muons

As mentioned earlier, events must fire one of the HLT muon triggers HLT_Mu9, HLT_Mu11, HLT_Mu13_v1 or HLT_Mu15_v1. Events must have at least one muon reconstructed as global muon and the muon with highest p_T , the *leading muon*, must be within the acceptance of the measurement, $p_T > 20$ GeV and $|\eta| < 2.1$. To enable the measurement of the trigger efficiency, the leading muon must match with the trigger object that fired one of the considered muon triggers.

A series of identification criteria imposed on the leading muon removes contributions from fake muons and provides a first filtering against muons produced in jets. The muon must have at least 1 hit in the silicon pixel detector, at least 11 hits in the tracker, and at least 1 hit in the muon system. Its global fit must have $\chi^2 < 10$, and it must also succeed an alternative reconstruction as *tracker muon*. Finally, the associated charged-particle track must match with track segments in at least two muon stations.

A loose vertex criterion requires that the vertex of the leading muon is within 0.2 cm from the Primary Vertex (PV) along the transverse plane. This requirement removes cosmic muons and part of the contribution from decays of long-living particles involving muons. To further decrease the contribution from QCD multi-jet production the isolation criterion requires $I_{rel}^{0.3} < 0.15$, with $I_{rel}^{0.3}$ as defined in Equation 6.1.

Z-veto

To remove contributions from Z production and to keep our analysis statistically independent from the $Z + \text{jets}$ analysis, we apply a Z veto. We veto events with a second muon matching the following criteria: it has $p_T > 10$ GeV and $|\eta| < 2.5$, it is reconstructed as global muon and finally, the invariant mass of the di-muon system is between 60 and 120 GeV.

Transverse mass, m_T

The E_T^{miss} is reconstructed from all PF particles and used together with the leading muon to derive the transverse mass m_T as described in Section 6.3. Events are required to have $m_T > 20$ GeV, removing most of the QCD background and causing

a loss of $W(\rightarrow \mu\nu)$ events of only 5 to 10%, depending on the jet multiplicity.

Jets

Jets are clustered with the anti- k_T algorithm with radius parameter $R = 0.5$ from all PF particles except the leading muon. The pile-up contribution to the jet energies is removed on a jet-by-jet basis using the prescription in [105]. This technique first estimates the average energy density not related to the hard interaction. Then, it estimates the jet area for each jet and subtracts the corresponding energy not related to the hard interaction. After pile-up subtraction we apply the Jet Energy Corrections, determined from measurements in data as a function of jet p_T and η [106].

Jets are counted with $p_T > 30$ GeV and $\eta < 2.4$, matching the definition of the acceptance of the measurement. A set of loose jet identification criteria removes fake jets: the fraction of the jet energy carried by neutral hadrons must be above 0 and below 0.99; the fraction of the jet energy carried by photons must be below 0.99; also the fraction of the jet energy carried by electrons must be below 0.99; and finally the jet must have at least 2 constituents.

b -tagging

In the signal extraction we identify b -jets making use of b -tagging. The b -tag discriminator used is the *Track Counting High Efficiency* algorithm [53]. If for a jet, the value of the discriminator is above 3.3 the jet is b -tagged. As such the tag efficiency for b -jets, or *b -tag efficiency*, is roughly 60% while for other jets the tag efficiency, or *mistag efficiency*, is about 1%.

Cut flow

We apply this selection both to the data and the MC simulated events. The composition of the sample in MC simulated events is shown in Table 9.2. $W(\rightarrow \mu\nu)$ dominates the sample followed by the background from QCD. The contribution from top quark production is negligible or small in events with 0, 1 and 2 jets. In events with 3 jets, this contribution is of the same order as the signal contribution and in events with 4 jet or more, top quark production dominates. Table 9.3 compares the number of events observed in data and MC simulation.

Table 9.2 – Composition of the selected events in MC simulation as a function of the number of jets. The numbers of events observed in the MC simulation were scaled to represent an integrated luminosity of 35.9pb^{-1} . Uncertainties are statistical only.

	$W(\rightarrow \mu\nu)$	QCD	top	$W(\rightarrow \mu\nu)$	Z
0 jets	150333 ± 184	11818 ± 42	18 ± 1	6679 ± 39	6618 ± 16
1 jet	17126 ± 62	6170 ± 30	114 ± 1	987 ± 15	1449 ± 7
2 jets	3101 ± 26	849 ± 11	301 ± 2	219 ± 7	238 ± 3
3 jets	515 ± 11	153 ± 5	433 ± 3	48 ± 3	45 ± 1
≥ 4 jets	101 ± 5	27 ± 2	398 ± 3	14 ± 2	10 ± 1

Table 9.3 – Number of selected events in data and in MC simulation. The numbers of events observed in the MC simulation were scaled to represent an integrated luminosity of 35.9pb^{-1} . Uncertainties are statistical only.

	data	MC
0 jets	175240 ± 419	175466 ± 193
1 jet	24638 ± 157	25846 ± 71
2 jets	5299 ± 73	4708 ± 30
3 jets	1154 ± 34	1194 ± 13
≥ 4 jets	437 ± 21	550 ± 6

9.4 Selection efficiency for $W(\rightarrow \mu\nu)$

For our final measurements to cover the whole phase space within acceptance, we must take into account the finite efficiency by which $W(\rightarrow \mu\nu)$ events within acceptance, pass the selection criteria. Therefore, we estimate this efficiency as a function of the p_T and η of the leading muon and the number of jets in the event. Then, when the signal contribution is extracted in each jet bin, we weight the data set event-by-event with the inverse of the efficiency. We take into account the efficiencies related to the requirements on the leading muon and the efficiency related to the m_T cut. Loss of signal due to other selection criteria is negligible. Also negligible and not taken into account, is the correlation between the efficiency of the reconstruction and selection of the leading muon and the efficiency of the m_T cut.

In order to estimate the efficiency for signal events within acceptance to pass the

leading muon criteria, we factorize it as follows:

$$\epsilon_\mu = p(\text{trigger}|\text{id}, \text{reco}, \text{track}) p(\text{id}|\text{reco}, \text{track}) p(\text{reco}|\text{track}) p(\text{track}) \quad (9.1)$$

with

- $p(\text{track})$ the probability that the muon is reconstructed as tracker track,
- $p(\text{reco}|\text{track})$ the probability for a muon that is reconstructed as a tracker track to be reconstructed as global muon as well,
- $p(\text{id}|\text{reco}, \text{track})$ the probability for a muon that is reconstructed as a tracker track and as global muon to pass the identification criteria, the vertex criterion and the isolation criterion,
- $p(\text{trigger}|\text{id}, \text{reco}, \text{track})$ the probability for a muon that is reconstructed as a tracker track and as global muon and further passes identification, vertex and isolation criteria to pass the trigger criterion.

$p(\text{track})$ is measured to be about 100% for muons within the acceptance of the measurement [107]. All other probabilities are measured separately with the Tag and Probe technique (TnP) in $Z(\rightarrow \mu\mu)$ events as will be explained in the next Sections.

The efficiency of the complete selection, combining the muon criteria and the m_T cut is then estimated as

$$\epsilon = \epsilon_\mu \cdot \epsilon_{m_T} \quad (9.2)$$

with ϵ_{m_T} the efficiency for $W(\rightarrow \mu\nu)$ events that pass the muon criteria to pass the m_T cut. This efficiency is measured in MC and cross checked in $Z(\rightarrow \mu\mu)$ data with the TnP technique as explained in Section 9.4.1.

9.4.1 Tag and Probe

With the TnP technique we select a clean sample of muons from $Z(\rightarrow \mu\mu)$ events in data in which we measure the efficiencies listed above. Because the Z and W production and decay are very similar, we expect the efficiency for muon reconstruction and selection in this sample and in the $W(\rightarrow \mu\nu)$ sample to be very similar as well. The small differences originate mainly from differences in the muon p_T and η spectra, which is why we measure the efficiency ϵ as a function of p_T and η .

For events to be included in the TnP measurement, a first muon, the *tag* must be present. It must pass all criteria imposed on the leading muon in the $W(\rightarrow \mu\nu)$ analysis, as described in the previous section, except for looser kinematic cuts, $p_T >$

10 GeV and $|\eta| < 2.4$. The altered kinematics cuts increase the available statistics and, because efficiencies are measured as a function of muon p_T and η , they do not bias the result.

Then, *probes* are selected. Probes are defined as objects, tracks or muons, that when combined with the tag, have an invariant mass close to the Z -mass, between 60 and 120 GeV. After this requirement, the sample of probes consists mainly of muons originating from $Z(\rightarrow \mu\mu)$. Further base requirements depend on the efficiency to be measured and are explained later. Then, the efficiency of a certain requirement of interest is estimated as follows:

- The probes that fail the requirement constitute the subsample of *failing probes*.
- The probes that pass the requirement constitute the subsample of *passing probes*.
- Contributions from probes that do not originate from Z decays must not be taken into account in the efficiency measurement since this would possibly bias the result. Therefore the $Z(\rightarrow \mu\mu)$ contribution is estimated in both the failing and the passing probes, making use of Maximum Likelihood fits of the invariant mass of the tag-probe systems.
- The result of the fits is an estimate of the number of $Z(\rightarrow \mu\mu)$ probes failing the requirement and the number of $Z(\rightarrow \mu\mu)$ probes passing the requirement, enabling the calculation of the efficiency of the requirement of interest. The estimates obtained from the fits have a statistical uncertainty, which is propagated to the estimated efficiency.

As an illustration, Figure 9.1 shows the fits for the TnP measurement of the efficiency of the muon identification, isolation and vertex requirement in events with 0 jets, which is explained in detail further-on in this section.

To measure efficiencies as a function of muon p_T and η , we apply this procedure in bins of probe p_T and η . To measure efficiencies as a function of jet multiplicity we apply the procedure on subsamples of events of definite jet multiplicity.

Reconstruction efficiency

For the measurement of $p(\text{reco}|\text{track})$, probes are tracker tracks with $p_T > 20$ GeV and $|\eta| < 2.4$. Probes pass if a global muon is found within a cone of radius $R < 0.01$

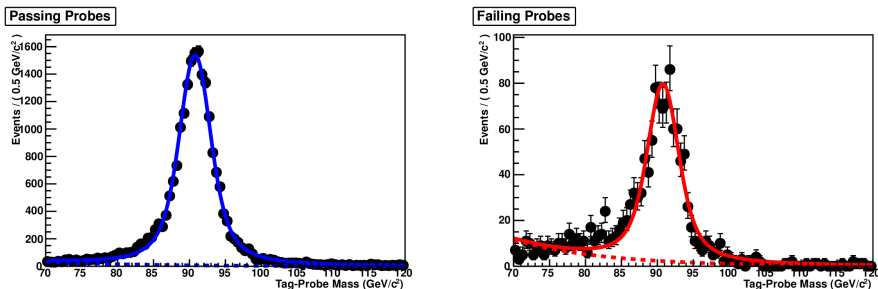


Figure 9.1 – Fits for the measurement of the efficiency of the muon identification, isolation and vertex requirements in events with 0 jets. The black dots show the invariant mass distribution of the tag-probe systems for passing probes (left) and failing probes (right). The dotted and continuous lines show the fit result. The dotted line represent the probability density function (PDF) for the background and the full line the total PDF.

around the track. The efficiency is found to be close to 1 and shows very little dependence on muon p_T and η . The dependence on the number of jets is found to be negligible and therefore this efficiency was measured as a function of muon p_T and η only. Table 9.4 lists the measured efficiencies.

Efficiency of muon identification, isolation and vertex requirements

For the measurement of $p(\text{id|reco, track})$ probes are global muons with $p_T > 15$ GeV and $|\eta| < 2.1$. Probes pass if they match the identification, vertex and isolation criteria. The measured efficiency ranges from 0.8 to 0.95 and shows a clear dependence on muon p_T , η and n^{jets} . For $n^{\text{jets}} = 0, 1$, the efficiency was measured in bins of muon p_T , η and as a function of n^{jets} . However, for $n^{\text{jets}} > 1$ the number of probes is too small to bin in p_T , η and the efficiency is measured as a function of n^{jets} only. For those higher jet multiplicities we assume that the efficiency shows the same dependence in p_T and η as for the low jet multiplicities and write

$$\begin{aligned}
 p(\text{id|reco, track}; p_T, \eta, (n^{\text{jets}} = N)) = \\
 p(\text{id|reco, track}; p_T, \eta, (n^{\text{jets}} = 1)) \frac{p(\text{id|reco, track}; (n^{\text{jets}} = N))}{p(\text{id|reco, track}; (n^{\text{jets}} = 1))} \quad N = 2, 3, \geq 4
 \end{aligned} \tag{9.3}$$

Tables 9.6 and 9.7 list the measured efficiencies in events with 0 and 1 jets, while Table 9.5 lists the measured efficiency as a function of n^{jets} .

Muon trigger efficiency

For the measurement of $p(\text{trigger}|\text{id}, \text{reco}, \text{track})$ probes are global muons passing identification, vertex and isolation criteria. Probes pass if they match the trigger criterion. The measured efficiency shows a clear dependence on p_T and η . The dependency on the number of jets is found to be negligible. Therefore, this efficiency was measured as a function of muon p_T and η only. Table 9.8 lists the measured efficiencies.

Efficiency of the m_T cut

The efficiency for signal events within acceptance to pass the cut on m_T was estimated from simulated $W(\rightarrow \mu\nu)$ events as a function of the number of jets. The resulting efficiencies are listed in Table 9.9.

A cross check is performed, again with TnP in $Z(\rightarrow \mu\mu)$ data. Tags are leading muons that pass all the leading muon criteria from the $W(\rightarrow \mu\nu)$ analysis. and probes are second leading muons that are global and have $p_T > 10$ GeV and $\eta < 2.4$. To decide whether a probe passes, it is treated as if it were a neutrino, invisible and contributing to the E_T^{miss} . The jet clustering is repeated under this assumption and we reconstruct the transverse mass m_T from the leading muon and the E_T^{miss} . Because Z bosons are about 10 GeV heavier than W -bosons, the resulting m_T distribution in $Z(\rightarrow \mu\mu)$ events is rescaled with a factor M_W/M_Z to represent the m_T distribution in $W(\rightarrow \mu\nu)$ events. Here, M_W and M_Z are the masses for respectively the W and Z bosons as recommended by the Particle Data Group (PDG) [20]. Probes pass if the rescaled m_T is above 20 GeV. This cross check was performed as a function of the jet multiplicity and is listed in Table 9.9. The table also lists the efficiency to pass the 20 GeV cut on the rescaled m_T for simulated $Z(\rightarrow \mu\mu)$ events with a valid tag and a valid probe.

Within uncertainties, there is an excellent agreement between the results from the simulated $Z(\rightarrow \mu\mu)$ and $W(\rightarrow \mu\nu)$ events, validating the m_T calculation for $Z(\rightarrow \mu\mu)$ events. Also the agreement between TnP and the estimates from MC is excellent. However, the uncertainties on the TnP measurements are quite large.

Table 9.4 – Efficiency for muons that are reconstructed as tracker tracks to be reconstructed as global muons. The efficiency is measured with TnP in $Z(\rightarrow \mu\mu)$ data as a function of muon p_T and η . Uncertainties are statistical only.

	$0.0 \leq \eta < 0.8$	$0.8 \leq \eta < 1.7$	$1.7 \leq \eta < 2.1$
$20 \leq p_T < 25$	0.958 ± 0.037	0.945 ± 0.028	0.898 ± 0.041
$25 \leq p_T < 30$	0.990 ± 0.008	0.976 ± 0.015	1.000 ± 0.008
$30 \leq p_T < 35$	1.000 ± 0.001	1.000 ± 0.004	1.000 ± 0.005
$35 \leq p_T < 40$	0.998 ± 0.002	0.996 ± 0.003	0.995 ± 0.005
$40 \leq p_T < 50$	0.998 ± 0.002	0.996 ± 0.003	1.000 ± 0.001
$50 \leq p_T < 100$	1.000 ± 0.001	1.000 ± 0.004	0.963 ± 0.019

Table 9.5 – Efficiency for global muons to pass the identification, vertex and isolation criteria. The efficiency is measured with TnP in $Z(\rightarrow \mu\mu)$ data as a function of the number of jets. Uncertainties are statistical only.

0 jets	1 jet	2 jets	3 jets	≥ 4 jets
0.952 ± 0.002	0.925 ± 0.006	0.915 ± 0.014	0.916 ± 0.048	0.843 ± 0.091

Table 9.6 – Efficiency for global muons in events with 0 jets to pass the identification, vertex and isolation criteria. The efficiency is measured with TnP in $Z(\rightarrow \mu\mu)$ data as a function of muon p_T and $|\eta|$. Uncertainties are statistical only.

	$0.0 \leq \eta < 0.8$	$0.8 \leq \eta < 1.2$	$1.2 \leq \eta < 1.7$	$1.7 \leq \eta < 2.1$
$20 \leq p_T < 25$	0.939 ± 0.017	0.956 ± 0.016	0.944 ± 0.018	0.916 ± 0.011
$25 \leq p_T < 30$	0.953 ± 0.010	0.938 ± 0.017	0.960 ± 0.013	0.942 ± 0.015
$30 \leq p_T < 35$	0.942 ± 0.008	0.947 ± 0.013	0.958 ± 0.011	0.943 ± 0.013
$35 \leq p_T < 40$	0.956 ± 0.005	0.957 ± 0.009	0.946 ± 0.009	0.931 ± 0.011
$40 \leq p_T < 50$	0.965 ± 0.000	0.948 ± 0.006	0.965 ± 0.004	0.962 ± 0.006
$50 \leq p_T < 100$	0.963 ± 0.007	0.953 ± 0.013	0.968 ± 0.011	0.968 ± 0.011

DATA AND SIMULATION FOR $W(\rightarrow \mu\nu)$ MEASUREMENTS

Table 9.7 – Efficiency for global muons in events with 1 jet to pass the identification, vertex and isolation criteria. The efficiency is measured with TnP in $Z(\rightarrow \mu\mu)$ data as a function of muon p_T and $|\eta|$. Uncertainties are statistical only.

	$0.0 \leq \eta < 0.8$	$0.8 \leq \eta < 1.2$	$1.2 \leq \eta < 1.7$	$1.7 \leq \eta < 2.1$
$20 \leq p_T < 25$	0.821 ± 0.047	0.818 ± 0.058	0.903 ± 0.062	0.956 ± 0.043
$25 \leq p_T < 30$	0.953 ± 0.024	0.848 ± 0.042	0.954 ± 0.002	0.879 ± 0.055
$30 \leq p_T < 35$	0.913 ± 0.029	0.945 ± 0.027	0.823 ± 0.049	0.889 ± 0.054
$35 \leq p_T < 40$	0.929 ± 0.216	0.960 ± 0.028	0.955 ± 0.025	0.877 ± 0.028
$40 \leq p_T < 50$	0.911 ± 0.019	0.947 ± 0.023	0.922 ± 0.026	0.942 ± 0.035
$50 \leq p_T < 100$	0.952 ± 0.011	0.961 ± 0.016	0.962 ± 0.013	1.000 ± 0.001

Table 9.8 – Efficiency for global muons passing identification, vertex and isolation criteria to pass the trigger requirement. The efficiency is measured with TnP in $Z(\rightarrow \mu\mu)$ data as a function of p_T and $|\eta|$. Uncertainties are statistical only.

	$0.0 \leq \eta < 0.8$	$0.8 \leq \eta < 1.2$	$1.2 \leq \eta < 1.7$	$1.7 \leq \eta < 2.1$
$20 \leq p_T < 25$	0.963 ± 0.012	0.877 ± 0.022	0.911 ± 0.018	0.869 ± 0.024
$25 \leq p_T < 30$	0.966 ± 0.008	0.868 ± 0.010	0.903 ± 0.015	0.858 ± 0.022
$30 \leq p_T < 35$	0.964 ± 0.006	0.879 ± 0.015	0.939 ± 0.011	0.844 ± 0.020
$35 \leq p_T < 40$	0.959 ± 0.005	0.873 ± 0.013	0.910 ± 0.011	0.873 ± 0.004
$40 \leq p_T < 50$	0.962 ± 0.003	0.856 ± 0.008	0.925 ± 0.006	0.869 ± 0.010
$50 \leq p_T < 100$	0.973 ± 0.005	0.868 ± 0.015	0.917 ± 0.011	0.839 ± 0.020

Table 9.9 – Efficiency for $W(\rightarrow \mu\nu)$ events within the acceptance of the measurement to pass the cut $m_T > 20$ GeV. The efficiency is measured as a function of the jet multiplicity in three independent ways: with TnP in $Z(\rightarrow \mu\mu)$ data (TnP); from $Z(\rightarrow \mu\mu)$ MC simulation ($Z(\rightarrow \mu\mu)$ MC); directly from $W(\rightarrow \mu\nu)$ MC simulation ($W(\rightarrow \mu\nu)$ MC). See text for details. Uncertainties are statistical only.

	$Z(\rightarrow \mu\mu)$ MC	$Z(\rightarrow \mu\mu)$ TnP	$W(\rightarrow \mu\nu)$ MC
0 jets	0.995 ± 0.003	1.00 ± 0.02	0.994 ± 0.002
1 jet	0.935 ± 0.008	0.96 ± 0.03	0.933 ± 0.005
2 jets	0.92 ± 0.02	0.94 ± 0.06	0.92 ± 0.01
3 jets	0.91 ± 0.05	0.9 ± 0.2	0.91 ± 0.02
≥ 4 jets	0.9 ± 0.1	0.9 ± 0.4	0.91 ± 0.06

10

Measurements of $W(\rightarrow \mu\nu) +$ jets production

The sample of events selected as described in the previous chapter, is dominated by $W(\rightarrow \mu\nu)$ events, the signal for this analysis. However, important backgrounds arise from QCD multi-jet production and top quark production. We devised a data driven method to extract the signal contribution to the sample as a function of the jet multiplicity, making use of Maximum Likelihood (ML) fits to the distribution of the transverse mass m_T and the number of b -tagged jets $n^{b \text{ tag}}$.

10.1 Discriminating variables

To discriminate between $W(\rightarrow \mu\nu)$ signal and background from QCD multi-jet production, we make use of the transverse mass m_T of the leading muon and the missing transverse energy \vec{E}_T^{miss} . The data points in Figures 10.1 and 10.2 show the m_T distribution in selected MC simulated events for different processes and jet multiplicities. The full lines show the Probability Density Functions (PDFs) that are used for the signal extraction, as explained further-on. For $W(\rightarrow \mu\nu)$ events, the distribution of this variable shows a peaking behavior with a maximum around 80 GeV, while for QCD jet production the distribution falls steeply. We exploit this behavior to subtract contributions from QCD multi-jet production from our sample. The decay

of a real W boson to a muon and a neutrino is a signature of both $W(\rightarrow \mu\nu)$ signal and the background from top quark production. Thus, m_T exhibits a very similar behavior for these two processes and hardly any discriminating power.

To discriminate against top quark production we exploit the b -jet multiplicity. In $W(\rightarrow \mu\nu)$ events, the production of b -quarks is rare, while in top quark events typically 2 b -quarks are produced. This behavior is reflected in the number of b -tagged jets, $n^{b \text{ tag}}$. The data points in Figure 10.3 shows the distribution of $n^{b \text{ tag}}$ in selected MC events as a function of the process and the jet multiplicity. The full lines show the PDFs that are used for the signal extraction, as explained further-on. Clearly, with respect to $n^{b \text{ tag}}$ there is a significant difference between $W(\rightarrow \mu\nu)$ and top quark production.

10.2 Maximum Likelihood fits

We measure the $W(\rightarrow \mu\nu)$ signal contribution in the selected sample as a function of the jet multiplicity. To this end, the data are divided into 4 exclusive jet bins of events with exactly 0, 1, 2 or 3 jets and 1 inclusive jet bin of events with at least 4 jets. We estimate the $W(\rightarrow \mu\nu)$ signal contribution $n_j^{W(\rightarrow \mu\nu)}$ in each of the jet bins j with a Maximum Likelihood (ML) fit of the transverse mass m_T and the number of b -tagged jets $n^{b \text{ tag}}$. For this fit we build a model in which 5 species or processes contribute to each jet bin:

- $W(\rightarrow \mu\nu)$ signal events,
- QCD events: strong production of u , b , c , s and b -quarks and gluons,
- top quark events, including both top quark pair and single top production,
- $W(\rightarrow \mu\nu)$, all W production other than $W(\rightarrow \mu\nu)$,
- Z events, production of Z bosons.

10.2.1 Likelihood function

In each jet bin j we construct for each species s a PDF for m_T and $n^{b \text{ tag}}$ of the form

$$P_j^s(m_T, n^{b \text{ tag}} | \theta_{j,m_T}^s, \theta_{j,b}^s) = P_j^s(m_T | \theta_{j,m_T}^s) P_j^s(n^{b \text{ tag}} | \theta_{j,b}^s), \quad (10.1)$$

where θ_{j,m_T}^s and $\theta_{j,b}^s$ denote the parameters related to respectively the m_T and the $n^{b \text{ tag}}$ PDFs. Any relation between m_T and $n^{b \text{ tag}}$ within any of the defined species is neglected.

MEASUREMENTS OF $W(\rightarrow \mu\nu) + \text{JETS PRODUCTION}$

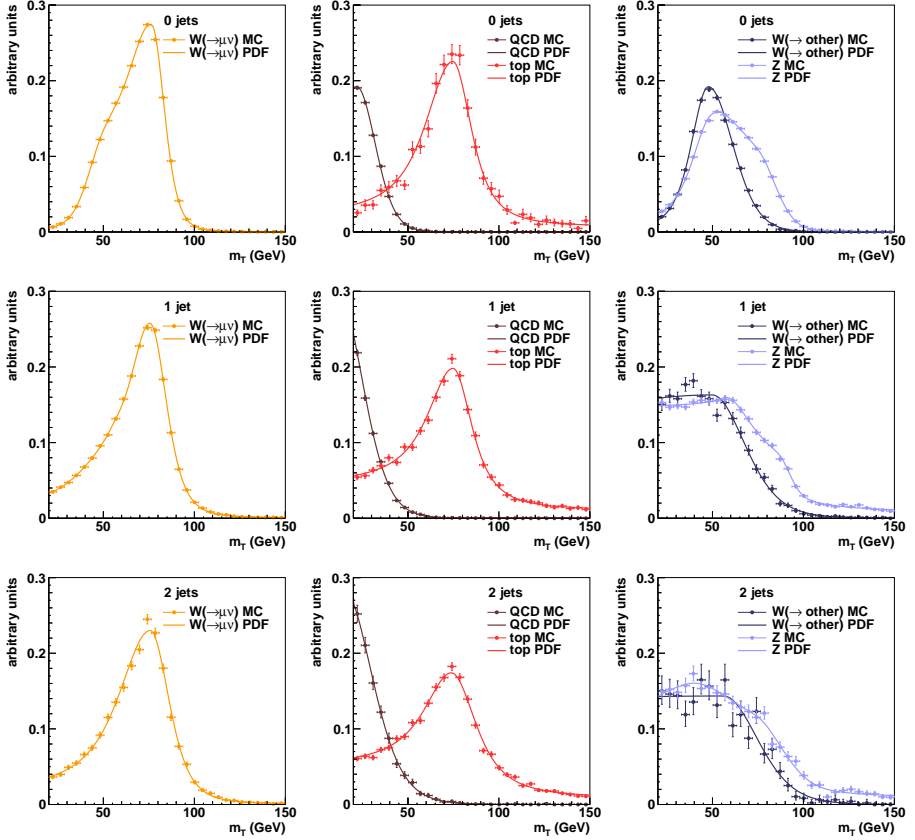


Figure 10.1 – The distribution of the transverse mass in selected MC simulated events for $W(\rightarrow \mu\nu)$, QCD, top quark, Z and $W(\leftrightarrow \mu\nu)$ production in events with 0, 1 and 2 jets. The error bars indicate the statistical uncertainties. The full lines represent the Probability Density Functions (PDFs) that model the m_T distributions in the signal extraction.

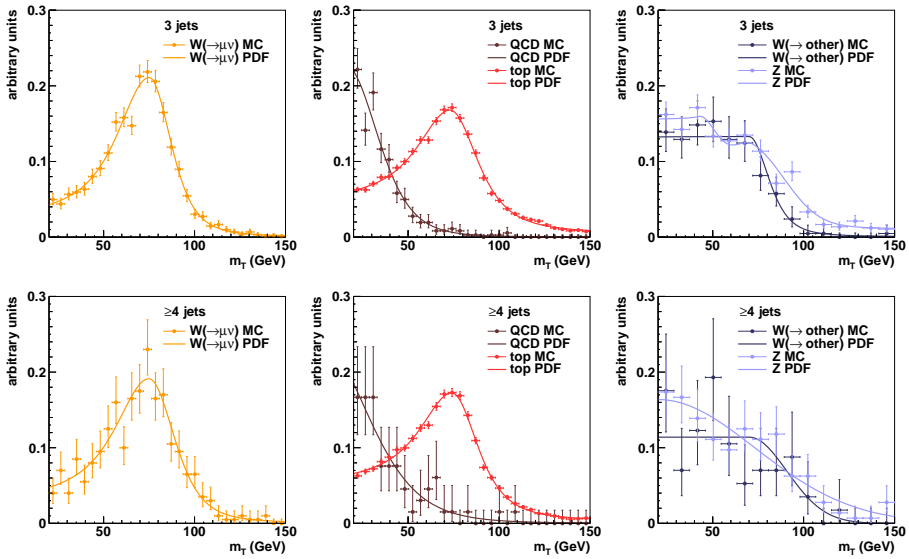


Figure 10.2 – The distribution of the transverse mass in selected MC simulated events for $W(\rightarrow \mu\nu)$, QCD, top quark, Z and $W(\rightarrow \mu\nu)$ production in events with 3 and ≥ 4 jets. The error bars indicate the statistical uncertainties. The full lines represent the Probability Density Functions (PDFs) that model the m_T distributions in the signal extraction.

MEASUREMENTS OF $W(\rightarrow \mu\nu) + \text{JETS PRODUCTION}$

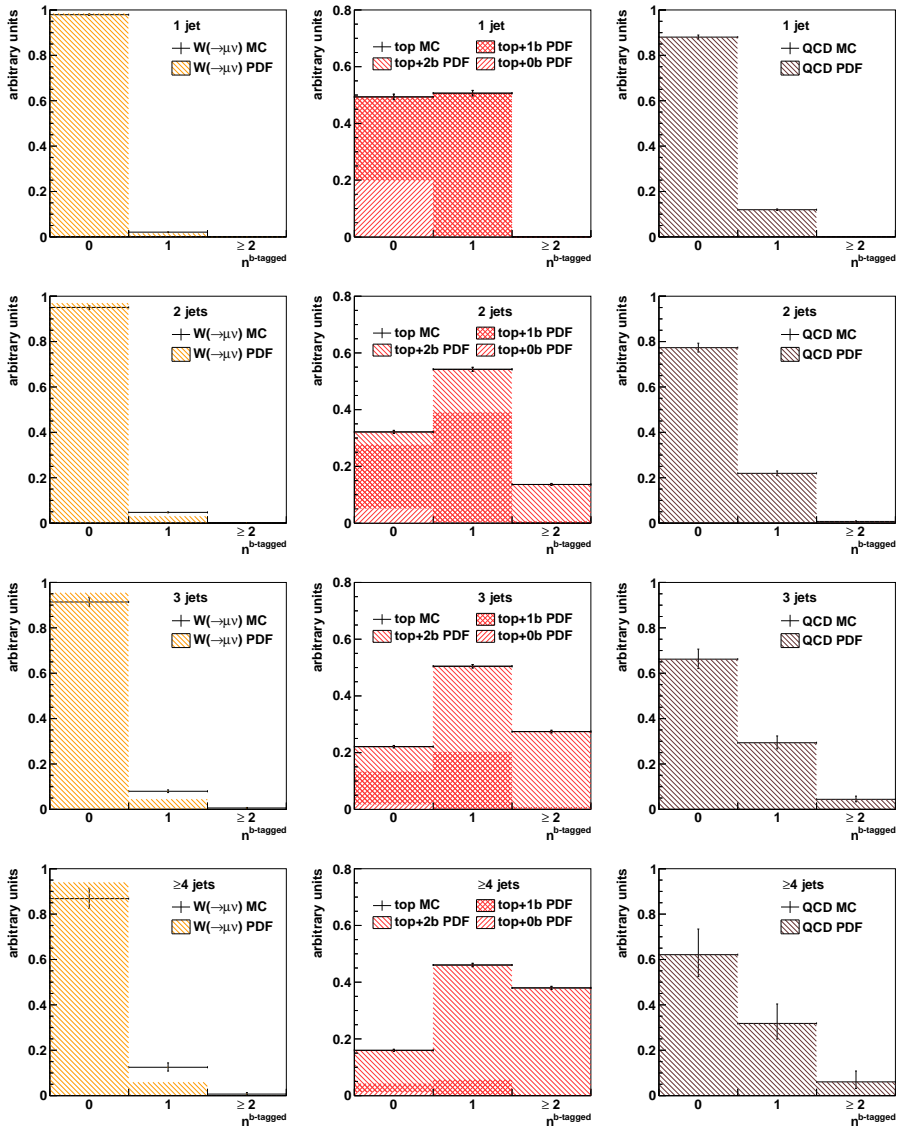


Figure 10.3 – The distribution of the number of b -tagged jets in selected MC simulated events for $W(\rightarrow \mu\nu)$, QCD, top quark, Z and $W(\rightarrow \mu\nu)$ production in events with 1, 2, 3 and ≥ 4 jets. The error bars indicate the statistical uncertainties. Filled areas represent the Probability Density Functions that model the $n^{b\text{ tag}}$ distributions in the signal extraction.

From these PDFs we build likelihood functions

$$\begin{aligned}
 L_j(n_j^{s=1..S}, \theta_{j,m_T}^{s=1..S}, \theta_{j,b}^{s=1..S}) &= P_j((m_T, n^{b \text{ tag}})_{e=1..N} | n_j^{s=1..S}, \theta_j^{s=1..S}) \\
 &= \frac{e^{-n_j} (n_j)^{N_j}}{N_j!} \prod_e \left[\sum_s \frac{n_j^s}{n_j} P_j^s(m_T, n^{b \text{ tag}} | \theta_{j,m_T}^s, \theta_{j,b}^s) \right],
 \end{aligned}
 \tag{10.2}$$

with

- N_j the number of events observed in jet bin j ,
- S the number of species,
- n_j^s the number of expected events for species s in jet bin j ,
- $n_j = \sum_s n_j^s$, the total number of expected events in jet bin j ,
- e an index for the event number and
- $e = 1..N$ or similar, denoting a set corresponding to indices 1 to N .

An estimate for $n_j^{W(\rightarrow\mu\nu)}$ is obtained by maximizing the likelihood function. The fits are implemented in the statistical framework `Roofit` [108]. This provides an interface to the minimization algorithm `Minuit` [109], used to find the maximum of the likelihood function. The uncertainty on the ML estimates is derived making use of the `Hesse`-algorithm within `Minuit`. This algorithm estimates the second derivatives for all floated parameters and then assumes a Gaussian shape for the maximum of the likelihood function to estimate the error matrix for the floated parameters.

The amount of signal that is lost in the event selection is corrected for, by weighting the data sample event-by-event with the inverse of the signal efficiency. As explained in Section 9.4, the signal efficiency is measured as a function of the leading muon p_T and η and the jet multiplicity.

10.2.2 Modeling the transverse mass

We model the m_T behavior for each of the species making use of an empirical function, the Cruiff function

$$\mathcal{C}(x; m, \sigma_L, \sigma_R, \alpha_L, \alpha_R) = \begin{cases} \exp\left(-\frac{(x-m)^2}{2\sigma_L^2 + \alpha_L(x-m)^2}\right) & \text{if } x \leq m \\ \exp\left(-\frac{(x-m)^2}{2\sigma_R^2 + \alpha_R(x-m)^2}\right) & \text{if } x > m \end{cases} \quad \alpha_L, \alpha_R \geq 0. \tag{10.3}$$

The Cruiff function has a Gaussian core with asymmetric width. Its tails are asymmetrically enhanced with respect to the Gaussian function if $\alpha_L, \alpha_R > 0$.

For signal events, the core of the m_T distribution in jet bins 0 and 1 exhibits a shoulder on the left-hand side. We describe this shoulder with an additional Cruijff function and the PDF of m_T for signal in those bins is the double Cruijff function

$$\begin{aligned} \mathcal{DC}(x; f, m, \sigma_L, \sigma_R, \alpha_L, \alpha_R; m', \sigma'_L, \sigma'_R, \alpha'_L, \alpha'_R) \\ = f \cdot \mathcal{C}(x; m, \sigma_L, \sigma_R, \alpha_L, \alpha_R) + (1 - f) \cdot \mathcal{C}(x; m', \sigma'_L, \sigma'_R, \alpha'_L, \alpha'_R) \\ \alpha_L, \alpha_R, \alpha'_L, \alpha'_R \geq 0, f > 0.5, m > m'. \end{aligned} \quad (10.4)$$

which is simply the weighted sum of two Cruijff functions. The first Cruijff describes the bulk of the distribution and the second the shoulder on the left. The double Cruijff function is furthermore used to model the m_T distribution in Z events.

For QCD events, the m_T distribution shows a falling spectrum which we describe with the right side of a Cruijff function

$$\mathcal{C}_R(x; m, \sigma_R, \alpha_R) = \mathcal{C}(x; m, \sigma_L, \sigma_R, \alpha_L, \alpha_R), \quad m < 20, \alpha_L = 1, \sigma_L = 1. \quad (10.5)$$

Table 10.1 lists the chosen PDFs for each species s and jet bin j .

The fraction of signal events with $m_T > 150$ GeV is negligible. This is also true for QCD events, the background species for which the m_T dimension in the fit is aimed for. Therefore the fit region in the m_T dimension is defined as $20 \text{ GeV} < m_T < 150 \text{ GeV}$.

We evaluate the quality of the modeling for m_T in MC simulated events. For each species and each jet bin we create a sample of MC simulated events in which we perform an ML fit on m_T using the respective PDF as likelihood function and floating all its parameters. The resulting shapes are shown in Figures 10.1 and 10.2 and compared to the m_T distributions in the MC simulated events. The estimates for the likelihood parameters resulting from these ML fits are used in the final ML fit on data to fix the values for parameters that cannot be floated in the fit¹ For parameters that can be floated in the fit, the estimates serve as initial values in the fit. Which parameters can be floated in the fit is determined in Section 10.3.

10.2.3 Modeling the multiplicity of b -tagged jets

Given a sample of events with definite jet multiplicity n^{jets} , definite true b -jet multiplicity n^b , and average b -tag and mistag efficiency $\bar{\epsilon}^b$ and $\bar{\epsilon}^{\text{no } b}$ the probability for

¹These parameters were estimated from MC simulated events passing all selection criteria. However, the data are reweighted to correct for signal efficiency. Thus, in principle the MC events should be required to pass the muon related selection criteria. The effect is considered negligible though.

Table 10.1 – PDFs modeling the m_T distribution in the final ML fits. For each species and each jet bin the functional form is given together with its parameters floated in the final ML fits.

species	jet bin	$f(m_T)$	floating params
$W(\rightarrow \mu\nu)$	0 jets	\mathcal{DC}	$f, m, \sigma_L, \sigma_R, \alpha_R$
	1 jet	\mathcal{DC}	$m, \sigma_L, \sigma_R, \alpha_R$
	2 jets	\mathcal{C}	m, σ_R, α_R
	3 jets	\mathcal{C}	σ_R, α_R
	≥ 4 jets	\mathcal{C}	-
QCD	0, 1, 2, 3 jets	\mathcal{C}_R	σ_R
	≥ 4 jets	\mathcal{C}_R	-
top	0, 1, 2, 3, ≥ 4 jets	\mathcal{C}	-
$W(\rightarrow \mu\nu)$	0, 1, 2, 3, ≥ 4 jets	\mathcal{C}	-
Z	0, 1, 2, 3, ≥ 4 jets	\mathcal{DC}	-

events to have 0, 1 or ≥ 2 b -tagged jets is given by the following b -tag PDF \mathcal{T} :

$$\mathcal{T}_{n^b} (n^{b \text{ tag}}, n^{\text{jets}}, \bar{\epsilon}^b, \bar{\epsilon}^{\text{no } b}) = \begin{cases} (1 - \bar{\epsilon}^b)^{n^b} \cdot (1 - \bar{\epsilon}^{\text{no } b})^{n^{\text{jets}} - n^b} & \text{if } n^{b \text{ tag}} = 0, \\ (n^{\text{jets}} - n^b) \cdot \bar{\epsilon}^{\text{no } b} \cdot (1 - \bar{\epsilon}^{\text{no } b})^{n^{\text{jets}} - n^b - 1} \cdot (1 - \bar{\epsilon}^b)^{n^{\text{jets}} - n^b} \\ \quad + n^b \cdot \bar{\epsilon}^b \cdot (1 - \bar{\epsilon}^b)^{n^b - 1} \cdot (1 - \bar{\epsilon}^{\text{no } b})^{n^{\text{jets}} - n^b} & \text{if } n^{b \text{ tag}} = 1, \\ 1 - \mathcal{T}_{n^b} (0; n^{\text{jets}}, \bar{\epsilon}^b, \bar{\epsilon}^{\text{no } b}) - \mathcal{T}_{n^b} (1; n^{\text{jets}}, \bar{\epsilon}^b, \bar{\epsilon}^{\text{no } b}) & \text{if } n^{b \text{ tag}} \in [2, +\text{inf}]. \end{cases} \quad (10.6)$$

These PDFs are shown for different jet and b -jet multiplicities in Figure 10.4. It is clear that the shape of the PDFs depends dramatically on the number of b -tagged jets. We make use of this significant dependence to separate the $W(\rightarrow \mu\nu)$ signal events from top quark production as explained in the following paragraphs.

This modeling is approximate. It assumes that within an event with a given number of jets and b -jets, the probabilities for the different jets to be tagged are independent. This not completely true since there is some correlation between the kinematics of the jets and because the b -tag and mistag probability depend on the jet kinematics.

We describe the $n^{b \text{ tag}}$ distribution in $W(\rightarrow \mu\nu)$ with \mathcal{T}_0 , neglecting signal events with true b -jets. The fraction of such signal events is small as shown in Table 10.2 which lists the number of events in MC simulation as a function of the process and the

MEASUREMENTS OF $W(\rightarrow \mu\nu) + \text{JETS PRODUCTION}$

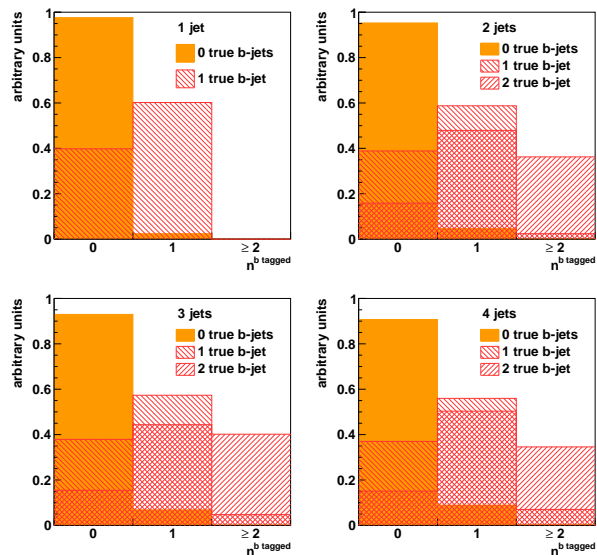


Figure 10.4 – The b -tag PDFs for events with 1, 2, 3 and 4 jets and 0, 1 and 2 true b -jets, with average b -tag efficiency and mistag efficiency set to 60.2% and 2.4%, which are the values found for the selected simulated signal and top quark events.

multiplicity of jets and true b -jets. When compared to the statistical and systematic uncertainties on the final results these small fractions are indeed negligible. The parameter n^{jets} in \mathcal{T}_0 is set to the value corresponding to the jet bin.

From the same table it appears that top quark production mainly gives rise to events with 1 and 2 true b -jets and a small amount of events with 0 true b -jets. We describe its n^b_{tag} distribution with the following PDF

$$P_j^{\text{top}}(n^b_{\text{tag}} | \bar{c}^b, \bar{c}^{\text{no } b}) = \frac{n_{j,0}^{\text{top } b} \cdot \mathcal{T}_0 + n_{j,1}^{\text{top } b} \cdot \mathcal{T}_1 + n_{j,2}^{\text{top } b} \cdot \mathcal{T}_2}{n_j^{\text{top}}}. \quad (10.7)$$

where $n_{j,0}^{\text{top } b}$, $n_{j,1}^{\text{top } b}$ and $n_{j,2}^{\text{top } b}$ are the expected contributions from top quarks with respectively 0, 1 and 2 true b -jets. Thereby we neglect the small contribution from top quark production with more than 2 true b -jets. The parameter n^{jets} in the \mathcal{T}_n PDFs is set to the value corresponding to the jet bin.

The QCD species is well-separated from all others using the m_T distributions. There-

fore we describe the $n^{b \text{ tag}}$ distribution with the simplest possible binned PDF \mathcal{B} :

$$\mathcal{B} \left(n^{b \text{ jets}}; f_1^j, f_2^j \right) = \begin{cases} f_1^j & \text{if } n^{b \text{ jets}} = 0 \\ f_1^j \cdot (1 - f_2^j) & \text{if } n^{b \text{ jets}} = 1 \\ 1 - f_1^j - f_1^j \cdot (1 - f_2^j) & \text{if } n^{b \text{ jets}} \in [2, +\text{inf}[, \end{cases} \quad (10.8)$$

where the index j denotes the jet bin and the fractions $f_1, f_2 \in [0, 1]$. Table 10.3 lists for each of the species and each jet bin the PDF that models the $n^{b \text{ tag}}$ spectrum.

In Figure 10.3 is shown how well the proposed PDFs for $n^{b \text{ tag}}$ describe MC simulated events for the main species and for each jet bin. For $W(\rightarrow \mu\nu)$ we compare the simulated data directly to the \mathcal{T}_0 PDF. In the 1 and 2 jet bins the description performs very well, while there is some discrepancy of the order of 5% for events in the 3 and ≥ 4 jet bins. This latter discrepancy is mainly due to the larger contribution from $W(\rightarrow \mu\nu)$ with true b -jets in those higher jet multiplicity bins. The $n^{b \text{ tag}}$ distribution of the less abundant species Z and $W(\rightarrow \mu\nu)$ is, just like $W(\rightarrow \mu\nu)$ described with \mathcal{T}_0 . The quality of the description is similar to that of the description of $W(\rightarrow \mu\nu)$.

To evaluate the modeling for top quark events, we perform a ML fit to the $n^{b \text{ tag}}$ distribution in each jet bin of the simulated top quark events. As likelihood function we use the PDF in Equation 10.7. The contributions $n_{j,0}^{top \ b}$, $n_{j,1}^{top \ b}$ and $n_{j,2}^{top \ b}$ are floated, while $\bar{\epsilon}^{no \ b}$ and $\bar{\epsilon}^b$ are fixed parameters and are estimated from simulated W and top quark events. Figure 10.3 compares for each jet bin the results of these fits with the $n^{b \text{ tag}}$ distribution in MC. The PDFs perfectly fit the distributions which is to be expected since the problem has as many constraints as degrees of freedom. Important here, is that only a small fraction of the top events is identified as having 0 true b -jets.

Likewise, we perform a ML fit of $n^{b \text{ tag}}$ in MC simulated QCD events. Here we use the PDF in Equation 10.8 as Likelihood and float the fractions f_1 and f_2 . For each jet bin, the results of the fits are compared to the $n^{b \text{ tag}}$ distribution in Figure 10.3. Again the problem has as many constraints as degrees of freedom and thus the modeling fits perfectly.

These ML fits on $n^{b \text{ tag}}$ in MC simulated events yield estimates for the parameters f_1 and f_2 in the modeling for QCD events and $n_{j,0}^{top \ b}$, $n_{j,1}^{top \ b}$ and $n_{j,2}^{top \ b}$ in the modeling for the top species. The estimates for $n_{j,0}^{top \ b}$ are used in the final ML fit on data in which this parameter is not floated. The other parameters are floated in the final ML fit and the estimates derived here from MC simulation serve as starting values.

MEASUREMENTS OF $W(\rightarrow \mu\nu) + \text{JETS PRODUCTION}$

Table 10.2 – Number of events in MC simulated data versus species, the number of jets and the number of true b -jets. Uncertainties are statistical only.

		0 b	1 b	≥ 2 b
$W(\rightarrow \mu\nu)$	0 jets	150333 ± 184	-	-
	1 jet	17065 ± 62	61 ± 3	-
	2 jets	3033 ± 26	52 ± 3	16 ± 1
	3 jets	494 ± 10	14 ± 1	7 ± 1
	≥ 4 jets	96 ± 4	3 ± 0	2 ± 0
QCD	0 jets	11818 ± 41	-	-
	1 jet	5158 ± 27	1013 ± 12	-
	2 jets	559 ± 9	259 ± 6	31 ± 2
	3 jets	84 ± 3	49 ± 2	20 ± 1
	≥ 4 jets	15 ± 1	7 ± 1	5 ± 0
top	0 jets	18 ± 0	-	-
	1 jet	28 ± 0	86 ± 0	-
	2 jets	22 ± 0	142 ± 1	137 ± 1
	3 jets	10 ± 0	112 ± 1	311 ± 2
	≥ 4 jets	3 ± 0	48 ± 0	347 ± 2
$W(\rightarrow \mu\nu)$	0 jets	6679 ± 38	-	-
	1 jet	978 ± 14	9 ± 1	-
	2 jets	205 ± 6	10 ± 1	4 ± 0
	3 jets	44 ± 3	2 ± 0	2 ± 0
	≥ 4 jets	11 ± 1	1 ± 0	2 ± 0
Z	0 jets	6618 ± 15	-	-
	1 jet	1428 ± 7	21 ± 0	-
	2 jets	227 ± 2	9 ± 0	2 ± 0
	3 jets	42 ± 1	2 ± 0	1 ± 0
	≥ 4 jets	9 ± 0	0 ± 0	1 ± 0

Table 10.3 – PDFs modeling the $n^{b \text{ tag}}$ distribution in the final ML fits. For each species and each jet bin the functional form $f(n^{b \text{ tag}})$ is given together with its parameters floated in the final ML fits.

species	jet bin	$f(n^{b \text{ tag}})$	floating params
$W(\rightarrow \mu\nu)$	0 jets	-	-
	1, 2, 3, ≥ 4 jets	\mathcal{T}_0	-
QCD	0 jets	-	-
	1, 2, 3, 4 jets	\mathcal{B}	f_1, f_2
top	0 jets	-	-
	1 jets	$(n_{j,0 b}^{\text{top}} \cdot \mathcal{T}_0 + n_{j,1 b}^{\text{top}} \cdot \mathcal{T}_1) / n_j^{\text{top}}$	t_0, t_1
	1, 2, 3, ≥ 4 jets	$(n_{j,0 b}^{\text{top}} \cdot \mathcal{T}_0 + n_{j,1 b}^{\text{top}} \cdot \mathcal{T}_1 + n_{j,2 b}^{\text{top}} \cdot \mathcal{T}_2) / n_j^{\text{top}}$	t_0, t_1, t_2
$W(\nrightarrow \mu\nu)$	0 jets	-	-
	1, 2, 3, ≥ 4 jets	\mathcal{T}_0	-
Z	0 jets	-	-
	1, 2, 3, ≥ 4 jets	\mathcal{T}_0	-

10.2.4 Fixed likelihood contributions

The likelihood for the ML fit is designed to decompose the selected sample into contributions from $W(\rightarrow \mu\nu)$, QCD and top quark production in a data-driven way. To keep the discrimination between these three main contribution as high as possible, we choose to fix the number of events from the less abundant species, Z and $W(\nrightarrow \mu\nu)$ in the fit to the estimates described in this section. Further, with respect to m_T and $n^{b \text{ tag}}$, the subcontribution from top quarks without true b -jets and the $W(\rightarrow \mu\nu)$ species behave in the same manner, and thus, also this contribution is fixed in the fit. An overview of which contributions are fixed and which are floated in the fit is given in Table 10.4.

The number of top quark events without true b -jets $n_{j,0 b}^{\text{top}}$ is estimated as described in the previous section from ML fits on MC simulated top quark events. The resulting estimates are listed in Table 10.5.

The contribution from $W(\nrightarrow \mu\nu)$ is fixed relative to the total W contribution through the fractions $n_j^{W(\nrightarrow \mu\nu)} / n_j^{W(\rightarrow \mu\nu)}$ with j denoting the jet bin. This fraction is estimated for each jet bin separately from MC simulated W events using the numbers in Table 9.2.

Table 10.4 – Yields of species and subspecies in the ML fit. The second column indicates whether yields are floated or fixed in the ML fit.

$n_j^{W(\rightarrow\mu\nu)}$	floated
n_j^{QCD}	floated
$n_{j,0}^{top\ b}$	fixed
$n_{j,1}^{top\ b}$	floated
$n_{j,2}^{top\ b}$	floated
$n_j^{W\rightarrow\mu\nu}$	fixed relative to $n_j^{W(\rightarrow\mu\nu)}$
n_j^Z	fixed

Table 10.5 – Estimates for the number of selected top quark events with 0 true b -jets as a function of the jet multiplicity. The estimate for events with 0 jets was obtained by simple counting. For other jet bins the estimates are derived from the ML fits on $n^{b\ \text{tag}}$ in MC simulated top quark events described in Section 10.2.3.

	$n_{0\ b}^{top}$
0 jets	19
1 jet	27
2 jet	19
3 jet	10
≥ 4 jets	5

In the fit, we fix the absolute contribution from Z events, n_j^Z , in each jet bin j . The numbers n_j^Z are estimated in a semi data-driven way, based on the observed numbers of Z events in the parallel $Z(\rightarrow \mu\mu)$ +jets analysis. Z events passing the $W(\rightarrow \mu\nu)$ selection are $Z(\rightarrow \mu\mu)$ events with one muon passing the leading muon criteria and the other muon, either not within the acceptance of the Z analysis, or not reconstructed. Both sources of Z events are derived from the observed number of $Z(\rightarrow \mu\mu)$ events in the $Z(\rightarrow \mu\mu)$ analysis multiplied by a dedicated factor. For the first source, this factor is derived from MC only. For the second source, the scaling factor is derived from the muon reconstruction efficiencies measured with the TnP technique as described in Section 9.4, where the efficiencies are integrated over muon η and p_T using MC. The resulting estimates for n^Z are listed in Table 10.6.

Table 10.6 – Estimates for the contributions from $Z(\rightarrow \mu\mu)$ in the selected sample derived from measured cross sections $\sigma[Z \rightarrow \mu\mu + \geq j \text{ jets}]$ and conversion factors derived per jet bin from MC simulated $Z(\rightarrow \mu\mu)$ events. Uncertainties cover the statistical uncertainty on the cross sections and the conversion factors.

	$n^{Z(\rightarrow \mu\mu)}$
0 jets	6402 ± 91
1 jet	679 ± 29
2 jets	127 ± 16
3 jets	16 ± 6
≥ 4 jets	11 ± 6

10.3 Fit performance

10.3.1 Toy MC studies

The robustness of the fit was studied extensively with toy MC experiments. For each jet bin we generated 1000 Toy MC samples from the likelihoods described in Section 10.2, with all parameter values set to the estimates obtained from MC simulation as described in the previous sections. We determined which combination of parameters may be floated in the fit without causing significant bias on the estimates for the number of signal events per jet bin, $n_j^{W(\rightarrow \mu\nu)}$. Therefore, we applied the ML fit in many different configurations to the toy samples, each time floating different combinations of parameters. The following paragraphs explain how we conclude that the ML fit, with parameters floated as indicated in Tables 10.1, 10.3 and 10.4, yields

unbiased results. In these tests events were not weighted for efficiency.

We evaluate the ability of the ML fit to estimate a true parameter value θ based on the distribution of the associated pull $_{\theta}$

$$\text{pull}_{\theta} = \frac{\hat{\theta} - \theta}{\sigma(\hat{\theta})}, \quad (10.9)$$

with $\hat{\theta}$ the fit's estimate for θ and $\sigma(\hat{\theta})$ the fit's estimate for the statistical uncertainty on $\hat{\theta}$. If the fit yields unbiased estimates for θ , the mean of the pull distribution is zero. If the fit correctly estimates the statistical uncertainty on $\hat{\theta}$, the pull has a Gaussian shape with standard deviation equal to 1.

Figure 10.5 shows the pull distribution for $n_j^{W(\rightarrow\mu\nu)}$ in the 1000 toy experiments. The nominal combination of parameters was floated in the ML fits and fixed parameters were set to the values estimated from MC simulated events. To each of the distributions we fitted a Gaussian function using the χ^2 -method. The χ^2 and number of degrees of freedom (ndof) of the fit are displayed together with the resulting estimates for the mean (μ) and standard deviation (σ) of the pull distribution. The Gaussian functions fit well. The means of these Gaussian functions are consistent with or close to 0, proving unbiased estimates for $n_j^{W(\rightarrow\mu\nu)}$. The standard deviations are consistent with or close to 1, demonstrating proper estimates for the statistical uncertainty. Nowhere is the mean of the Gaussian larger than about 0.1 and thus, any potential bias will be negligible compared to the statistical uncertainty. We conclude that, if our model is accurate, the ML fit is stable and provides unbiased estimates for $n_j^{W(\rightarrow\mu\nu)}$ and a proper estimate for the associated statistical uncertainty.

10.3.2 Full MC tests

The successful studies with toy MC prove that the ML fit provides good estimates, under the condition that our modeling is accurate. However, while building our likelihood function we made several approximations. For example, we neglect any relation between m_T and $n^{b \text{ tag}}$. Furthermore, we neglect the modest dependence of the b -tag and mistag efficiency ϵ^b and $\bar{\epsilon}^{\text{no } b}$, on the jet and b -jet multiplicity. This dependence can be seen in Table 10.7 and 10.8 which list the average b -tag and mistag efficiencies in MC simulated top quark and W events as a function of the number of jets and true b -jets.

To validate all these approximations, we perform the fit in several independent samples of events, generated with full MC simulation, including all relevant processes. To

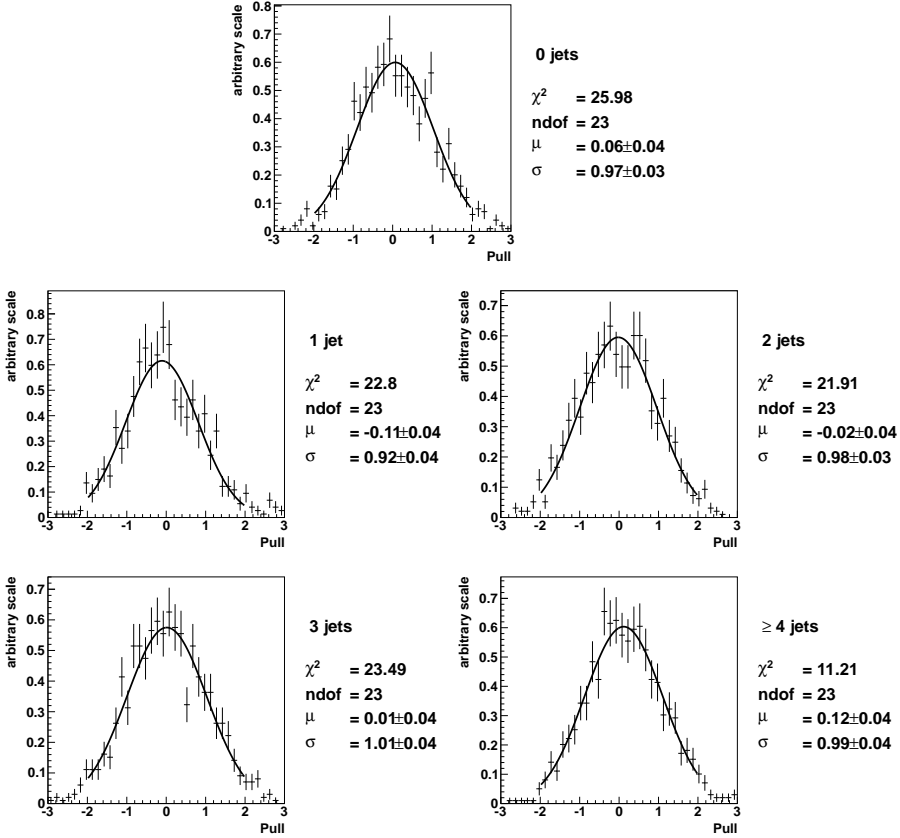


Figure 10.5 – Pull distribution in toy MC experiments for the expected number of signal events $n_j^{W(\rightarrow \mu\nu)}$ in the different jet bins j . The distributions are fit with a Gaussian function. The number of degrees of freedom is displayed together with the resulting χ^2 and estimates for the mean (μ) and standard deviation (σ) of the pull distribution.

Table 10.7 – Average b -tag efficiency (%) in MC simulated $W(\rightarrow \mu\nu)$ and top quark events. Uncertainties are statistical only

	1 b	2 b
1 jet	51.7 ± 0.8	-
2 jets	58.2 ± 0.6	59.8 ± 0.9
3 jets	61.7 ± 0.5	61.9 ± 0.3
4 jets	62.7 ± 0.6	62.2 ± 0.3

MEASUREMENTS OF $W(\rightarrow \mu\nu) + JETS$ PRODUCTION

Table 10.8 – Average mistag efficiency (%) in MC simulated $W(\rightarrow \mu\nu)$ and top quark events. Uncertainties are statistical only.

	0 b	1 b	2 b
1 jet	1.54 ± 0.02	-	-
2 jets	1.73 ± 0.04	2.91 ± 0.18	-
3 jets	1.90 ± 0.08	2.88 ± 0.09	3.43 ± 0.12
4 jets	2.33 ± 0.17	3.02 ± 0.11	2.92 ± 0.05

mimic actual data, the number of events in each of the samples equals the expected number of events for 35.9 pb^{-1} , smeared according to a Poisson distribution to simulate statistical fluctuations. Only 10 independent samples could be constructed, because the total number of available events generated with full MC was limited.

We perform the ML fits on each of the samples and calculate the mean and standard deviation of the resulting estimates of $n_j^{W(\rightarrow \mu\nu)}$. These are listed in Table 10.9 and compared to the expected values². Since the fit does not recognize W with true b -jets as signal, the listed expected estimates do not include such contributions. Small deviations on the % level are observed, and we conclude that any observed bias is negligible with respect to the uncertainties on the final results.

Table 10.9 – Average estimate for n_j^W from ML fits on 10 full MC samples representing the the expected statistics in data (\bar{n}_{fit}^W). This average is compared to the expected results (n_{exp}^W). Contributions from W with true b -jets are not included in the expectations.

	\bar{n}_{fit}^W	n_{exp}^W
0 jets	157040 ± 150	157012
1 jet	18207 ± 61	18043
2 jet	3302 ± 16	3238
3 jet	531 ± 5	538
≥ 4 jets	104 ± 3	107

² For historical reasons a slightly modified likelihood function is adopted for these tests. In this alternative likelihood function all W events are treated as one species. This is taken into account when listing the expected results.

10.4 Estimates for shape parameters

For the important m_T and $n^{b \text{ tag}}$ shape parameters that are fixed in the likelihood functions, we developed data driven estimates. These estimates are used directly in the fit or otherwise, the difference between the value estimated from MC and the data driven estimate serves as a systematic uncertainty on a given parameter.

10.4.1 Average mistag efficiency

We define the average mistag efficiency $\bar{\epsilon}^{\text{no } b}$ as the tag efficiency averaged over all jets other than true b -jets in simulated $W(\rightarrow \mu\nu)$ and top quark events, weighted according to the respective cross sections. Deviations in the mistag efficiencies between MC simulated events and events in data have been observed and measured as scaling factors $SF(p_T, \eta) = \epsilon^{\text{data}}(p_T, \eta)/\epsilon^{\text{MC}}(p_T, \eta)$ in bins of jet p_T and η [53]. These SF were taken into account and the resulting average mistag efficiency is shown in Table 10.10. The systematic uncertainty was derived by moving all scaling factors simultaneously up and then simultaneously down with their total uncertainty. The average absolute value of the resulting shift of the average mistag efficiency is adopted as systematic uncertainty.

Table 10.10 – Estimates for the average b -tag and mistag efficiencies $\bar{\epsilon}^b$ and $\bar{\epsilon}^{\text{no } b}$ in $W(\rightarrow \mu\nu)$ and top quark events. The average mistag rate is estimated from MC simulated events and corrected for measured difference between data and MC. The average b -tag efficiency is obtained directly from MC simulated events while its uncertainty is derived from a control sample of top quark events in data.

$\bar{\epsilon}^{\text{no } b}$	$2.4 \pm 0.03(\text{stat}) \pm 0.5(\text{syst}) \%$
$\bar{\epsilon}^b$	$60.2 \pm 0.2 (\text{stat}) \pm 7 (\text{syst}) \%$

10.4.2 Average b -tag efficiency

The average b -tag efficiency is estimated directly from MC and listed in Table 10.10. However, we developed a cross-check on a control sample in data mainly populated with top quark pair events in which both W bosons decay leptonically. The results of the test allow a conservative estimate of the uncertainty on $\bar{\epsilon}^b$.

The data used for the control sample are the data described in Section 9.1, and in addition data collected with electron triggers during the same data-taking period. For

MEASUREMENTS OF $W(\rightarrow \mu\nu) + \text{JETS PRODUCTION}$

technical reasons the selection and physics object definition for this control sample are somewhat different. Events are required to have at least 10 tracks, and at least 25% of the tracks must pass tight reconstruction quality criteria. At least one PV must be present, selected in the same way as for the default selection. Events must have 2 leptons, electrons or muons, with $p_T > 20$ GeV and respectively $\eta < 2.5$ and $\eta < 2.4$. The leptons must be isolated with $I_{\text{rel}}^{0.3} < 0.15$ where I_{rel}^R is defined as

$$I_{\text{rel}}^R = \frac{I_{\text{ECAL}}^R + I_{\text{HCAL}}^R + I_{\text{TRACK}}^R}{\max(20 \text{ GeV}/c, p_T^l)}, \quad (10.10)$$

with $I_{\text{ECAL}} + I_{\text{HCAL}} + I_{\text{TRACK}}$ the isolation variables as defined in Section 6.3 and p_T^l the lepton p_T . For electrons, I_{ECAL}^R is replaced with $\max(0, I_{\text{ECAL}}^R - 1)$. Electrons must pass tight identification and conversion rejection criteria [110]. Identification criteria for muons are based on the number of hits in the muon system and the χ^2 of the global fit. Both muons must be within 1 cm along the z -axis from the selected PV with the highest value for the scalar sum of the transverse momenta of all associated tracks.

The two as such selected leptons must have opposite charge. If several combinations of two such leptons are present leptons with higher p_T are preferred. To avoid contributions from low mass Drell-Yann production we require $M_{ll} > 12$ GeV with M_{ll} the invariant mass of the di-lepton system. If the two leptons have the same flavor we veto Z events by requiring $|M_{ll} - M_Z| > 15$ GeV with M_Z the PDG [20] value for the Z boson mass.

Jets are clustered from all PF particles in the event and must have $p_T > 30$ GeV and $|\eta| < 2.4$. To veto isolated leptons identified as jets, all jets within a cone $R < 0.4$ around a selected lepton are discarded. We require events to have at least 2 jets. Purity is increased by requiring $E_T^{\text{miss}} > 30$ GeV, exploiting the presence of two neutrinos with high p_T in top quark pair events in which both W bosons decay leptonically.

Table 10.11 shows the composition of the selected sample in terms of top quark events and other events in MC simulated events. For these estimates we use the default MC samples and in addition WW , WZ , ZZ and $ZZ\gamma$ samples generated with MADGRAPH interfaced with PYTHIA, electron enriched QCD samples generated with PYTHIA and photon + jets samples generated with ALPGEN interfaced with PYTHIA. The table also lists the number of events observed in data.

To estimate the average b -tag efficiency $\bar{\epsilon}^b$ we perform a fit. First the data are binned according to the number of jets: 2, 3 or ≥ 4 jets. Then we perform three simultaneous

ML fits on $n^{b \text{ tag}}$, one in each jet bin j . The $n^{b \text{ tag}}$ distribution in each jet bin j is described with the following likelihood function:

$$P_j(n^{b \text{ tag}} | \bar{\epsilon}^b, \bar{\epsilon}^{\text{no } b}, n_{j,b}) = \frac{e^{-n_j} (n_j)^{N_j}}{N_j!} \prod_e \sum_b \left[\frac{n_{j,b}}{n_j} \mathcal{T}_b(n^{b \text{ tag}}; n^{\text{jets}}, \bar{\epsilon}^b, \bar{\epsilon}^{\text{no } b}) \right]. \quad (10.11)$$

Here, n_j is the expected number of events in jet bin j and $n_{j,b}$ the expected number of events in jet bin j with b true b -jets. N_j is the observed number of events in jet bin j and \mathcal{T}_b is defined in Equation 10.6. The average mistag efficiency $\bar{\epsilon}^{\text{no } b}$ is fixed to the estimate described in the previous section. Furthermore, $n_{j,0}$ is set to the expected number of non-top quark events, listed in Table 10.11 and estimated from the MC simulation. The ratio $n_{j,1}/n_{j,2}$ is also fixed to the values observed in MC simulation. The parameters floated in the fit are the sums $n_{j,1} + n_{j,2}$ and the average b -tag efficiency $\bar{\epsilon}^b$. Maximizing the likelihood function results in the following estimate for $\bar{\epsilon}^b$:

$$\bar{\epsilon}^b = 62.7 \pm 7.6(\text{stat})\%.$$

In the final ML fit we use the estimate from MC listed in Table 10.10, which is consistent with this data driven estimate. However, the statistical uncertainty on the data driven estimate serves as systematic uncertainty on the MC estimate.

Table 10.11 – Composition of the top control sample. Number of top quark events in MC simulation (n^{top}), Number of other events in MC simulation (n^{other}), the expected ratio $\frac{n^{\text{top}}}{n^{\text{top}}+n^{\text{other}}}$ (purity), and the number of events selected in data (n^{data}).

channel	n^{top}	n^{other}	purity	n^{data}
ee	16.3	2.6	86%	19
$\mu\mu$	19.4	4.0	83%	28
$e\mu$	48.0	3.6	93%	47

10.4.3 Parameters for the m_T shape in $W(\rightarrow \mu\nu)$ and top

In the final ML fits, the likelihood parameters related to the m_T distribution for $W(\rightarrow \mu\nu)$ production are partly floated and partly fixed. The floated parameters are estimated in the final fits themselves while the fixed parameters are estimated from MC simulated events. For this purpose, fits are performed in samples of MC simulated events of the particular fit species as described in Section 10.2.2. The latter estimates require that the MC provides an accurate description of the m_T distribution. We developed two complementary strategies to verify and quantify this accuracy.

MEASUREMENTS OF $W(\rightarrow \mu\nu) + \text{JETS PRODUCTION}$

A first strategy is based on the final ML fits themselves. We compare the PDFs of m_T for $W(\rightarrow \mu\nu)$ events obtained from the final fits on data to the PDFs obtained for $W(\rightarrow \mu\nu)$ from the fits on $W(\rightarrow \mu\nu)$ MC events shown in Figures 10.1 and 10.2. Figure 10.6 shows this comparison for each jet bin except the 4th bin in which none of the relevant PDF parameters is floated in the fits on data. In each of the jet bins both PDFs compare almost perfectly. Especially the resemblance in the 0 jet bin, where almost all important parameters are floated, proves the excellent ability of the MC to model the m_T behavior in signal events.

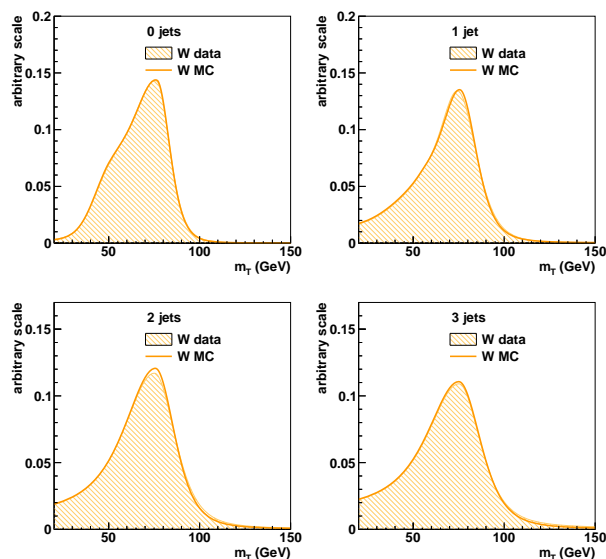


Figure 10.6 – PDFs of m_T for $W(\rightarrow \mu\nu)$. For PDFs labeled “MC”, all parameters are set to the estimates from fits of m_T in MC simulation. For PDFs labeled “data”, all parameters that are floated in the final ML fits on data are set to the estimates obtained from these latter fits. Differences between both PDFs are extremely small and hardly visible.

A second strategy is based on a “ Z -as- W ” control sample. In this sample Z candidates are treated as if they were W candidates, ignoring one of the two leptons from the Z decay. Events are included in the control sample if they pass all nominal selection criteria except the Z veto. As such, the sample is completely dominated by $Z(\rightarrow \mu\mu)$ events. In the jet clustering and the m_T reconstruction, the second muon is then treated as if it were a neutrino, invisible and contributing to the E_T^{miss} . The m_T distribution in such events is expected to behave very similar to the m_T distribution in W events. This is illustrated in Figure 10.7 where the m_T distribution in MC simulated $W(\rightarrow \mu\nu)$ events is compared to the m_T distribution in the Z -as- W

control sample in data. To make for an easier comparison, the m_T in the $Z(\rightarrow \mu\mu)$ events is scaled with a factor M_W/M_Z with M_W and M_Z the PDG values [20] for respectively the W and Z mass. Only few qualitative differences are observed between both distributions.

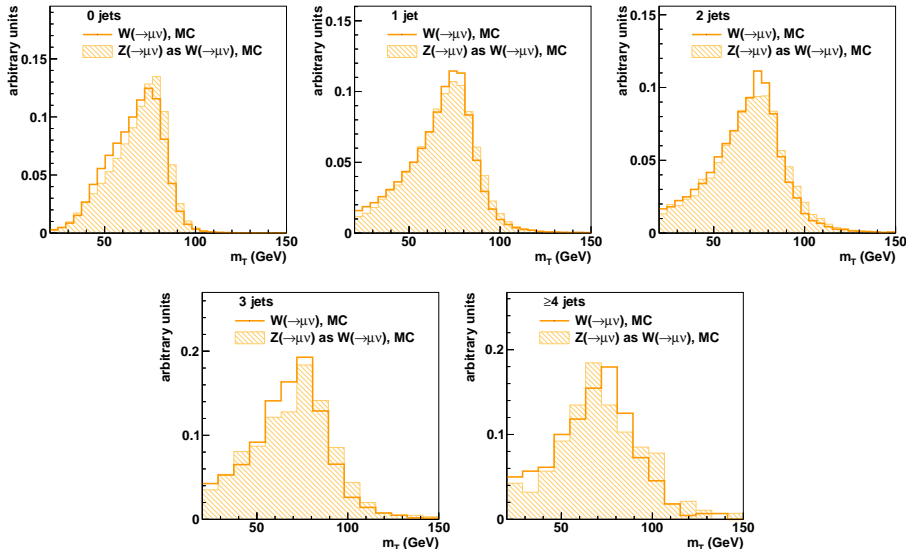


Figure 10.7 – The m_T distribution in MC simulated $W(\rightarrow \mu\nu)$ events passing the nominal selection and MC simulated $Z(\rightarrow \mu\mu)$ events in the Z -as- W control sample. m_T in the Z -as- W control sample is scaled with M_W/M_Z with M_W and M_Z the PDG values for respectively the W and Z mass.

Because the behavior of the Z -as- W events is so similar to the behavior of $W(\rightarrow \mu\nu)$ events, discrepancies between data and MC, related to the m_T distribution in $W(\rightarrow \mu\nu)$ will also show up in the m_T distribution of Z -as- W events. We make use of this as follows: we perform ML fits to the m_T distribution in Z -as- W events in data and Z -as- W events in MC simulated Z events. As likelihood functions we use the same double Cruijff function used to model the m_T distribution in signal events. All likelihood parameters are floated in the fit. Figure 10.8 compares the resulting PDFs. The agreement is again excellent, providing additional proof for the MC simulation’s ability to model the m_T distribution in signal events. A few small differences may be observed in the left tails of the distributions, though. These differences most probably arise from background processes present in the data sample, while the control sample in MC only includes simulated $Z(\rightarrow \mu\mu)$ events. Thus, the actual difference between data and MC is most probably smaller than observed here. In jet bins higher than 0

and 1, statistics is too low to make a meaningful comparison and these bins are not shown.

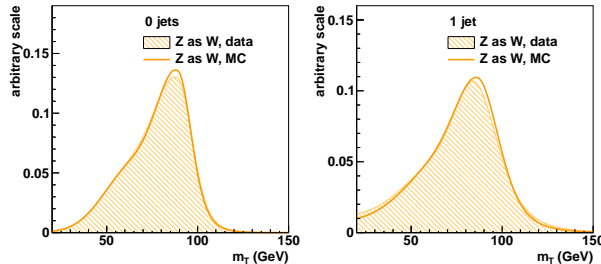


Figure 10.8 – PDFs of m_T for $W(\rightarrow \mu\nu)$. For PDFs labeled “MC”, all parameters are set to values obtained from the Z -as- W control sample in Z MC. For PDFs labeled “data”, all parameters are set to values obtained from the Z -as- W control sample in data. Differences between both PDFs are small and hardly visible.

From the above comparisons between data and MC we derive systematic uncertainties for likelihood parameters that are related to the m_T distribution in $W(\rightarrow \mu\nu)$ events and that are fixed in final ML fits on data: Let θ be a likelihood parameter that is fixed in the final ML fits, for which we obtained an estimate $\hat{\theta}_{\text{MC}}$ with statistical uncertainty $\hat{\sigma}(\theta)_{\text{MC}}$. Let us furthermore denote furthermore the estimates for θ obtained in control samples in data and MC as respectively $\hat{\theta}_{\text{data,Ctrl}}$ and $\hat{\theta}_{\text{MC,Ctrl}}$ with respective uncertainties $\hat{\sigma}(\theta)_{\text{data,Ctrl}}$ and $\hat{\sigma}(\theta)_{\text{MC,Ctrl}}$. A conservative systematic uncertainty $\hat{\sigma}(\theta)_{\text{sys}}$ on the MC estimate $\hat{\theta}_{\text{MC,Ctrl}}$ is then given by the following formula:

$$\hat{\sigma}(\theta)_{\text{sys}} = \sqrt{\hat{\sigma}(\theta)_{\text{MC,Ctrl}}^2 + (\hat{\theta}_{\text{MC,Ctrl}} - \hat{\theta}_{\text{data,Ctrl}})^2 + \hat{\sigma}(\theta)_{\text{data,Ctrl}}^2 + \hat{\sigma}(\theta)_{\text{MC}}^2}. \quad (10.12)$$

Table 10.12 shows the control samples used to derive the systematic uncertainties on the fixed likelihood parameters related to the m_T distribution in $W(\rightarrow \mu\nu)$. Uncertainties on the parameters of the second Cruiff in jet bins 0 and 1 have negligible effects and are not considered.

Because, with respect to m_T , the behavior of top quark production is so similar to the behavior of $W(\rightarrow \mu\nu)$ production, we estimate the systematic uncertainties on the parameters related to the m_T distribution in top quark events from the same data-versus-MC comparisons. Table 10.13 lists for each of these parameters the control sample used to derive the systematic uncertainties.

Table 10.12 – Control samples used to derive the systematic uncertainties on the likelihood parameters fixed in the final ML fit and related to the PDFs of m_T for $W(\rightarrow \mu\nu)$.

parameter	jet bin	systematic uncertainty estimated from
α_L	0	Z as W in jet bin 0
	1, 2, 3, ≥ 4	Z as W in jet bin 1
f	1	final ML fit, $W(\rightarrow \mu\nu)$ PDF, jet bin 0
σ_L	2, 3, ≥ 4	final ML fit, $W(\rightarrow \mu\nu)$ PDF, jet bin 1
m	3, ≥ 4	final ML fit, $W(\rightarrow \mu\nu)$ PDF, jet bin 2
σ_R, α_R	≥ 4	final ML fit, $W(\rightarrow \mu\nu)$ PDF, jet bin 3

Table 10.13 – Control samples used to derive the systematic uncertainties on the likelihood parameters fixed in the final ML fit and related to the PDFs of m_T for top quark events.

parameter	jet bin	systematic uncertainty estimated from
α_L	all	Z as W in jet bin 1
f	all	final ML fit, $W(\rightarrow \mu\nu)$ PDF, jet bin 0
σ_L	all	final ML fit, $W(\rightarrow \mu\nu)$ PDF, jet bin 1
m	all	final ML fit, $W(\rightarrow \mu\nu)$ PDF, jet bin 2
σ_R, α_R	all	final ML fit, $W(\rightarrow \mu\nu)$ PDF, jet bin 3

10.4.4 Parameters for the m_T shape in QCD

Also for QCD some of the parameters related to m_T modeling are fixed in the final ML fit while others are floated. The values for the fixed parameters are estimated from the fits on MC described in Section 10.2.2. We evaluate the quality of those estimates in two ways.

First, we compare the PDFs after the final ML fits on data, to the PDFs with all parameters estimated from MC simulation. Figure 10.9 shows this comparison for each jet bin. The 4th jet bin is not shown since in this bin none of the relevant parameters is floated. The observed differences are significant, indicating that QCD jet production is not very well modeled in the MC simulation.

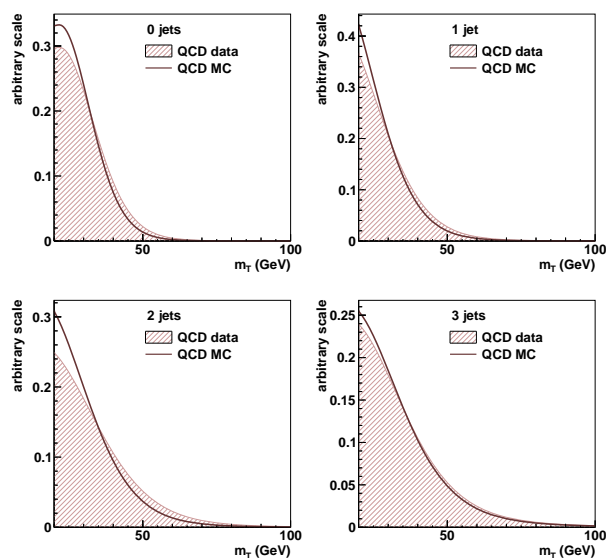


Figure 10.9 – PDFs of m_T for QCD. For PDFs labeled “MC”, all parameters are set to values estimated from MC. For PDFs labeled “data”, values for parameters that are floated in the final ML fits on data are set to the estimates obtained from these fits.

A second approach makes use of a control sample completely dominated by QCD. The sample is selected with the nominal $W(\rightarrow \mu\nu)$ selection with the isolation criterion inverted. This control sample is referred to as the anti-lepton sample. The m_T distribution in this sample is expected to be similar but not identical to the one for QCD events in the nominal sample. This is illustrated in Figure 10.10. In this figure, the m_T distribution is shown for both MC simulated QCD events passing nominal

selection criteria and QCD events in the anti-lepton sample.

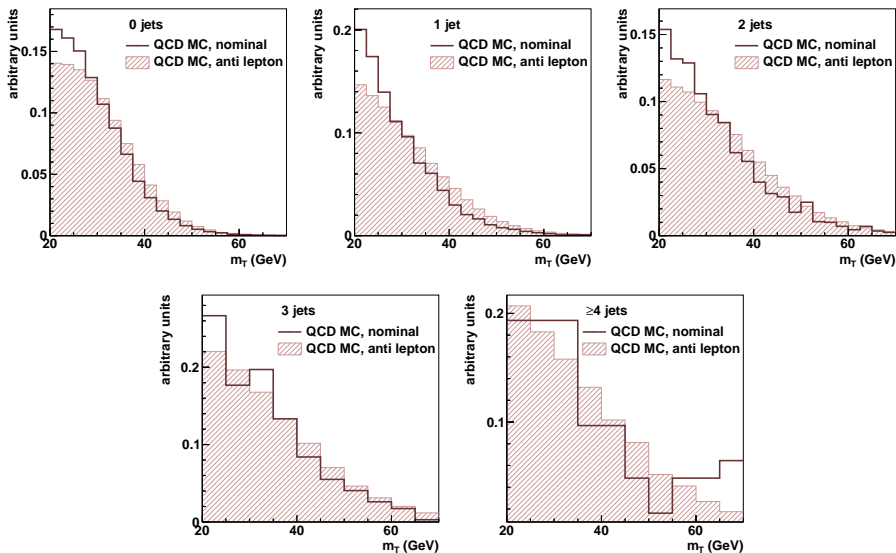


Figure 10.10 – The m_T distribution in MC simulated QCD events passing the nominal selection and MC simulated QCD events passing the nominal selection with the isolation criterion inverted.

We perform ML fits on the m_T distribution in the anti-lepton sample in data and the anti-lepton sample in MC simulated QCD events. The chosen likelihood function is the right-hand Cruiff function, the same function as for the QCD species in the final ML fits. The resulting PDFs are displayed in Figure 10.11. Significant differences are observed between the results obtained from fits in data and fits in MC, indicating again that the MC does not model QCD jet production very well.

As in the previous section we use Equation 10.12 to derive from the above data-versus-MC comparisons a systematic uncertainty on parameters related the m_T distribution in QCD jet production. Table 10.14 lists the origin of the estimate for the systematic uncertainty on the relevant parameters.

10.5 Measured signal on reconstruction level

We perform the ML fits in the 5 jet bins in data. Figures 10.12 and 10.12 show the good comparison between the resulting PDFs and the data for the distributions of m_T and $n^{b \text{ tag}}$. Table 10.15 lists the results, the estimates for $n^{W(\rightarrow\mu\nu)}$. The column “fit” lists the results of the nominal fit on data, while the column “fit, no eff.” lists

MEASUREMENTS OF $W(\rightarrow \mu\nu) + \text{JETS PRODUCTION}$

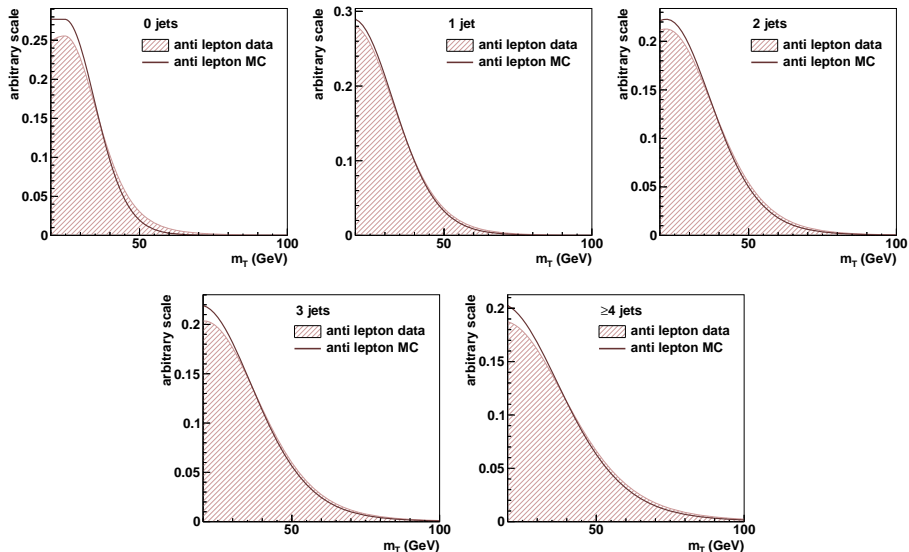


Figure 10.11 – PDFs of m_T for QCD jet production. For PDFs labeled “MC”, all parameters are set to estimates obtained in the anti-lepton control sample in MC simulated QCD events. For PDFs labeled “data”, all parameters are set to estimates obtained in the anti-lepton control sample in data.

Table 10.14 – Origin of the estimates for systematic uncertainties on likelihood parameters related to the PDFs of m_T for QCD and fixed in the final ML fits on data.

parameter	jet bin	systematic uncertainty estimated from
m	1, 2, 3, ≥ 4	anti-lepton control sample, jet bin 3
σ_R	≥ 4	final ML fit, $W(\rightarrow \mu\nu)$ PDF, jet bin 3

the results of the fit without taking into account event weights. The latter can be compared to the columns “MC, no eff.” which lists the expected signal contribution in the selected sample without any efficiency corrections. The given uncertainties are statistical only. Within uncertainties the numbers compare well, except for the 0 jet bin where a significant deviation of about 7% is observed. In the next section we derive systematic uncertainties on the measured values for $n^{W(\rightarrow\mu\nu)}$ and unfold these results for detector effects related to jet counting.

Table 10.15 – $W(\rightarrow\mu\nu)$ contribution to the selected sample of events per jet bin: as estimated from the ML fits in data with efficiency corrections (fit), as estimated from the ML fits in data without correction for selection efficiency (fit, no eff.) and in MC simulated events without efficiency corrections (MC, no eff.). Uncertainties are statistical only.

	MC, no eff.	fit, no eff.	fit
0 jets	150333 ± 183	140649 ± 460	165211 ± 500
1 jet	17126 ± 62	17084 ± 176	21936 ± 199
2 jets	3101 ± 26	3233 ± 88	4250 ± 102
3 jets	515 ± 10	545 ± 35	726 ± 41
≥ 4 jets	101 ± 5	67 ± 18	102 ± 21

10.6 Systematic uncertainties

10.6.1 Jet counting

We take into account the following sources of uncertainties on the jet energy:

- **Jet Energy Correction factors (JECs).**

Jet energy calibration factors, usually referred to as JECs were measured in data as a function of jet p_T and η [106]. Their uncertainties are considered as a function of jet p_T and η .

- **Jet flavor composition.**

The detector response to the jet energy depends on the parton that “initiates” the jet. In $W(\rightarrow\mu\nu)$ events, the flavor composition of the jet-initiating partons slightly differs from the flavor composition in the sample in which the JECs are measured. Therefore we assign an additional 2% systematic uncertainty on the jet energy. This uncertainty was derived assuming a conservative 5% difference in the detector response between gluon-initiated and light-quark-initiated jets,

MEASUREMENTS OF $W(\rightarrow \mu\nu) + \text{JETS PRODUCTION}$

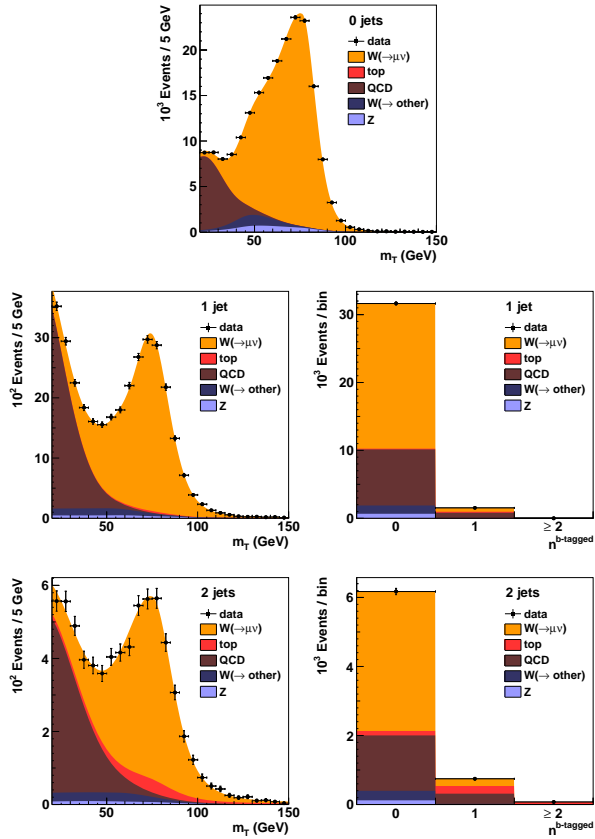


Figure 10.12 – PDFs of m_T (left) and $n^{b \text{ tag}}$ (right) after the ML fits compared to the distributions in data in events with 0, 1 and 2 jets.

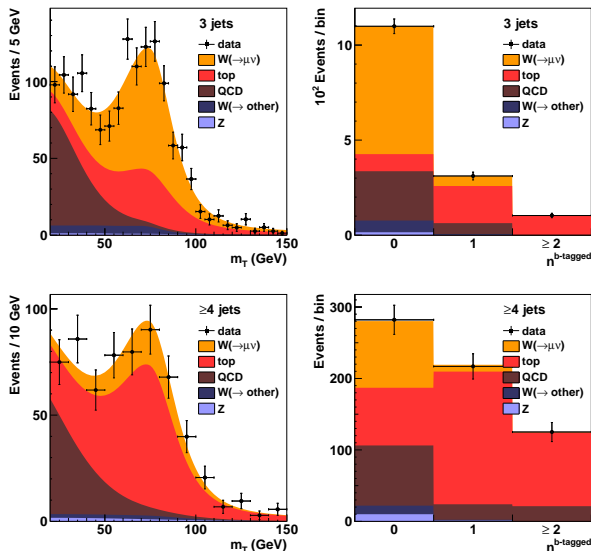


Figure 10.13 – PDFs of m_T (left) and $n^{b \text{ tag}}$ (right) after the ML fits compared to the distributions in data in events with 3 and ≥ 4 jets.

and the difference in flavor composition between $W(\rightarrow \mu\nu)$ and the sample for the JEC measurement observed in MC simulation. The different detector response for b and c -initiated jets is neglected since it has a negligible effect on the estimates for $n_j^{W(\rightarrow \mu\nu)}$.

- **Pile up subtraction.**

In MC simulation with pile-up included, the pile-up subtraction method is found to decrease the jet energy with on average 500 MeV. Therefore, we assign another 500 MeV uncertainty on the jet energy, in both directions.

- **Jet Energy Resolution**

The jet energy resolution in MC simulated events is found to be underestimated by about 10% [111]. This affects the smearing matrices used in the unfolding of the results described in Section 10.7. The effects of this underestimate was evaluated in MC simulation and found to have effects of about 2% on the jet energy. Therefore, an additional 2% uncertainty is assigned to the jet energy.

The effect of these uncertainties on the yields $n_j^{W(\rightarrow \mu\nu)}$ is studied in MC simulated $W(\rightarrow \mu\nu)$ events. For each jet, we add the uncertainties listed above in quadrature. We estimate the effect of the uncertainty on the jet energy on $n_j^{W(\rightarrow \mu\nu)}$ by scaling the jet energy in MC simulated signal events simultaneously up and then simultane-

MEASUREMENTS OF $W(\rightarrow \mu\nu) + JETS$ PRODUCTION

ously down with the uncertainty on the jet energy and repeat the jet counting. The resulting shifts on the signal yields $n_j^{W(\rightarrow \mu\nu)}$ are adopted as asymmetric uncertainties on the signal yield.

In MC simulated $W(\rightarrow \mu\nu)$ events without pile-up, the pile-up subtraction was seen to affect the $W(\rightarrow \mu\nu)$ yields up to 5% depending on the jet multiplicity. Therefore, we add an additional 5% systematic uncertainty to the estimates for $n_j^{W(\rightarrow \mu\nu)}$ related to pile-up. The uncertainty between the 0 jet bin and the other jet bins is assumed to be 100% anti-correlated. Table 10.16 lists the total systematic uncertainty on the estimates for $n_j^{W(\rightarrow \mu\nu)}$ related to the jet counting.

Table 10.16 – Relative uncertainties on the measured $W(\rightarrow \mu\nu)$ yields in % related to jet counting. Uncertainties related to overestimates (underestimates) of jet energy are indicated with JEC $-\sigma$ (JEC $+\sigma$).

	JEC $-\sigma$	JEC $+\sigma$
0 jets	+5	-5
1 jet	-8	+8
2 jets	-10	+11
3 jets	-12	+14
≥ 4 jets	-15	+16

10.6.2 Signal selection efficiency

To propagate the uncertainty on the efficiency of the leading muon selection, the analysis is repeated once with all muon efficiencies scaled up and once with all muon efficiencies scaled down. The resulting relative differences in the measured signal yields are listed in Table 10.17 and adopted as additional systematic uncertainties. The uncertainties on the efficiency of the m_T cut were propagated in the exact same way and are listed in Table 10.17 as well. The uncertainties are combined by first taking for each source of uncertainty the average of the upward and downward deviation and then, summing the squares of these averages. The square root of this sum is the total systematic uncertainty.

10.6.3 Signal extraction

The uncertainties on fixed likelihood parameters are propagated to the estimates for the $W(\rightarrow \mu\nu)$ yield making use of Toy MC experiments. We generate 100 Toy MC data sets from the ML fit likelihoods. All parameters that are floated in the final

Table 10.17 – Relative uncertainties on the measured $W(\rightarrow \mu\nu)$ yields in %. Listed are the uncertainties related to potential underestimates and overestimates of the leading muon efficiency (respectively $\epsilon^\mu + \sigma$ and $\epsilon^\mu - \sigma$), equivalent uncertainties for the m_T cut ($\epsilon^{m_T} + \sigma$ and $\epsilon^{m_T} - \sigma$), and the combined relative uncertainty (total).

	$\epsilon^\mu - \sigma$	$\epsilon^\mu + \sigma$	$\epsilon^{m_T} - \sigma$	$\epsilon^{m_T} + \sigma$	total
0 jets	3.0	-3.2	0.3	-0.3	3
1 jet	5.5	-6.6	0.9	-0.9	6
2 jets	6.0	-7.3	2.1	-2.3	7
3 jets	9.1	-11.6	5.2	-6.0	12
≥ 4 jets	12	-20	11	-14	19

ML fits are set to the estimates obtained from the fit in data, such that the toy data sets mimic the data to the best of our knowledge. All other parameters are set to the estimates derived from MC simulated events. The ML fits are performed a first time in these toy data sets with the fixed parameters set to their nominal values. Then, we perform on each data set a number of alternative ML fits in which each time a certain group of fixed likelihood parameters is set to random values, uniformly distributed within the envelopes defined by their uncertainties. The uncertainty on the $W(\rightarrow \mu\nu)$ yield associated to a given group of parameters is then estimated as the distance between the signal contribution as estimated from the nominal fit and the one from the alternative fits, averaged over the 100 toy experiments.

For this purpose we group the fixed parameters as follows:

- **Mistag efficiency**

The mistag efficiency $\epsilon^{\text{no } b}$ is considered one group. The estimate of the uncertainty on this parameter is described in Section 10.4.1.

- **b -tag efficiency**

Also the b -tag efficiency is considered one group. The estimate of the uncertainty on this parameter is described in Section 10.4.2.

- **Contribution from Z**

Each of the parameters n_j^Z with $j = 0, \dots, 4$ is considered a group. The uncertainty on the value of these parameters is described in Section 10.2.4.

- **Parameters in the PDFs of m_T**

Also these parameters are grouped per jet bin and we furthermore distinguish

MEASUREMENTS OF $W(\rightarrow \mu\nu) + JETS$ PRODUCTION

between $W(\rightarrow \mu\nu)$, QCD and top quark production. The estimates for the uncertainties on parameters related to $W(\rightarrow \mu\nu)$ and top quark production are described in Section 10.4.3, for QCD uncertainties are described in Section 10.4.4.

Uncertainties on any other parameter are considered negligible. This is very reasonable since those parameters are related to the rare species and subspecies $W(\rightarrow \mu\nu)$, Z and the fraction of $W(\rightarrow \mu\nu)$ events in the left shoulder of the m_T distribution in jet bins 0 and 1. Table 10.18 lists the resulting relative uncertainties on $n_j^{W(\rightarrow \mu\nu)}$ per group of parameters. Uncertainties are combined by taking the square root of the sum of squares.

Table 10.18 – Relative uncertainties on the measured $W(\rightarrow \mu\nu)$ yields in % related to the average b -tag and mistag efficiency (respectively $\bar{\epsilon}^b$ and $\bar{\epsilon}^{\text{no } b}$), estimates for the background from Z production (n^Z) and the parameters in the PDFs of m_T for $W(\rightarrow \mu\nu)$, top and QCD. The combined uncertainties are listed as well (total).

	$\bar{\epsilon}^b$	$\bar{\epsilon}^{\text{no } b}$	n^Z	PDF of m_T			total
				$W(\rightarrow \mu\nu)$	top	QCD	
0 jets	-	-	0.1	1	0	0.2	1
1 jet	0.1	0.3	0.1	3	0.1	0.3	3
2 jets	0.4	0.5	0.1	3	0.2	0.5	4
3 jets	1.2	2	0.4	3	0.5	1	5
≥ 4 jets	9	1.2	3	6	6.5	13	19

10.7 Unfolding

The finite resolution of the jet energy and direction measurement and the finite jet reconstruction and identification efficiency distort the jet counting. These detector effects cause a fraction of the events that resides in a particular jet bin on the particle level to reside in a different jet bin on reconstruction level. We estimate the degree of *migration* or *smearing* for $W(\rightarrow \mu\nu)$ events in MC simulated events passing all selection criteria and derive a smearing or folding matrix. This matrix is shown in Table 10.19 and provides the probability for events in a given jet bin on particle level to be measured in a certain jet bin on reconstruction level. Jets on particle level are clustered from all visible particles other than the muon from the $W(\rightarrow \mu\nu)$ decay.

To correct for these effects, we unfold the measured $n^{W(\rightarrow \mu\nu)}$ spectrum. We use

Table 10.19 – Smearing or folding matrix for the $n^{W(\rightarrow\mu\nu)}$ spectrum derived from $W(\rightarrow\mu\nu)$ events in simulation. The table provides the probability for events in a given jet bin on particle level to be measured in a certain jet bin on reconstruction level.

		particle level				
		0	1	2	3	≥ 4
reco level	0	0.981365	0.103588	0.009475	0.001065	0.000000
	1	0.017870	0.866066	0.142727	0.019531	0.003091
	2	0.000729	0.029313	0.813240	0.199929	0.024730
	3	0.000032	0.000976	0.033404	0.749290	0.214838
	≥ 4	0.000004	0.000057	0.001154	0.030185	0.757342

the Singular Value Decomposition (SVD) method with regularization parameter $k_{SVD} = 5$ within the `Roofold` framework [112] [113]. The adopted migration matrix is the one given in Table 10.19. The statistical uncertainty and the uncorrelated systematic uncertainties, which are related to selection efficiency and signal extraction, are propagated through the unfolding, making use of the built-in error propagation function in the SVD unfolding algorithm. The correlated systematic uncertainties, which are related to the jet counting, are propagated by scaling $n^{W(\rightarrow\mu\nu)}$ up or down with the systematic uncertainty and repeating the unfolding procedure. Thereby 100% correlation is assumed between jet bins 1, 2, 3 and 4 and -100% between jet bin 0 and all other bins.

We attribute additional systematic uncertainty to the unfolding. A first source of uncertainty originates from the smearing matrix. To estimate this uncertainty the unfolding is repeated with alternative smearing matrices derived from $W(\rightarrow\mu\nu)$ events simulated with *i)* PYTHIA TuneZ2 and *ii)* MADGRAPH interfaced with PYTHIA TuneD6T. A second uncertainty originates from the unfolding method itself. We estimate this uncertainty by performing unfolding with an alternative unfolding algorithm. We choose an iterative procedure based on Bayes' theorem, also available within the `Roofold` framework [114] where we set the number of iterations to 4. As systematic uncertainty we adopt the envelope that contains the nominal result and the two alternative results.

The unfolded results are presented with their uncertainties in the summary in Section 10.10.

10.8 Measurement of Berends-Giele scaling

10.8.1 Maximum likelihood fit

We measure the BG parameters α and β defined in Equation 8.3. For that purpose, we perform the fits described in Chapter 10 simultaneously in all 5 jet bins. In order to obtain estimates on the particle level, we make the following parameter transformation in the joint likelihood function.

- The parameters $n_j^{W(\rightarrow \mu\nu)}$ representing the signal yields in jet bin j on reconstructed level are transformed, or unfolded, to the corresponding parameters on particle level making use of the smearing matrix in Table 10.19
- The unfolded yields in the exclusive jet bins 1, 2 and 3 are transformed to yields in inclusive jet bins
- We impose the relation in Equation 8.3 on the unfolded inclusive yields in jet bins 1, 2, 3 and 4.

With these constraints, maximizing the likelihood function yields direct estimates of the BG parameters α and β on the particle level.

10.8.2 Toy Monte Carlo studies

The fit for the BG parameters was tested with toy MC experiments. 1000 toy data sets were generated from the likelihood that is described in the previous paragraph, with all parameters set to values estimated from MC simulated events. The ML fits were applied in different configurations, floating and fixing different groups of parameters. It was found that this fit does not converge easily and that in order to obtain reasonable results it is required to fix all parameters related to the PDFs of m_T . The floating likelihood parameters are then:

- For $W(\rightarrow \mu\nu)$: the signal yield in the exclusive 0 jet bin after unfolding; the signal yield in the inclusive 1 jet bin after unfolding; the BG parameters α and β .
- For QCD: the fractions f_1 and f_2 in the PDFs \mathcal{B} of $n^{b \text{ tag}}$ defined in Equation 10.8.
- For top quark events: the yields $n_{j,1}^{top b}$ and $n_{j,2}^{top b}$.

The fits were performed with this configuration on each of the toy data sets. Figure 10.14 shows the distribution of the resulting estimates and uncertainties for α and β . It appears that the fit is not entirely stable. The statistical uncertainty on α and β , $\sigma(\alpha)$ and $\sigma(\beta)$ shows two distinct peaks. When we categorize the toy experiments according to $\sigma(\alpha)$, we find that the toys in the peak with $\sigma(\alpha) < 0.3$ have an irregular pull distribution with a width far above 1. However, in the other experiments the fit appears to behave reasonably well. We fit a Gaussian to the pull distributions of α and β in the well-behaving toy experiments, from which we conclude that the fits with $\sigma(\alpha) > 0.3$ perform well. The estimates for both α and β show only a small bias, of the order of 20% of the statistical uncertainty and the statistical uncertainty is only slightly overestimated.

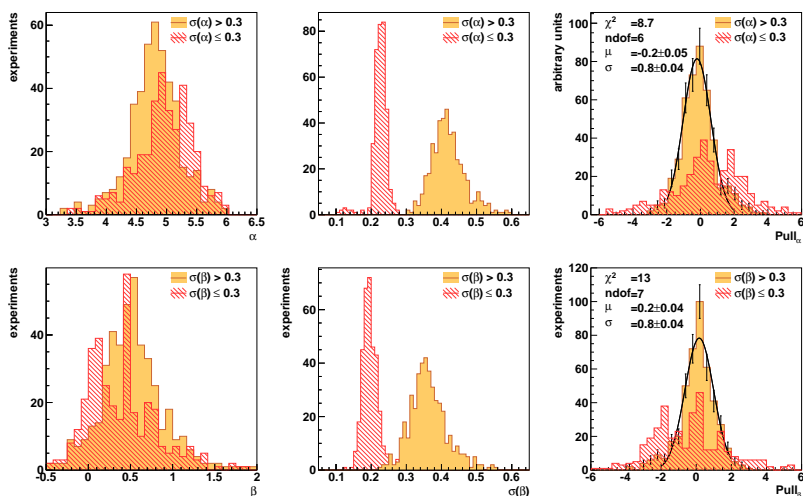


Figure 10.14 – Results from 1000 Toy MC experiments for the ML fit for the BG measurement. We show the distribution of the estimates for the BG parameters α (top-left) and β (bottom-left), the estimates for the uncertainties on the BG parameters $\sigma(\alpha)$ (top-center) and $\sigma(\beta)$ (bottom-center) and the pull distributions for α (top-right) and β (bottom-right). The pull distributions are fit with a Gaussian function. χ^2 , degrees of freedom (ndof), the estimate for the mean (μ) and the standard deviation (σ) are given in the figures.

Figure 10.15 shows the 2 dimensional distributions of the estimates for α and β and the estimates for $\sigma(\alpha)$ and $\sigma(\beta)$ in the toy experiments. In both cases the estimates show important correlations.

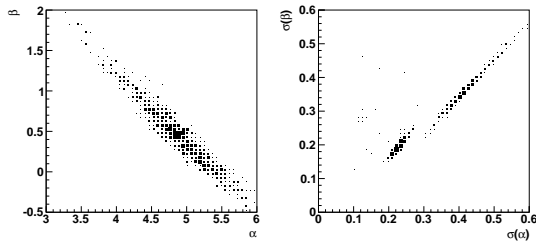


Figure 10.15 – Results from 1000 Toy MC experiments for the ML fit for the BG measurement. The scatter plots show the distributions of the estimate for β versus the estimates for α (left) and the estimates for the statistical uncertainties $\sigma(\beta)$ versus the estimates for $\sigma(\alpha)$ (left).

10.8.3 Fit procedure

We are able to reproduce the behavior of the fit as observed in the toy experiments in the ML fits on data. For that purpose, we repeat the ML fits on data 20 times with random initial values for α and β . As in the toy experiments, part of the results are clustered around smaller values for the statistical uncertainties on α and β , corresponding to the ill-behaving toy experiments. The other results are clustered around larger values for the statistical uncertainties and correspond to the well-behaving toy experiments. We select the fit result with the highest likelihood as our final result. This result is found to be part of the cluster of well-behaving results.

The results, measurements of α and β are presented in the summary in Section 10.10.

10.9 Measurement of charge asymmetry

We estimate the charge asymmetry, as defined in Equation 8.5, with yet another fit. The data are binned according to the jet multiplicity, 0, 1, 2 and ≥ 3 jets and according to the charge of the W candidate, the leading muon. The fit for the signal extraction that was defined in Section 10.2 is now applied in each of the jet bins with following modest changes:

- The values for m_T parameters that are fixed in the ML fits are determined from fits in simulated $W(\rightarrow \mu\nu)$ events as a function jet multiplicity and the W charge.
- We estimate n_j^Z , the number of background events from $Z(\rightarrow \mu\mu)$, for each bin by dividing the estimates given in Section 10.2.4 by two.

- The selection efficiency is almost independent from the W charge and therefore we do not weight the events in the ML fits.

Table 10.21 lists the resulting charge asymmetry as a function of inclusive jet multiplicity with relative statistical uncertainty (stat).

The impact of the uncertainties on the jet energy are studied by scaling the jet energies simultaneously up and simultaneously down while repeating the measurement. Relative to the statistical uncertainties, these systematic uncertainties are found to be negligible.

The probability for a muon to be reconstructed with the wrong charge is found to be of the order of 10^{-5} in MC and 10^{-4} in detector studies with cosmic muons [115]. Thus, we may safely ignore charge misidentification as a source of systematic uncertainty. The ratio ϵ^+/ϵ^- of the selection efficiency for positively charged muons ϵ^+ to the selection efficiency for negatively charged muons ϵ^- was measured with the TnP technique and found to be 1 within the statistical uncertainty of 2% [116]. This 2% statistical uncertainty corresponds roughly to a 1% uncertainty on the charge asymmetry. Systematic uncertainties related to the signal extraction were evaluated as was done for the measurement of the $W(\rightarrow \mu\nu)$ rates described in Section 10.6.3. We assume the uncertainties for the parameters to be to be 100% correlated between W^+ and W^- . No unfolding procedure was applied on the measured charge asymmetry since it was found to have negligible impact on the results.

The results, measurements of the charge W asymmetry as a function of the jet multiplicity are presented in the summary in Section 10.10.

10.10 Summary

Table 10.20 lists the measured $n^{W(\rightarrow \mu\nu)}$ spectrum after unfolding. We list the statistical uncertainty separately (stat) and combined in quadrature with uncorrelated systematic uncertainties (stat + uncor. syst). We show the deviations of the results for the case of an overestimate of the jet energies (JES - σ) and an underestimate (JES + σ). For the unfolding related uncertainty (unfold) we list the deviations from the central result, when using the alternative unfolding algorithm (algo), when using the smearing matrix derived from MC simulation with a different generator for the hard interaction (generator), and when using a smearing matrix derived with an alternative tune for the underlying event (tune). These numbers are used to calcu-

MEASUREMENTS OF $W(\rightarrow \mu\nu) + \text{JETS PRODUCTION}$

late the ratios in Equations 8.1, 8.2 and 8.4. Thereby, uncertainties related to signal efficiency and extraction are treated as uncorrelated. The uncertainties related to jet energy, including pile-up effects, are treated as 100% anti-correlated between jet bin 0 and the other jet bins and as 100% correlated between jet bins 1, 2, 3 and 4. The shift with respect to the central result, when varying the unfolding procedure is also considered 100% correlated between jet bins.

Table 10.20 – Measured signal yields $n^{W(\rightarrow \mu\nu)}$ after unfolding with relative uncertainties in %. The statistical uncertainty only (stat) and combined with uncorrelated systematic uncertainties (stat + uncor. syst), uncertainties related to an overestimate of jet energies (JES - σ) and an underestimate (JES + σ). For the uncertainties on unfolding we list the shift in the results when using a different unfolding algorithm (algo), when calculating the smearing matrix from MC with an alternative generator for the hard interaction (generator) and an alternative tune for the underlying event (tune).

	$n^{W(\rightarrow \mu\nu)}$	stat	stat + uncor. syst	JES		unfold		
				$-\sigma$	$+\sigma$	algo	generator	tune
0 jets	166144	0.4	3	6	-6	-0.1	-0.1	-0.1
1 jet	21162	2	6	-11	11	0.2	-1.2	-0.6
2 jet	4168	4	7	-12	13	-0.7	8	5
3 jet	682	8	9	-11	13	5	11	6
≥ 4 jets	114	20	32	-16	18	-12	-22	1

Table 10.21 lists the measured charge asymmetry as a function of inclusive jet multiplicity with the relative statistical uncertainty (stat) and the relative systematic uncertainties related to the muon reconstruction and selection efficiency (ϵ^+/ϵ^-) and the signal extraction (fit).

Table 10.21 – Measured charge asymmetry with relative uncertainties in %. The statistical uncertainty (stat) is provided together with systematic uncertainties related to the modeling for the signal extraction (fit) and to the potential differences of the selection efficiency between W^+ and W^- (ϵ^+/ϵ^-).

	A	uncertainties (%)		
		stat	ϵ^+/ϵ^-	fit
≥ 0 jets	0.223	2	1	0.2
≥ 1 jet	0.17	6	1	2
≥ 2 jets	0.18	17	1	2
≥ 3 jets	0.22	32	1	4

Table 10.22 shows the measured values for α and β with statistical uncertainties (central). The uncertainty originating from the unfolding is estimated by repeating the measurement using alternative smearing matrices as described in Section 10.7. The results are listed in the table (TuneD6T and PYTHIA). The uncertainty related to the selection efficiencies for the leading muon and the m_T cut are also listed (ϵ^μ and ϵ^{m_T}). These were obtained by repeating the analysis with efficiencies scaled up and down as described in more detail in Section 10.6.2. Uncertainties related to the modeling of m_T and $n^{b \text{ tag}}$ in the likelihood (fit m_T and fit $n^{b \text{ tag}}$) are obtained with toy experiments. We adopt again the method described in Section 10.6.3. Finally the systematic uncertainties related to systematic over- and underestimates of the jet energy (JEC $-\sigma$ and JEC $+\sigma$) are obtained by repeating the analysis while altering the jet energy as explained in Section 10.6.1.

Table 10.22 – Measured values for the BG parameters α and β (central). BG parameters obtained with alternative smearing matrices (TuneD6T and PYTHIA). Systematic uncertainties related to the efficiency of selection of the leading muon selection and the m_T cut (ϵ^μ and ϵ^{m_T}). Systematic uncertainties related to the modeling of the transverse mass and $n^{b \text{ tag}}$ in the ML fit (fit m_T and fit $n^{b \text{ tag}}$). Systematic uncertainties related to systematic over- and underestimates of the jet energy (JEC $- \sigma$ and JEC $+ \sigma$).

	α	β
central	4.6 ± 0.3	0.7 ± 0.3
TuneD6T	4.1 ± 0.3	3.5 ± 0.4
PYTHIA	3.5 ± 0.4	1.3 ± 0.3
ϵ^μ	± 0.2	± 0.2
ϵ^{m_T}	± 0.1	± 0.2
fit m_T	± 0.1	± 0.1
fit $n^{b \text{ tag}}$	± 0.1	± 0.1
JEC $- \sigma$	$- 0.3$	$+ 0.3$
JEC $+ \sigma$	$+ 0.1$	$- 0.2$

11

Results

Results are given at the particle level [100], within the detector acceptance and using the jet definitions described in Section 8.2. We do not combine the results for the electron and muon channels, since the adopted definitions for the acceptance and the clustering of jets are different.

A first set of ratios, $\sigma(V+ \geq n \text{ jets})/\sigma(V)$ defined in Equation 8.1, is calculated and listed in Tables 11.1 for $W(\rightarrow \mu\nu)$ and $W(\rightarrow e\nu)$ and 11.2 for $Z(\rightarrow \mu\mu)$ and $Z(\rightarrow ee)$. A second set of ratios, $\sigma(V+ \geq n \text{ jets})/\sigma(V+ \geq (n-1) \text{ jets})$ defined in Equation 8.2, is calculated and listed in Tables 11.3 for $W(\rightarrow \mu\nu)$ and $W(\rightarrow e\nu)$ and 11.4 for $Z(\rightarrow \mu\mu)$ and $Z(\rightarrow ee)$. These tables list the measured values for the ratios with statistical and systematic uncertainties. The statistical uncertainty (stat.) includes only the statistical uncertainty on the signal extraction. It is combined with the systematic uncertainties related to signal selection efficiency and signal extraction (stat. + efficiency and signal extraction). These uncertainties are not correlated between jet bins. The uncertainties related to the jet energy and pile-up effects (energy scale) are mentioned separately (energy scale), as are the uncertainties associated with the unfolding (unfolding). The latter two sources of uncertainty are highly correlated between jet bins.

We compare these results to two sets of theoretical predictions for W and Z + jets in Figures 11.1 to 11.4. For the first set of predictions, generated with the Monte Carlo event generator PYTHIA 6.422 [24] (Pythia), the hard interaction is described by LO

diagrams with an outgoing boson and 0 or 1 outgoing partons. For the second set of predictions, generated with MADGRAPH 4.4.13 [60] interfaced with PYTHIA 6.422 (MadGraph), the hard interaction is described by tree-level matrix elements with an outgoing boson and up to 5 outgoing partons. In both cases, showering and hadronization is included in the simulation and described by PYTHIA 6.422. The CTEQ6L1 PDFs [102] are used to model the proton structure. For the MADGRAPH sample, the generated hard interactions are interfaced to the showering mechanism according to the MLM jet matching prescription [28]. The tune for the underlying event is set to TuneZ2 or D6T [103]. To take part in the predictions, simulated events must pass the acceptance criteria described in Section 8.2. Jets are clustered and counted as described in the same section. No pile-up or detector effects are included in these simulations, which is appropriate since our measurements are given at the particle level.

For $n \geq 2$ jets, the predictions generated with PYTHIA fail to describe the data, while the MADGRAPH +PYTHIA predictions agrees well with the experimental spectrum. Because of the high threshold for the transverse momentum of the jets, $p_T > 30$ GeV, the sensitivity to the tuning of the underlying event is negligible. Thus, in further comparisons of our measurements to theoretical predictions, we will only consider the Z2 tune.

The ratios of W + jets and Z + jets cross sections, defined in Equation 8.4, are shown in Fig. 11.5. Many important systematic uncertainties, such as those on integrated luminosity and to some extent the jet energy reconstruction and selection efficiency, cancel in the ratio. The maximal difference observed between the measured and predicted values is at the level of one standard deviation (neglecting uncertainties on the predictions). The difference between the predicted value of the ratio in the electron and muon channels is due to the larger acceptance in η for electrons.

The measured charge asymmetry, defined in Equation 8.5, is listed in Table 11.5 and shown in Figure 11.6. The systematic uncertainties include those from the jet energy scale, the charge misidentification, and the positive versus negative lepton efficiency difference. The charge asymmetry depends on the number of associated jets because the fraction of u (d) quarks contributing to the process is different in each case. The measured values are found to be in good agreement with the predictions from MADGRAPH + PYTHIA with the Z2 tune for the underlying event. The predictions generated with PYTHIA do not describe well the W charge asymmetry, even for events with a single associated jet.

RESULTS

Finally, we present the measured parameters α and β , defined in Equation 8.3, describing the Berends-Giele scaling. Figure 11.7 shows the measurement in the (α, β) plane and compares them to predictions from MADGRAPH + PYTHIA with the Z2 tune for the underlying event. The electron and muon predicted values differ mostly because of the $\Delta R > 0.3$ requirement between the jets and the leptons, which is applied only in the electron channel. The ellipses correspond to 68% confidence level contours using the statistical uncertainty only. The arrows show the displacement of the central value when varying each indicated parameter by its estimated uncertainty. The fit results are also reported in Tables 11.6 and 11.7. The listed systematic uncertainties are related to the jet energy reconstruction, the selection efficiency and the description of the underlying event (tune) adopted in the simulation that is used to unfold the jet multiplicity spectrum. The data are in agreement with predictions within one or two standard deviations depending on the channel. Furthermore, the Berends-Giele scaling hypothesis i.e., $\beta = 0$, is confirmed to work well up to the production of 4 jets; The β parameter lies within one standard deviation from zero for the $W + \text{jets}$ case and within 0.5 standard deviations for the $Z + \text{jets}$ case.

Table 11.1 – Results for $\sigma(W + \geq n \text{ jets})/\sigma(W)$ in the electron and muon channels. A full description of the uncertainties is given in the text.

n jets	$\frac{\sigma(W + \geq n \text{ jets})}{\sigma(W)}$	stat.	stat. + efficiency and signal extraction	energy scale	unfolding
electron channel					
≥ 1 jets	0.133	0.002	0.002	$+0.019$ -0.017	± 0.001
≥ 2 jets	0.026	0.001	0.001	± 0.004	± 0.001
≥ 3 jets	0.0032	0.0004	0.0004	$+0.0006$ -0.0005	± 0.0001
≥ 4 jets	0.00056	0.00017	0.00018	$+0.00012$ -0.00010	$+0.00006$ -0.00001
muon channel					
≥ 1 jets	0.136	0.002	0.007	$+0.019$ -0.017	± 0.001
≥ 2 jets	0.026	0.001	0.002	± 0.004	$+0.002$ -0.001
≥ 3 jets	0.0041	0.0003	0.0005	$+0.0008$ -0.0006	$+0.0003$ -0.0001
≥ 4 jets	0.00059	0.00011	0.00017	$+0.00012$ -0.00010	$+0.00001$ -0.00015

Table 11.2 – Results for $\sigma(Z + \geq n \text{ jets})/\sigma(Z)$ in the electron and muon channels. A full description of the uncertainties is given in the text.

n jets	$\frac{\sigma(Z + \geq n \text{ jets})}{\sigma(Z)}$	stat.	stat. + efficiency and signal extraction	energy scale	unfolding
electron channel					
≥ 1 jets	0.151	0.006	0.006	$+0.021$ -0.019	± 0.001
≥ 2 jets	0.028	0.003	0.003	± 0.004	± 0.001
≥ 3 jets	0.0039	0.0009	0.0009	$+0.0007$ -0.0006	$+0.0003$ -0.0001
≥ 4 jets	0.00070	0.00036	0.00036	$+0.00014$ -0.00012	$+0.00005$ -0.00004
muon channel					
≥ 1 jets	0.149	0.005	0.011	$+0.022$ -0.020	± 0.001
≥ 2 jets	0.027	0.003	0.004	± 0.004	± 0.001
≥ 3 jets	0.0042	0.0011	0.0012	$+0.0008$ -0.0006	$+0.0001$ -0.0003
≥ 4 jets	0.00087	0.00050	0.00056	$+0.00017$ -0.00015	$+0.00010$ -0.00001

RESULTS

Table 11.3 – Results for $\sigma(W+ \geq n \text{ jets})/\sigma(W+ \geq (n-1) \text{ jets})$ in the electron and muon channels. A full description of the uncertainties is given in the text.

n jets	$\frac{\sigma(W+ \geq n \text{ jets})}{\sigma(W+ \geq (n-1) \text{ jets})}$	stat.	stat. + efficiency and signal extraction	energy scale	unfolding
electron channel					
$\geq 1 / \geq 0$ jets	0.133	0.002	0.002	+0.019 -0.017	± 0.001
$\geq 2 / \geq 1$ jets	0.195	0.007	0.007	+0.002 -0.001	+0.012 -0.001
$\geq 3 / \geq 2$ jets	0.125	0.014	0.015	± 0.004	+0.002 -0.004
$\geq 4 / \geq 3$ jets	0.173	0.046	0.049	+0.003 -0.004	+0.017 -0.003
muon channel					
$\geq 1 / \geq 0$ jets	0.136	0.002	0.007	+0.019 -0.017	± 0.001
$\geq 2 / \geq 1$ jets	0.190	0.005	0.014	+0.004 -0.003	+0.016 -0.001
$\geq 3 / \geq 2$ jets	0.160	0.011	0.018	+0.004 -0.003	+0.004 -0.002
$\geq 4 / \geq 3$ jets	0.144	0.025	0.037	+0.002 -0.003	+0.001 -0.043

Table 11.4 – Results for $\sigma(Z+ \geq n \text{ jets})/\sigma(Z+ \geq (n-1) \text{ jets})$ in the electron and muon channels. A full description of the uncertainties is given in the text.

n jets	$\frac{\sigma(Z+ \geq n \text{ jets})}{\sigma(Z+ \geq (n-1) \text{ jets})}$	stat.	stat. + efficiency and signal extraction	energy scale	unfolding
electron channel					
$\geq 1 / \geq 0$ jets	0.151	0.006	0.006	+0.021 -0.019	± 0.001
$\geq 2 / \geq 1$ jets	0.185	0.017	0.017	+0.002 -0.001	+0.006 -0.001
$\geq 3 / \geq 2$ jets	0.138	0.030	0.030	± 0.004	+0.008 -0.003
$\geq 4 / \geq 3$ jets	0.181	0.085	0.085	+0.003 -0.004	+0.014 -0.021
muon channel					
$\geq 1 / \geq 0$ jets	0.149	0.005	0.011	+0.022 -0.020	± 0.001
$\geq 2 / \geq 1$ jets	0.180	0.016	0.023	± 0.003	+0.011 -0.001
$\geq 3 / \geq 2$ jets	0.158	0.036	0.043	+0.002 -0.001	+0.001 -0.017
$\geq 4 / \geq 3$ jets	0.207	0.104	0.117	+0.002 -0.003	+0.031 -0.001

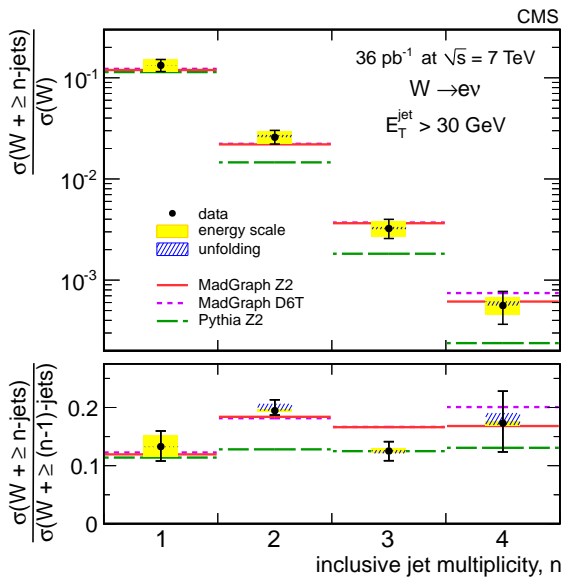


Figure 11.1 – The measured ratios $\sigma(W + \geq n \text{ jets})/\sigma(W)$ (top) and $\sigma(W + \geq n \text{ jets})/\sigma(W + \geq (n - 1) \text{ jets})$ (bottom) in the electron channel. The measurements are compared to the predictions generated with PYTHIA (Pythia) and MADGRAPH + PYTHIA (MadGraph) described in the text. Predictions are generated using the Z2 or D6T tune for the underlying event as indicated in the figure. Points with error bars correspond to the data. The uncertainties due to the jet energy reconstruction and due to the unfolding procedure are shown as yellow and hatched bands, respectively. The error bars represent the total uncertainty.

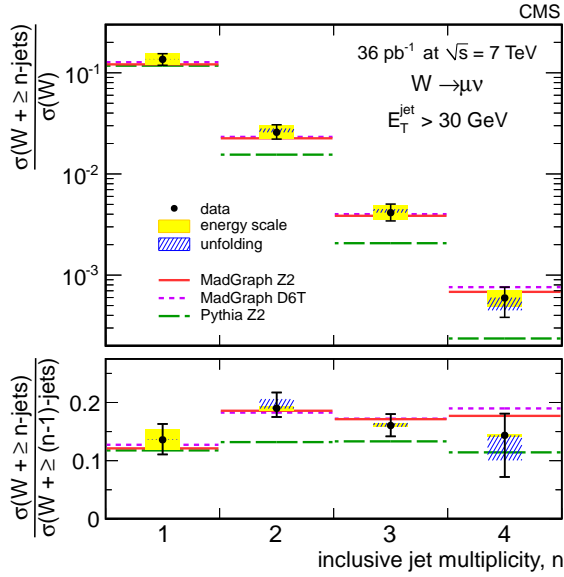


Figure 11.2 – The measured ratios $\sigma(W + \geq n \text{ jets})/\sigma(W)$ (top) and $\sigma(W + \geq n \text{ jets})/\sigma(W + \geq (n - 1) \text{ jets})$ (bottom) in the muon channel. The measurements are compared to the predictions generated with PYTHIA (Pythia) and MADGRAPH + PYTHIA (MadGraph) described in the text. Predictions are generated using the Z2 or D6T tune for the underlying event as indicated in the figure. Points with error bars correspond to the data. The uncertainties due to the jet energy reconstruction and due to the unfolding procedure are shown as yellow and hatched bands, respectively. The error bars represent the total uncertainty.

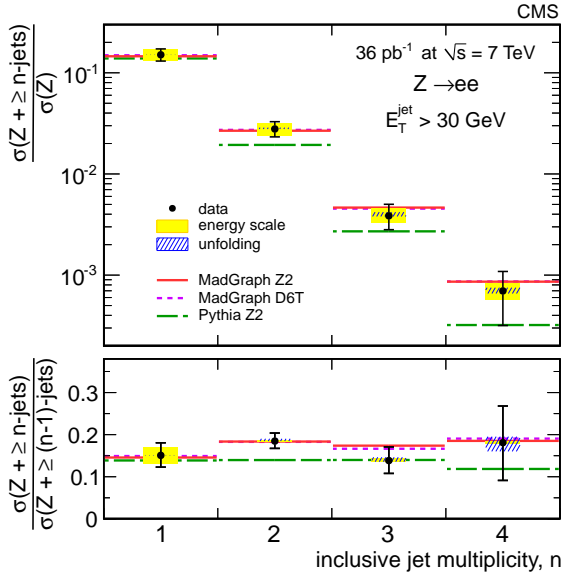


Figure 11.3 – The measured ratios $\sigma(Z + \geq n \text{ jets})/\sigma(Z)$ (top) and $\sigma(Z + \geq n \text{ jets})/\sigma(Z + \geq (n - 1) \text{ jets})$ (bottom) in the electron channel. The measurements are compared to the predictions generated with PYTHIA (Pythia) and MADGRAPH + PYTHIA (MadGraph) described in the text. Predictions are generated using the Z2 or D6T tune for the underlying event as indicated in the figure. Points with error bars correspond to the data. The uncertainties due to the jet energy reconstruction and due to the unfolding procedure are shown as yellow and hatched bands, respectively. The error bars represent the total uncertainty.

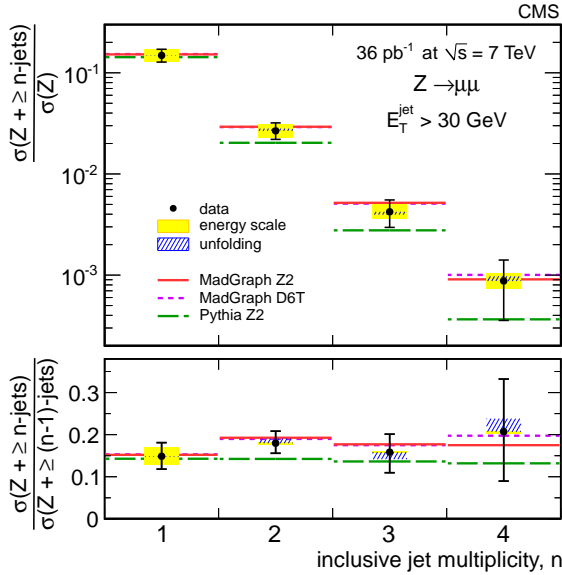


Figure 11.4 – The measured ratios $\sigma(Z + \geq n \text{ jets})/\sigma(Z)$ (top) and $\sigma(Z + \geq n \text{ jets})/\sigma(Z + \geq (n - 1) \text{ jets})$ (bottom) in the muon channel. The measurements are compared to the predictions generated with PYTHIA (Pythia) and MADGRAPH + PYTHIA (MadGraph) described in the text. Predictions are generated using the Z2 or D6T tune for the underlying event as indicated in the figure. Points with error bars correspond to the data. The uncertainties due to the jet energy reconstruction and due to the unfolding procedure are shown as yellow and hatched bands, respectively. The error bars represent the total uncertainty.

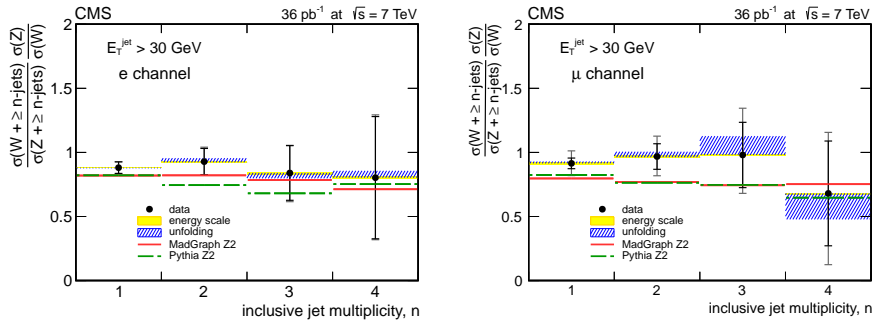


Figure 11.5 – Measured ratio of the $W + \text{jets}$ and $Z + \text{jets}$ cross sections for the electron channels (left) and the muon channels (right) as a function of the jet multiplicity. The ratios are normalized to the inclusive W/Z cross section. The measurements are compared to the predictions generated with PYTHIA (Pythia) and MADGRAPH + PYTHIA (MadGraph) described in the text. Predictions are generated using the Z2 tune for the underlying event as indicated in the figure. Points with error bars correspond to the data. The uncertainties due to the jet energy reconstruction and due to the unfolding procedure are shown as yellow and hatched bands, respectively. The error bars represent the statistical and total uncertainty on the measurements.

Table 11.5 – Measured W charge asymmetry A_W , compared to the predictions generated with PYTHIA (Pythia) and MADGRAPH + PYTHIA (MadGraph) described in the text. Predictions are generated using the Z2 tune for the underlying event. The uncertainties on the predictions are statistical only.

n jets	data	MADGRAPH Z2	PYTHIA Z2
electron channel			
≥ 0	$0.217 \pm 0.004(\text{stat}) \pm 0.006(\text{syst})$	0.228 ± 0.001	0.216 ± 0.003
≥ 1	$0.179 \pm 0.010(\text{stat}) \pm 0.007(\text{syst})$	0.179 ± 0.004	0.267 ± 0.007
≥ 2	$0.16 \pm 0.03(\text{stat}) \pm 0.01(\text{syst})$	0.183 ± 0.010	0.281 ± 0.020
≥ 3	$0.17 \pm 0.08(\text{stat}) \pm 0.06(\text{syst})$	0.19 ± 0.02	0.33 ± 0.05
muon channel			
≥ 0	$0.223 \pm 0.003(\text{stat}) \pm 0.010(\text{syst})$	0.224 ± 0.001	0.237 ± 0.003
≥ 1	$0.175 \pm 0.010(\text{stat}) \pm 0.011(\text{syst})$	0.179 ± 0.003	0.222 ± 0.008
≥ 2	$0.18 \pm 0.03(\text{stat}) \pm 0.02(\text{syst})$	0.190 ± 0.008	0.273 ± 0.023
≥ 3	$0.22 \pm 0.07(\text{stat}) \pm 0.02(\text{syst})$	0.19 ± 0.02	0.26 ± 0.06

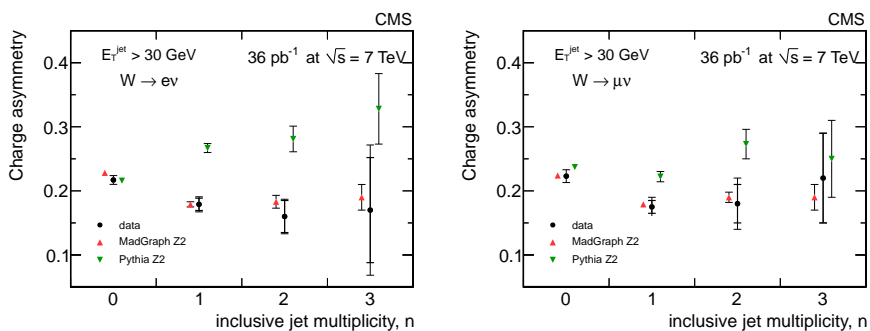


Figure 11.6 – Measured W charge asymmetry A_W as a function of the inclusive jet multiplicity. The measurements are compared to the predictions generated with PYTHIA (Pythia) and MADGRAPH + PYTHIA (MadGraph) described in the text. Predictions are generated using the Z2 tune for the underlying event. Error bars on the data points represent the statistical and total uncertainty. Error bars on the predictions correspond to the statistical uncertainty only. Left: electron decay channel, right: muon decay channel.

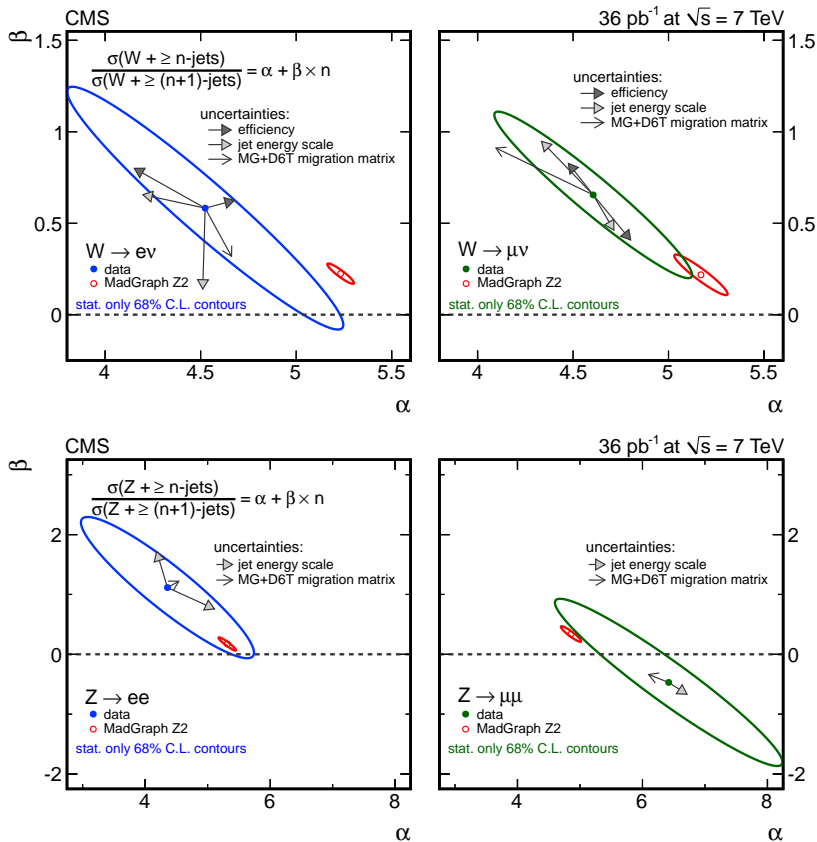


Figure 11.7 – Measurement for the Berends-Giele scaling parameters α and β for $W + \text{jets}$ (top) and $Z + \text{jets}$ (bottom) in the electron channels (left) and the muon channels (right). The measurements are compared to the predictions generated with MADGRAPH + PYTHIA (MadGraph) described in the text, with the Z2 tune for the underlying event. The ellipses correspond to 68% confidence level contours considering the statistical uncertainty only, for both data and simulation. The arrows show the displacement of the central value when varying each indicated parameter by its estimated uncertainty. The arrows labeled “MG+D6T migration matrix” correspond to the displacement of the measurements when the D6T tune is adopted to describe the underlying event in the simulation that is used to unfolding the jet multiplicity spectrum.

RESULTS

Table 11.6 – Measurement of the Berends-Giele parameters α and β for $W/Z + \text{jets}$ in the electron channel. The measurements are compared to the predictions generated with MADGRAPH + PYTHIA described in the text, with the Z2 tune for the underlying event. The statistical and systematic uncertainties on the measurements are described in the text. The uncertainty on the predictions is statistical only.

		data	stat.	energy scale	efficiency	tune	theory
W	α	4.5	± 0.5	$\begin{smallmatrix} +0.1 \\ -0.3 \end{smallmatrix}$	$\begin{smallmatrix} +0.2 \\ -0.4 \end{smallmatrix}$	+0.1	5.20 ± 0.05
	β	0.6	± 0.4	$\begin{smallmatrix} +0.1 \\ -0.4 \end{smallmatrix}$	$\begin{smallmatrix} +0.2 \\ -0.1 \end{smallmatrix}$	-0.3	0.20 ± 0.04
Z	α	4.4	± 0.9	$\begin{smallmatrix} +0.8 \\ -0.2 \end{smallmatrix}$	± 0.05	+0.2	5.3 ± 0.1
	β	1.1	± 0.8	$\begin{smallmatrix} +0.6 \\ -0.4 \end{smallmatrix}$	± 0.3	+0.1	0.17 ± 0.07

Table 11.7 – Measurement of the Berends-Giele parameters α and β for $W/Z + \text{jets}$ in the muon channel. The measurements are compared to the predictions generated with MADGRAPH + PYTHIA described in the text, with the Z2 tune for the underlying event. The statistical and systematic uncertainties on the measurements are described in the text. The uncertainty on the predictions is statistical only.

		data	stat.	energy scale	efficiency	tune	theory
W	α	4.6	± 0.3	$\begin{smallmatrix} +0.1 \\ -0.3 \end{smallmatrix}$	$\begin{smallmatrix} +0.2 \\ -0.1 \end{smallmatrix}$	-0.5	5.17 ± 0.09
	β	0.7	± 0.3	$\begin{smallmatrix} +0.3 \\ -0.2 \end{smallmatrix}$	± 0.3	+0.3	0.22 ± 0.07
Z	α	6.4	± 1.2	$\begin{smallmatrix} +0.1 \\ -0.3 \end{smallmatrix}$	± 0.1	-0.3	4.8 ± 0.1
	β	-0.5	± 0.9	$\begin{smallmatrix} +0.1 \\ -0.2 \end{smallmatrix}$	± 0.2	+0.1	0.34 ± 0.09

12

Discussion

An evaluation

The W and $Z + \text{jets}$ measurements described in this thesis constitute, together with the simultaneous measurements at the ATLAS detector [73] [74], the first detailed study of vector boson production in association with jets in pp collisions at $\sqrt{s} = 7$ TeV. As this was an early study that made use of the data collected during the first year of data-taking by CMS, the available statistics are rather low, leading to fairly large statistical uncertainties on the results. Furthermore, at the time of this measurement, the confidence in the detector understanding was still at a rather low level, leading to systematic uncertainties that are fairly large as well. Nevertheless, this measurement was quite successful, providing meaningful and useful results. Theoretical predictions were held against these results and found to be in good agreement. This is an important step in the validation of the SM predictions used to model the SM background in searches for new physics. The paper documenting this measurement is now accepted for publication [16].

While developing this measurement, much care was paid to keep the dependence on theoretical predictions and detector simulation as low as reasonably possible. The key features of the analysis that enabled this low dependence are the following:

i) The measurement of ratios.

We measured ratios of observables that show a positive correlation with respect to

various important systematic uncertainties, drastically reducing the sensitivity of our measurement to these uncertainties.

ii) The measurement of signal efficiency in data.

In the muon channels, the loss of events due to the finite signal efficiency was compensated by weighting the selected sample event-by-event by $1/\epsilon$, with ϵ the signal efficiency as a function of the kinematic properties of the reconstructed boson decay products and the jet multiplicity. This efficiency was measured in $Z \rightarrow \mu\mu$ data with the tag and probe technique.

iii) A data-driven signal extraction method.

The maximum likelihood fit used to determine the signal strength in the selected sample of events relies relatively little on theoretical predictions and detector simulation. The main assumptions that are made relate only to the very broad features of the signal processes and the main background processes.

Keeping the dependence on predictions and detector simulation at such a low level is probably our most important achievement. This approach is by far not the easiest, and not at all common practice. Indeed, other measurements of $W/Z + \text{jet}$ production, performed at the Tevatron experiments D0 [67] and CDF [62] and the other general purpose LHC experiment, ATLAS [74], dependent to a significantly greater extent on predictions and simulation. Most often, a rather pure but less efficient selection is adopted, and the signal strength is determined by simply subtracting the background as predicted with MC simulation. Such approach may be appropriate in regions of phase space where the signal dominates completely over background, however, when this is not the case such approach should be regarded with a healthy level of skepticism. An example of such a background dominated region of phase space is the region with multiple jets with high transverse momentum, that for the $W + \text{jets}$ measurement presented here is completely dominated by top quark pair-production.

Towards a Bayesian approach?

While performing the SUSY search described in this thesis, I caught the Bayesian virus and I believe that the $W/Z + \text{jets}$ measurements could benefit from a Bayesian approach as well. Making assumptions about parameters is unavoidable for $W/Z + \text{jets}$ measurements, just like it is for almost any measurement at the LHC. I believe that admitting this explicitly and adopting a coherent Bayesian approach could be very opportune in various manners.

In a Bayesian approach, each of the relevant parameters of the measurement is as-

DISCUSSION

signed a prior probability density function. If priors are chosen in a well-motivated objective way, based on careful studies of the detector performance and a thorough evaluation of the theoretical predictions, the $W/Z + \text{jets}$ studies at CMS would certainly prosper.

A concrete example of where this measurement could benefit from the Bayesian approach is the signal extraction. Indeed, unlike in the maximum likelihood approach, one does not have to care about fit stability. Setting part of the nuisance parameters to fixed values in order to avoid biased results is then obsolete. That is because in the Bayesian approach, any nuisance parameter of the likelihood is integrated out, according to its prior probability density, which if well defined, encodes its uncertainty. That every single parameter is varied within uncertainties and not just a few implies in fact a larger impact of the data on the results with respect to the Maximum Likelihood approach.

In this Bayesian approach, including more nuisance parameters in the likelihood becomes realistic. For example, the important jet calibration factors could be incorporated. In practice this would work as follows: first, a prior probability density for the calibration factors must be constructed, encoding their current understanding; second, a large number of jet calibration scenarios should be sampled from this probability density; finally, the measurement should be repeated for each of the scenarios. If uncertainties related to several parameters are treated as such, scenarios should be sampled from a joined prior probability density, and adopting an MCMC sampling technique might be appropriate.

Priors for parameters related to detector performance are ideally based on measurements in data and otherwise on measurements in Monte Carlo simulation. Most often these measurements are performed in bins of some kinematic variables. For instance, for this measurement the signal selection efficiency was measured in bins of muon transverse momentum and pseudorapidity. It would be interesting to investigate whether the binning can be avoided, and to use for instance neural networks to construct smooth functions that describe the detector performance. A practical neural network technique are Bayesian neural networks, which are very robust against overtraining and provide meaningful uncertainties on the functional forms they provide [117].

Ideally but may be not realistic, after the marginalization of the nuisance parameters, this Bayesian approach would result in a single, multi-dimensional posterior probability density function of the measured cross sections in all exclusive jet bins

and channels. Such posterior would contain all essential information of our measurement, including the correlations between the different cross sections. It would allow to derive the several interesting cross section ratios, taking into account all correlations with great precision. It would also allow to make a meaningful, well-motivated decision on whether or not the data are in agreement with the predictions. Of course such posterior can not be published on paper, but making it available in electronic format would certainly add significant value to any future $W/Z + \text{jets}$ publications.

To allow a frequentist interpretation of the results, or the use of alternative priors for the cross sections, it is also very useful to publish a likelihood function for the cross sections, with all nuisance parameters marginalized. In such approach the nuisance parameters are still treated Bayesian. However, although not always explicitly mentioned as such in publications, many measurements treat nuisance parameters in a Bayesian way, integrating them out according to a certain prior.

Improving signal extraction

The weak point of our signal extraction method is situated in the top versus $W + \text{jets}$ discrimination. A small fraction of $W + \text{jets}$ production is identified as top quark production and vice versa. This, introduces a dependence on predictions, related to splitting of gluons to $b\bar{b}$ and the presence of b -quarks in the quark sea of the proton. The fraction is predicted to be small, much smaller than the uncertainties on the results of the early $W/Z + \text{jets}$ studies presented here. However, in future measurements this fraction will probably become significant.

Important efforts were invested to avoid this dependence, by replacing in the fit for the signal extraction, the b -tagged jet multiplicity with an alternative discriminating variable. Several candidate variables were found, however they turned out to have less discriminating power, to depend on other predictions or to be correlated with the other discriminating variable m_T . Further efforts in this direction may be appropriate, but before that, it is worthwhile to evaluate in more detail how this particular dependence affects any future measurement.

Differential cross sections

Future studies of $W/Z + \text{jets}$ production at CMS will include more detailed differential cross sections. Differential cross sections as a function of the jet and boson kinematics are extremely useful for the validation of theoretical predictions. Mea-

DISCUSSION

measurements of additional differential cross sections, as a function of search related variables such as E_T^{miss} and H_T , or high jet multiplicities can even be direct searches for new physics.

It is questionable whether the current low dependence on predictions and detector simulation can be maintained for that purpose. Measuring $W/Z + \text{jets}$ production in small bins of jet and boson p_T or η , using the current signal extraction technique, is probably not a very good option, leading to high statistical uncertainties and drastically increasing the level of complexity of the measurement.

The application of the sPlot technique might provide a solution [118] [119]. sPlots are a way to derive differential cross sections as a function of certain variables x , based on signal extraction that make use of discriminating variables y . The condition for this technique to work, is that x and y are uncorrelated. The kinematics of jets and boson are certainly correlated to the discriminating variables used in the current signal extraction. However, it is probably possible to extend the sPlot method such that it works for correlated variables, provided that these correlations are known. The question then is whether it pays off to use the data driven techniques for the signal extraction in combination with sPlots if these correlations are to be measured from MC simulation.

Part III

Search for SUSY in all-hadronic events with b -jets

13

Introduction

Notwithstanding tremendous efforts and a wide range of search strategies, no hints of SUSY-like signatures were found yet in the proton-proton data collected by the LHC experiments in 2010 and 2011. However, the new data do contain valuable new information about new physics and imply important constraints on the parameters of many of the popular new physics models (e.g. [120] [121]). As the LHC will provide us with many more data, and will significantly upgrade the center of mass energy of the proton-proton collisions, there is plenty of reason to increase and optimize our search efforts, to further expand the range of search strategies and to develop new ways of data exploration.

This part of the thesis contributes to this mission, by focusing on the interpretation of measurements within new physics models and the potential benefits of a careful interpretation of the existing measurements on the design of a next, more powerful generation of searches. At present, most searches for new physics at CMS are count experiments and the observations are interpreted with the frequentist CLs method [122]. Discoveries are (not) claimed with a certain significance α and limits are set at a confidence level $(1-\beta)$. While the statistical uncertainties are treated with a frequentist approach, systematic uncertainties are usually treated in a Bayesian manner.

Search results are most often interpreted within the context of the constrained MSSM (cMSSM) [23] or within simplified models (SMS) [123]. The cMSSM is a realization

of the MSSM with 5 free parameters, obtained with constraints that are mainly related to universality. Working within a new physics model of such reduced dimensionality has some practical advantages. However, one must be careful when drawing conclusions from such models, especially if the motivation for the reduction of the complexity is on the philosophical side such as, arguably, is the case for the cMSSM.

To avoid such constraints while retaining the practical advantages of a low dimensionality, CMS is investing important efforts in the interpretation of searches within simplified models. In general, a simplified model describes the production of a single type of new physics particle and includes only one or few decay modes. Its free parameters are the production cross section and the masses of the particles involved. The result of the interpretation is an upper limit for the production cross sections as a function of the other free parameters. It is supposed that the resulting upper limits are fairly universal and valid in the context of most new physics models.

In this part of the thesis we construct and explore an alternative method for the interpretation of measurements performed at the LHC. First of all, we wish to make use of the intuitively appealing concepts of *probability of a hypothesis* and *probability density of a parameter of a hypothesis*, and for that purpose we adopt a Bayesian approach [124]. In Chapter 14 we build a coherent Bayesian framework for the interpretation of count experiments. We construct both a model-dependent and a model-independent method, where the former tests the presence of a non-specified source of new physics events, while the latter evaluates the impact of a count experiment on new physics models with free parameters. As explained in the final section of the chapter, within this framework the simultaneous interpretation of combinations of independent count experiments is straightforward.

In the same chapter 14 we explain how these interpretation methods lead in a natural way to an optimization method for searches for new physics. Under the hypothesis of a certain new physics model with free parameters, and considering the results of the existing measurements, this procedure finds the event selection that maximizes the probability for discovery.

The Bayesian approach requires to choose prior probabilities or probability densities for the hypotheses and parameters under study. In order to reduce the influence of priors on the inference, we make use of the well-motivated reference priors [125] [126] [127], wherever possible. Reference priors are by definition the priors that maximize the influence of the observation on the results of the inference. Another important and attractive property is that under any one-to-one transformation

INTRODUCTION

the reference prior remains the reference prior. This, e.g. in contrast to the flat prior which in does remain flat under non-trivial one-to-one transformations. Whenever the use of reference priors is not feasible, we make use of flat priors.

Also on the matter of the physics model under study we take an approach that is rather uncommon. In Chapter 15 we explain how to use our Bayesian framework to interpret searches within the phenomenological MSSM (pMSSM) [23], A 19-dimensional realization of the MSSM. In contrast to the cMSSM, the assumptions of the pMSSM are mainly based on stringent experimental constraints, which is reflected in its higher dimensionality and its diverse range of final states. An advantage of using the pMSSM rather than the simplified models is that it allows to incorporate information from previous measurements of many different origins. Earlier interpretations of measurements in High Energy Physics within the pMSSM are e.g. [128] and [129].

We demonstrate the Bayesian interpretation tools in chapter 16. For that purpose, we perform a search in a sample of proton-proton collisions with a center of mass energy of $\sqrt{s} = 7$ TeV and corresponding to 3.270 fb^{-1} . The selection is based on jet multiplicity, total hadronic energy, missing transverse energy and the multiplicity of b -jets. Twelve independent search regions are defined based on jet and b -jet multiplicity, and the observed number of events in each region is compared to the Standard Model predictions. The observations are interpreted in the model-independent way and within the pMSSM, where we combine the observations with several pre-LHC measurements and the CMS “ α_T ” measurement [130].

The Bayesian tools for interpretation lead in a natural way to a procedure to guide the design of new searches based on the results of existing measurements. In Chapter 17 we discuss a first application of this method on a single count experiment and elaborate on a potential road towards the optimization of multiple count experiments.

14

A Bayesian statistical framework

14.1 Bayes' Theorem

In this section, we develop a statistical framework for the interpretation and optimization of searches for new phenomena in count experiments at particle colliders. Our approach is based on Bayesian inference, and thus makes abundant use of Bayes' Theorem,

$$P(H|X) = \frac{P(X|H)P(H)}{P(X)}. \quad (14.1)$$

In Bayesian inference, this equation is interpreted as follows: X denotes a certain observation and H is a certain hypothesis. $P(H)$ is called the prior probability for H and quantifies the belief, prior to the observation, that the hypothesis H is true; $P(X|H)$ is the probability to observe X if the hypothesis H is true; $P(X)$ is a normalization factor, the overall probability for the observation X ; finally, $P(H|X)$ is the posterior probability for H , the probability that H is true after having made the observations;

This relation holds also if the hypothesis H is replaced by its parameters θ

$$P(\theta|X) = \frac{P(X|\theta)P(\theta)}{P(X)}. \quad (14.2)$$

In that case, $P(\theta)$ is the prior probability density for θ , which quantifies our assumptions before the observation X . $P(X|\theta)$ is the likelihood function for θ and $P(\theta|X)$ is the posterior probability density for θ , that encodes our knowledge about θ after the observation X is made.

In the following, we denote observed quantities with capitals and parameters of hypotheses with lower-case characters. Probabilities are denoted with P if they are proper, i.e. normalized to 1, and with p if they are not necessarily proper. Reference prior probabilities are denoted with π .

14.2 Bayesian hypothesis testing

14.2.1 General formulation

In Bayesian inference, the impact of a certain observation on a set of hypotheses is most often assessed in two ways [131]: *i*) through the posterior probabilities of the given hypotheses *ii*) through the posterior probability densities of the interesting parameters of the hypotheses.

Let X be the observed data, and H_i , $i = 1, \dots, n$ the considered hypotheses with prior probabilities $P(H_i)$. The posterior probability of any of the hypotheses H_i is then written as follows:

$$P(H_i|X) = \left(\sum_{j=1}^{j=n} B_{ji}(X) \frac{P(H_j)}{P(H_i)} \right)^{-1}, \quad (14.3)$$

with $B_{ij}(X)$ the Bayes factor

$$B_{ij}(X) = \frac{P(X|H_i)}{P(X|H_j)}, \quad (14.4)$$

and $P(X|H_i)$ the probability to observe the data X under the hypothesis H_i . These posterior probabilities are only meaningful if all involved probabilities and probability densities are proper, or, if normalization constants cancel out in the derivation of B_{ij} . Indeed, this condition is required such that the posterior probabilities for the hypotheses are proper themselves and all lie in the interval $[0, 1]$ and sum to 1.

A regular case when only two hypotheses are tested against each other, say H_0 and H_1 , and the two prior probabilities are chosen to equal $1/2$. In that case, the posterior probability for H_1 is

$$P(H_1|X) = \frac{B_{10}(X)}{B_{10}(X) + 1}, \quad (14.5)$$

and similar for H_0 .

In general, each hypothesis H_i depends on a set of parameters, say θ_i , that dwell in a parameter space Θ_i . The likelihoods $P(X|H_i)$ in Equation 14.4 must then be written as

$$P(X|H_i) = \int_{\Theta_i} P(X|\theta_i, H_i)P(\theta_i|H_i)d\theta_i \quad (14.6)$$

with $P(X|\theta_i, H_i)$ the likelihood function for θ_i under the hypothesis H_i and $P(\theta_i)$ the prior probability density for θ_i under the hypothesis H_i .

The posterior probability density $P(\theta_i|H_i)$ for the parameter set θ_i under the hypothesis H_i can then be written as

$$P(\theta_i|X, H_i) = \frac{P(X|\theta_i, H_i)P(\theta_i|, H_i)}{\int_{\Theta_i} P(X|\theta_i, H_i)P(\theta_i|, H_i)d\theta_i}. \quad (14.7)$$

If one is interested in the posterior probability of a subset of θ_i , say θ_i^* , the other parameters can be marginalized as follows:

$$P(\theta_i^*|X, H_i) = \int_{\Theta'_i} P(X|\theta'_i, \theta_i^*, H_i)P(\theta'_i|\theta_i^*, H_i)d\theta'_i, \quad (14.8)$$

with θ'_i the complement of θ_i^* and Θ'_i the subspace of Θ defined by the dimensions of θ'_i .

14.2.2 Count experiments

Let there be a count experiment at a particle collider. In our null hypothesis, H_0 , the SM is the True State of Nature (TSN). Under this hypothesis, the expected number of events is denoted as μ . In the alternative hypothesis, the SM production processes are joined by an unknown additional production process that causes an excess of events. with respect to the SM expectations The expected number of events under H_1 is denoted as $\mu + s$, where s is the expected excess. Events that originate from SM processes are referred to as background events and events originating from new phenomena are referred to as signal events.

Both hypotheses assume that the number of observed events N follows a Poisson distribution and we may write the likelihood for μ and s as

$$P(N|s, \mu) = \frac{(\mu + s)^N e^{-(\mu+s)}}{N!}, \quad (14.9)$$

with $\mu \geq 0$ and with s equal to zero under H_0 and at least zero under the alternative hypothesis H_1 .

We adopt equal prior probabilities for H_0 and H_1 and thus obtain the posterior probability for H_1 as written in Equation 14.5. The Bayes factor in this equation is worked out in this section, by making use of Equation 14.6 to write $P(N|H_0)$ and $P(N|H_1)$ as

$$P(N|H_0) = \int_0^{+\infty} \frac{(\mu)^N e^{-\mu}}{N!} P(\mu) d\mu. \quad (14.10)$$

$$P(N|H_1) = \int_0^{+\infty} \int_0^{+\infty} \frac{(\mu + s)^N e^{-(\mu+s)}}{N!} P(\mu, s) d\mu ds. \quad (14.11)$$

In the latter equation, the prior for μ and s , $P(\mu, s)$ is decomposed as follows

$$P(\mu, s) = P(s|\mu)P(\mu), \quad (14.12)$$

and the prior for μ , $P(\mu)$, and the conditional prior for s , $P(s|\mu)$, are derived in the following 2 paragraphs.

Prior probability for the expected background

For μ , we assume that an external estimate $\hat{\mu}$ is available with uncertainty $\delta\hat{\mu}$. Defining $b = \hat{\mu}/\delta\hat{\mu}^2$ and $Y = b\hat{\mu}$, we may adopt the proper and evidence-based prior for μ suggested in [126]:

$$\begin{aligned} P(\mu) &= \frac{(b\mu)^Y e^{-b\mu} \pi^0(\mu)}{\int_0^{+\infty} (b\mu)^Y e^{-b\mu} \pi^0(\mu) d\mu}, \\ &= \frac{b(b\mu)^{(Y-1/2)} e^{-b\mu}}{\Gamma(Y + 1/2)} \end{aligned} \quad (14.13)$$

with $\Gamma(x)$ the Gamma function and $\pi^0(\mu) = 1/\sqrt{\mu}$ as initial prior for μ , which is, for this case, both the reference and Jeffrey's prior [126]. Figure 14.1 shows $P(\mu)$ for an estimate $\hat{\mu} = 16$ and for different values for the uncertainty $\delta\hat{\mu}$. It is clear how the influence of the initial prior for μ decreases with smaller uncertainties on the prediction $\hat{\mu}$.

The motivation for this prior is easily understood. For instance, the estimate $\hat{\mu}$ may be based on the observation of Y events in a MC simulation of the count experiment under H_0 . If b is the ratio of the simulated integrated luminosity to the actual integrated luminosity for the count experiment, it follows that $Y = b\hat{\mu}$. If we neglect any uncertainty on b , the expected number of events in the MC simulation is $b\mu$ and its probability density is written as follows:

$$P(b\mu|Y) = \text{Poisson}(Y; b\mu) \pi^0(\mu) / b / p(Y) = P(\mu), \quad (14.14)$$

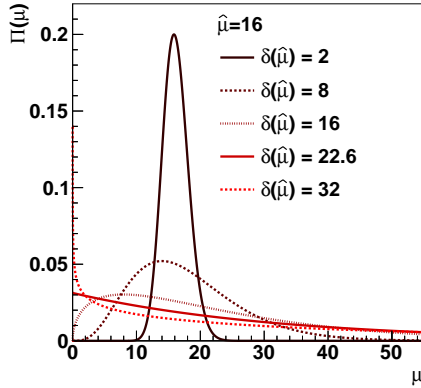


Figure 14.1 – The prior for μ as defined in equation 14.13, for an estimate $\hat{\mu} = 16$ and several values for its uncertainty, $\delta\hat{\mu}$.

The statistical uncertainty on Y is \sqrt{Y} and thus the statistical uncertainty on $\hat{\mu}$ is $\sqrt{Y}/b = \delta\hat{\mu}$, from which follows that $b = \hat{\mu}/\delta\hat{\mu}^2$. This approach covers in principle only the statistical uncertainties of the estimate. However, other uncertainties can be included approximately by incorporating them in $\delta\hat{\mu}$ and thus scaling up b . This approach can in fact serve to derive meaningful priors from almost any kind of estimate for μ .

Prior probability for the expected signal

The prior for s is an important element of our approach, encoding our prior belief about potential signal strength in the count experiment. Since we have in fact very little prior knowledge about this strength, we want to be as objective as possible, making no additional assumptions on the potential new physics. Therefore, we adopt as initial prior for s the reference prior, which for this case is Jeffrey’s prior $\pi^0(s|\mu) = 1/\sqrt{s + \mu}$. Reference priors are constructed such that on average the data have maximum influence on the posterior.

However, for s , a proper prior is required. Therefore, a small fraction of the data are sacrificed, and not considered for the final interpretation. Instead it is used to construct from the initial reference prior a proper prior. We define a parameter f , the ratio of the sacrificed data to the data used for the final interpretation. With N_f the number of events observed in the fraction f we construct following posterior for

s which will serve as a prior for the final interpretation:

$$\begin{aligned}
 P(s|\mu) &= \frac{f^{N_f}(\mu + s)^{N_f} e^{-f(\mu+s)} \pi^0(s|\mu)}{\int_0^{+\infty} f^{N_f}(\mu + s)^{N_f} e^{-f(\mu+s)} \pi^0(s|\mu) ds} \\
 &= \frac{f(f\mu + fs)^{N_f-1/2} e^{-f(\mu+s)}}{\Gamma(N_f + 1/2, f\mu)}.
 \end{aligned}
 \tag{14.15}$$

Figure 14.2 shows this prior for s , under the condition $\mu = 16$. We choose $f = 0.1$ and show the prior for different values of N_f . The figure shows clearly how the influence of the initial prior decreases with an increasing number of observed events.

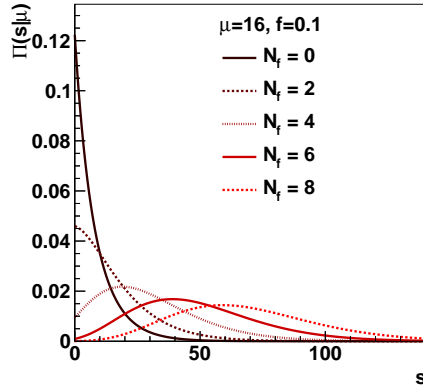


Figure 14.2 – The prior for s as defined in equation 14.15, under the condition $\mu = 16$. The fraction f is set to 0.1 and the prior is shown for different values for N_f .

Posterior probabilities for the tested hypotheses

After substitution of the prior for μ defined in Equation 14.1 and the prior for s in Equation 14.1 in the likelihood for μ and s in Equation 14.9, we may derive $P(N|H_0)$ and $P(N|H_1)$, the ingredients of the Bayes factor B_{10} . The derivations are detailed in Appendix A. For $P(N|H_0)$ we obtain

$$\begin{aligned}
 P(N|H_0) &= \int_0^{+\infty} P(N|\mu, H_0) P(\mu) d\mu, \\
 &= \frac{1}{N!} \frac{b^{Y+1/2}}{\Gamma(Y+1/2)} \frac{\Gamma(N+Y+1/2)}{(1+b)^{N+Y+1/2}},
 \end{aligned}
 \tag{14.16}$$

and for $P(N|H_1)$ we obtain

$$\begin{aligned}
 P(N|H_1) &= \int_0^{+\infty} P(N|\mu, s)P(s|\mu)P(\mu)d\mu, \\
 &= \frac{1}{N!} \frac{b^{Y+1/2}}{\Gamma(Y+1/2)} \\
 &\quad \times \int_0^\infty \frac{\Gamma(N+N_f+1/2, (1+f)\mu)}{(1+f)^{N+N_f+1/2}} \frac{f^{N_f+1/2}}{\Gamma(N_f+1/2, f\mu)} \mu^{Y-1/2} e^{-b\mu} d\mu,
 \end{aligned} \tag{14.17}$$

with $\Gamma(x, y)$ the incomplete Gamma function. The integration in the latter equation is easily derived with numerical methods as for instance explained in Appendix A.

Figure 14.3 shows $P(N, H_0)$ and $P(N|H_1)$, given an estimate $\hat{\mu} = 16$ for μ . For H_0 , the probability density is shown for different values for the uncertainty $\delta\hat{\mu}$. For H_1 , we show the probability density for $\delta\hat{\mu} = 8$ and $f = 0.1$ and several values for N_f .

With all the ingredients of the Bayes factor defined, we can derive the posterior probability of H_1 , $p(H_1, N)$, in Equation 14.5. Figure 14.4 shows this probability as a function of the observed counts N , given an estimate $\hat{\mu} = 16$ for μ . On the left, the posterior probability is shown for $N_f = 2$, $f = 0.1$ and several values for the uncertainty $\delta\hat{\mu}$ on $\hat{\mu}$. On the right, the posterior probability is shown for $\delta\hat{\mu} = 8$, $f = 0.1$ and several values for N_f . From the left figure it follows that for count experiments with too large uncertainties on $\hat{\mu}$, the posterior probability for H_1 never reaches the value 1. From the right figure it follows that a larger number of observed events in the data fraction f results in a steeper “turn-on” of $P(H_1|N)$ that starts off at higher values for N .

Posterior probability for the expected signal s

The next important element in the interpretation of a count experiment is the posterior probability of s :

$$P(s|N, H_1) = \frac{\int_0^{+\infty} P(N|s, \mu)P(s|\mu)P(\mu)d\mu}{P(N|H_1)} \tag{14.18}$$

All elements of this posterior were defined earlier: The likelihood $P(N|s, \mu)$ is defined in Equation 14.9; the priors for μ and s are defined in Equations 14.13 and 14.15 respectively; the likelihood $P(N|H_1)$ has been worked out in equation 14.17. Substitution

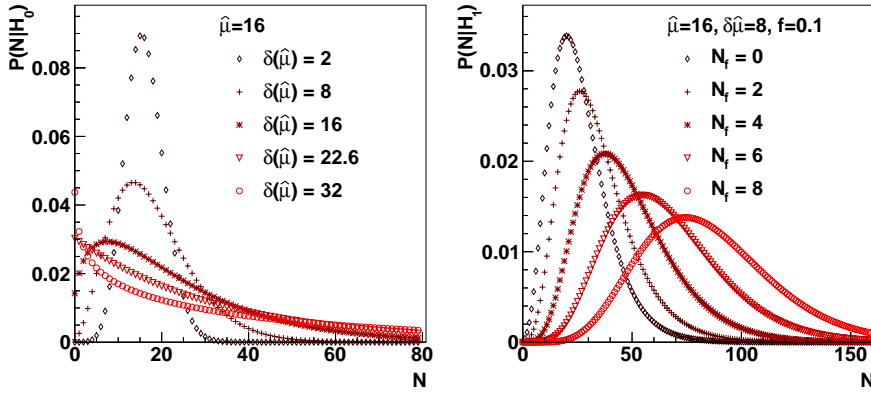


Figure 14.3 – The probability densities $P(N|H_0)$ (left) and $P(N|H_1)$ (right), defined respectively in Equations 14.16 and 14.17. The probability densities are shown for an estimate $\hat{\mu} = 16$ for μ . For H_0 , the probability density is shown for different values for the uncertainty $\delta\hat{\mu}$. For H_1 , we show the probability density for $\delta\hat{\mu} = 8$ and $f = 0.1$ and several values for N_f .

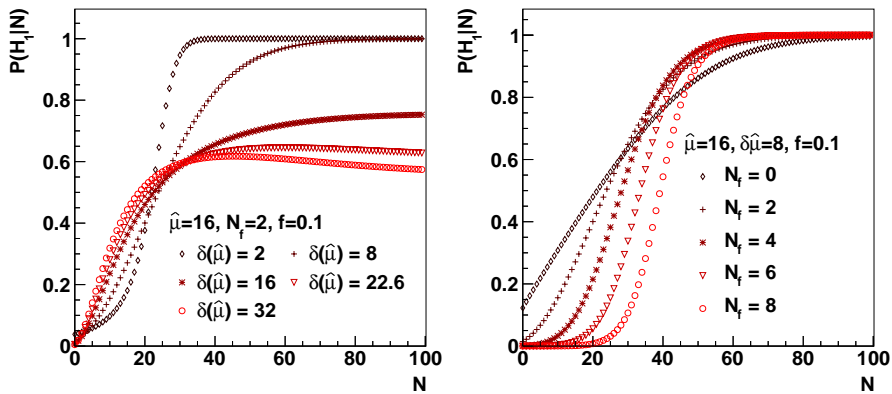


Figure 14.4 – Posterior probability for the hypothesis H_1 , given an estimate $\hat{\mu} = 16$ for μ . On the left, the posterior probability is shown for $N_f = 2$, $f = 0.1$ and several values for the uncertainty $\delta\hat{\mu}$ on $\hat{\mu}$. On the right, the posterior probability is shown for $\delta\hat{\mu} = 8$, $f = 0.1$ and several values for N_f .

of all these elements results in:

$$P(s|N, H_1) = \frac{1}{P(N|H_1)} \times \int_0^{+\infty} \frac{(\mu + s)^N e^{-(\mu+s)}}{N!} \frac{f(f\mu + fs)^{N_f-1/2} e^{-f(\mu+s)}}{\Gamma(N_f + 1/2, f\mu)} \frac{b(b\mu)^{(Y-1/2)} e^{-b\mu}}{\Gamma(Y + 1/2)} d\mu. \quad (14.19)$$

The integral over μ is easily derived numerically as for instance explained in Appendix A.

Posterior probability densities for parameters of new physics models

The previous paragraphs dealt with the question whether or not there is a source of events, other than the SM sources, that contributes to a certain count experiment, and, what the strength of such source might be. Apart from its additive character, no assumption were made on the properties of this *generic* new physics source of events. In this section, we will make the further assumption that the TSN is within the parameter space of a certain new physics model with free parameters and explain how a count experiment may provide us with information about these parameters.

Denote the parameter space of the given physics model with Θ and a single point in the parameter space with θ . The hypothesis that the TSN lays within Θ is denoted with H_{NP} . As before, we assume that the number of observed events under H_{NP} follows a Poisson distribution with expected value $\mu + s$, with s depending on θ .

Usually, given a certain θ , s is predicted with finite precision, e.g. based on Monte Carlo simulation. Let there be such prediction \hat{s}^θ with uncertainty $\delta\hat{s}^\theta$ and define $b^\theta = \hat{s}^\theta / \delta\hat{s}^{\theta 2}$ and $Z^\theta = b^\theta \hat{s}^\theta$. The relation between s and θ can then be described with following prior for s :

$$\begin{aligned} P(s|\theta) &= \frac{(b^\theta s)^{(Z^\theta)} e^{-b^\theta s} \pi^0(s)}{\int_0^{+\infty} (b^\theta s)^{(Z^\theta)} e^{-b^\theta s} \pi^0(s) ds}, \\ &= \frac{b^\theta (b^\theta s)^{(Z^\theta-1/2)} e^{-b^\theta s}}{\Gamma(Z^\theta + 1/2)}. \end{aligned} \quad (14.20)$$

As initial prior for s we choose to use $\pi^0(s) = 1/\sqrt{s}$, which for this case, is both the reference prior and Jeffrey's prior. The motivation for choosing this prior is equal to the motivation given for the prior for μ in Equation 14.13.

With this prior we can derive the likelihood for θ as a function of the outcome of the

count experiment:

$$\begin{aligned}
 P(N|\theta, H_{\text{NP}}) &= \int_0^{+\infty} \int_0^{+\infty} \frac{(\mu + s)^N e^{-\mu+s}}{N!} P(s|\theta) P(\mu) ds d\mu \\
 &= \frac{1}{N!} \frac{(b^\theta)^{(Z^\theta+1/2)}}{\Gamma(Z^\theta + 1/2)} \frac{b^{Y+1/2}}{\Gamma(Y + 1/2)} \\
 &\quad \times \sum_{n=0}^{n=N} \left[\binom{N}{n} \frac{\Gamma(N + Z^\theta - n + 1/2)}{(1 + b^\theta)^{N+Z^\theta-n+1/2}} \frac{\Gamma(n + Y + 1/2)}{(1 + b)^{n+Y+1/2}} \right],
 \end{aligned} \tag{14.21}$$

with as probability density for μ the prior defined in Equation 14.13. The derivation of $P(N|\theta, H_{\text{NP}})$ is worked out in detail in Appendix A, where also an exact and relatively efficient method is suggested for the sum over n in this equation.

Finally, the posterior probability for θ becomes

$$p(\theta|N, H_{\text{NP}}) = P(N|\theta, H_{\text{NP}})p(\theta) \tag{14.22}$$

with $p(\theta)$ a prior for θ . Section 14.5 will explain how a prior of θ can be constructed from theoretical assumptions and previous measurements.

14.3 Bayesian optimization

14.3.1 General formulation

We suggest two approaches to the optimization of searches. The first one is based on the expected value of a certain evidence measure $e(X)$ under the assumption of a specific new physics model H_{NP} :

$$E(e(X)|H_{\text{NP}}) = \int e(X')P(X'|H_{\text{NP}})dX', \tag{14.23}$$

where the integration runs over all possible outcomes X' of the experiment. To emphasize that this equation makes use of random data only, we introduce the notation X' .

The second approach is based on the probability that the evidence measure $e(X)$ is above a certain threshold e^* :

$$P(e(X) > e^*|H_{\text{NP}}) = \int H(e(X') - e^*)P(X'|H_{\text{NP}})dX' \tag{14.24}$$

with H the Heaviside step function.

We suggest to define the measure of evidence adopting a Bayesian approach. Therefore a null hypothesis H_0 and a new physics hypothesis H_1 is defined. We give both

hypotheses equal prior probability and define our measure of evidence for new physics as the posterior probability of H_1 in Equation 14.5. H_1 may or may not equal H_{NP} , the earlier mentioned specific new physics model.

The introduction of two separate new physics hypotheses may seem artificial and slightly confusing. However, this approach has some important advantages. Using a specific new physics model for H_{NP} allows, as we will show furtheron, to introduce prior information, originating from previous measurements, theory and cosmology, and to let this guide the design of searches. However, often it is preferred to maintain an “inclusive” attitude in the interpretation, an attitude as independent from any new physics model as possible. It is for this purpose that we introduce a new physics hypothesis with minimal assumptions, H_1 , to define, together with the null hypothesis H_0 , the evidence. For instance, the new physics hypothesis H_1 , introduced in Section 14.2.2 in the context of a count experiment has as only assumption that potential new physics sources of events work purely additive with respect to the SM sources.

If the new physics model in the hypothesis H_{NP} has free parameters, we may write the probability density for X , $P(X|H_{\text{NP}})$, in Equation 14.23 as

$$P(X|H_{\text{NP}}) = \int_{\Theta} P(X|\theta, H_{\text{NP}})P(\theta|H_{\text{NP}})d\theta, \quad (14.25)$$

where θ again denotes a point in the parameter space Θ of the new physics model, and $P(\theta|H_{\text{NP}})$ is the prior for θ . The prior for θ is the essential ingredient to this optimization method, holding all available information about the given new physics model of both theoretical and experimental origin, steering the optimization, by taking into account all available constraints for the given new physics model.

14.3.2 Count experiments

To optimize a count experiment, all essential ingredients are in fact already in place. The integral in the definition of the expected evidence in Equation 14.23 becomes a sum over the observed number of events N . The first factor within this summation, $P(H_1|N)$, can be derived as described in detail in Section 14.2.2. The second factor, $P(N|H_{\text{NP}})$ is obtained by marginalizing the likelihood for θ defined Equation 14.21 over θ :

$$P(N|H_{\text{NP}}) = \int_{\Theta} P(N|\theta)P(\theta)d\theta. \quad (14.26)$$

Exact integration over θ is usually not possible and an approximate method is outlined in Section 14.5.

14.4 Combination of count experiments

Conceptually, generalizing this interpretation and optimization approach to combinations of statistically independent count experiments is straightforward. Let there be m statistically independent count experiments and let N_j , $j = 1, \dots, m$ be the observed numbers of events in each of these experiments. The probability for observing a certain set of counts N_1, \dots, N_m is then given by the product of the probabilities to observe the individual counts:

$$P(N_1, \dots, N_m | \mu_1, \dots, \mu_m, s_1, \dots, s_m) = \prod_{j=1}^{j=m} \frac{(\mu_j + s_j)^{N_j} e^{-(\mu_j + s_j)}}{N_j!}, \quad (14.27)$$

with μ_i and s_i the expected number of background and signal events. We define H_0 as the hypothesis that all s_i are equal to zero and H_1 as the hypothesis that all s_i are at least zero. It follows that for the probability densities $P(N_1, \dots, N_m | H_0)$ and $P(N_1, \dots, N_m | H_1)$ the following relations hold:

$$P(N_1, \dots, N_m | H_0) = \prod_{j=1}^{j=m} P(N_j | H_0), \quad (14.28)$$

$$P(N_1, \dots, N_m | H_1) = \prod_{j=1}^{j=m} P(N_j | H_1), \quad (14.29)$$

and thus for the Bayes factor:

$$B_{10}(N_1, \dots, N_m) = \prod_{j=1}^{j=m} B_{10}^j(N_j). \quad (14.30)$$

With these relations, all ingredients to derive the posterior probability of H_1 , our measure of evidence for new physics, is in place.

Similarly, the likelihood function for θ in a multiple count experiment is

$$P(N_1, \dots, N_m | \theta, H_{\text{NP}}) = \prod_{j=1}^{j=m} P(N_j | \theta, H_{\text{NP}}) \quad (14.31)$$

with $P(N_j | \theta, H_{\text{NP}})$ the likelihood function for θ in a single count experiment, as defined in Equation 14.21.

With the posterior probability for H_1 , $P(N | H_1)$, and the probability density for N under H_{NP} , $P(N, H_{\text{NP}})$, defined, the ingredients for the optimization of multiple count experiments are in place as well.

14.5 Integration over the parameter space

The prior probability density of θ , $p(\theta|H_{\text{NP}})$, is a crucial ingredient to our method. This function contains all available prior information, both of theoretical and experimental origin, concerning the new physics model of interest. It steers the optimization, assigning more weight to regions that are more favored by the prior information.

Adopting the notation \mathcal{X} for data from previous measurements, the prior $p(\theta|H_{\text{NP}})$ may be written as

$$p(\theta|H_{\text{NP}}) \equiv p(\theta|\mathcal{X}, H_{\text{NP}}) \propto \prod_{i=1}^{i=u} p(\mathcal{X}_i|\theta, H_{\text{NP}})p^0(\theta|H_{\text{NP}}), \quad (14.32)$$

where $p(\mathcal{X}_i|\theta)$ are u likelihoods that incorporate the information gained from each previous measurement or theoretical assumption i and $p^0(\theta)$ is the initial prior. This initial prior encodes our assumptions about the parameter space at the beginning of the inference chain. The simplest and most popular choice for $p^0(\theta)$ is a flat prior, where $p^0(\theta) = 1$. However, there exist better founded choices such as reference priors [126] [127], which are, unfortunately, often prohibitively complicated.

An exact calculation of the integral in Equation 14.25 would be extremely difficult. Instead, one can use the Markov Chain Monte Carlo (MCMC) technique to sample over the parameter space Θ from the probabilities $p^t(\theta|H_{\text{NP}})$, where t likelihoods are used out of a total of u to compute $p^t(\theta|H_{\text{NP}})$,

$$p^t(\theta|H_{\text{NP}}) = \prod_{i=1}^{i=t} p(\mathcal{X}_i|\theta, H_{\text{NP}})p^0(\theta|H_{\text{NP}}). \quad (14.33)$$

After having sampled M points from $p^t(\theta|H_{\text{NP}})$, we can approximate the integration of a function $f(\theta)$ over the parameter space Θ with a sum as follows:

$$\int_{\Theta} f(\theta)p(\theta|H_{\text{NP}})d\theta \approx \sum_{j=1}^{j=M} [f(\theta_j)p^{u-t}(\theta_j)], \quad (14.34)$$

with

$$p^{u-t}(\theta) = \prod_{i=t+1}^{i=u} p(\mathcal{X}_i|\theta, H_{\text{NP}}). \quad (14.35)$$

For instance, Equation 14.25 for $p(X|H_{\text{NP}})$ becomes:

$$p(X|H_{\text{NP}}) \approx \sum_{j=1}^{j=M} [p(X|\theta_j, H_{\text{NP}})p^{u-t}(\theta_j)]. \quad (14.36)$$

Because the sum over j is finite, it is always possible to properly normalize $p(X|H_{\text{NP}})$. The exact form of the likelihoods $p(\mathcal{X}_i|\theta, H_{\text{NP}})$ depends on the origin of the data and the particular new physics model.

14.6 Summarizing example

A summarizing example is shown in Figure 14.5 and brings together the main ingredients for the hypothesis testing and optimization of count experiments. A hypothetical single count experiment is defined with a background estimate $\hat{\mu} \pm \delta\hat{\mu} = 16 \pm 2$. A fraction $f = 0.1$ of the data are used in which $N_f = 2$ events were observed, to define the prior for s with Equation 14.15. As such, the probability densities $P(N|H_0)$ and $P(N|H_1)$ in Equations 14.16 and 14.17 are defined and so is the Bayes factor. Choosing $P(H_0) = P(H_1) = 0.5$ as prior probabilities for H_0 and H_1 also defines the suggested measure of evidence, the posterior probability for H_1 in Equation 14.5. The latter is shown in red as a function of the observed counts N .

In black is the probability to observe N events as a function of N under a fictive new physics hypothesis H_{NP} . 3 points are sampled from the likelihood $p^t(\theta|H_{\text{NP}})$ in Equation 14.33: $(\hat{s}^\theta \pm \delta\hat{s}^\theta, p^{u-t}(\theta)) = (4 \pm 0.9, 0.25)$, $(30 \pm 1.7, 0.1)$, $(60 \pm 1.7, 0.2)$ with the likelihood $p^{u-t}(\theta)$ as defined in Equation 14.35 and the estimates for the signal strength $s^\theta \pm \delta s^\theta$ obtained from MC. $P(N|H_{\text{NP}})$ is then derived as in Equation 14.36. With $P(N|H_{\text{NP}})$ and B_{10} fully defined for this fictive experiment, calculating the optimization variables from Section 14.3 is straightforward.

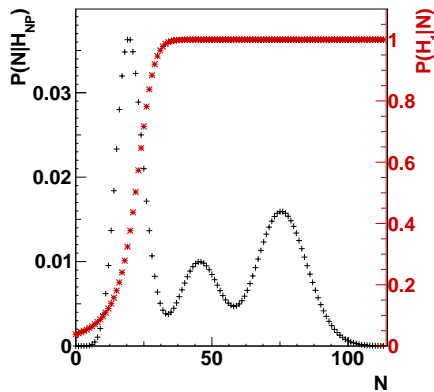


Figure 14.5 – A summarizing example, illustrating the main features of the presented approach for the interpretation and optimization of count experiments. See text for more information.

15

The phenomenological MSSM

The phenomenological MSSM (pMSSM) [23] is a 19-dimensional realization of the Minimal Supersymmetric extension of the Standard Model (MSSM) [14]. In the next chapters, we make use of this model to interpret a search and to attempt the optimization of a search. Therefore, this chapter provides a brief introduction to the pMSSM and explains how we constrain this model based on previous measurements.

In the pMSSM, the MSSM's assumptions of a minimal gauge group, minimal particle content, R-parity conservation and soft SUSY breaking are joined with three additional assumptions:

- There are no sources of CP-violation other than the SM sources,
- There are no flavor changing neutral currents,
- Universality of first and second generation sfermions: the sfermion masses of the first and the second generation are degenerate.

In addition we will require that the lightest neutralino is the Lightest Supersymmetric Particle (LSP). These assumptions, based on stringent experimental constraints, reduce the number of free parameters, not related to the SM, from 105 in the MSSM to the following 19 parameters in the pMSSM:

- The ratio of the vacuum expectation values of the Higgs doublet fields, $\tan \beta$,

- the mass of the pseudo-scalar Higgs boson, M_A ,
- the Higgs-higgsino mass parameter, μ ,
- the bino, wino and gluino mass parameters, M_1 , M_2 , and M_3 ,
- the masses of sfermions of the first and second generation,
 $m_{\tilde{q}}, m_{\tilde{u}_R}, m_{\tilde{d}_R}, m_{\tilde{l}}, m_{\tilde{e}_R}$,
- the masses of the sfermions of the third generation,
 $m_{\tilde{Q}}, m_{\tilde{t}_R}, m_{\tilde{b}_R}, m_{\tilde{L}}, m_{\tilde{\tau}_R}$,
- third generation trilinear couplings, A_t , A_b and A_τ ,

where we adopted the notation from [23].

We will show that this well-motivated reduction of dimensionality enables a detailed study of the impact of LHC and other experimental results on the pMSSM. It is important to note that the pMSSM imposes no correlations between the sparticle masses, leading to a fairly general model with a rich phenomenology. Therefore, also the conclusions that are drawn with the help of the pMSSM can be considered as fairly general.

15.1 Impact from existing measurements

We evaluate the impact from previous measurements, based on the strategy developed in [120]. The chain of inference starts with a flat prior on the parameter space of the pMSSM. Then, information from previous measurements is taken into account making use of Equation 14.32. Two classes of measurements are used, namely, pre-LHC measurements (PLMs), and CMS measurements. The former will constitute the product of likelihoods in Equation 14.33 from which a large number of parameter points is sampled with an MCMC technique. This allows for an effective sampling from the 19-dimensional parameter space of the pMSSM. Then, information from CMS measurements is included. These will constitute the product of likelihoods in Equation 14.35 that weight the sampled points in the sum in Equation 14.34. The considered pre-LHC measurements and their likelihoods are explained in Section 15.1.1 and the CMS measurements and their likelihoods are explained in Section 15.1.2.

15.1.1 Pre-LHC measurements and likelihoods

In the calculation of the likelihood for pre-LHC measurements $p(\text{PLM}|\theta)$, we include the experimental information for the muon anomalous magnetic moment, the branching ratio $b \rightarrow s\gamma$, the branching ratio $B_s \rightarrow \mu\mu$, the ratio of SUSY and SM branching ratios for $B_u \rightarrow \tau\nu$, the top mass, the bottom mass, the strong coupling constant at the Z -mass, and Higgs and SUSY mass limits from LEP and the Tevatron. Table 15.1 lists the pre-LHC measurements with the latest values taken from the PDG [20], and the mathematical forms of the likelihoods constructed for each of the observables.

For observables for which there exists a central value and a symmetric error, a Gaussian likelihood is used. If we denote the experimental value of an observable as x_0 , the uncertainty on this measurement as σ_x and the prediction for the observable given the parameters of the model as x , the likelihood has the form

$$\mathcal{L}_{\text{Gauss}} = \exp\left(-\frac{(x - x_0)^2}{2\sigma_x^2}\right). \quad (15.1)$$

If the measurement quotes different positive and negative errors σ_{x+}^2 and σ_{x-}^2 , we use a two-sided Gaussian, which can be expressed as

$$\mathcal{L}_{\text{AsymGauss}} = \begin{cases} \exp\left(-\frac{(x-x_0)^2}{2\sigma_{x-}^2}\right), & \text{if } x < x_0 \\ \exp\left(-\frac{(x-x_0)^2}{2\sigma_{x+}^2}\right), & \text{if } x \geq x_0 \end{cases}. \quad (15.2)$$

In the case of the muon anomalous magnetic moment, there exist two measurements $x^{(1)} \pm \sigma_{x^{(1)}}$ and $x^{(2)} \pm \sigma_{x^{(2)}}$, so we combine them using a weighted Gaussian as follows

$$\begin{aligned} & \mathcal{L}_{\text{WeightedGauss}} \\ &= \exp\left(-\frac{\sigma_{x^{(1)}}^2}{\sigma_{x^{(1)}}^2 + \sigma_{x^{(2)}}^2} \frac{(x - x_0^{(1)})^2}{2\sigma_{x^{(2)}}^2} - \frac{\sigma_{x^{(2)}}^2}{\sigma_{x^{(1)}}^2 + \sigma_{x^{(2)}}^2} \frac{(x - x_0^{(2)})^2}{2\sigma_{x^{(1)}}^2}\right). \end{aligned} \quad (15.3)$$

In case the results quote a 95% exclusion upper limit x_0 for an observable, the likelihood takes the form

$$\mathcal{L}_{\text{UL}} = \frac{1}{1 + \exp\left(\frac{x-x_0}{\Delta x}\right)}, \quad (15.4)$$

where Δx is taken to be 1% of the value of the upper limit to mimic the 95% exclusion limit.

To compute the expected value for the observables for each of the pMSSM points, following tools are used: `SoftSUSY`[132] to calculate the SUSY spectrum, `SuperIso`[133] for the low-energy constraints, `micrOMEGAs`[134] for the SUSY mass limits. For the limits on the Higgs mass, `HiggsBounds`[135] is used.

Table 15.1 – List of pre-LHC measurements (PLMs) contributing to the likelihood $p(\text{PLM}|\theta)$ and the mathematical forms of their individual likelihoods. The measurements are taken from PDG 2011 [20].

i	Observable	Limit	Likelihood function
1	Δa_μ	$(28.7 \pm 8.0) \times 10^{-10} [e^+e^-]$ $(19.5 \pm 8.3) \times 10^{-10} [\text{taus}]$	Weighted Gaussian average
2	$BR(b \rightarrow s\gamma)$	$(3.55 \pm 0.34) \times 10^{-4}$	Gaussian
3	$BR(B_s \rightarrow \mu\mu)$	$\leq 4.7 \times 10^{-8}$	Upper limit
4	$R(B_u \rightarrow \tau\nu)$	1.66 ± 0.54	Gaussian
5	m_t	173 ± 1.1	Gaussian
6	$m_b(m_b)$	$4.19^{+0.18}_{-0.06}$	Two-sided Gaussian
7	$\alpha_s(M_Z)$	0.117 ± 0.002	Gaussian
8	m_h	LEP & Tevatron (HiggsBounds)	$L_8 = 1$ if allowed. $L_8 = 10^{-9}$ if m'_h sampled from $Gauss(m_h, 1.5)$ is excluded
9	SUSY mass	LEP & Tevatron (micrOMEGAs)	$L_9 = 1$ if allowed $L_9 = 10^{-9}$ if excluded

15.1.2 CMS measurements and likelihoods

CMS has performed searches for SUSY-like final states using the 2010 and 2011 data, which already allows us to make scientifically interesting statements about the pMSSM. The full likelihood functions are not available for these analyses. However, given that they are all cut-and-count analyses, we can use the likelihood from Equation 14.21 for each of the search regions in these analyses. The parameters $b^\theta = \hat{s}^\theta / \delta \hat{s}^{\theta^2}$ and $Z^\theta = b^\theta \hat{s}^\theta$ in these likelihoods are obtained for each point in parameter space from MC simulation of the count experiment under the corresponding new physics hypothesis, generated as explained in Section 16.3. The parameters $b = \hat{\mu} / \delta \hat{\mu}^2$ and $Y = b \hat{\mu}$ are derived from the published background estimates $\hat{\mu} \pm \delta \hat{\mu}$ for each of the search regions. As explained in Section 14.4, statistically independent count experiments can easily be combined, and thus, we choose the considered set of experiments such that they all are independent from each other.

We take into account the eight search regions in the “hadronic sample” of the CMS α_T analysis in 1.1 fb^{-1} of the 2011 data [55]. These search regions are statistically independent bins, in the H_T distribution of the selected sample. Table 15.2 lists for each of the bins the observed number of events N , and the corresponding estimates for the expected number of SM events, $\hat{\mu} \pm \delta \hat{\mu}$. The listed uncertainties $\delta \hat{\mu}$ are combined statistical and systematic uncertainties. The analysis quotes asymmetric uncertainties and we use the average of the two sides to determine $\delta \hat{\mu}$.

Table 15.2 – Results of the CMS α_T analysis in 1.1 fb^{-1} of the 2011 data [55] used to constrain the pMSSM. For each of the H_T bins in the “hadronic sample” of this analysis the number of observed events N are listed with the SM prediction $\hat{\mu} \pm \delta\hat{\mu}$.

H_T -bin	N	$\hat{\mu}$	$\delta\hat{\mu}$
275-325	782	787	27
325-375	321	310	10
375-475	196	202	9
475-575	62	60.4	3.6
575-675	21	20.3	1.5
675-775	6	7.7	0.7
775-875	3	3.2	0.3
> 875	1	2.8	0.3

16

Search with jets, b -jets and E_T^{miss}

This chapter demonstrates and discusses the use of the Bayesian tools for interpretation, developed in Chapter 14. For that purpose, we first perform a series of count experiments. Then, we interpret the observations in the model-independent manner and verify whether or not they indicate the presence of a new physics source of events and how they constraint the potential strength of such a source. Finally we interpret the observations within the pMSSM, combining them with the pre-LHC measurements and the α_T measurement, as explained in Sections 15.1.1 and 15.1.2.

To highlight all aspects of these interpretation tools, we perform a new search, designed for this very purpose. First of all, we want to demonstrate how combining measurements of different origins benefits to the interpretation. Therefore, we design the new search such that, with respect to the pre-LHC and α_T measurements, we expect complementary information about the pMSSM. More specifically, we design a search that is expected to be sensitive to new physics scenarios with an enhanced production of b -quarks. To enable the combination of the new search with the α_T measurement, we ensure that both measurements are independent by applying the new search on a data set that is not used by the α_T measurement. To emphasize the ease by which the results of many count experiments are interpreted simultaneously, the new search consists of a relatively large number of independent search regions.

The new search studies proton-proton collisions at a center of mass energy of $\sqrt{s} = 7$ TeV, in a data set corresponding to an integrated luminosity of 3.27 fb^{-1} . The desired sensitivity to new physics scenarios with an enhanced production of b -quarks is obtained by selecting events with abundant missing transverse energy, several highly energetic jets and at least one b -jet. The event selection and object definition are based on an existing CMS search [136].

Since the main purpose of this new search is the illustration and validation of the Bayesian interpretation tools, we take a somewhat simplified approach to predict the number of SM and signal events in the search regions. Predictions are obtained directly from Monte Carlo simulation, without explicitly evaluating the performance of the simulation. The only systematic uncertainties taken into account are the uncertainties related to the limited size of the Monte Carlo samples. For that reason, the actual results of the interpretation should be considered cautiously, being rather qualitative.

16.1 Data samples

We study data from proton-proton collisions with a center of mass energy of $\sqrt{s} = 7$ TeV, collected by CMS during the 2011 runs. The data set paths and run ranges of the data used for this analysis are listed in Table 16.1 together with the integrated luminosity per data set. The total integrated luminosity is also listed and amounts 3.27 fb^{-1} . Part of the 2011 data collected by CMS are not used by this measurement and not listed: the first 1.1 fb^{-1} of data collected in 2011 are not included because they were used by the α_T measurement, from which our measurement must be independent; another 0.24 fb^{-1} of data in the run range 160404-177515 are not included as they are used to “train” our Bayesian interpretation, as will be explained in Section 16.6; the last few hundred pb^{-1} of data collected in 2011 are not included since they were not processed in time for this analysis.

The considered data are collected with combined H_T and H_T^{miss} triggers. These triggers fire if the online reconstructed H_T , defined in Equation 6.2, and the online reconstructed H_T^{miss} , the magnitude of the vectorial sum of the jet momenta, are above certain thresholds. The threshold values have changed over time, due to the rising instantaneous luminosity and the limited band width. Table 16.1 lists the trigger paths, from which the threshold values for H_T and H_T^{miss} can be read, versus the run range in which they were applied. None of the used triggers was prescaled at the time of use.

Table 16.1 – Recorded proton-proton collision data at $\sqrt{s} = 7$ TeV used in the analysis. Listed are the data set paths, the run ranges and the integrated luminosity for each data set, together with the total integrated luminosity.

data set	run range	$\int d\mathcal{L}$ (fb $^{-1}$)
/HT/Run2011A-05Aug2011-v1/AOD	170053-172619	0.373
/HT/Run2011A-PromptReco-v6/AOD	172620-175770	0.655
/HT/Run2011B-PromptReco-v1/AOD	175832-180252	2.241
total		3.270

16.2 Standard Model predictions

The SM predictions used for this search are derived from MC simulation. We make use of samples that are centrally produced by the CMS collaboration during the **Summer11** campaign [137]. The simulation includes the hard interaction, showering, hadronization underlying event and pile-up. Also the CMS detector is included in the simulation, making use of the **GEANT4** package [104]. All considered samples are listed in Table 16.3. The table mentions for each sample the process name, the data set paths and the cross sections used to scale the number of events observed in the simulation to the integrated luminosity of the collected data. The cross sections were adopted from the CMS measurement on which the event selection and object definitions of this search are based [136].

The HLT is not included in the MC simulation. Therefore we will adopt an event selection in which the HLT is known to be around 100% efficient as explained in Section 16.5. Also, the pile-up scenario in the MC samples is not realistic and therefore, the MC samples are weighted event-by-event to obtain a realistic distribution of the

Table 16.2 – The triggers used to collect the data considered for this analysis. Listed are the trigger paths and the run ranges in which each trigger was used.

run range	trigger
170053-170064	HLT_HT300_MHT80_v1
170065-173211	HLT_HT300_MHT80_v2
173212-176544	HLT_HT300_MHT90_v2
176545-178410	HLT_HT350_MHT90_v1
178411-180252	HLT_HT350_MHT110_v3

number of pile-up events per bunch crossing. Other known or suspected discrepancies between data and simulation are not corrected for since the uncertainties on the corresponding correction factors are usually within one to two sigma from one.

Table 16.3 – Simulated data samples used to model background processes. For QCD samples, the data set paths are shown stripped from the right from /Summer11-PU_S3_START42.V11-v2/AODSIM. Other samples are stripped from /Summer11-PU_S4_START42.V11-v1/AODSIM.

process	data set	σ
QCD $\hat{p}_T \in [0,5[$ GeV	/QCD_Pt-0to5_TuneZ2.7TeV_pythia6	4.84×10^{10}
QCD $\hat{p}_T \in [5,15[$ GeV	/QCD_Pt-5to15_TuneZ2.7TeV_pythia6	3.68×10^{10}
QCD $\hat{p}_T \in [15,30[$ GeV	/QCD_Pt-15to30_TuneZ2.7TeV_pythia6	8.16×10^8
QCD $\hat{p}_T \in [30,50[$ GeV	/QCD_Pt-30to50_TuneZ2.7TeV_pythia6	5.31×10^7
QCD $\hat{p}_T \in [50,80[$ GeV	/QCD_Pt-50to80_TuneZ2.7TeV_pythia6	6.36×10^6
QCD $\hat{p}_T \in [80,120[$ GeV	/QCD_Pt-80to120_TuneZ2.7TeV_pythia6	7.84×10^5
QCD $\hat{p}_T \in [120,170[$ GeV	/QCD_Pt-120to170_TuneZ2.7TeV_pythia6	1.15×10^5
QCD $\hat{p}_T \in [170,300[$ GeV	/QCD_Pt-170to300_TuneZ2.7TeV_pythia6	2.43×10^4
QCD $\hat{p}_T \in [300,470[$ GeV	/QCD_Pt-300to470_TuneZ2.7TeV_pythia6	1.17×10^3
QCD $\hat{p}_T \in [470,600[$ GeV	/QCD_Pt-470to600_TuneZ2.7TeV_pythia6	7.02×10^1
QCD $\hat{p}_T \in [600,800[$ GeV	/QCD_Pt-600to800_TuneZ2.7TeV_pythia6	1.56×10^1
QCD $\hat{p}_T \in [800,1000[$ GeV	/QCD_Pt-800to1000_TuneZ2.7TeV_pythia6	1.84×10^0
QCD $\hat{p}_T \in [1000,1400[$ GeV	/QCD_Pt-1000to1400_TuneZ2.7TeV_pythia6	3.32×10^{-1}
QCD $\hat{p}_T \in [1400,1800[$ GeV	/QCD_Pt-1400to1800_TuneZ2.7TeV_pythia6	1.09×10^{-2}
QCD $\hat{p}_T \in [1800,\text{inf}[$ GeV	/QCD_Pt-1800_TuneZ2.7TeV_pythia6	3.58×10^{-4}
$t\bar{t}$ +jets inclusive	/TTJets_TuneZ2.7TeV-madgraph-tauola	1.58×10^2
W +jets	/WJetsToLNu_TuneZ2.7TeV-madgraph-tauola	3.13×10^4
DY +jets $\rightarrow l m(l l) < 50$	/DYJetsToLL_TuneZ2.M-50.7TeV-madgraph-tauola	3.05×10^3
$Z \rightarrow \nu\nu$ +jets ($200 < H_T < \text{inf}$)	/ZJetsToNuNu_200_HT_inf.7TeV-madgraph	3.29×10^1
WW	/WW_TuneZ2.7TeV_pythia6-tauola	2.78×10^1
WZ	/WZ_TuneZ2.7TeV_pythia6-tauola	1.05×10^1
ZZ	/ZZ_TuneZ2.7TeV_pythia6-tauola	4.29×10^0
t (s-channel)	/T_TuneZ2_s-channel.7TeV-powheg-tauola	3.19×10^0
\bar{t} (s-channel)	/Tbar_TuneZ2_s-channel.7TeV-powheg-tauola	1.44×10^0
t (t-channel)	/T_TuneZ2_t-channel.7TeV-powheg-tauola	4.19×10^1
\bar{t} (t-channel)	/Tbar_TuneZ2_t-channel.7TeV-powheg-tauola	2.26×10^1
t (tW channel)	/T_TuneZ2_tW-channel-DR.7TeV-powheg-tauola	7.87×10^0
\bar{t} (tW channel)	/Tbar_TuneZ2_tW-channel-DR.7TeV-powheg-tauola	7.87×10^0

16.3 Predictions for the pMSSM

The interpretation of this search within the pMSSM requires predictions for a large number of pMSSM scenarios. For each of the scenarios, 10000 proton-proton events with sparticle production were simulated with MC. The hard interaction, showering, hadronization, underlying event and pile-up are described with PYTHIA 6 [24], while the CMS detector is simulated with the CMS `FastSimulation` package [138]. As for the SM predictions, the HLT is not included and the sample is weighted to obtain a realistic pile-up scenario.

16.4 Definition of physics objects

The final states of proton-proton collisions, both in data and in MC simulation, are reconstructed with the PF algorithm. From the resulting PF particles, several physics objects are compiled, such as jets, E_T^{miss} , isolated muons and electrons, following the prescription provided by the PF2PAT sequence included in the `SusyPatLayer1DefV10` configuration [139], however, with τ -identification disabled. Further requirements are implied on the physics objects as explained in the following paragraphs.

16.4.1 Primary vertex

Events are required to have at least one PV. As such, backgrounds caused by detector noise and cosmic rays are reduced, without an impact on the potential signal efficiency. In addition, the presence of a reconstructed PV is required in the reconstruction and selection of other physics objects. If events have more than one PV, the scalar sum of the momenta of the associated tracks is derived for each PV, and the PV with the highest sum is selected (this is the first element in the PV collection). We demand that the selected PV is close to the beam spot, the position where the proton-beams cross, and that a minimum number of tracks is associated by requiring more than 4 degrees of freedom for the PV-fit. The PV definition is detailed in Table 16.4.

Table 16.4 – Implementation of the primary vertex definition.

class	<code>reco::Vertex</code>
label	<code>offlinePrimaryVertices</code>
first vertex in collection	
<code>isFake()</code>	
<code>fabs(z())</code>	< 24
<code>position().Rho()</code>	< 2
<code>ndof()</code>	> 4

16.4.2 Jets and H_T

In general, the production of pairs of SUSY particles gives rise to long decay chains with multiple quarks in the decay products. This results in final states with multiple and often highly energetic jets. In this analysis, jets are clustered from PF particles using the anti- k_T algorithm with a cone radius of $R = 0.5$ [52]. The clustering does not include isolated electrons and muons, but no attempt is made to identify and

exclude isolated τ -leptons. We require the jets to have a transverse momentum $p_T > 50$ GeV, a pseudorapidity $|\eta| < 2.4$ and to pass the loose PF jet identification criteria [140]. The energy and momentum of the jets is corrected for pile-up contributions (L1FastJet corrections) and a p_T and η dependent calibration is applied (L2 and L3 jet corrections). Table 16.5 lists the details of the implementation of this jet definition. All the as such reconstructed and selected jets are included in the definition of the transverse hadronic energy, H_T , defined in Equation 6.2, that summarizes the jet activity per event.

Table 16.5 – Implementation of the jet definition.

class	<code>pat::Jet</code>
label	<code>selectedPatJetsPF</code>
<code>pt()</code>	> 50 GeV
<code>fabs(eta())</code>	< 2.4
<code>numberOfDaughters()</code>	> 1
<code>neutralEmEnergyFraction()</code>	< 0.99
<code>chargedMultiplicity()</code>	< 0.99

16.4.3 E_T^{miss} and $\Delta\Phi_{min}^N$

In most popular SUSY scenarios, the lightest SUSY particle is the lightest neutralino and is stable, constituting a good dark matter candidate. In such scenarios, the decay chains of each sparticle ends with this stable, weakly interacting particle, and thus the potential production of sparticle pairs in proton-proton collisions gives rise to high amounts of missing transverse energy, E_T^{miss} , defined in Equation 6.3. We reconstruct the E_T^{miss} from all PF particles, without applying any calibration. Information on E_T^{miss} is contained in the PAT class `pat::MET` with label `patMETsPF`.

The failed reconstruction and misreconstruction of particles is a source of fake E_T^{miss} . In events whitout genuine source of E_T^{miss} and serious particle misreconstruction, the E_T^{miss} is usually aligned or anti-aligned with one of the jets, where most particle reconstruction failures occur. Such events are most often vetoed by requiring that the angular distance between the E_T^{miss} and the closest jet, $\Delta\Phi^{min}$, is above a certain value. Following [136], we adopt a related, more advanced variable, $\Delta\Phi_{min}^N$:

$$\Delta\phi_{Nj} = \frac{\Delta\phi(j, E_T^{miss})}{\tan^{-1}(\Delta_{Tj}/E_T^{miss})}, \quad (16.1)$$

with

$$\Delta_{Tj} = 0.1 \frac{\sqrt{\sum_{i \neq j} \left[p_x^j p_y^i - p_y^j p_x^i \right]^2}}{p_T^j}. \quad (16.2)$$

where the sum runs over all jets passing the selection criteria with a relaxed p_T threshold of 30 GeV. $\Delta\Phi_{min}^N$ is then defined as the smallest of the $\Delta\phi_{Nj}$ for the 3 selected jets with the highest p_T .

Originally, this variable was adopted because it shows only little correlation with the magnitude of the E_T^{miss} , which is useful for data driven background estimates. Although we make no use here of such data driven background estimates we still adopt this variable for reasons of consistency.

16.4.4 Vetoing isolated leptons

We veto the presence of isolated leptons with vertices close to the beam spot. With this veto, some important SM backgrounds with high amounts of E_T^{miss} , such as W +jets and top quark pair production, are drastically reduced.

Muons are required to have a transverse momentum $p_T > 10$ GeV and pseudorapidity $|\eta| < 2.1$ and they must be reconstructed both as tracker and as global muon. Furthermore they must satisfy the `GlobalMuonPromptTight` identification requirements, have at least 1 pixel hit and have a vertex close to the beam spot. Finally, we require the muons to be isolated from any other PF particles. All details of the implementation of this muon definition are shown in Table 16.6.

Table 16.6 – Implementation of the muon definition.

class	pat::Muon
label	selectedPatMuonsPF
GlobalMuonPromptTight()	== 1
isTrackerMuon()	== 1
pt()	≥ 10 GeV
fabs(eta())	< 2.4
innerTrack().numberOfValidHits()	≥ 11
track().hitPattern().numberOfValidPixelHits()	≥ 1
fabs(dB())	< 0.02
fabs(vz() - vertex.z())	< 1
(chargedHadronIso() + photonIso() + neutralHadronIso())/pt()	< 0.2

Electrons are required to have a transverse momentum $p_T > 10$ GeV and pseudora-

pidity $|\eta| < 2.4$. They must also be outside the barrel-endcap transition region at $1.4442 < |\eta| < 1.566$ and isolated from other PF particles. Electrons from photon conversion are rejected by requiring that none of the expected hits in the inner tracker are missing. Finally, to exclude electrons originating from decays of long lived particles, the electron vertex must be close to the PV. The details of the implementation of the above definition are listed in Table 16.7.

Table 16.7 – Implementation of the electron definition.

class	pat::Electron
label	selectedPatElectronsPF
pt()	≥ 10
fabs(superCluster().eta())	< 2.5
fabs(superCluster().eta())	$\notin [1.4442, 1.566]$
gsfTrack()->trackerExpectedHitsInner().numberOfLostHits	≥ 1
dB()	< 0.02
fabs(vz() - vertex.z())	< 1
(chargedHadronIso() + photonIso() + neutralHadronIso())/pt()	< 0.2

τ -leptons are not included in this veto as these are difficult to reconstruct with high purity and thus vetoing the presence of τ -leptons would imply a potentially important loss of signal.

16.4.5 b -tagged jets

Since we are interested in new physics scenarios with an enhanced production of b -quarks, we identify and count the b -jets in events. We use the Combined Secondary Vertex (CSV) b -tagger to identify b -jets [141]. A jet is considered b -tagged if the CSV-discriminator for the jet has a value greater than 0.679. This specific value is referred to as the CSV Medium working point (CSVM) and was chosen to have a mistag efficiency of the order of 1% [142]. The b -tagged jets are selected with the same criteria as regular jets except, for a looser threshold for the transverse momentum, $p_T > 30$ GeV.

16.5 Event selection

Based on the physics objects just described, we apply an events selection, enhancing the contribution of the potential new physics events we are interested in:

- events must have at least one PV,
- only events with $H_T > 400$ GeV are accepted,
- events must have at least 3 jets,
- events with isolated muons or electrons are discarded,
- the E_T^{miss} must be above 250 GeV,
- events must have at least one b -jet.

Table 16.8 shows the number of events at different stages of this selection. SM predictions are shown per process and the total SM prediction is compared to the number of events observed in the data. Event numbers in MC are scaled to an integrated luminosity of 3.27 fb^{-1} . The quoted uncertainties are statistical only.

In the first stages of the selection, there are large discrepancies between the observed and the predicted numbers of events, mainly because our predictions do not take into account the HLT. In addition, the simulation does not take into account a number of detector effects that affect the measurement of the E_T^{miss} . Events in data that show such effect are rejected (E_T^{miss} cleaning [136]). After all selection steps the agreement between data and MC is good. Events that pass all selection criteria, except the HLT requirement are measured to pass the HLT with an efficiency of $97.56^{+0.19}_{-0.21}$ [136]. Since this is close to one, we neglect the effects of the HLT in our final predictions.

16.5.1 Search regions

We define 12 statistically independent search regions. These regions are defined by the number of jets and b -jets in the events. We distinguish between events with 1, 2 or 3 b -jets and between events with 3, 4, 5 or 6 jets. Table 16.9 lists for each of the search regions the expected number of events per process and in total for an integrated luminosity of 3.27 fb^{-1} . The uncertainties are statistical only. Figure 16.1 illustrates the expected composition of the selected SM events in each of the search regions. In most cases, the production of top quark pairs and single top dominates.

Table 16.8 – Observed and expected numbers of events at different stages of the selection. The data correspond to an integrated luminosity of 3.27 fb^{-1} and the expected number of events are scaled accordingly. Uncertainties are statistical only. The significant differences between the observed and the expected numbers in the earlier stages of the selection are understood and described in the text.

	$t\bar{t}, t$	QCD	EWK	$Z \rightarrow \nu\nu$
Vertex	$7.944 \pm 0.003 \times 10^5$	$2.785 \pm 0.002 \times 10^{14}$	$1.122 \pm 0.001 \times 10^8$	$1.076 \pm 0.001 \times 10^5$
$H_T \geq 300$	$7.499 \pm 0.010 \times 10^4$	$1.359 \pm 0.387 \times 10^9$	$5.906 \pm 0.029 \times 10^4$	$8.032 \pm 0.017 \times 10^3$
≥ 3 jets	$7.230 \pm 0.010 \times 10^4$	$8.360 \pm 2.879 \times 10^8$	$3.439 \pm 0.022 \times 10^4$	$4.040 \pm 0.012 \times 10^3$
e-veto	$6.592 \pm 0.010 \times 10^4$	$8.360 \pm 2.879 \times 10^8$	$2.745 \pm 0.020 \times 10^4$	$4.038 \pm 0.012 \times 10^3$
μ -veto	$5.966 \pm 0.009 \times 10^4$	$8.360 \pm 2.879 \times 10^8$	$2.016 \pm 0.017 \times 10^4$	$4.037 \pm 0.012 \times 10^3$
$E_T^{miss} > 250$	315 ± 7	679 ± 35	599 ± 30	400 ± 4
$\Delta\Phi_{min}^N > 4$	260 ± 6	100 ± 18	460 ± 27	369 ± 4
≥ 1 b-tagged jet	219 ± 6	20 ± 3	84 ± 12	56 ± 2
E_T^{miss} cleaning	215 ± 6	13 ± 3	78 ± 11	56 ± 2
		total MC	data	
Vertex		$2.785 \pm 0.002 \times 10^{14}$	5.875×10^6	
$H_T \geq 300$		$1.359 \pm 0.387 \times 10^9$	1.999×10^6	
≥ 3 jets		$8.362 \pm 2.879 \times 10^8$	1.261×10^6	
e-veto		$8.361 \pm 2.879 \times 10^8$	1.254×10^6	
μ -veto		$8.361 \pm 2.879 \times 10^8$	1.246×10^6	
$E_T^{miss} > 250$		1994 ± 47	2310	
$\Delta\Phi_{min}^N > 4$		1189 ± 33	1414	
≥ 1 b-tagged jet		379 ± 13	411	
E_T^{miss} cleaning		361 ± 13	343	

Table 16.9 – Observed and expected numbers of events in each of the search regions. The data correspond to an integrated luminosity of 3.27 fb^{-1} and the expected numbers of events are scaled accordingly. Uncertainties are statistical only.

3 jets, 1 b -jet		3 jets, 2 b -jets		3 jets, 3 b -jets	
$t\bar{t}, t$	51.4 \pm 4.0	$t\bar{t}, t$	33.3 \pm 3.0	$t\bar{t}, t$	4.5 \pm 0.9
QCD	7.4 \pm 3.0	QCD	1.2 \pm 0.7	QCD	0.2 \pm 0.1
EWK	54.2 \pm 11.0	EWK	3.4 \pm 3.0	EWK	0.0 \pm 0.0
$Z \rightarrow \nu\nu$	33.3 \pm 2.0	$Z \rightarrow \nu\nu$	4.8 \pm 0.5	$Z \rightarrow \nu\nu$	0.2 \pm 0.1
total MC	146.4 \pm 12.0	total MC	42.7 \pm 4.0	total MC	4.9 \pm 1.0
data	138	data	33	data	5
4 jets, 1 b -jet		4 jets, 2 b -jets		4 jets, 3 b -jets	
$t\bar{t}, t$	40.3 \pm 3.0	$t\bar{t}, t$	30.3 \pm 3.0	$t\bar{t}, t$	4.2 \pm 0.9
QCD	3.1 \pm 2.0	QCD	0.1 \pm 0.1	QCD	0.1 \pm 0.1
EWK	13.2 \pm 6.0	EWK	3.9 \pm 3.0	EWK	0.0 \pm 0.0
$Z \rightarrow \nu\nu$	11.5 \pm 0.7	$Z \rightarrow \nu\nu$	2.4 \pm 0.3	$Z \rightarrow \nu\nu$	0.1 \pm 0.1
total MC	68.1 \pm 7.0	total MC	36.6 \pm 4.0	total MC	4.4 \pm 0.9
data	75	data	29	data	3
5 jets, 1 b -jet		5 jets, 2 b -jets		5 jets, 3 b -jets	
$t\bar{t}, t$	15.4 \pm 2.0	$t\bar{t}, t$	18.4 \pm 2.0	$t\bar{t}, t$	2.8 \pm 0.7
QCD	0.1 \pm 0.0	QCD	0.9 \pm 0.8	QCD	0.0 \pm 0.0
EWK	2.7 \pm 3.0	EWK	0.0 \pm 0.0	EWK	0.0 \pm 0.0
$Z \rightarrow \nu\nu$	2.4 \pm 0.3	$Z \rightarrow \nu\nu$	0.4 \pm 0.1	$Z \rightarrow \nu\nu$	0.0 \pm 0.0
total MC	20.6 \pm 3.0	total MC	19.7 \pm 3.0	total MC	2.8 \pm 0.7
data	33	data	11	data	3
6 jets, 1 b -jet		6 jets, 2 b -jets		6 jets, 3 b -jets	
$t\bar{t}, t$	6.8 \pm 2.0	$t\bar{t}, t$	5.3 \pm 1.0	$t\bar{t}, t$	1.7 \pm 0.6
QCD	0.1 \pm 0.1	QCD	0.0 \pm 0.0	QCD	0.0 \pm 0.0
EWK	0.7 \pm 0.7	EWK	-	EWK	0.0 \pm 0.0
$Z \rightarrow \nu\nu$	0.4 \pm 0.1	$Z \rightarrow \nu\nu$	0.1 \pm 0.1	$Z \rightarrow \nu\nu$	-
total MC	8.0 \pm 2.0	total MC	5.4 \pm 1.0	total MC	1.7 \pm 0.6
data	3	data	5	data	5

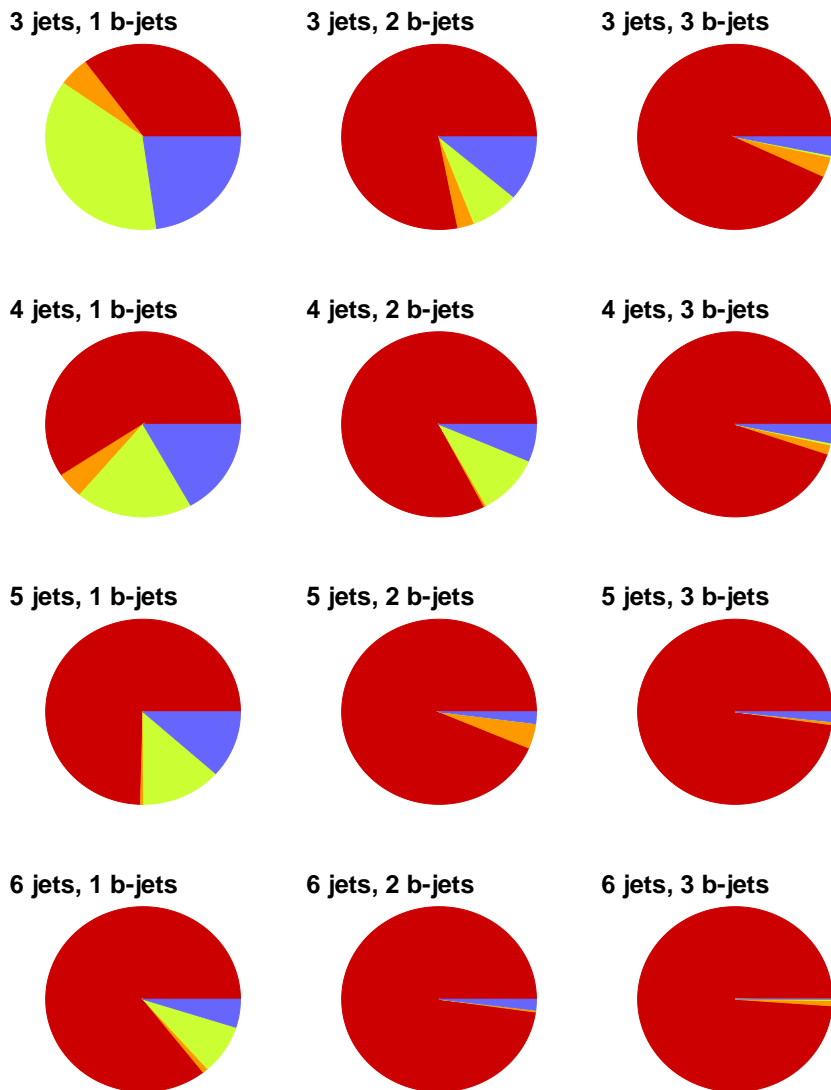


Figure 16.1 – Pie charts illustrating the predicted composition of the SM events in each of the search regions. Events are categorized as top events (red), QCD events (orange), EWK events (green) or $Z \rightarrow \nu\nu$ events (blue).

16.6 Results

16.6.1 Model-independent interpretation

The Bayesian tools for the model-independent interpretation of count experiments, developed in Chapter 14, are applied to the observed numbers of events in each of the search regions. We verify whether or not these numbers are compatible with the SM and how they constrain the potential signal strength in each search region.

First, we derive for each search region the prior probability density for the expected number of background events, $P(\mu)$, as defined in Equation 14.13. The parameters $b = \hat{\mu}/\delta\hat{\mu}^2$ and $Y = b\hat{\mu}$ are derived from the SM estimates in table 16.9, where the uncertainties $\delta\hat{\mu}$ only include the statistical uncertainties from the MC simulation that was used for the SM predictions. Other systematic uncertainties are neglected.

Next, we derive for each search region the conditional prior probability density for the expected number of signal events, $\Pi(s|\mu)$, as defined in Equation 14.15. The small amount of data, used to derive this prior, corresponds to an integrated luminosity of 0.24 fb^{-1} and thus, this prior's parameter f equals 0.075. Figure 16.2 shows the priors for s and μ , $\Pi(s, \mu) = \Pi(s|\mu)\Pi(\mu)$ and displays the values for each of the relevant parameters.

Then, we determine how the observed numbers of events constrain the potential signal strength, by deriving the posterior probability density for the expected number of signal events s , making use of Equation 14.19, for each of the search regions. The observed numbers of events N in these equations are taken from Table 16.9. Figure 16.3 shows the resulting probability densities.

Finally, we calculate the posterior probability of the hypothesis that new physics contributes to the observed numbers of events. For each search region we derive the Bayes factor as defined in Equation 14.4. The numerators of the Bayes factors are the likelihoods for the background plus signal hypothesis, given in Equation 14.17, and the denominators are the likelihoods of the background-only hypothesis, defined in Equation 14.17. These Bayes factors are substituted in Equation 14.5 to acquire the posterior probability for the signal hypothesis per search region, listed in Table 16.10. In addition, these Bayes factors are used to draw the overall Bayes factor, making use of Equation 14.30, and the overall posterior probability of the new physics hypothesis.

The posterior probabilities for s , shown in Figure 16.3 are all compatible with the

zero-signal-strength hypothesis and, except for a few regions, favor new physics hypotheses with small signal strengths. An exception is the search region with 3 jets and 1 b -jet. In this region, new physics hypotheses with only few expected signal events are disfavored. However, since the posterior for this region does not exclude the zero-signal-strength hypothesis, this might be due to a fluctuation in the data or in the MC simulation used for the SM background predictions. The small probability for the zero-signal-strength hypothesis might also be related to an underestimate of the uncertainty on the background prediction, due to our incomplete treatment of systematic uncertainties.

The per-search-region posterior probabilities for the new physics hypothesis are all relatively moderate, ranging between 0.07 and 0.75. Thus, looking at one search region at a time, the measurements do not provide firm answers to whether or not new physics is present. However, when combining all search regions, the new physics hypothesis is strongly disfavored, having a posterior probability of the order 10^{-6} . The huge difference between the individual posterior probabilities and the combined posterior probability might seem somewhat counter-intuitive at first sight. However, this is a desirable and reasonable consequence of our Bayesian approach that inherently takes into account the look-elsewhere effect by punishing the complexity of the new physics scenario, that increases with every additional search region. Indeed, the Bayes factor for this problem,

$$B_{10} = \frac{\int \int P(\vec{N}|\vec{\mu}, \vec{s}, H_1) d\vec{\mu} d\vec{s}}{\int P(\vec{N}|\vec{\mu}, H_0) d\vec{\mu}}, \quad (16.3)$$

implies a penalty for the complexity and unconstrainedness of the new physics hypothesis which has twice as much dimensions as the SM hypothesis.

10^{-6} seems like an extremely small number. Nevertheless, the new physics hypothesis should not be considered as completely excluded. The small probability simply learns us that the particular, very unrestricted new physics hypothesis assumed here, does not improve our understanding of this particular measurement. When considering other search regions, when updating the measurement with additional data, or with more precise background predictions, the new physics hypothesis might become more likely or even necessary to explain the observed counts.

16.6.2 Interpretation within the pMSSM

In this section we apply the Bayesian tools for the model-dependent interpretation of count experiments. We evaluate the impact of our observations in the twelve search

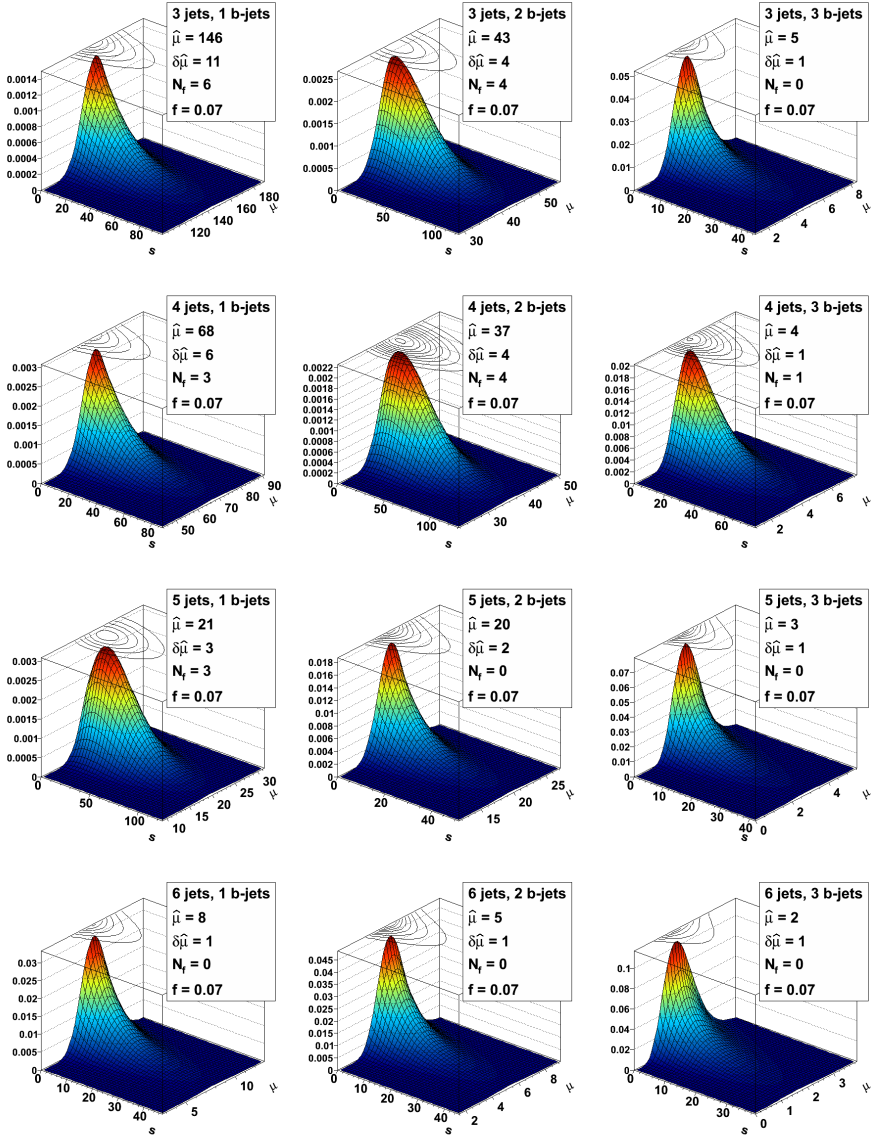


Figure 16.2 – The prior $\Pi(s, \mu) = \Pi(s|\mu)\Pi(\mu)$ for the expected number of SM events μ and signal events s in each of the search regions.

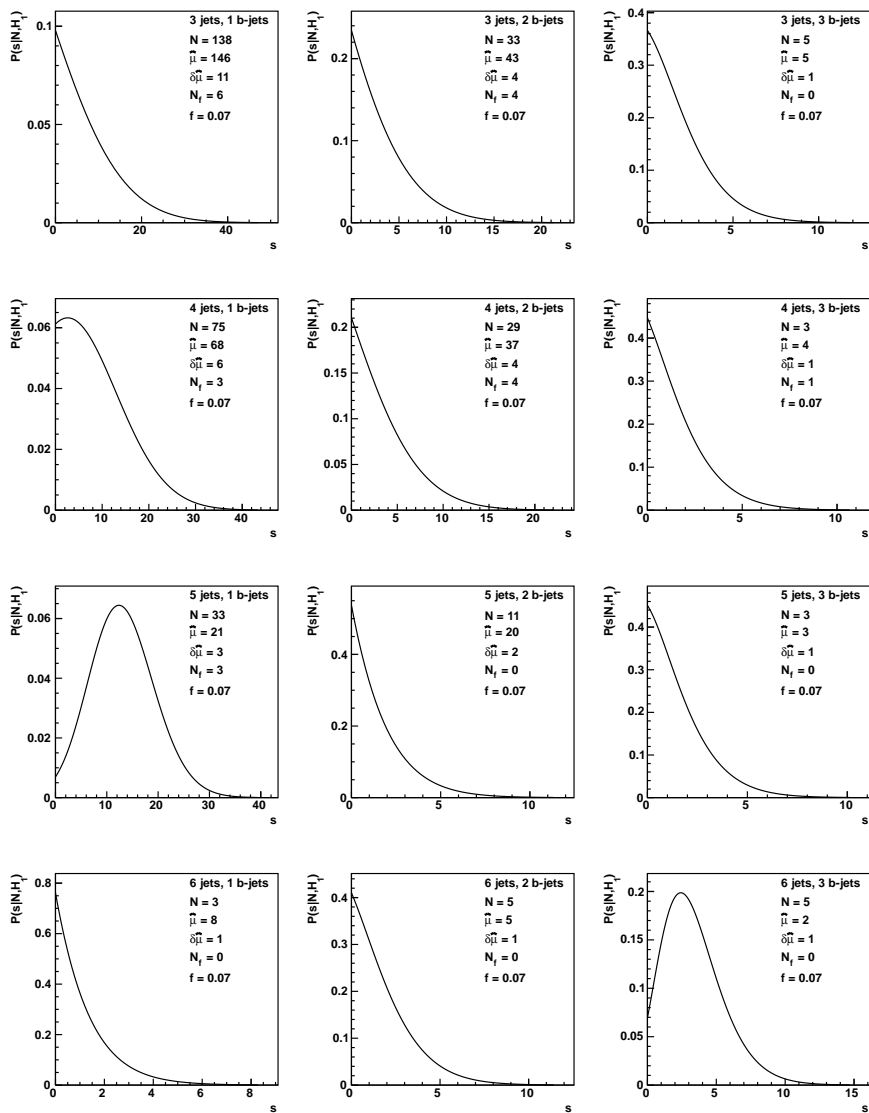


Figure 16.3 – Posterior probability density for the expected number of signal events s , $P(s|N)$, in each of the search regions.

Table 16.10 – Posterior probability $P(H_1|N)$ for the signal + background hypothesis H_1 in each of the search regions and for the combination of search regions.

	1 b -jet	2 b -jets	3 b -jets
3 jets	0.29	0.079	0.25
4 jets	0.43	0.071	0.079
5 jets	0.74	0.15	0.24
6 jets	0.13	0.23	0.69
combined : 8.3×10^{-7}			

regions on a particular new physics model, the pMSSM. A posterior probability density for the parameters of the pMSSM is derived, taking into account information from previous measurements, as explained in Chapter 15.

First of all, the constraints from the PLMs are taken into account by sampling parameter points from the PLM likelihood described in Section 15.1.1. Millions of points are sampled, from which 12000 points were selected randomly for further inference. Then, for each selected point, we calculate the likelihoods for each of the search regions of the α_T measurement and the measurement presented in this chapter. For that purpose we generate a sample of 10000 proton-proton events for each of the 12000 selected parameter point as described in Section 16.3, from which the likelihoods are obtained following the procedure described in Section 15.1.2. The search regions are all independent and thus can be combined by simple multiplication.

Because we assume a flat prior and because the selected parameter points are distributed according to the PLM likelihoods, the posterior probability density of the pMSSM parameters is approximately the distribution of the parameters of the selected parameter points, weighted with the likelihoods from the α_T measurement and the measurement presented in this chapter. Figures 16.4, 16.5, 16.6 and 16.7 show the marginalized posterior probability densities for most of the sparticle masses¹. The filled blue distributions show the posterior probability density including the PLMs only; the blue curves show the posterior probability density after including both the PLMs and the CMS SUSY search presented in this chapter; the yellow curves show the posterior probability density after including both the PLMs and the CMS

¹Due to a problem in the CMS software, part of the sampled points could not be processed. Especially the points with low gluino mass are affected. Only points that passed all processing steps are included in the interpretation. Appendix B compares the distributions of the sparticle masses between all sampled points and the sampled points that passed all processing steps.

α_T measurement; finally, the red curves show the posterior probability density after including the PLMs and both the CMS measurements.

The CMS searches clearly have an important impact on the mass of the gluino and the masses of the first and second generation of squarks. The main constraints come from the α_T measurement, however, for the gluino mass, both measurements perform similarly and combining the both adds significantly to the constraints in the region between 500 and 1000 GeV. The impact on the masses of the second generation of squarks is rather limited, except for the \tilde{b}_1 mass, where the search presented in this chapter implies important constraints. The impact of the CMS measurements on the slepton masses is again rather limited, only slightly disfavoring the low mass regions with respect to the PLM likelihoods. Also the impact on the masses of the neutralinos and charginos is modest.

The interpretation in this section demonstrates the feasibility to draw meaningful conclusions from CMS measurements within the context of highly dimensional new physics models. It also illustrates the ease by which independent measurements are combined within this Bayesian framework and some of the benefits of such combinations: different measurements may carry different kinds of information; including more data increases the significance of conclusions and reduces the influence of the initial priors.

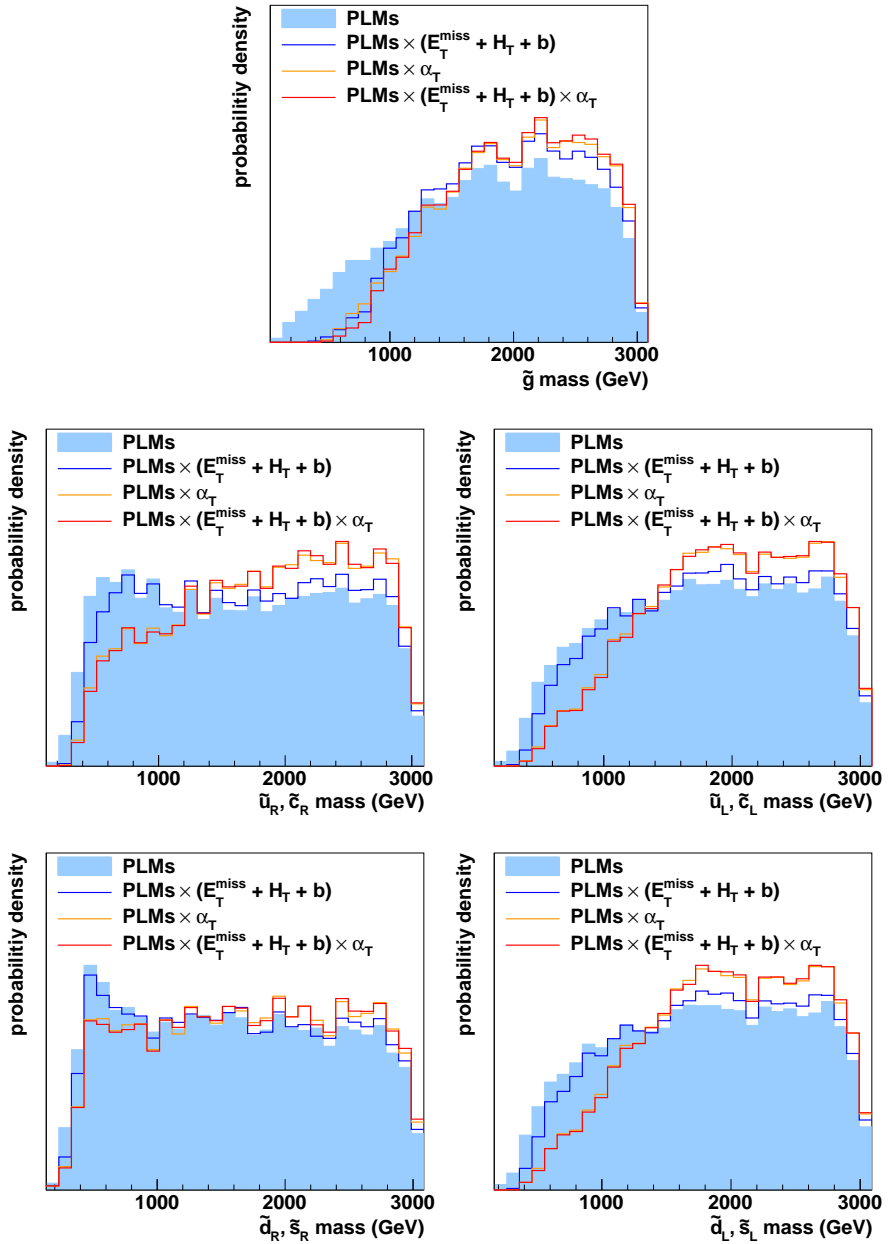


Figure 16.4 – Marginalized posterior probability densities of the gluino and squark masses of the first and second sfermion generations: after including PLMs only (blue area) and after combining PLMs with the CMS SUSY search presented in this chapter (blue line), the CMS α_T measurement (yellow line), both the CMS measurements (red line).

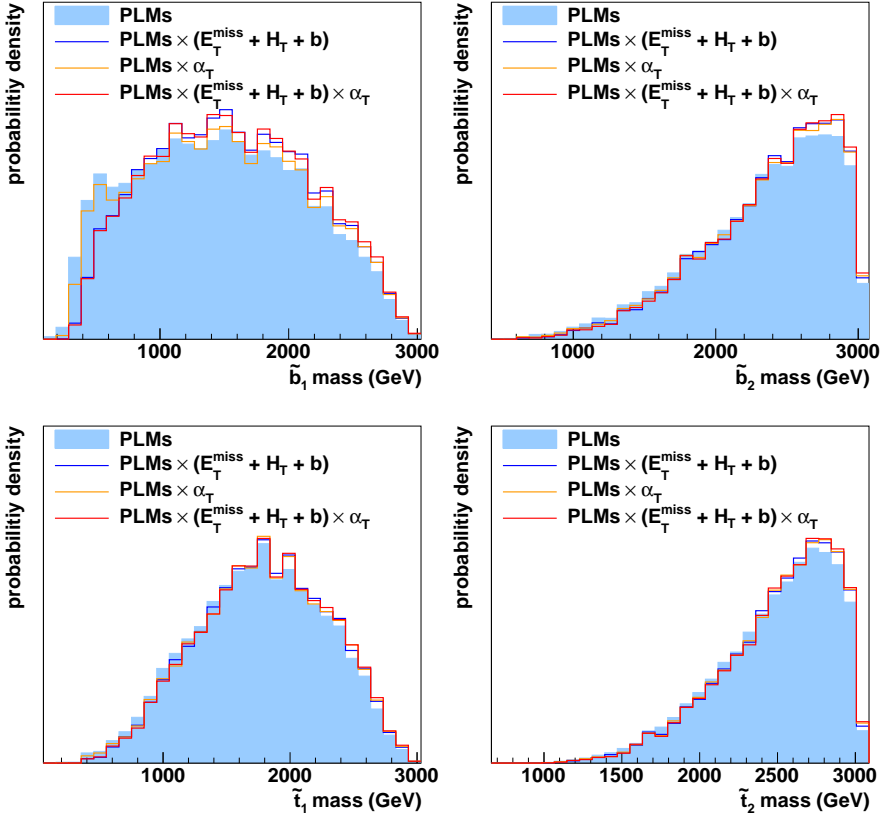


Figure 16.5 – Marginalized posterior probability densities of squark masses of the third sfermion generation: after including PLMs only (blue area) and after combining PLMs with the CMS SUSY search presented in this chapter (blue line), the CMS α_T measurement (yellow line), both the CMS measurements (red line).

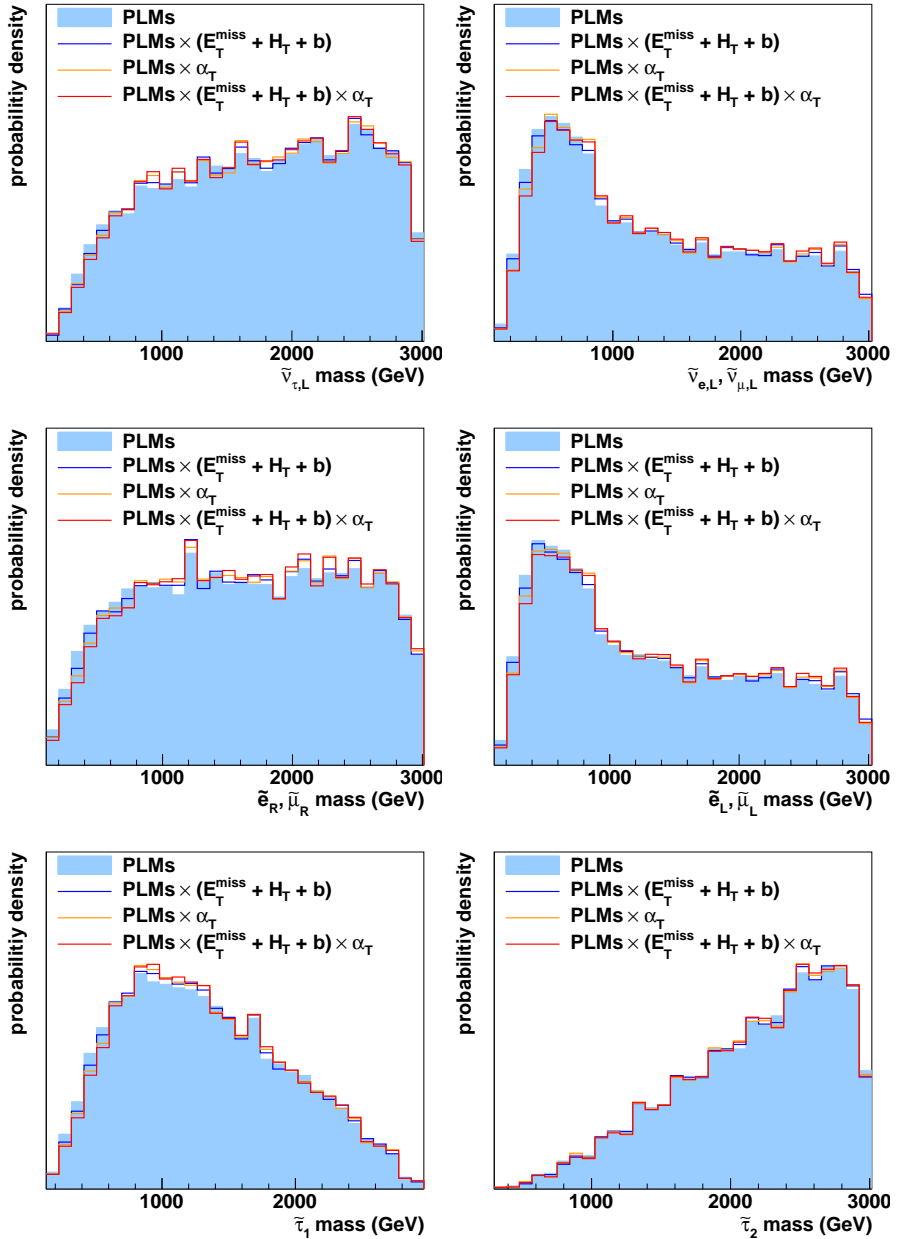


Figure 16.6 – Marginalized posterior probability densities of slepton masses: after including PLMs only (blue area) and after combining PLMs with the CMS SUSY search presented in this chapter (blue line), the CMS α_T measurement (yellow line), both the CMS measurements (red line).

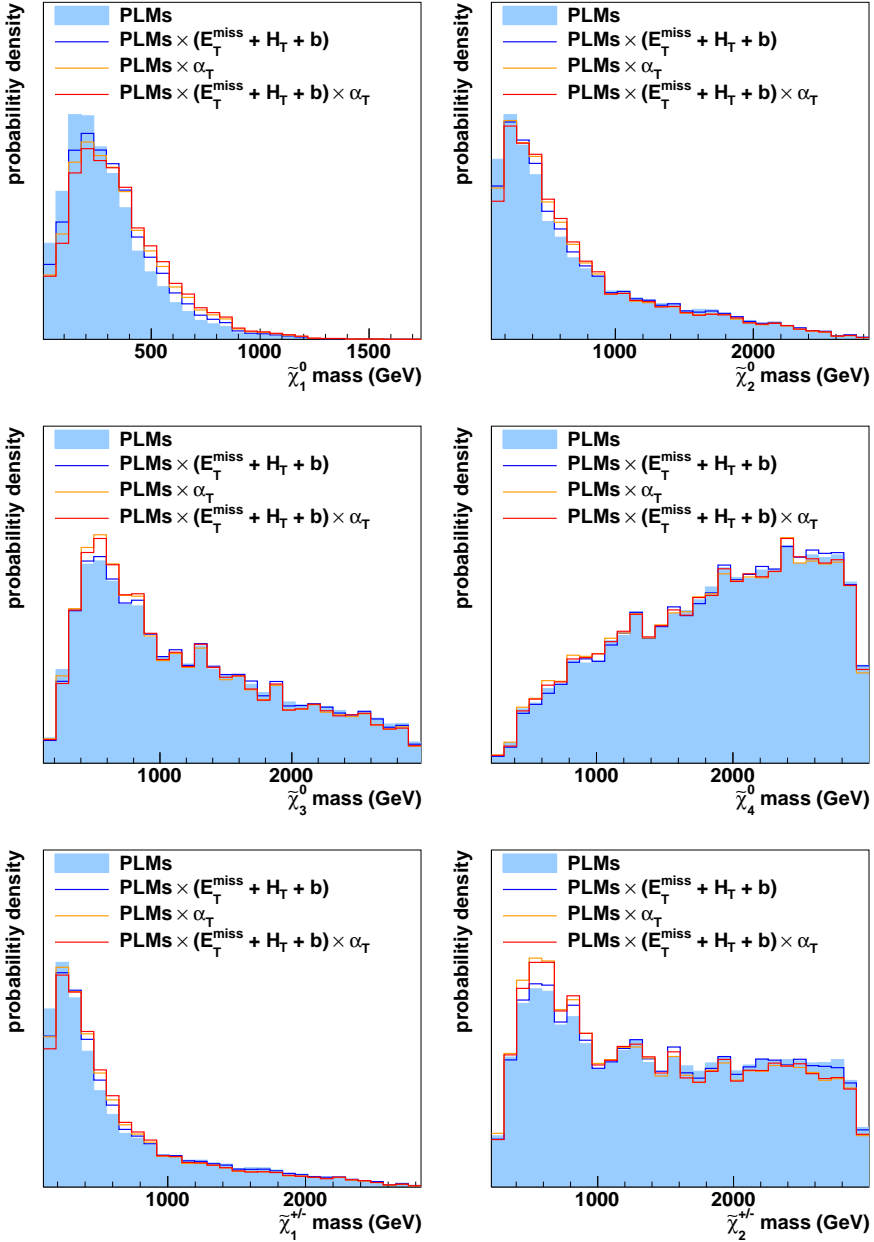


Figure 16.7 – Marginalized posterior probability densities of neutralino and chargino masses: after including PLMs only (blue area) and after combining PLMs with the CMS SUSY search presented in this chapter (blue line), the CMS α_T measurement (yellow line), both the CMS measurements (red line).

17

Bayesian tools for the design of searches for new physics

With the help of the LHC and other experiments, physicists hope to boost our understanding of nature. Many different measurements are being performed and their results are carefully interpreted to update our understanding of nature. In the previous chapter for example, we interpreted a couple of LHC measurements to understand whether or not they provide hints or proof for beyond the SM physics; what the potential signal strength might be in the considered search regions; what might be the True State of Nature (TSN) under the assumption of the pMSSM. To that end we used the Bayesian tools described in Chapter 14.

Bayesian inference implies an iterative approach. The chain of inference is initiated from some prior belief or understanding of nature, quantified as prior probabilities of hypotheses and prior probability densities of parameters. Using Bayes' Theorem, these priors are updated with certain observations, resulting in posterior probabilities and probability densities that represent the understanding after considering the particular observations. In a next iteration, when additional measurements are included in the chain of inference, these posteriors serve as priors. With a growing number of considered measurements, the understanding of nature increases while the influence of the initial priors decreases.

Its iterative character and its particular interpretation of probability provides the Bayesian methodology with some powerful, yet not fully exploited means for the design of new, powerful measurements. It allows to let existing measurements guide the design of new measurements, such that the expected impact of the new measurements is optimal. In fact, designing new measurements based on the results of existing measurements is quite common, however has been following a rather intuitive approach.

We believe that our field would benefit from more systematic and better motivated methods for the design of new searches. Especially because the interesting new physics models have all multiple free parameters, which causes human intuition to fall short. Therefore, in the next sections, we illustrate and discuss a novel procedure for the optimization of new count experiments, based on the results of existing measurements.

17.1 Optimization of single count experiments

Probably the easiest and most often used method to search for new physics is the single count experiment. In such a measurement the number of events that pass a certain event selection is counted. A significant excess of the observed number with respect over the number predicted by the SM would prove the existence of beyond the SM physics.

In [143] we applied and refined a novel method for the optimization of the event selection of single count experiments, first developed in [144]. A short description of this procedure follows and for further details we refer to [143]. The method is devised to optimize searches within the context of a new physics model of interest with free parameters. It copes with the challenge of finding a single event selection that shows an overall good performance, given the many very different scenarios that my dwell within a single new physics model.

The optimization criterion of the method is simple, sensible and intuitively attractive:

The optimal event selection for a single count experiment is the event selection that, with respect to all possible other event selections, maximizes the probability for discovering new physics, under the assumption of a certain new physics model of interest.

Given an events selection c , the probability for discovering new physics is defined as

follows:

$$P(\text{disc}_c|H_{\text{NP}}) = \int_{\Theta} p(\text{disc}_c|\theta, H_{\text{NP}})p(\theta)d\theta \quad (17.1)$$

where we make use of Bayesian statistics and the notation of Chapter 14. For the discovery likelihood, $p(\text{disc}_c|\theta, H_{\text{NP}})$, we used a simple definition that is often used in optimization procedures:

$$p(\text{disc}_c|\theta, H_{\text{NP}}) = \begin{cases} 0 & \text{if } S_c^\theta/\sqrt{S_c^\theta + B_c} < 3 \\ 1 & \text{if } S_c^\theta/\sqrt{S_c^\theta + B_c} \geq 3, \end{cases} \quad (17.2)$$

with B_c the number of background events that pass event selection c , as predicted by the SM, and S_c^θ the number of signal events that pass, as expected under the new physics hypothesis H_{NP} for the parameter point θ .

The crucial and novel ingredient to this optimization method is the probability density of the parameters of the new physics model, $p(\theta)$. Such probability density may be obtained from theoretical considerations and experimental observations such as e.g. explained for the pMSSM in Chapter 15 and Section 16.6.2. With this probability density we assign more weight to theoretically and experimentally favored regions in the parameter space of the particular new physics model, and less to disfavored regions. In other words, we let existing measurements guide the design of a new search.

Usually, a full integration over the parameter space of the new physics model is technically impossible and thus, as explained in Section 14.5, we replace the integral in Equation 17.1 with a sum:

$$P(\text{disc}_c|H_{\text{NP}}) \approx \sum_{j=1}^{j=M} [p(\text{disc}_c|\theta, H_{\text{NP}})p^{u-t}(\theta_j)]. \quad (17.3)$$

The sum runs over M points of the parameter space of the new physics model, sampled from a likelihood $p^t(\theta|H_{\text{NP}})$ that, together with the likelihood $p^{u-t}(\theta_j|H_{\text{NP}})$, represents the current understanding of the particular new physics model and defines the probability density $p(\theta|H_{\text{NP}}) = p^t(\theta_j|H_{\text{NP}})p^{u-t}(\theta_j|H_{\text{NP}})$, choosing a flat prior for θ .

The optimization procedure can be sketched as follows:

1. A large number of points in the parameter space of the new physics model of interest is sampled from the likelihood $p^t(\theta|H_{\text{NP}})$, that combines a series of PLMs (see e.g. Section 15.1.1 for the pMSSM). For each parameter point, a data

set of simulated new physics events is generated with MC. With this simulation and with additional simulation for SM processes, the likelihoods $p^{u-t}(\theta_j|H_{\text{NP}})$ are derived for each of the sampled points (see e.g. Section 16.6.2). After weighting with $p^{u-t}(\theta_j|H_{\text{NP}})$, the sampled parameter points are distributed according to $p(\theta|H_{\text{NP}}) = p^t(\theta|H_{\text{NP}})p^{u-t}(\theta_j|H_{\text{NP}})$.

2. A large number of candidate event selections is sampled, making use of an algorithm called ‘‘Random Grid Search’’ [145]. With this algorithm, we determine for each sampled point θ separately the event selection c that maximizes $S_c^\theta / \sqrt{S_c^\theta + B_c}$.
3. For each of the sampled event selections c , we determine the discovery probability $P(\text{disc}_c|H_{\text{NP}})$ defined in Equation 17.3. The event selection with the highest discovery probability is the optimal event selection.

As an illustration of this optimization procedure, we show here the results of the optimization of a count experiment with jets, b -jets and E_T^{miss} in the context of the pMSSM. Events are preselected if they have at least three jets, one b -jet, H_T above 200 GeV and E_T^{miss} above 100 GeV. For further details of the preselection and the object definitions we refer again to [143]. The search region is defined with lower cuts on H_T , E_T^{miss} and an angular variable $\Delta\Phi_{\text{min}}^N$. With the procedure just described we find the discovery probability as a function of the cut definition.

In Figure 17.1 we show the resulting discovery probability projected on the cut value for H_T , E_T^{miss} and $\Delta\Phi_{\text{min}}^N$. The red dots show the discovery probability for a search in 2 fb^{-1} of proton-proton data taken at a center of mass energy of $\sqrt{s} = 7 \text{ TeV}$ and the black dots show the discovery probability for a search in 5 fb^{-1} of data. We observe that a broad range of cut points provide similar, near optimal, discovery probabilities. We conclude that the results of this optimization procedure should be regarded as relatively loose guidelines, thus providing much flexibility to for example the methods for data driven background estimates.

17.2 Refinements and generalization

In Section 14.3 we propose two alternative measures for the optimization of searches. The first method maximizes the expected value of a given evidence measure $e(X)$. This expectation value is defined in Equation 14.23. The second method maximizes the probability that this measure of evidence is above a threshold value e^* . This

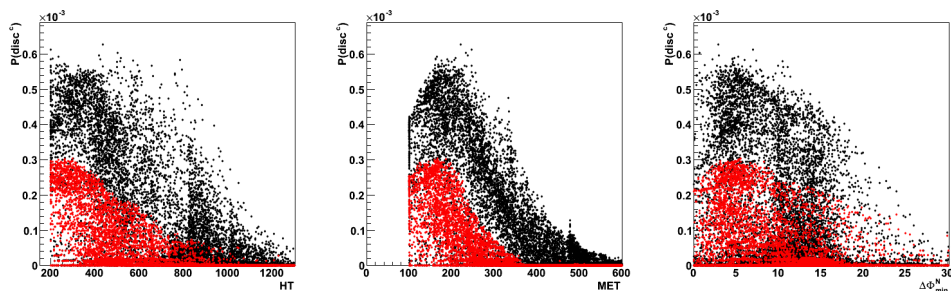


Figure 17.1 – Discovery probability for a count experiment with jets, b -jets and E_T^{miss} , under assumption of the pMSSM, projected on the values for the lower cuts on H_T (left), E_T^{miss} (center) and $\Delta\Phi_{min}^N$ (right). The red dots show the discovery probability for a search in 2 fb^{-1} of proton-proton data taken at a center of mass energy of $\sqrt{s} = 7 \text{ TeV}$ and the black dots show the discovery probability for a search in 5 fb^{-1} of data.

probability is defined in Equation 14.24. The latter method corresponds to maximizing the discovery probability and is a generalization of the optimization concept introduced in the previous section.

These two methods can be applied in a very broad context. In principle they can be used for any kind of search. Section 14.3.2 explains how this method can be used for single count experiments; with the help of section 14.4 this approach can be expanded to multiple count experiments; and in principle the methods can be applied to optimize the event selection or the observables used in shape analyses.

When applied to count experiments, as proposed in Section 14.3.2, the two methods differ from the method presented in the previous chapter on an important subject. The method in the previous section is based on what we could interpret as the expected evidence. Only the parameter points with an expected evidence above the threshold are considered discoverable. In contrast the two new methods discussed here take into account the full probability density of the evidence. This may be an advantage, since for some new physics scenarios no firm evidence is expected on average, while the probability for firm evidence might be significant. E.g. the presence of signal might increase the probability for a significant excess, while no significant excess is expected on average. However, this may also be a disadvantage since these methods will also be influenced by the small probability for firm evidence under new physics scenarios with negligible signal strength, caused by background fluctuations.

At the time of writing, the two methods discussed are being investigated in the context of single and multiple count experiments. The measures of evidence under study are $P(H_1)$ and $B_{10}(X)$ defined in Section 14.2.2 for single count experiments and extended to multiple count experiments in Section 14.4. Rather than providing a complete discussion of these ongoing studies, we list here their most important, preliminary conclusions.

When the expected evidence is used as the optimization measure for a multiple count experiment, it is computationally advantageous to adopt B_{10} as the measure of evidence. Indeed, in this case the expected evidence has the following shape:

$$\begin{aligned}
 E(B_{10}(\vec{N})|H_{\text{NP}}) &= \sum_{N_1=0}^{N_1=\infty} \dots \sum_{N_m=0}^{N_m=\infty} \left[B_{10}(\vec{N})P(\vec{N}|H_{\text{NP}}) \right] \\
 &= \prod_{i=1}^{i=m} \left[\sum_{N_i=0}^{N_i=\infty} B_{10}(N_i)P(N_i|H_{\text{NP}}) \right] \tag{17.4}
 \end{aligned}$$

with m the number of count experiments. Thus, the optimization measure is simply the product of m one-dimensional sums. When instead $P(H_1)$ is used as the measure of evidence or if the probability $P(e(X) > e^*|H_{\text{NP}})$ is used as optimization measure, the m dimensional sum cannot be reduced as such.

The expected evidence as optimization measure shows important instabilities with respect to the absolute background conditions. This behavior is not fully understood yet and needs further investigation. However, it is probably caused by the sensitivity of $E(e|H_{\text{NP}})$ in Equation 17.4 to the core of $P(\vec{N}|H_{\text{NP}})$, which is usually mainly determined by the background conditions.

This unstable behavior is probably a good argument for the use of the optimization measure $P(e(X) > e^*|H_{\text{NP}})$ which is most sensitive to the tails of $P(\vec{N}|H_{\text{NP}})$, that are usually mainly determined by the signal conditions. To increase the influence of the signal conditions on the tails of $P(\vec{N}|H_{\text{NP}})$ it might be wise not to consider new physics scenarios with negligible signal strength in the optimization. As mentioned earlier, $P(e(X) > e^*|H_{\text{NP}})$ implies some computational challenges in the context of multiple count experiments. Its calculation would probably require a careful sampling strategy.

To conclude, guiding the design of new searches by the results of existing measurements in a systematic, algorithmic fashion is still under study and needs further efforts. As explained in the previous section, the basic principle has proven to be

useful in the context of single count experiments. Therefore we believe that the further development of this approach deserves the necessary efforts and may lead eventually to significant improvements to our field.

Appendices

Appendix A

Calculations for the Bayesian statistical framework

A.1 Often used definitions

Let y be a complex number. The Gamma function $\Gamma(y)$ is then defined as

$$\Gamma(y + 1) = \int_0^{\infty} x^y e^{-x} dx. \quad (\text{A.1})$$

The gamma function converges if the real part of $y + 1$ is positive. Let furthermore $z \geq 0$ be a real number, the incomplete Gamma function $\Gamma(y, z)$ is then defined as

$$\Gamma(y + 1, z) = \int_z^{\infty} x^y e^{-x} dx \quad (\text{A.2})$$

A.2 Often used properties

An often used property of the Gamma function is:

$$\Gamma(z + 1) = z\Gamma(z), \quad (\text{A.3})$$

With N integer and $N \geq 0$ the gamma function $\Gamma(N + 1)$ reduces to the factorial of N :

$$\Gamma(N + 1) = N!. \quad (\text{A.4})$$

APPENDIX A

For x and y complex numbers and N a positive integer, the Binomial theorem states

$$(x + y)^N = \sum_{n=0}^{n=N} \binom{N}{n} x^{n-k} y^k. \quad (\text{A.5})$$

with $\binom{N}{n}$ the binomial coefficient defined as

$$\binom{N}{n} = \frac{N!}{(N-n)!n!} \quad (\text{A.6})$$

From Equation A.1 follows that

$$\begin{aligned} \int_0^\infty x^y e^{-ax} dx &= \frac{\int_0^\infty x'^y e^{-x'} dx'}{a^{y+1}} \\ &= \frac{\Gamma(y+1)}{a^{y+1}}, \end{aligned} \quad (\text{A.7})$$

with $x' = ax$.

From Equation A.2 follows that

$$\begin{aligned} \int_0^\infty (x+b)^y e^{-a(x+b)} dx &= \frac{\int_0^\infty (x'+b')^y e^{-(x'+b')} dx}{a^{y+1}} \\ &= \frac{\int_{b'}^\infty x'^y e^{-x'} dx'}{a^{y+1}} \\ &= \frac{\Gamma(y+1, ab)}{a^{y+1}}, \end{aligned} \quad (\text{A.8})$$

with $x' = ax$ and $b' = ab$.

From Equation A.4 and Equation A.5 follows that

$$\begin{aligned} \int_0^\infty (x+b)^N e^{-a(x+b)} dx &= e^{-ab} \sum_{n=0}^{n=N} \left[\binom{N}{n} b^n \int_0^\infty x^{N-n} e^{-ax} dx \right] \\ &= \sum_{n=0}^{n=N} \left[\binom{N}{n} \frac{(N-n+1)!}{a^{N-n+1}} b^n \right] e^{-ab} \end{aligned} \quad (\text{A.9})$$

with $x' = ax$ and $b' = ab$.

A.3 Likelihoods

The probability $P(N|H_0)$, defined in Equation 14.16, to observe N events under the hypothesis H_0 is worked out as follows:

$$\begin{aligned}
 P(N|H_0) &= \int_0^\infty \frac{\mu^N e^{-\mu} \pi(\mu)}{N!} d\mu \\
 &= \frac{1}{N!} \frac{b^{Y+1/2}}{\Gamma(Y+1/2)} \int_0^\infty \mu^{N+Y-1/2} e^{-(1+b)\mu} d\mu \\
 &= \frac{1}{N!} \frac{b^{Y+1/2}}{\Gamma(Y+1/2)} \frac{\Gamma(N+Y+1/2)}{(1+b)^{N+Y+1/2}},
 \end{aligned} \tag{A.10}$$

where the prior for μ , defined in Equation 14.13, was used.

With the priors for μ and s as defined in Equations 14.13 and 14.15, the probability $P(N|H_1)$, defined in Equation 14.17, to observe N events under the hypothesis H_1 is worked out as follows:

$$\begin{aligned}
 P(N|H_1) &= \int_0^\infty \int_0^\infty \frac{(\mu+s)^N e^{-(\mu+s)}}{N!} \pi(s|\mu) \pi(\mu) d\mu ds \\
 &= \frac{1}{N!} \frac{b^{Y+1/2}}{\Gamma(Y+1/2)} \\
 &\quad \times \int_0^\infty \left[\int_0^\infty (\mu+s)^{N+N_f-1/2} e^{-(1+f)(\mu+s)} ds \right] \frac{f^{N_f+1/2} \mu^{Y-1/2} e^{-b\mu}}{\Gamma(N_f+1/2, f\mu)} d\mu \\
 &= \frac{1}{N!} \frac{b^{Y+1/2}}{\Gamma(Y+1/2)} \\
 &\quad \times \int_0^\infty \frac{\Gamma(N+N_f+1/2, (1+f)\mu)}{(1+f)^{N+N_f+1/2}} \frac{f^{N_f+1/2}}{\Gamma(N_f+1/2, f\mu)} \mu^{Y-1/2} e^{-b\mu} d\mu.
 \end{aligned} \tag{A.11}$$

The integral over μ can be calculated easily with simple numerical techniques such as the QAGS algorithm as implemented in QUADPACK [146] or Gnu Scientific Library (GSL) [147].

Substitution of the priors for μ and s defined in Equations 14.13 and 14.20 in the

APPENDIX A

likelihood function $p(N|\theta, H_{\text{NP}})$ in Equation 14.21 leads to:

$$\begin{aligned}
 & P(N|\theta, H_{\text{NP}}) \\
 &= \int_0^\infty \int_0^\infty \frac{(\mu + s)^N e^{-(\mu+s)}}{N!} \pi(\mu, s|\theta, H_{\text{NP}}) \text{d}s \text{d}\mu, \\
 &= \frac{1}{N!} \frac{(b^\theta)^{(Z^\theta+1/2)}}{\Gamma(Z^\theta + 1/2)} \frac{b^{Y+1/2}}{\Gamma(Y + 1/2)} \\
 &\quad \times \int_0^\infty \int_0^\infty (\mu + s)^N e^{-(\mu+s)} s^{Z^\theta-1/2} e^{-b^\theta s} \mu^{Y-1/2} e^{-b\mu} \text{d}s \text{d}\mu \\
 &= \frac{1}{N!} \frac{(b^\theta)^{(Z^\theta+1/2)}}{\Gamma(Z^\theta + 1/2)} \frac{b^{Y+1/2}}{\Gamma(Y + 1/2)} \\
 &\quad \times \int_0^\infty \left[\int_0^\infty (\mu + s)^N e^{-(1+b^\theta)(\mu+s)} s^{Z^\theta-1/2} \text{d}s \right] \mu^{Y-1/2} e^{-(1+b-b^\theta)\mu} \text{d}\mu.
 \end{aligned} \tag{A.12}$$

The integration over s in Equation A.12 is worked out as follows:

$$\begin{aligned}
 & \int_0^\infty (\mu + s)^N e^{-(1+b^\theta)s} s^{Z^\theta-1/2} \text{d}s \\
 &= \sum_{n=0}^{n=N} \left[\binom{N}{n} \int_0^\infty \mu^n s^{N-n} e^{-(1+b^\theta)s} s^{Z^\theta-1/2} \text{d}s \right] \\
 &= \sum_{n=0}^{n=N} \left[\binom{N}{n} \mu^n \int_0^\infty s^{N+Z^\theta-n-1/2} e^{-(1+b^\theta)s} \text{d}s \right] \\
 &= \sum_{n=0}^{n=N} \left[\binom{N}{n} \mu^n \frac{\Gamma(N + Z^\theta - n + 1/2)}{(1 + b^\theta)^{N+Z^\theta-n+1/2}} \right].
 \end{aligned} \tag{A.13}$$

Substitution of Equation A.13 in Equation A.12 results in

$$\begin{aligned}
 & P(N|\theta, H_{\text{NP}}) \\
 &= \frac{1}{N!} \frac{(b^\theta)^{(Z^\theta+1/2)}}{\Gamma(Z^\theta + 1/2)} \frac{b^{Y+1/2}}{\Gamma(Y + 1/2)} \\
 &\quad \times \sum_{n=0}^{n=N} \left[\binom{N}{n} \frac{\Gamma(N + Z^\theta - n + 1/2)}{(1 + b^\theta)^{N+Z^\theta-n+1/2}} \int_0^\infty \mu^n \mu^{Y-1/2} e^{-(1+b)\mu} \text{d}\mu \right] \\
 &= \frac{1}{N!} \frac{(b^\theta)^{(Z^\theta+1/2)}}{\Gamma(Z^\theta + 1/2)} \frac{b^{Y+1/2}}{\Gamma(Y + 1/2)} \\
 &\quad \times \sum_{n=0}^{n=N} \left[\binom{N}{n} \frac{\Gamma(N + Z^\theta - n + 1/2)}{(1 + b^\theta)^{N+Z^\theta-n+1/2}} \frac{\Gamma(n + Y + 1/2)}{(1 + b)^{n+Y+1/2}} \right].
 \end{aligned} \tag{A.14}$$

Since the following identities hold:

$$\begin{aligned}\Gamma(N + Z^\theta - n + 1/2) &= \Gamma(Z^\theta + 1/2) \prod_{j=1}^{j=N-n} (Z^\theta - 1/2 + j), \\ \Gamma(n + Y + 1/2) &= \Gamma(Y + 1/2) \prod_{j=1}^{j=n} (Y + 1/2 + j)\end{aligned}\tag{A.15}$$

we may rewrite $P(N|\theta, H_{\text{NP}})$ as

$$\begin{aligned}P(N|\theta, H_{\text{NP}}) &= \frac{1}{N!} \left(\frac{b^\theta}{1 + b^\theta} \right)^{Z^\theta + 1/2} \left(\frac{b}{1 + b} \right)^{Y + 1/2} \\ &\times \sum_{n=0}^{n=N} \left[\frac{N!}{(N-n)!n!} \prod_{j=1}^{j=N-n} \frac{Z^\theta - 1/2 + j}{1 + b^\theta} \prod_{j=1}^{j=n} \frac{Y - 1/2 + j}{1 + b} \right] \\ &= \sum_{n=0}^{n=N} A_n^N.\end{aligned}\tag{A.16}$$

with A_n^N defined as

$$\begin{aligned}A_n^N &= \left(\frac{b^\theta}{1 + b^\theta} \right)^{Z^\theta + 1/2} \left(\frac{b}{1 + b} \right)^{Y + 1/2} \\ &\times \prod_{j=1}^{j=N-n} \left[\frac{Z^\theta - 1/2 + j}{j(1 + b^\theta)} \right] \prod_{j=1}^{j=n} \left[\frac{Y - 1/2 + j}{j(1 + b)} \right]\end{aligned}\tag{A.17}$$

Following recurrence relations are valid for A_n^N :

$$A_n^N = \frac{Z^\theta - 1/2 + N - n}{(N - n)(1 + b^\theta)} A_n^{N-1},\tag{A.18}$$

$$A_n^N = \frac{(N - n + 1)(1 + b^\theta)}{Z^\theta - 1/2 + N - n + 1} \frac{Y - 1/2 + n}{n(1 + b)} A_{n-1}^N.\tag{A.19}$$

These relations can speed up exact calculation of the likelihood; e.g. to calculate $p(N|\theta, H_{\text{NP}})$ one can first derive A_0^0 , from which one can derive A_0^N using the relation in Equation A.18. Subsequently, using the relation in Equation A.19, one can derive all A_n^N for $n = 0, \dots, N$ and thus $P(N|\theta, H_{\text{NP}})$.

Appendix B

Notes on the interpretation

Of the 12000 pMSSM points sampled from the PLM likelihood that were used in Section 16.6, about 20% could not be processed due to a problem in the CMS simulation or reconstruction software. Especially points with low gluino mass are affected. To estimate the influence of this failure on the interpretation within the pMSSM, of the presented SUSY search, Figures B.1, B.2, B.3 and B.4 compare the distributions of the sparticle masses between all sampled points and the sampled points that pass all processing steps.

APPENDIX B

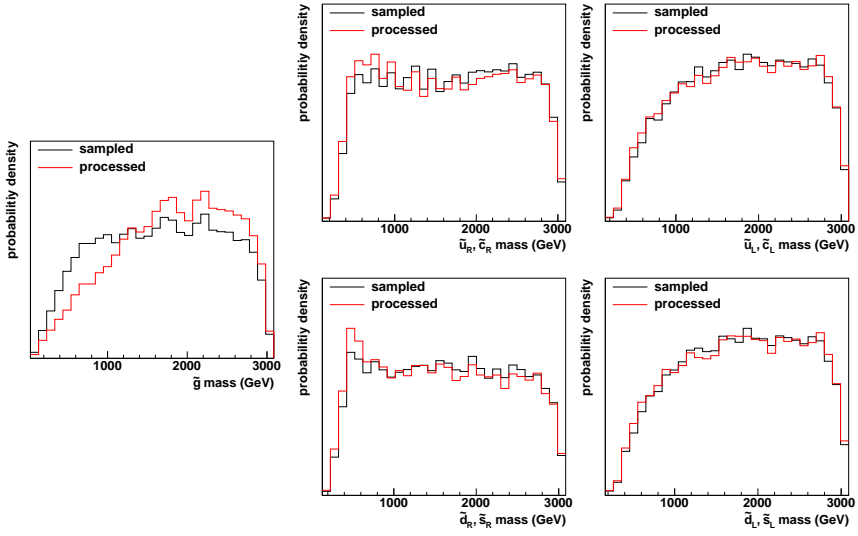


Figure B.1 – Posterior probability densities for the gluino mass, and the squark masses in the first and second sfermion generations.

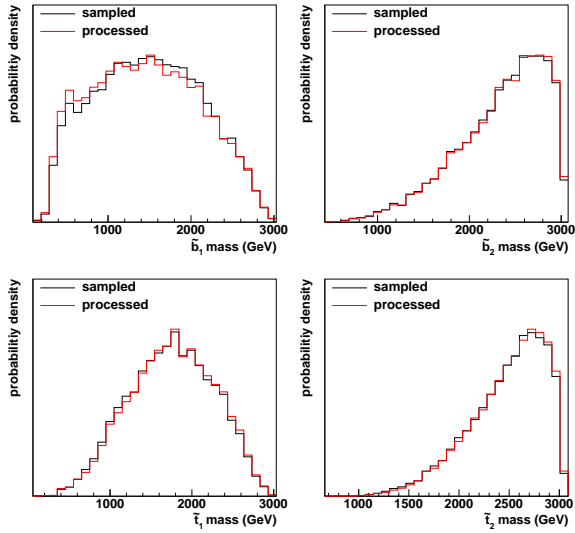


Figure B.2 – Posterior probability densities for the squark masses in the third sfermion generation.

NOTES ON THE INTERPRETATION

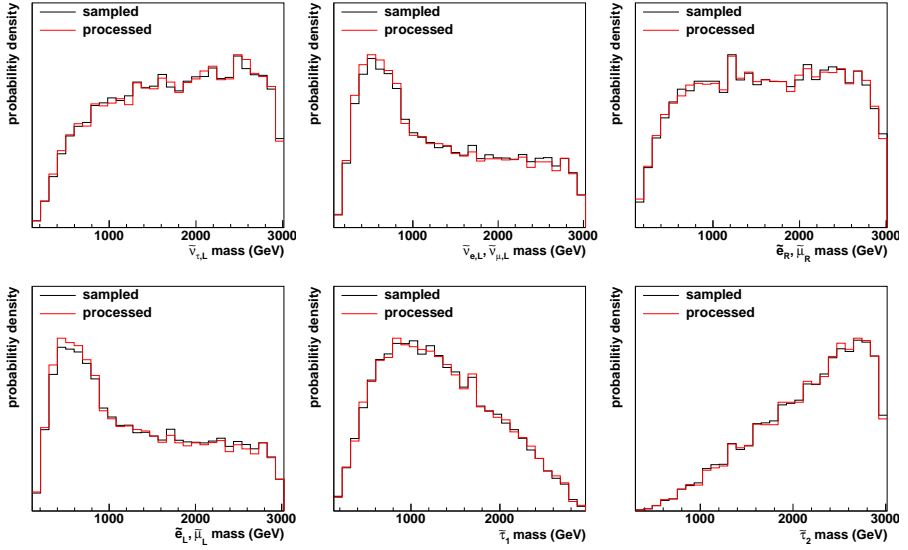


Figure B.3 – Posterior probability densities for the slepton masses.

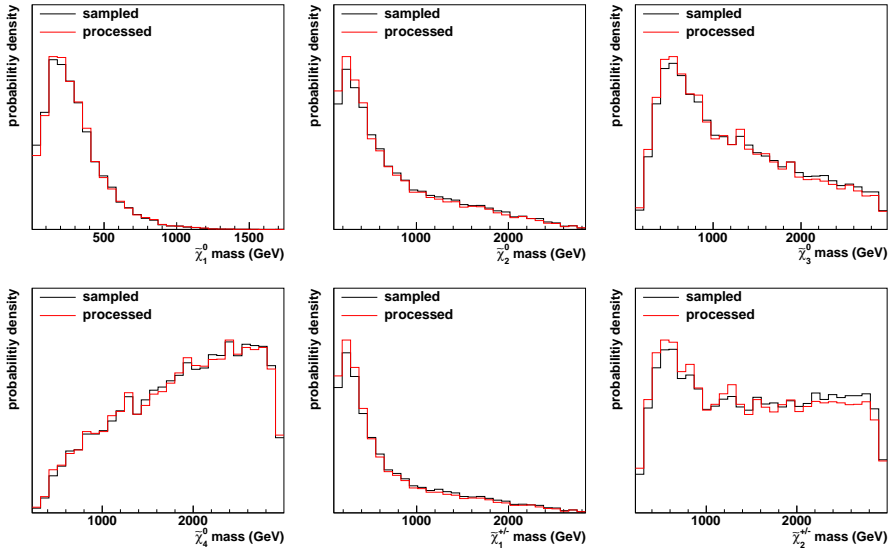


Figure B.4 – Posterior probability densities for the neutralino and chargino masses.

Samenvatting

Ons Universum is opgebouwd uit onvoorstelbaar veel onverstelbaar kleine deeltjes. De waarneembare materie bestaat uit up en down quarks en electronen. De up en down quarks zijn de bouwstenen van protonen en neutronen. De electronen vormen samen met protonen en neutronen de atomen. Ook heel courant zijn de neutrinos. Deze amper waarneembare spookdeeltjes bewegen dwars door alle materie heen.

In totaal hebben fysici twaalf soorten materiedeeltjes kunnen identificeren, zes zogenaamde quarks en zes zogenaamde leptonen. Deze materiedeeltjes interageren met elkaar door het uitwisselen van verschillende soorten krachtdeeltjes: fotonen voor de electro-magnetische kracht, gluonen voor de sterke kernkracht en vector bosonen voor de zwakke kernkracht. Deze deeltjes en hun interacties worden allen beschreven in een mathematisch model dat het Standaard Model van de deeltjesfysica wordt genoemd. Het Standaard Model werd in de jaren 60 en 70 ontwikkeld uit quantummechanica en relativiteitstheorie, gedreven door de spectaculaire experimentele bevindingen uit die periode. De experimenten uit de daarop volgende decenia maakten van het Standaard Model een van de meest succesvolle theorieën ooit, want keer op keer werden de voorspellingen van het Standaard Model bevestigd.

Echter, fysici zijn nog niet tevreden met het Standaard Model:

- Eerst en vooral is de experimentele bevestiging van het Standaard Model niet volledig zolang het zogenaamde Higgs-deeltje niet experimenteel is waargenomen. Het Higgs-deeltje is immers een hoeksteen van het Standaard Model die het mathematisch mogelijk maakt dat deeltjes een bepaalde massa bezitten.

SAMENVATTING

- Het model is ook niet allesomvattend, want de zwaartekracht kan er niet in opgenomen worden.
- Verder bezit het Standaard Model geen deeltjes met de eigenschappen van de zogenaamde donkere materie. Dit is een hypothetische vorm van materie die mee kan verklaren waarom sterrenstelsels zich net iets anders gedragen dan verwacht.
- Tenslotte zijn er een aantal zogenaamde fine-tuning problemen. Een fine-tuning treedt op wanneer kleine verandering in de theorie leiden tot enorme veranderingen in de voorspellingen. Volgens vele fysici vormt dit een aanwijzing dat het standaard model niet de meest fundamentele eigenschappen van de natuur beschrijft.

Dit, zijn de belangrijkste redenen waarom vele fysici de fundamentele eigenschappen van de materie blijven bestuderen. Enerzijds wil men de experimentele bevestiging van het Standaard Model vervolledigen door op zoek te gaan naar het Higgs-deeltje. Anderzijds denkt men theorieën uit die de 3 laatstgenoemde problemen oplossen en gaan ze op zoek naar experimentele bewijzen voor deze alternatieve of aanvullende theorieën.

Eén van de meest populaire en meest onderzochte aanvulling of uitbreiding van het Standaard Model is Super-Symmetrie, kortweg SUSY. Volgens het SUSY-model bestaat voor elk type Standaard Model deeltje een “super-symmetrische partner”. Dit is een deeltje met zeer gelijkaardige eigenschappen, behalve dat het een grotere massa heeft. Het bestaan van zulke SUSY-deeltjes lost de gekende fine-tuning problemen in belangrijke mate op, biedt een verklaring voor de donkere materie en zou misschien ook zwaartekracht kunnen omvatten. Tot nog toe kon echter geen enkel overtuigend experimenteel bewijs voor SUSY gevonden worden.

De zoektocht naar het Higgs-deeltje en naar SUSY-deeltjes vormden de belangrijkste motivatie voor de constructie van de Large Hadron Collider (LHC) te Genève, Zwitserland. Met behulp van deze deeltjesversneller proberen fysici Higgs-deeltjes en SUSY-deeltjes te produceren en op te meten. De LHC bevindt zich in een cirkelvormige tunnel, 27 km in omtrek en ongeveer 100 m onder de grond. Protonen worden er versneld in wijzers- en tegenwijzerszin en met elkaar in botsing gebracht op vier vaste punten. Rond deze botsingspunten zijn enorme detectoren gebouwd om deze botsingen als het ware te fotograferen. Het onderzoek beschreven in deze thesis speelt zich af aan één van deze detectoren, de Compact Muon Solenoid (CMS).

SAMENVATTING

Botsingen tussen protonen zijn extreem ingewikkelde processen. Vooreerst is elk proton een ingewikkeld systeem op zich, bestaande uit een groot aantal interagerende quarks en gluonen. Een botsing tussen twee protonen is dus in feite een botsing tussen twee gecompliceerde kluwen van quarks en gluonen. Wanneer daarbij twee quarks of gluonen hard met elkaar in botsing komen, dan worden nieuwe deeltjes gevormd. In extreem zeldzame gevallen zou dat kunnen gaan om Higgs- of SUSY-deeltjes. Hoe frequent deze zeldzame deeltjes geproduceerd worden, hangt sterk af van de bewegingsenergie van de botsende quarks en/of gluonen. Hoe groter die energie, hoe groter de kans op de productie van zware deeltjes zoals Higgs- en SUSY-deeltjes. Het is dus van groot belang dat de protonen voor het botsen tot een zo hoog mogelijke snelheid gebracht worden. LHC versnelt protonen tot een energie van 14TeV (net niet de lichtsnelheid), het absolute maximum binnen de huidige technische mogelijkheden. Deze drang naar een grote energie en dus snelheid verklaart ook de enorme afmetingen van LHC; een grotere versnelleromtrek laat een grotere protonenergie toe ¹.

De deeltjes die bij een proton-proton botsing gevormd worden, kennen een extreem kort bestaan, zo kort, dat deze deeltjes op geen enkele wijze rechtstreeks kunnen waargenomen worden. Wat wel kan waargenomen worden zijn de lawines aan secundaire deeltjes die de botsingen met zich meebrengen. Inderdaad, de initieel gevormde deeltjes vervallen quasi-onmiddellijk naar twee of meer deeltjes, die op hun beurt heel snel vervallen naar nog meer deeltjes. Op die manier wordt een kettingproces op gang gezet en ontstaan als het ware lawines van deeltjes die van het botsingspunt wegbewegen. Het zijn deze lawines van vervaldeeltjes die door De Cosmic Muon Solenoid opgemeten en geanalyseerd worden om zo na te gaan of er zich onder de initieel gevormde deeltjes Higgs- of SUSY-deeltjes bevinden.

Met de CMS detector tracht men dus de lawines van secundaire deeltjes die ontstaan bij de botsing tussen twee protonen op een zo precies en volledig mogelijke manier te “fotograferen”. Een eerste belangrijk element van CMS zijn de deeltjesdetectoren. Deze zijn in concentrische schillen geplaatst rond één van de botsingspunten van LHC. De binnenste schil ligt op slechts enkele centimeters van het botsingspunt terwijl de buitenste schil er meer dan tien meter van verwijderd is. Wanneer de lawinedeeltjes door deze concentrische schillen vliegen laten zij een spoor van licht achter, veroorzaakt door interacties met het detectormateriaal. Deze lichtsporen worden opgemeten door de deeltjesdetectoren, wat toelaat om zowel de trajecten als de energie van deze

¹Hoe groter de energie van het proton, hoe dichter zijn snelheid bij die van het licht komt. Om een proton tot de snelheid van het licht te brengen moet het, volgens de relativiteitstheorie, een oneindige hoeveelheid energie meegegeven worden, wat uiteraard onmogelijk is.

SAMENVATTING

deeltjes te reconstrueren. Om deze lichtsporen en dus het traject en de energie van elk lawinedeeltje met grote precisie te kunnen bepalen, bevat CMS ongeveer 100 miljoen individuele detectie-elementen.

Het andere belangrijke element van CMS is de magneet, een solenoïde van 4 meter doorsnede en 6 meter in lengte. Deze magneet is één van de krachtigste en grootste magneten ter wereld. Het enorme magnetische veld buigt geladen lawine-deeltjes af wanneer ze zich van het bostingspunt wegbewegen. Het opmeten van de afbuiging van een deeltje laat toe diens massa te bepalen.

Indien het Higgs-deeltje bestaat of als SUSY-deeltjes bestaan, worden zij in slechts een extreem klein fractie van de proton-proton botsingen geproduceerd. Het vinden van Higgs en SUSY-deeltjes in de vele miljoenen “foto’s” genomen door CMS wordt soms vergeleken met het zoeken naar een naald in een hooiberg. Deze vergelijking geeft echter de verhoudingen niet correct weer want de zoektocht naar deze hypothetische deeltjes is veel en veel moeilijker. Daarbij is de kennis van “achtergrond” processen van het grootste belang. Met achtergrond, bedoelen we hier elke gebeurtenis die kan geïnterpreteerd worden als de productie van Higgs- of SUSY-deeltjes, maar dat eigenlijk niet is. Zo een achtergrond gebeurtenis kan bijvoorbeeld veroorzaakt worden doordat elektronische ruis in de detectoren het beeld op één van de “foto’s” vervormt. Of, soms ontsnappen een deel van de deeltjes in de lawines de detector zonder enig spoor na te laten. Ook dit kan de beelden van CMS drastisch vervormen en de productie van een Higgs- of SUSY-deeltje emuleren.

Het eerste deel van het doctoraatsonderzoek beschreven in deze thesis behandelt een andere vorm van “achtergrond”. Het gaat hier om een type proton-proton botsingen waarbij het reeds gekend W -boson gevormd wordt. Het W -boson maakt deel uit van het Standaard Model. Het is een elektrisch geladen deeltje met een massa die 80 keer groter is dan de massa van het proton. Een kleine fractie van dit type botsingen lijkt erg goed op de productie van Higgs- en SUSY-deeltjes. In absolute cijfers verwacht men dat het aantal zulke botsingen erg klein is. Echter, vergeleken met het aantal botsingen waarbij Higgs- of SUSY-deeltjes gevormd zouden worden, kan dit aantal vrij groot zijn. Het is dan ook erg belangrijk om de productie van W -bosonen heel gedetailleerd in kaart te brengen. Daarom werd in de context van dit doctoraatsonderzoek de productiefrequentie van W -bosonen in proton-proton botsingen bepaald bij verschillende experimentele omstandigheden en vergeleken met geavanceerde voorspelling binnen het Standaard Model. We konden vaststellen dat, binnen de experimentele en theoretische onzekerheden, de voorspellingen erg goed overeenkomen met

SAMENVATTING

onze meetresultaten. Met behulp van dit resultaat kon een belangrijk deel van de achtergrondafschatting voor de zoektocht naar Higgs en SUSY gevalideerd worden.

Het tweede luik van het doctoraatsonderzoek beschreven in deze thesis behandelt de specifieke zoektocht naar SUSY-deeltjes. Een statistisch framework werd ontwikkeld om de resultaten van zulke zoektochten te interpreteren. Er wordt nagegaan of de resultaten van experimenten al dan niet aanwijzingen bevatten voor het bestaan van SUSY deeltjes en wat de implicaties zijn van experimentele bevindingen op de eigenschappen van eventuele SUSY-deeltjes.

De ontwikkelde methoden werden toegepast op een analyse van LHC data. Er werden geen aanwijzingen voor het bestaan van SUSY gevonden. Echter, de data bleek significante informatie te bevatten over de mogelijke eigenschappen van SUSY deeltjes.

Aldus draagt dit doctoraatsonderzoek op twee erg verscheiden manieren bij aan de zoektocht naar het Higgs-deeltje en naar SUSY-deeltjes. Enerzijds werd het begrip van de achtergrond processen verbeterd door de studie van het W -boson; anderzijds werd een statistisch framework ontwikkeld voor de interpretatie van LHC data in de zoektocht naar tot nog toe onbekende deeltjes, zoals SUSY-deeltjes.

Summary

The best of our knowledge about the fundamental building blocks of nature is synthesized in the Standard Model of particle physics. This model was developed during the seventies, driven by a number of spectacular experimental findings and revolutionary theoretical ideas. The following decades, the Standard Model became one of the greatest successes in physics ever, as it was able to describe almost all subsequent experimental findings in particle physics. At present, the last missing experimental corner stone is the long anticipated discovery of the Higgs boson.

Notwithstanding its great successes, it is generally accepted that the Standard Model cannot be the final theory of nature. The principal reason is that this model does not accommodate the fundamental interaction that is gravity. Furthermore, the Standard Model suffers from several fine tuning problems. These are extreme sensitivities of the theoretical predictions to small changes in the theory. Although not actual inconsistencies, many physicists believe that such sensitivities should not be expected from a fundamental theory. Another often used argument for the incompleteness of the Standard Model is that it does not possess a particle that has the right properties to constitute dark matter. Dark matter is a hypothetical form of matter in the Universe, that was introduced to explain the observed behavior of Galaxies.

Physicists have developed several theoretical scenarios that solve one or more of these problems. Most of these scenarios predict, apart from the Standard Model particles, the existence of additional particles. Probably the most popular such theory is Super Symmetry (SUSY). In this model, each of the Standard Model particle types possesses a Super Symmetric partner with similar properties, though larger mass.

SUMMARY

The search for the Higgs boson and for SUSY particles is the main reason for the construction of the Large Hadron Collider (LHC) and its experiments. The LHC is a circular accelerator that collides protons at a center of mass energy of 7 TeV and, within a few years, around 14 TeV. Physicists record and analyze these collisions which huge particle detectors, built around the 4 fixed collision points in LHC. In these recorded collisions, physicists hope to find evidence for the production of Higgs bosons, SUSY particles or any other never-observed phenomenon, not accommodated by the Standard Model.

A condicio sine qua non for the experimental confirmation or exclusion of such hypothetical phenomena, is a good understanding of the Standard Model processes that take place in proton-proton collisions. Indeed the predicted production rate of the new phenomena is often extremely low, and not rarely are these new phenomena barely distinguishable from certain Standard Model processes. This implies that, in order to prove the production of unknown particles, the known Standard Model particle production processes must be understood in great detail.

One of the most important such Standard Model processes is the production of W and Z + jets, which forms the first research topic of this thesis. The production of W and Z in association with multiple jets shows properties that are very similar to the expected properties of many of the new phenomena anticipated at the LHC, and thus, the searches for these phenomena depend dramatically on a detailed understanding of the W and Z + jets production processes. The prediction of W and Z + jets production is however, quite a challenging business and therefore, the validation of these predictions with measurements is a crucial prerequisite for the potential discovery of new physics.

For that reason, we studied in the first part of this thesis, the production of W and Z + jets, in the proton-proton collision data collected by the Compact Muon Solenoid in 2010. The analyzed data correspond to an integrated luminosity of 35 pb^{-1} and the studied proton collisions took place at a center of mass energy of $\sqrt{s} = 7 \text{ TeV}$. In these data, we measured the production rate as a function of the number of jets produced in association with the vector bosons.

Special care was taken to keep the dependence of this study on theoretical predictions and detector simulation at a low level. A first measure in this context is the measurement of ratios, in which several important systematic uncertainties cancel out or in which their impact reduces significantly. A second important measure is the design of the signal extraction. The developed signal extraction method makes use

SUMMARY

of an unbinned Maximum Likelihood fit with functional forms. The discriminating variables and functional forms used, were chosen such to enable a robust calibration and multiple cross checks in simultaneous measurements.

Our final measurement results are ratios of production rates or ratio-like variables such as the parameters describing the Berends-Giele scaling. All results were corrected to the particle level. This required to compensate the finite reconstruction and selection efficiency of the vector bosons, to correct for pile-up effects and to unfold the jet multiplicity spectrum for detector effects. Within the acceptance of the measurement, our results can be compared directly to predictions that include parton showering, hadronization and underlying event. Comparing our results to similar measurements, also quoted on the particle level, requires straightforward but model-dependent corrections for the differences in acceptance.

We compared our results to theoretical predictions. A first set of predictions was generated with PYTHIA 6. In these predictions, vector boson production with 0 and 1 jets is calculated exactly at leading order. Higher order corrections leading to additional jets are included in the parton shower and also the effects of hadronization and the underlying event are included in these predictions. As expected, these predictions describe very well our measurements for W and Z production with 0 and 1 jets, but break down at higher jet multiplicities. The other set of predictions to which we compared our results, was generated with MADGRAPH 4, for the hard interaction, interfaced with PYTHIA 6 according to the MLM description, to describe the parton shower, hadronization and underlying event. These MADGRAPH predictions include exact leading order calculations for the production of vector bosons in association with up to 5 hard partons. Within uncertainties, these predictions describe our measurements very well.

The second research topic of this thesis deals with searches for new phenomena. Most searches for new physics make use of count experiments. Such experiments simply count the number of events that pass certain selection criteria and compares the observed number of events to predictions. In this thesis, a Bayesian framework for searches for new physics in count experiments is set up. Three basic interpretation elements are constructed:

i) posterior probability for a generic new physics source

This posterior quantifies whether or not the observation provides evidence for the presence of a new physics source of events without making assumptions about the properties of the new physics.

SUMMARY

ii) posterior probability density for the strength of the generic new physics source

In the same model independent manner we construct a posterior probability density for the potential strength of the generic new physics source.

iii) posterior probability density for the parameters of a specific new physics model

We propose a method to evaluate the impact of the observation on a specific new physics model with free parameters. Thereby we take into account all available other information, both from experimental and theoretical origin.

A straightforward generalization to the combined interpretation of count experiments is also provided.

The developed Bayesian tools are applied in a search in pp collision data at $\sqrt{s} = 7$ TeV, corresponding to 3.270 fb^{-1} and collected by CMS in 2011. Events are selected with $H_T > 400$ GeV, $E_T^{miss} > 250$ GeV and at least 3 jets. An angular variable is used to reject events with fake E_T^{miss} , originating from jet mismeasurement. Since this search focused on b -rich SUSY scenarios events must have at least one b -jet. In the selected part of phase space, 12 independent count experiments are defined, corresponding to events with 3, 4, 5 and 6 jets and events with 1, 2 and 3 b -jets. The model independent interpretation is applied to the observations in all 12 count experiments simultaneously and no indications for new physics is found.

Then, we interpret these observations within the phenomenological MSSM, a rather unconstrained 19-dimensional realization of the MSSM. To evaluate the current experimental status of the pMSSM, we perform a combined interpretation of our search, a number of important pre-LHC measurements, and another CMS search, the “ α_T ” measurement. The both CMS measurements significantly disfavor the regions of low mass for several squarks and the gluino. In general the “ α_T ” measurement provides more stringent constraints than our measurement, except for the case of the sbottom mass, where our measurement has the most constraining power.

The developed Bayesian tools for the interpretation of count experiments lead in a natural way to an elegant method for the optimization of searches. A preliminary attempt was made to apply this optimization method to the search presented in this thesis. The findings are described in the discussion of this thesis.

Thus, the PhD research presented in this thesis contributed in two very diverse ways to the search for new phenomena at the LHC. On the one hand, through the study of W and $Z +$ jets production it enabled a better understanding of the Standard Model background to searches. On the other hand, a Bayesian framework

SUMMARY

for the interpretation of searches for new physics in count experiments was developed and validated in a search with jets, b -jets and E_T^{miss} . Furthermore a method for the optimization of searches was suggested which might contribute to more efficient search efforts at the LHC.

List of acronyms

CMS	Compact Muon Solenoid
DT	Drift Tube
RPC	Resistive Plate Chamber
CSC	Cathode Strip Chamber
L1	Level 1
HLT	High Level Trigger
LHC	Large Hadron Collider
LEP	Large Electron Positron collider
QCD	Quantum Chromo Dynamics
NLO	Next to Leading Order
NNLO	Next to Next to Leading Order
LO	Leading Order
PDF	Parton Density Function
PDF	Probability Density Function
MC	Monte Carlo
KF	Kalman Filter
GSF	Gaussian Sum Filter
PV	Primary Vertex
TCHE	Track Counting High Efficiency <i>b</i> -tagger
TCHEM	TCHEM Medium workpoint
IP	Impact Parameter
CSV	Combined Secondary Vertex <i>b</i> -tagger
CSV	CSV Medium workpoint
SM	Standard Model

LIST OF ACRONYMS

EWK	Electro WeaK
PDG	Particle Data Group
SUSY	SUperSYmmetry
LSP	Lightest Supersymmetric Particle
MSSM	Minimal Supersymmetric extension of the Standard Model
pMSSM	Phenomenological MSSM
cMSSM	Constrained MSSM
SMS	Simplified ModelS
PLM	Pre-LHC Measurement
TSN	True State of Nature
GSL	Gnu Scientific Library
MCMC	Markov Chain Monte Carlo
BG	Berends-Giele
TnP	Tag and Probe
JEC	Jet Energy Correction
ML	Maximum Likelihood
SVD	Singular Value Decomposition
PF	Particle Flow
JES	Jet Energy Scaling
HCAL	Hadronic CALorimeter
ECAL	Electromagnetic CALorimeter
HB	Hadronic calorimeter in Barrel region
HO	Hadronic calorimeter in barrel region
PS	PreShower

Bibliography

- [1] Donald H. Perkins, “Introduction to high energy physics,” Cambridge University Press (2000).
- [2] C. D. Anderson, “The Apparent Existence of Easily Deflectable Positives,” *Science* **76**, 238-239 (1932).
- [3] S. H. Neddermeyer, C. D. Anderson, “Note On The Nature Of Cosmic Ray Particles,” *Phys. Rev.* **51**, 884-886 (1937).
- [4] E. D. Bloom, D. H. Coward, H. C. DeStaebler, J. Drees, G. Miller, L. W. Mo, R. E. Taylor, M. Breidenbach *et al.*, “High-Energy Inelastic e p Scattering at 6-Degrees and 10-Degrees,” *Phys. Rev. Lett.* **23**, 930-934 (1969).
- [5] M. Breidenbach, J. I. Friedman, H. W. Kendall, E. D. Bloom, D. H. Coward, H. C. DeStaebler, J. Drees, L. W. Mo *et al.*, “Observed Behavior of Highly Inelastic electron-Proton Scattering,” *Phys. Rev. Lett.* **23**, 935-939 (1969).
- [6] F. J. Hasert *et al.* [Gargamelle Neutrino Collaboration], “Observation of Neutrino Like Interactions Without Muon Or Electron in the Gargamelle Neutrino Experiment,” *Phys. Lett.* **B46**, 138-140 (1973).
- [7] G. Arnison *et al.* [UA1 Collaboration], “Experimental Observation of Isolated Large Transverse Energy Electrons with Associated Missing Energy at $s^{1/2} = 540$ -GeV,” *Phys. Lett.* **B122**, 103-116 (1983).
- [8] M. Banner *et al.* [UA2 Collaboration], “Observation of Single Isolated Electrons of High Transverse Momentum in Events with Missing Transverse Energy at the CERN anti-p p Collider,” *Phys. Lett.* **B122**, 476-485 (1983).

BIBLIOGRAPHY

- [9] G. Arnison *et al.* [UA1 Collaboration], “Experimental Observation of Lepton Pairs of Invariant Mass Around 95-GeV/ c^2 at the CERN SPS Collider,” Phys. Lett. **B126**, 398-410 (1983).
- [10] P. Bagnaia *et al.* [UA2 Collaboration], “Evidence for $Z^0 \rightarrow e^+ e^-$ at the CERN anti-p p Collider,” Phys. Lett. **B129**, 130-140 (1983).
- [11] G. S. Abrams, C. Adolphsen, D. Averill, J. Ballam, B. C. Barish, T. Barklow, B. A. Barnett, J. E. Bartelt *et al.*, “Measurements of Z Boson Resonance Parameters in e^+e^- Annihilation,” Phys. Rev. Lett. **63**, 2173 (1989).
- [12] S. Abachi *et al.* [D0 Collaboration], “Search for high mass top quark production in $p\bar{p}$ collisions at $\sqrt{s} = 1.8$ TeV,” Phys. Rev. Lett. **74**, 2422-2426 (1995). [hep-ex/9411001].
- [13] F. Abe *et al.* [CDF Collaboration], “Observation of top quark production in $p\bar{p}$ collisions,” Phys. Rev. Lett. **74**, 2626-2631 (1995). [hep-ex/9503002].
- [14] S. P. Martin, “A Supersymmetry primer,” In *Kane, G.L. (ed.): Perspectives on supersymmetry* 1-98. [hep-ph/9709356].
- [15] Peccei, R. D. and Quinn, Helen R., “CP Conservation in the Presence of Pseudoparticles,” Phys. Rev. Lett. **34**, 1440–1443 (1977). doi:10.1103/PhysRevLett.38.1440
- [16] CMS Collaboration, “Jet Production Rates in Association with W and Z Bosons in pp Collisions at $\sqrt{s} = 7$ TeV,” Accepted for publication by JHEP (2012). arXiv:1110.3226 [hep-ex].
- [17] M. E. Peskin and D. V. Schroeder “An Introduction to Quantum Field Theory,” Addison-Wesley Advanced Book Program (1995).
- [18] R. K. Ellis, W. J. Stirling, B. R. Webber, “QCD and Collider Physics,” Cambridge Monographs on Particle Physics, Nuclear Physics and Cosmology (1996).
- [19] B. Povh, K. Rith, C. Scholz, F. Zetsche, “Particles and Nuclei, An Introduction to the Physical Concepts,” Springer-Verlag Berlin Heidelberg (1995).
- [20] K. Nakamura *et al.* [Particle Data Group Collaboration], “Review of particle physics,” J. Phys. G **G37**, 075021 (2010) and 2011 partial update for the 2012 edition .
- [21] J. H. Schwarz, N. Seiberg, “String theory, supersymmetry, unification, and all that,” Rev. Mod. Phys. **71**, S112-S120 (1999). [hep-th/9803179].

BIBLIOGRAPHY

- [22] E. Komatsu *et al.* [WMAP Collaboration], “Five-Year Wilkinson Microwave Anisotropy Probe (WMAP) Observations: Cosmological Interpretation,” *Astrophys. J. Suppl.* **180**, 330-376 (2009). [arXiv:0803.0547 [astro-ph]].
- [23] MSSM Working Group, A. Djouadi *et al.*, “The Minimal supersymmetric standard model: Group summary report,” (1999). hep-ph/9901246
- [24] T. Sjostrand, S. Mrenna, P. Z. Skands, “PYTHIA 6.4 Physics and Manual,” *JHEP* **0605**, 026 (2006). [hep-ph/0603175].
- [25] J. M. Campbell, J. W. Huston, W. J. Stirling, “Hard Interactions of Quarks and Gluons: A Primer for LHC Physics,” *Rept. Prog. Phys.* **70**, 89 (2007). [hep-ph/0611148].
- [26] T. Gleisberg, S. Hoeche, F. Krauss, M. Schonherr, S. Schumann, F. Siegert, J. Winter, “Event generation with SHERPA 1.1,” *JHEP* **0902**, 007 (2009). [arXiv:0811.4622 [hep-ph]].
- [27] G. P. Salam, “Towards Jetography,” *Eur. Phys. J.* **C67**, 637-686 (2010). [arXiv:0906.1833 [hep-ph]].
- [28] M. L. Mangano, M. Moretti, F. Piccinini, M. Treccani, “Matching matrix elements and shower evolution for top-quark production in hadronic collisions,” *JHEP* **0701**, 013 (2007). [hep-ph/0611129].
- [29] S. Catani, F. Krauss, R. Kuhn, B. R. Webber, “QCD matrix elements + parton showers,” *JHEP* **0111**, 063 (2001). [hep-ph/0109231].
- [30] L. Lonnblad, “Correcting the color dipole cascade model with fixed order matrix elements,” *JHEP* **0205**, 046 (2002). [hep-ph/0112284].
- [31] R. D. Ball, L. Del Debbio, S. Forte, A. Guffanti, J. I. Latorre, J. Rojo and M. Ubiali, “A first unbiased global NLO determination of parton distributions and their uncertainties,” *Nucl. Phys. B* **838**, 136 (2010) [arXiv:1002.4407 [hep-ph]].
- [32] <https://indico.cern.ch/contributionDisplay.py?contribId=1&confId=145744>
- [33] A. Buckley, H. Hoeth, H. Lacker, H. Schulz, J. E. von Seggern, “Systematic event generator tuning for the LHC,” *Eur. Phys. J.* **C65**, 331-357 (2010). [arXiv:0907.2973 [hep-ph]].
- [34] L. Evans, (ed.), P. Bryant, (ed.), “LHC Machine,” *JINST* **3**, S08001 (2008).

BIBLIOGRAPHY

- [35] <https://twiki.cern.ch/twiki/bin/view/CMSPublic/LumiPublicResults>
- [36] <https://twiki.cern.ch/twiki/bin/view/AtlasPublic/LuminosityPublicResults>
- [37] <http://cerncourier.com/cws/article/cern/34932>
- [38] CMS Collaboration, “The CMS experiment at the CERN LHC,” JINST **3**, S08004 (2008).
- [39] CMS Collaboration, “Particle-Flow Event Reconstruction in CMS and Performance for Jets, Taus, and E_T^{miss} ,” CMS Physics Analysis Summary CMS-PAS-PFT-09-001 (2009).
- [40] CMS Collaboration, “Commissioning of the Particle-Flow Reconstruction in Minimum-Bias and Jet Events from pp Collisions at 7 TeV,” CMS Physics Analysis Summary CMS-PAS-PFT-10-002 (2010).
- [41] R. Fruhwirth, “Application of Kalman filtering to track and vertex fitting,” Nucl. Instrum. Meth. **A262**, 444-450 (1987).
- [42] CMS Collaboration, “Tracking and Primary Vertex Results in First 7 TeV Collisions,” CMS Physics Analysis Summary CMS-PAS-TRK-10-005 (2010).
- [43] CMS Collaboration, “Track reconstruction in the CMS Tracker,” unpublished manuscript, CMS Physics Analysis Summary CMS-PAS-TRK-09-001 (2009).
- [44] CMS Collaboration, “Performance of CMS Muon Reconstruction in Cosmic-Ray Events,” JINST **5**, T03022 (2010). [arXiv:0911.4994 [physics.ins-det]].
- [45] CMS Collaboration, “The CMS Physics Technical Design Report, Volume I: Detector Performance and Software,” CERN/LHCC 2006-001 (2006). CMS TDR.
- [46] CMS Collaboration, “Particle-flow commissioning with muons and electrons from J/Psi, and W events at 7 TeV,” CMS Physics Analysis Summary CMS-PAS-PFT-010-003 (2010).
- [47] F. Beaudette, *et al.*, “Electron Reconstruction within the Particle Flow Algorithm,” CMS Analysis Note CMS-AN-2010-034 (2009).
- [48] W. Adam, R. Fruhwirth, A. Strandlie, T. Todorov, “Reconstruction of electrons with the Gaussian sum filter in the CMS tracker at LHC,” Journal of Physics G: Nuclear and Particle Physics **31** (2005) N9. doi:10.1088/0954-3899/31/9/N01 [physics/0306087].

BIBLIOGRAPHY

- [49] Michele Pioppi, “Electron Pre-identification in the Particle Flow framework,” CMS Analysis Note CMS-AN-2008-032 (2008).
- [50] <http://tmva.sourceforge.net/docu/TMVAUsersGuide.pdf>
- [51] W. Erdman, “Offline Primary Vertex Reconstruction with Deterministic Annealing Clustering,” CMS Internal Note CMS-IN-2011-014.
- [52] M. Cacciari, G. P. Salam, G. Soyez, “The Anti- k_t jet clustering algorithm,” JHEP **0804**, 063 (2008). [arXiv:0802.1189 [hep-ph]].
- [53] CMS Collaboration, “Performance of b-jet identification in CMS,” CMS Physics Analysis Summary CMS-BTV-11-001 (2011).
- [54] C. Weiser “A Combined Secondary Vertex Based B-Tagging Algorithm in CMS,” CMS Note, CMS-NOTE-2006-014 (2006).
- [55] CMS Collaboration, “Search for Supersymmetry at the LHC in Events with Jets and Missing Transverse Energy,” [arXiv:1109.2352 [hep-ex]].
- [56] G. Aad *et al.* [Atlas Collaboration], “Search for new phenomena in final states with large jet multiplicities and missing transverse momentum using $\sqrt{s}=7$ TeV pp collisions with the ATLAS detector,” [arXiv:1110.2299 [hep-ex]].
- [57] CMS Collaboration, “Search for supersymmetry in events with a lepton, a photon, and large missing transverse energy in pp collisions at $\sqrt{s} = 7$ TeV,” JHEP **1106**, 093 (2011). [arXiv:1105.3152 [hep-ex]].
- [58] G. Aad *et al.* [Atlas Collaboration], “Search for supersymmetry using final states with one lepton, jets, and missing transverse momentum with the ATLAS detector in $\sqrt{s} = 7$ TeV pp,” Phys. Rev. Lett. **106**, 131802 (2011). [arXiv:1102.2357 [hep-ex]].
- [59] M. L. Mangano, M. Moretti, F. Piccinini, R. Pittau, A. D. Polosa, “ALPGEN, a generator for hard multiparton processes in hadronic collisions,” JHEP **0307**, 001 (2003). [hep-ph/0206293].
- [60] F. Maltoni, T. Stelzer, “MadEvent: Automatic event generation with MadGraph,” JHEP **0302** (2003) 027. [hep-ph/0208156].
- [61] F. Krauss, R. Kuhn, G. Soff, “AMEGIC++ 1.0: A Matrix element generator in C++,” JHEP **0202**, 044 (2002). [hep-ph/0109036].

BIBLIOGRAPHY

- [62] T. Aaltonen *et al.* [CDF Collaboration], “Measurement of the cross section for W -boson production in association with jets in $p\bar{p}$ collisions at $\sqrt{s} = 1.96$ -TeV,” *Phys. Rev.* **D77**, 011108 (2008). [arXiv:0711.4044 [hep-ex]].
- [63] T. Aaltonen *et al.* [CDF - Run II Collaboration], “Measurement of inclusive jet cross-sections in $Z/\gamma^*(\rightarrow e^+e^-) +$ jets production in $p\bar{p}$ collisions at $\sqrt{s} = 1.96$ -TeV,” *Phys. Rev. Lett.* **100**, 102001 (2008).
- [64] V. M. Abazov *et al.* [D0 Collaboration], “Measurements of differential cross sections of $Z/\gamma^*+jets+X$ events in proton anti-proton collisions at $s^{1/2} = 1.96$ -TeV,” *Phys. Lett.* **B678**, 45-54 (2009). [arXiv:0903.1748 [hep-ex]].
- [65] R. K. Ellis, K. Melnikov, G. Zanderighi, “W+3 jet production at the Tevatron,” *Phys. Rev.* **D80**, 094002 (2009). [arXiv:0906.1445 [hep-ph]].
- [66] C. F. Berger, Z. Bern, L. J. Dixon, F. Febres Cordero, D. Forde, T. Gleisberg, H. Ita, D. A. Kosower *et al.*, “Next-to-Leading Order QCD Predictions for W+3-Jet Distributions at Hadron Colliders,” *Phys. Rev.* **D80**, 074036 (2009). [arXiv:0907.1984 [hep-ph]].
- [67] V. M. Abazov *et al.* [D0 Collaboration], “Measurements of inclusive W +jets production rates as a function of jet transverse momentum in $p\bar{p}$ collisions at $\sqrt{s} = 1.96$ TeV,” Submitted to: *Phys.Lett.B.* [arXiv:1106.1457 [hep-ex]].
- [68] C. F. Berger, Z. Bern, L. J. Dixon, F. Febres Cordero, D. Forde, T. Gleisberg, H. Ita, D. A. Kosower *et al.*, “Precise Predictions for W + 4 Jet Production at the Large Hadron Collider,” *Phys. Rev. Lett.* **106**, 092001 (2011). [arXiv:1009.2338 [hep-ph]].
- [69] B. Cooper, J. Katzy, M. L. Mangano, A. Messina, L. Mijovic, P. Skands, “Monte Carlo tuning in the presence of Matching,” [arXiv:1109.5295 [hep-ph]].
- [70] T. Aaltonen *et al.* [CDF Collaboration], “First Measurement of the b-jet Cross Section in Events with a W Boson in p anti-p Collisions at $s^{**}(1/2) = 1.96$ -TeV,” *Phys. Rev. Lett.* **104**, 131801 (2010). [arXiv:0909.1505 [hep-ex]].
- [71] V. M. Abazov *et al.* [D0 Collaboration], “Measurement of the ratio of the $p\bar{p} \rightarrow W^+c^-$ jet cross section to the inclusive $p\bar{p} \rightarrow W +$ jets cross section,” *Phys. Lett.* **B666**, 23-30 (2008). [arXiv:0803.2259 [hep-ex]].
- [72] V. M. Abazov *et al.* [D0 Collaboration], “Measurement of the shape of the boson rapidity distribution for $p\bar{p} \rightarrow Z/\gamma^* \rightarrow e^+e^- + X$ events produced

BIBLIOGRAPHY

- at \sqrt{s} of 1.96-TeV,” Phys. Rev. **D76**, 012003 (2007). [hep-ex/0702025 [HEP-EX]]. hep-ex/0702025
- [73] The ATLAS collaboration, “Measurement of the production cross section for Z/ in association with jets in pp collisions at $s = 7$ TeV with the ATLAS Detector,” ATLAS-CONF-2011-042 (2011).
- [74] The ATLAS collaboration, “Measurement of the production cross section for W-bosons in association with jets in pp collisions using 33 pb⁻¹ at $\sqrt{s} = 7$ TeV with the ATLAS detector,” ATLAS-CONF-2011-060 (2011).
- [75] G. Aad *et al.* [ATLAS Collaboration], “A measurement of the ratio of the W and Z cross sections with exactly one associated jet in pp collisions at $\sqrt{s} = 7$ TeV with ATLAS,” [arXiv:1108.4908 [hep-ex]].
- [76] G. Aad *et al.* [ATLAS Collaboration], “Measurement of the cross-section for b-jets produced in association with a Z boson at $\sqrt{s}=7$ TeV with the ATLAS detector,” arXiv:1109.1403 [hep-ex].
- [77] G. Aad *et al.* [ATLAS Collaboration], “Measurement of the cross section for the production of a W boson in association with b-jets in pp collisions at $s = 7$ TeV with the ATLAS detector” arXiv:1109.1470v1 [hep-ex].
- [78] CMS Collaboration, “Measurement of the Polarization of W Bosons with Large Transverse Momenta in W+Jets Events at the LHC,” Phys. Rev. Lett. **107**, 021802 (2011).
- [79] CMS Collaboration, “Study of associated charm production in W final states at $\sqrt{s} = 7$ TeV,” CMS-PAS-EWK-11-013 (2011).
- [80] CMS Collaboration, “Observation of Z+b,” CMS-PAS-EWK-10-015 (2011).
- [81] S.D. Ellis, R. Kleiss, W.James Stirling, “W’s, Z’s and Jets,” Phys. Lett. **B154**, 435 (1985).
- [82] F. A. Berends, W. T. Giele, H. Kuijf, R. Kleiss, W. J. Stirling, “Multi-jet production in W, Z events at p anti-p colliders” Phys. Lett. **B224**, 237 (1989).
- [83] F. A. Berends, H. Kuijf, B. Tausk, W. T. Giele, “On the production of a W and jets at hadron colliders” Nucl. Phys. **B357**, 32-64 (1991).
- [84] M. Bona *et al.*, “The Z($\rightarrow ee$) + jets data candle,” CMS-AN-2008-092 (2008).
- [85] M. Bona *et al.*, “The Z($\rightarrow \mu\mu$) + jets data candle,” CMS-AN-2008-095 (2008).

BIBLIOGRAPHY

- [86] M. Bona *et al.*, “The Ratio of $W(\rightarrow e\nu) + N$ jets to $Z(\rightarrow ee) + N$ jets Versus N ,” CMS-AN-2008-096 (2008).
- [87] M. Bona *et al.*, “The Ratio of $W(\rightarrow \mu\nu) + N$ jets to $Z(\rightarrow \mu\mu) + N$ jets Versus N ,” CMS-AN-2008-105 (2008).
- [88] M. Bona *et al.*, “The W+jets/Z+jets Ratio at CMS with pp collisions at center-of-mass energy 10 TeV,” CMS-AN-2009-045 (2009).
- [89] M. Bona *et al.*, “The Z+jets candle in dielectron+jets and dimuon+jets final states at CMS with pp collisions at center-of-mass energy 10 TeV,” CMS-AN-2009-092 (2009).
- [90] S. Bolognesi *et al.*, “Measurement of Berends-Giele Scaling and Z+jets/W+jets cross-section ratio with muon final states using full Particle-Flow analysis,” CMS-AN-2010-384 (2010).
- [91] N. Akchurin *et al.*, “Measurement of the Associated Production of Vector Bosons and Jets in proton-proton collisions at $\sqrt{s} = 7$ TeV,” CMS-AN-2010-413 (2010).
- [92] S. Bolognesi *et al.*, “Measurement of the $W \rightarrow e\nu +$ jets and $Z \rightarrow ee +$ jets ratio in proton-proton collisions at $\sqrt{s} = 7$ TeV,” CMS-AN-2010-425 (2010).
- [93] S. Bolognesi *et al.*, “Subtracting the background from top quark production in the $W \rightarrow l\nu$ measurements,” CMS-AN-2010-461 (2010).
- [94] Massimo Nespolo, “Measurement of the production of W bosons in association with jets in pp collisions at $\sqrt{s} = 7$ TeV (muon channel),” CMS-AN-2011-008 (2011).
- [95] V. Ciulli, E. Gallo, S. Gonzi, P. Lenzi, “Extraction of $Z \rightarrow \mu\mu$ signal yields as a function of jet multiplicity at $\sqrt{s} = 7$ TEV,” CMS-AN-2011-014 (2011).
- [96] F. Cavallari, E. Di Marco, F. Micheli, C. Rovelli, “Measurement of the electron charge asymmetry in $W \rightarrow e\nu +$ jets in proton-proton collisions at $\sqrt{s} = 7$ TeV,” CMS-AN-2011-162 (2011).
- [97] S. Dasu *et al.*, “Efficiency correction and unfolding for V+jets events,” CMS-AN-2011-017 (2011).
- [98] N. Akchurin, J. Damgov, S.W. Lee, E. Yazgan, “Estimation of the systematic uncertainties in jet rates for V+jets, related to the uncertainties in jet and MET scale and resolution for pp at $\sqrt{s}=7$ TeV,” CMS-AN-2011-046 (2011).

BIBLIOGRAPHY

- [99] S. Dasu *et al.*, “Analysis of V+jets production in the electron channels,” CMS-AN-2011-136 (2011).
- [100] C. Buttar, J. D’Hondt, M. Kramer, G. Salam, M. Wobisch, N. E. Adam, V. Adler, A. Arbuzov *et al.*, “Standard Model Handles and Candles Working Group: Tools and Jets Summary Report,” Prepared for 5th Les Houches Workshop on Physics, [arXiv:0803.0678 [hep-ph]].
- [101] <https://twiki.cern.ch/twiki/bin/view/CMS/ProductionFall12010>
- [102] J. Pumplin, D. R. Stump, J. Huston, H. L. Lai, P. M. Nadolsky, W. K. Tung, “New generation of parton distributions with uncertainties from global QCD analysis,” JHEP **0207**, 012 (2002). [arXiv:hep-ph/0201195 [hep-ph]].
- [103] CMS Collaboration, “Measurement of the Underlying Event Activity in Proton-Proton Collisions at 900 GeV,” [arXiv:1006.2083v1 [hep-ex]]
- [104] S. Agostinelli *et al.* [GEANT4 Collaboration], “GEANT4: A Simulation toolkit,” Nucl. Instrum. Meth. **A506**, 250-303 (2003).
- [105] M. Cacciari, G. P. Salam, “Pileup subtraction using jet areas,” Phys. Lett. **B659**, 119-126 (2008). [arXiv:0707.1378 [hep-ph]].
- [106] CMS Collaboration, “Determination of Jet Energy Calibration and Transverse Momentum Resolution in CMS,” CMS-JME-10-011 (2010). [arXiv:1107.4277 [physics.ins-det]].
- [107] CMS Collaboration, “Measurement of Tracking Efficiency,” CMS-TRK-10-002 (2010).
- [108] <http://root.cern.ch/drupal/content/roofit>
- [109] F. James, M. Roos, “Minuit: A System for Function Minimization and Analysis of the Parameter Errors and Correlations,” Comput. Phys. Commun. **10**, 343-367 (1975).
- [110] https://twiki.cern.ch/twiki/bin/view/CMS/SimpleCutBasedEleID#Selections_and_How_to_use_them, the 90% working point.
- [111] CMS Collaboration, “Jet Energy Resolution in CMS at sqrt(s)=7 TeV,” CMS-PAS-JME-10-014 (2010).
- [112] A. Hocker, V. Kartvelishvili, “SVD approach to data unfolding,” Nucl. Instrum. Meth. **A372**, 469-481 (1996). [hep-ph/9509307].

BIBLIOGRAPHY

- [113] T. Adye, “Unfolding algorithms and tests using RooUnfold,” (2011). [arXiv:1105.1160 [physics.data-an]].
- [114] T. Adye, “Unfolding algorithms and tests using RooUnfold,” (2011). [arXiv:1105.1160 [physics.data-an]].
- [115] G. Majumder *et al.*, “Muon Pseudorapidity and Charge Asymmetry in Inclusive $pp \rightarrow W(\mu\nu) + X$ Production at $\sqrt{s} = 7$ TeV,” CMS Analysis Note AN-10-199 (2010).
- [116] J. Alcaraz Maestre *et al.*, “Updated Measurements of the Inclusive W and Z Cross Sections at 7 TeV,” CMS Analysis Note AN-10-264 (2010).
- [117] Neal, R. M., “Bayesian Learning for Neural Networks,” Ph.D. Thesis, Dept. of Computer Science, University of Toronto (1994). <http://www.cs.utoronto.ca/~radford/bnn.book.html>
- [118] M. Pivk, F. R. Le Diberder, “sPlot: a statistical tool to unfold data distributions,” Nucl. Instrum. Meth. A555:356-369 (2005) arXiv:physics/0402083v3 [physics.data-an].
- [119] M. Pierini, M. Spiropulu, L. Vanelderen, S. Sekmen, *et al.*, “Measurement of kinematic properties of top and W+jets processes in the $\mu + \geq 3$ jets channel using sPlots” CMS Analysis Note, CMS-AN-2010-251 (2010).
- [120] S. Sekmen, S. Kraml, J. Lykken, F. Moortgat, S. Padhi, L. Pape, M. Pierini and H. B. Prosper *et al.*, “Interpreting LHC SUSY searches in the phenomenological MSSM,” arXiv:1109.5119 [hep-ph].
- [121] <https://twiki.cern.ch/twiki/bin/view/CMSPublic/PhysicsResultsSUS>
- [122] T. Junk, “Confidence level computation for combining searches with small statistics,” Nucl. Instrum. Meth. A **434**, 435 (1999) [hep-ex/9902006].
- [123] D. Alves, N. Arkani-Hamed, S. Arora, Y. Bai, M. Baumgart, J. Berger, M. Buckley and B. Butler *et al.*, “Simplified Models for LHC New Physics Searches,” arXiv:1105.2838 [hep-ph].
- [124] James O. Berger. “Statistical Decision Theory and Bayesian Analysis,” Springer-Verlag New York Inc. (1985).
- [125] Berger, J. O. and Bernardo, J. M. and Sun, D., “The formal definition of reference priors,” Annals of Statistics 2009, Vol. 37, No. 2, 905-938 (2009). [arXiv:0904.0156v1 [math.ST]]

BIBLIOGRAPHY

- [126] L. Demortier, S. Jain, H. B. Prosper, “Reference priors for high energy physics,” *Phys. Rev.* **D82**, 034002 (2010). [arXiv:1002.1111 [stat.AP]].
- [127] M. Pierini, H. B. Prosper, S. Sekmen, M. Spiropulu, “Priors for New Physics,” [arXiv:1108.0523 [physics.data-an]].
- [128] C. F. Berger, J. S. Gainer, J. L. Hewett and T. G. Rizzo, “Supersymmetry Without Prejudice,” *JHEP* **0902**, 023 (2009) [arXiv:0812.0980 [hep-ph]].
- [129] S. S. AbdusSalam, B. C. Allanach, F. Quevedo, F. Feroz and M. Hobson, “Fitting the Phenomenological MSSM,” *Phys. Rev. D* **81**, 095012 (2010) [arXiv:0904.2548 [hep-ph]].
- [130] CMS Collaboration, “Search for Supersymmetry at the LHC in Events with Jets and Missing Transverse Energy,” arXiv:1109.2352 [hep-ex].
- [131] James Berger, “The Bayesian Approach to Discovery,” <http://indico.cern.ch/conference0therViews.py?view=standard&confId=107747>
- [132] B. C. Allanach, “SOFTSUSY: a program for calculating supersymmetric spectra,” *Comput. Phys. Commun.* **143**, 305 (2002) [hep-ph/0104145].
- [133] F. Mahmoudi, “SuperIso v2.3: A Program for calculating flavor physics observables in Supersymmetry,” *Comput. Phys. Commun.* **180**, 1579 (2009) [arXiv:0808.3144 [hep-ph]].
- [134] G. Belanger, F. Boudjema, A. Pukhov and A. Semenov, “MicrOMEGAs: A Program for calculating the relic density in the MSSM,” *Comput. Phys. Commun.* **149**, 103 (2002) [hep-ph/0112278].
- [135] P. Bechtle, O. Brein, S. Heinemeyer, G. Weiglein and K. E. Williams, “Higgs-Bounds 2.0.0: Confronting Neutral and Charged Higgs Sector Predictions with Exclusion Bounds from LEP and the Tevatron,” *Comput. Phys. Commun.* **182**, 2605 (2011) [arXiv:1102.1898 [hep-ph]].
- [136] J.W. Gary, *et al.*, “Search for New Physics in Event with b-jets and Missing Transverse Energy with the 2011 Data Sample,” CMS Analysis Note, CMS-AN-2011-409 (2011).
- [137] <https://twiki.cern.ch/twiki/bin/view/CMS/ProductionSummer2011>
- [138] <https://twiki.cern.ch/twiki/bin/view/CMSPublic/SWGuideFastSimulation?rev=403>

BIBLIOGRAPHY

- [139] <https://twiki.cern.ch/twiki/bin/view/CMS/SusyPatLayer1DefV10?rev=13>
- [140] <https://twiki.cern.ch/twiki/bin/view/CMS/JetID>
- [141] Weiser, Christian. “A Combined Secondary Vertex Based B-Tagging Algorithm in CMS,” CMS Note, CMS-NOTE-2006-014 (2006).
- [142] <https://twiki.cern.ch/twiki/bin/viewauth/CMS/BTagPerformanceOP>
- [143] H. B. Prosper , S. Sekmen, N. Strobbe, L. Vaneldereren, “Bayesian Search Optimization for Models with Free Parameters,” CMS Analysis Note, CMS-AN-2011-351 (2011).
- [144] N. Strobbe., “Event selection optimization for (b-)jets plus lepton supersymmetry searches with the CMS detector,” M.Sc. Thesis, Universiteit Gent (2011).
- [145] H. B. Prosper, “The Random Grid Search: A Simple Way to Find Optimal Cuts,” Conference on Computing in High Energy Physics (CHEP 95), Rio de Janeiro, Brazil, September 1995.
- [146] R. Piessens, E. De Doncker-Kapenga, C. W. Überhuber, “QUADPACK: a subroutine package for automatic integration.” Springer, ISBN: 3-540-12553-1. 1983.
- [147] http://www.gnu.org/software/gsl/manual/html_node/QAGS-adaptive-integration-with-singularities.html